universität wien

DISSERTATION / DOCTORAL THESIS

Titel der Dissertation /Title of the Doctoral Thesis

„Galaxy evolution in the clusters RXJ1347-1145, CL1604+4304 and XMMUJ2235-2557 at 0.5<z<1.5“

verfasst von / submitted by

Lic. Jose Manuel Perez Martinez MA

angestrebter akademischer Grad / in partial fulfilment of the requirements for the degree of

Doktor der Naturwissenschaften (Dr. rer. nat.)

Wien, 2019 / Vienna 2019

Studienkennzahl lt. Studienblatt / degree programme code as it appears on the student record sheet:	A 796 605 413
Dissertationsgebiet lt. Studienblatt / field of study as it appears on the student record sheet:	Astronomie
Betreut von / Supervisor:	Univ.-Prof. Dipl.-Phys. Dr. Bodo Ziegler

Abstract

by Jose Manuel Perez Martinez

The evolution of galaxies across cosmic time requires several physical processes acting together in a non trivial way to reproduce the galaxy populations we see in the local Universe today. In clusters, these transformations are boosted by the influence of environmental effects acting on both the stellar structure and the gas reservoir. Kinematic scaling relations describe strong connections between physical properties that enable us to understand the interplay between the luminous and the dark matter of the Universe. The flat rotation curves of spiral galaxies provide us with a proxy, the maximum circular velocity, to trace the total mass of the galaxy (including dark matter) as well as to study its relation with respect to the galaxies' size and stellar mass (or luminosity). These three parameters allow us examine the evolution of the Tully-Fisher relation, the velocity-size relation and the angular momentum-stellar mass relation. In this thesis, I quantitatively investigate the kinematic status and evolution of galaxies in several clusters at $0.5<z<1.5$ using 2D and 3D spectroscopy data from the VLT and GTC observatories. At low to intermediate redshift, the fraction of regular rotators is lower in the cluster than in the field, showing no clear correlation with cluster-centric distance or density. This implies that cluster-specific interactions are ubiquitous and supports the scenario where several mechanisms are simultaneously at play. In addition, we find no significant statistical differences in the evolution of the studied scaling relations between the cluster and field environments until redshift 1. However, at the highest redshifts probed, I find a population of galaxies that is exceedingly luminous (in B-band) in the TFR, display smaller sizes than expected in the VSR, and follow a different trend in the angular momentum-stellar-mass redshift evolution with respect to the field. In this thesis I investigated the probable causes and implications of these findings in the context of galaxy evolution in clusters across cosmic time.

Acknowledgements

In first place, I would like to thank my supervisor, Bodo Ziegler, for his continued support and patience during the last four and a half years. You have introduced me to the wonders of the research in extragalactic astrophysics and, thanks to your guidance an encouragement, I have become a better scientist than I could imagine when I started. I would also like to thank Asmus Böhm, for his useful scientific advices in times of need, for his insights on the methods to investigate the kinematic evolution of galaxies, for a substantial amount of interesting non science-related conversations, and for the many, wild and extremely fun chess games that I have had the privilege to share with him. I would also like to thank Miguel Verdugo and Christian Maier for helping me to solve all kinds of scientific and technical problems during the writing of this thesis. Your availability for discussion and your willingness to help have eased this path more than you can imagine. I am very grateful for having the opportunity to work with Helmut Dannerbauer during the last six months at the IAC headquarters. You have definitely contributed to open my eyes to a new wavelength window of research, and showed me the key importance of international collaborations in astronomy. Last, but not least, I would like to thank Angeles Diaz and Carlos Hoyos for embarking me in this trip more than five years ago, when I was just a Master student looking for an astrophysics project and had no idea where this path was going to take me. In the following paragraphs, I will switch to Spanish to properly thank family and friends from Spain, but before that I would like to express my gratitude to Gabriel Pfüner, for being the best flat-mate I could have ever found in Austria, for many hilarious evenings in Vienna, and for being always available to give a helping hand whenever I need to fight with some Austrian bureaucracy.

Hace 5 años, cuando la oportunidad de desarrollar una tesis doctoral en Viena se presentó ante mí no dudaba de que ese era el camino correcto. Sin embargo, sí albergaba dudas sobre si sería capaz de realizarlo dejando atrás mi país, mis amigos y mi familia. Esta tesis es el resumen de casi 5 años de trabajo científico, pero también es un pequeño monumento a todo el apoyo que he recibido durante este periodo, sin el cual, nada de esto hubiera sido posible.

Me gustaría agrader a Javs y Jorgs por ofrecer el escondrijo como piso franco de jueguis de mesa, tardes de switch, pavo days y otras festividades de guardar siempre que me ha sido posible regresar a Madrid. A Pepe y Elena

por tener las puertas de la madriguera siempre abiertas, por organizar la inmensa mayoría de quedadas cada vez que volvía y por sus famosas fiestas temáticas. A los cuatro, gracias de nuevo, porque cada uno de esos pequeños momentos en fines de semana aislados han contribuido a que esta tesis se hiciera menos cuesta arriba muchos lunes. A Colin y Acero por las numerosas (aunque nunca suficientes) tardes de CiV y por su inestimable ayuda para superar momentos de frustración a través de la destrucción de incontables civilizaciones inocentes. A Claudia y Quereda por todas las conversaciones (a menudo absurdas) que hemos tenido durante estos años y por todas las risas y el buen rollo que sois capaces de transmitir a pesar de que al igual que yo, también os encontreis desplazados. A Ana por toda su sabiduría japonesa (y general) que, no voy a negarlo, me salvaron la vida durante mi mes en la tierra del Sol naciente (a tope con el yoshinoya!), aunque me temo que en breve voy a necesitar de tus consejos una vez más. A Jesús por aguantar en la distancia nuestras turras eternas (especialmente mías) y seguir queriendonos igual, que paciencia tienes pisha! A Kike, Ro y Miguel por tantos buenos momentos, tantas tardes de estudio y nervios compartidos y por tantas encendidas (pero amistosas) discusiones durante la carrera. A Carmen, Adrián, Miguel Angel, Clara, Marina y Teresa porque aunque nos veamos poco, siempre es un placer tomarnos unas cervezas juntos cada vez que surge la oportunidad. Y a la Agrupación Astronómica Antares UAM por ser el lugar donde tuve el privilegio de conocer a la mayoría de esta maravillosa gente. Gracias.

A toda mi familia, tíos y tías, primos y primas, por apoyarme en la distancia, por vuestro sentido del humor y por vuestra paciencia al escuchar mis historias. A mi hermana Carmen, por su risa contagiosa, por sus animos, por creer siempre en mí, y porque si el barco de la ciencia naufraga necesitaré una economista capacitada a mi lado para reconducir la situación. A mis padres, porque esta tesis ha estado en construcción 4 años y medio, pero ha sido vuestro trabajo, vuestro cariño y vuestro apoyo continuo durante los últimos 29 años lo que cimenta todo el edificio, y lo que a día de hoy sigue haciendo posible que yo pueda seguir construyendo pisos hasta llegar a las estrellas. Y por último pero no menos importante, gracias a Roncillo, porque llegaste como mascota y te marchaste como miembro de la familia. Me hubiera gustado que tuvieras la oportunidad de saborear un ejemplar de esta tesis. Gracias a todos.

Contents

List of Figures

To my parents and sister

"In a spiral galaxy, the ratio of dark-to-light matter is about a factor of ten. That's probably a good number for the ratio of our ignorance to knowledge. We are out of kindergarten, but only in about third grade."

Vera Rubin

"Exploration is in our nature. We began as wanderers, and we are wanderers still."

Carl Sagan

Chapter 1

Introduction

1.1 Galaxies: The building blocks of our Universe

Nowadays we know that galaxies are astronomical objects typically made of stars, interstellar gas, dust, and dark matter. However, almost one hundred years ago, the nature of galaxies, or spiral nebulae as they were called at that time, was still a matter of controversy. The question span around two opposing positions: Were these spiral nebulae part of the Milky Way or, on the contrary, were they independent objects with similar properties with respect to our own galaxy?. This was one of the central questions during the so-called "Great Debate" between Harlow Shapley and Heber Curtis in 1920, who respectively defended the positions stated above. However, it was not until the mid twenties that Edmund Hubble closed this debate by measuring the distance to the Andromeda galaxy using Cepheid variable stars. He found that the distance between Andromeda and our galaxy is much larger than the size of the Milky Way. These discoveries led to establish the Hubble law, a relation between the radial velocity of galaxies and their distances (Hubble 1929) which settled many of these nebulae as Milky Way like independent distant objects, and provided the first observational proof of the expansion of the Universe. These events marked the birth of a new astronomy branch exclusively dedicated to the study of galaxies which has been of key importance during the last century even though its understanding remains one of the central challenges of extragalactic astronomy up to date.

From a cosmological point of view, galaxies represent the “building blocks” of the large scale structure of the Universe. According to the standard ΛCDM cosmological model, all galaxies are embedded in dark matter halos that

have grown through gravitational collapse from initial small amplitude density fluctuations (Davis et al. 1985). The amplitude of these fluctuations decreases with increasing scale, which favours the formation of low-mass objects at the early stages of the universe (Lacey and Cole 1993). The hierarchical growth of structures predicts that many of these objects will end up merging with each other due to their mutual gravitational attraction, giving birth to more massive haloes. According to simulations, the majority of dark matter haloes are distributed in a three-dimensional filamentary structure called cosmic web (de Lapparent, Geller, and Huchra 1986, Bond, Kofman, and Pogosyan 1996), where the most massive haloes reside in the junctions between several filaments (i.e. clusters of galaxies), permanently accreting smaller objects and growing in mass. Although this theoretical framework has succeed in reproducing the dark matter haloes mass functions, it still struggles to incorporate the physics of baryons and successfully reproduce the observed visible properties of galaxies. The fundamental challenge is to reconstruct the stellar mass-assembly history through the observation of galaxies at various cosmic epochs to constrain models of galaxy evolution.

However, galaxies display a wide variety of behaviours in terms of luminosity, mass, color, structure, gas content, heavy-element enrichment, and environment, many of which, in turn, are strongly correlated with each other. In astronomy, we refer to these correlations between fundamental physical parameters as scaling relations. Investigating how the global properties of galaxies are changing with time requires observations over a wide range of lookback times. This will eventually lead us to understand how the galaxies were formed and how they evolved from the cosmic dawn to the present day. Astronomers have constructed a rich and detailed description of the galaxy population and its properties today thanks to the latest generation of wide-field surveys of the local Universe (e.g. the SDSS survey, Abazajian et al. 2003). Generally speaking, galaxies can be divided in two distinct types: Star-forming galaxies have blue colors, typically disk-like morphologies and a relatively high star formation rate (SFR), whereas quiescent galaxies have redder colors, more spheroidal morphologies, and a (near) absence of star formation. These results are crucial in terms of providing an endpoint for our description of the formation and evolution of galaxies. However, we ultimately strive to tell that story from beginning to end, and to do so we must probe the origin of the global patterns observed in the current galaxy population by looking back to a time before this description was already in place.

1.2 The star formation history of the Universe

The evolutionary path of galaxies between the high redshift and the local Universe is complex, with many different processes influencing galaxies across cosmic time. One of the key properties is the star formation rate (SFR), i.e. the amount of mass in the form of new stars that a galaxy is able to produce within a given period of time. In order to sustain this process, it is required the continuous consumption of large amounts of cold gas, that acts as the fuel for star formation. However, the amount of gas available within a galaxy may change with time not only as a result of star formation, but due to other internal processes that may decrease the gas supply via outflows (such as supernova explosions and AGN activity), as well as external processes that may increase the galaxy's gas reservoir (e.g. inflowing gas from the intergalactic medium or as a consequence of a gas-rich merger event). At the same time, the efficiency of star formation strongly depends on the local conditions such as the neutral gas surface density, the chemical enrichment, the temperature or the shear where it should happen (Leroy et al. 2008).

Madau and Dickinson (2014) investigated the star formation activity of field galaxies throughout cosmic time using several SFR indicators at different wavelengths. According to Fig. 1.1, z$\sim$2 (around 3.5 billion years after the Big Bang) marks the peak epoch of star formation in the history of the Universe, while the SFR density monotonically decreases by up to an order of magnitude by z=0. Some of the reasons proposed to explain this behaviour are that at z$\sim$2 star-forming galaxies have higher gas fractions than in the local Universe (Daddi et al. 2010, Tacconi et al. 2010; Tacconi et al. 2013, from CO surveys), while at the same time, the star formation efficiency may be higher due to the unstable nature of diks at this redshift (Hopkins et al. 2006, Kartaltepe et al. 2010) and the higher frequency of galaxy interactions causing the triggering of starburst events (Elbaz et al. 2007, Bournaud et al. 2014, Dannerbauer et al. 2014). On the other hand, these processes are no longer efficient in enhancing the star formation density of galaxies at higher redshift, when a turn over is observed towards lower values both from the simulation and observational point of view (Springel and Hernquist 2003, Madau and Dickinson 2014). In addition, the same processes that boost the star formation in galaxies at z$\sim$2 (inflowing gas, merger events, disk instabilities) may channel large amounts of gas towards the innermost regions of the galaxy, feeding the central black hole. In fact, the peak of star formation in the history of the Universe coincides with an epoch of rapid growth of black holes

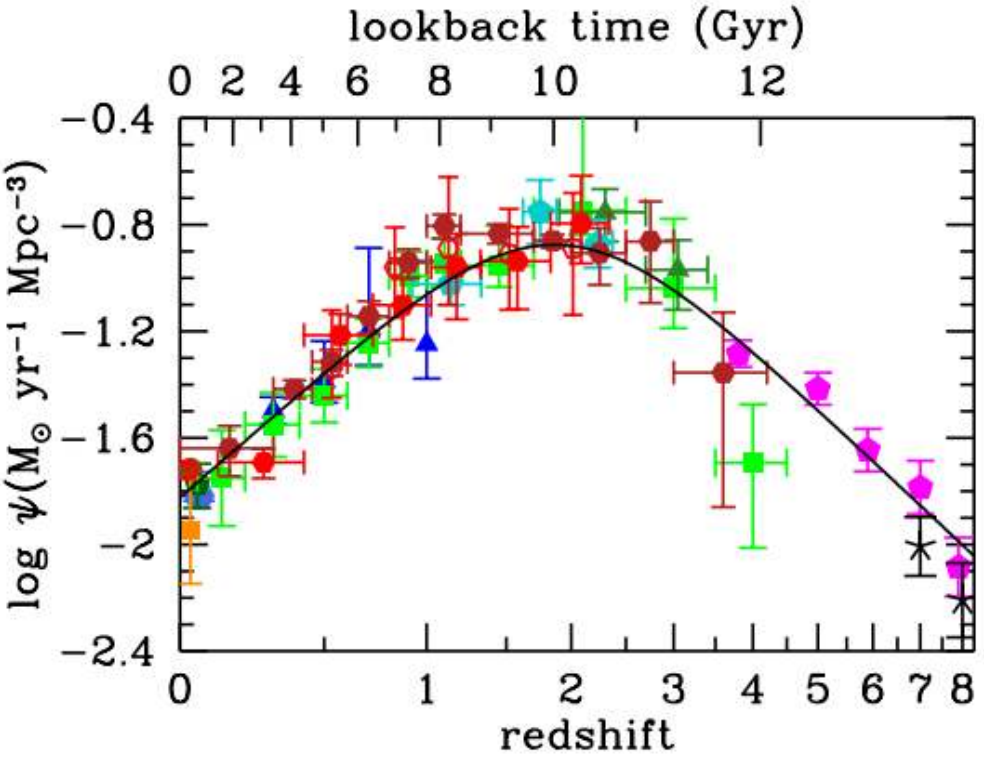

FIGURE 1.1: Star Formation history of the Universe. Green, blue (dark and light) and purple symbols are measurements from UV observations, while red and orange symbols coms from the IR. Figure taken from Madau and Dickinson (2014).

of galaxies, triggering violent episodes of AGN activity (z∼1–3, Wolf et al. 2003).

The majority of star-forming galaxies follow a tight power law relation between SFR and stellar-mass from the local Universe up to high redshift (Brinchmann et al. 2004, Elbaz et al. 2007, Koyama et al. 2013, Whitaker et al. 2014). These two quantities have a positive correlation with a typical intrinsic scatter of ∼0.3 dex encompassing most star-forming galaxies. This supports the idea that star formation is, in most cases, a continuous gentle process that progressively consumes the galaxies' gas reservoir during several billion years, and thus, astronomers have coined the term *main sequence* of star-forming galaxies to refer to this relation (Noeske et al. 2007). In fact, galaxies experiencing violent episodes of star-formation (starbursts) are identified as clear outliers of the main sequence, displaying very high SFR values (Daddi et al. 2007; Daddi et al. 2010). On the contrary, galaxies that are about to consume their gas reservoir abandon the main sequence towards low SFR values until they disappear of the diagram when no more star-formation is measurable in them. However, the zero point of the relation strongly evolves with redshift, reflecting the changes in the stellar populations and star-formation

throughout the history of the Universe (Speagle et al. 2014, Tomczak et al. 2016).

1.3 The morphology of galaxies

The morphology of a galaxy portrays the internal structure and distribution of its main baryonic components (i.e. stars, gas, and dust). Many efforts have been made to establish a morphology classification able to describe simultaneously both the appearance of galaxies and their probable structural evolution throughout the history of the Universe. One of the first attempts was done by Hubble (1926), who created a scheme that broadly separate galaxies into two groups according to their degree of roundness (ellipticals or disks), and add some other observational key characteristics to unfold these two general classes into a more precise morphological description (see Fig. 1.2). In the Hubble classification scheme, elliptical galaxies (E) are classified according to their axial ratio (b/a) and receive an integer index from 0 to 7 that reflects their similarity to an spherical distribution. The mathematical expression that accounts for this is:

$$n = 10(1 - \frac{b}{a}) \tag{1.1}$$

where a and b are the semi-major and semi-minor axes of the ellipsoid and n is the classification index. Therefore, an E0 galaxy would correspond to a spherical morphology while E7 would define an ellipsoid with $b/a = 0.3$. Beyond this point, an even flatter distribution of matter would define a transition type of galaxy between the triaxial distribution of elliptical galaxies and the approximate two-dimensional distribution of disks. These objects are called lenticular galaxies due to the similarities of their morphology with the shape of a lense, and are denoted by S0 in the Hubble scheme. This classification, however, depends on the inclination angle of the observed galaxies with respect to the line of sight, and therefore any measurement of b/a should take this into account.

On the other hand, the classification of spiral galaxies (S) is mainly based on the presence or lack of a central bar, the prominence of their bulges, and the number and distribution of the visible spiral arms. Therefore, spiral galaxies without a bar and with a decreasing presence of spiral arms and bulge-to-disk ratio can be classified as Sa, Sb or Sc, while barred spiral galaxies follow

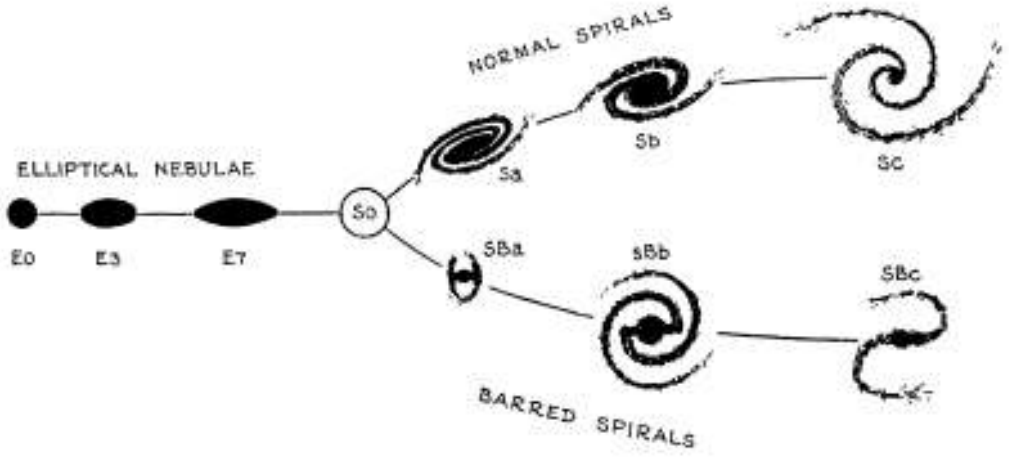

FIGURE 1.2: Hubble morphological classification of galaxies. Figure taken from Hubble (1936).

a similar scheme but adding the letter B to their nomenclature (i.e. SBa, SBb, SBc). This visual classification can be expanded by adding galaxy types that were not included at that time, such as bulgeless spirals with diffuse or broken arms (Sd), irregular galaxies (Im), dwarf galaxies (dE and dS), and low surface brightness galaxies (LSB).

Although Hubble's scheme is still used to describe the general morphological properties of galaxies, it is based on the visual inspection of these objects and, by definition, it is subject to observational biases and the subjective opinion of every observer. In order to provide a quantitative measurement of the structural properties of galaxies we should examine their light profiles. Sersic (1968) described the changes in the light intensity profiles of different galaxy as a function of radius through the following mathematical expression:

$$I_r = I_e \exp\left[-b_n\left(\left(\frac{r}{r_e}\right)^{1/n} - 1\right)\right] \tag{1.2}$$

where I_e is the surface brightness of the galaxy at the effective radius (r_e), n is the Sérsic index, and b_n is a polynomial with a dependence on n such that half of the total flux is always within r_e. The Sérsic model allows for a range of central light concentrations. For example, low n values result in flat galaxy cores and truncated light intensity profiles at $r > r_e$, while high n values produce high concentrations of light in the center of galaxies with very faint and extended light profiles at $r >> r_e$. Therefore, Eq. 1.2 reproduces

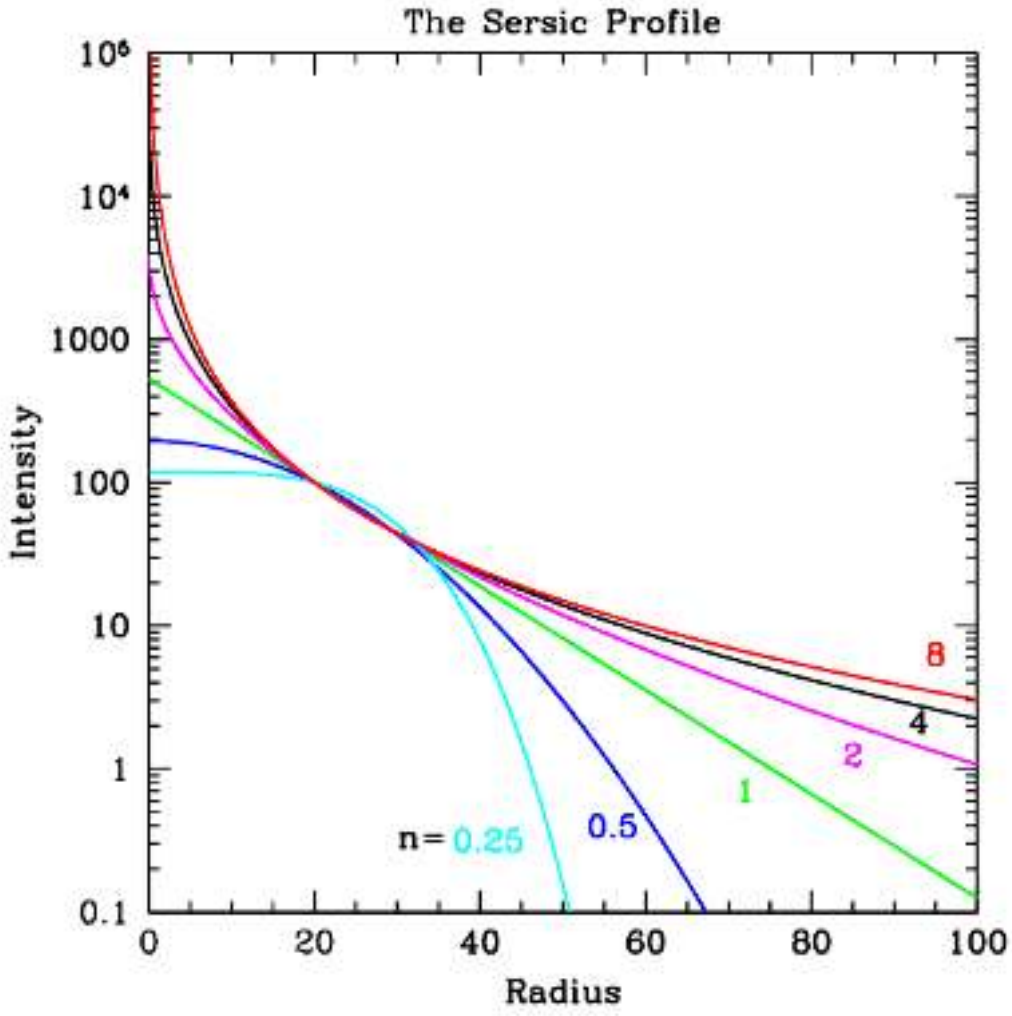

FIGURE 1.3: Light intensity profiles as a function of Sérsic index (n). Figure taken from Peng et al. (2010a).

a continuous sequence of light intensity profiles by changing the Sérsic index (see Fig. 1.3). Some of the examples show a Gaussian light distribution ($n = 0.5$), an exponential profile ($n = 1$) that is often used to match the light distribution of the disk component of spiral galaxies, and a de Vaucouleurs ($n = 4$, de Vaucouleurs 1948; de Vaucouleurs 1953) profile which provides an accurate description of the typical light distribution of elliptical galaxies. The Sérsic model provides a very good description of the light intensity profiles up to large galactocentric radii, so that the measurement of offsets in the observed light profile with respect to the models hints the probable presence of additional morphological features (bars, spiral arms, clumpy star forming regions, signs of minor mergers, etc).

1.4 Galaxy kinematics

The kinematics of galaxies reveals the orbits that stars, gas and dust particles follow within their host galaxy. In most cases, galaxies can be considered virialized systems either supported by random motions or by ordered rotation. Interestingly, these two behaviours generally match the two main populations of galaxies presented in previous sections.

In the case of spiral galaxies, rotation has been studied in depth during the last century and some of the discoveries in this field contributed to provide indirect proofs of the existence of dark matter. Measuring the rotation velocity (V_{rot}) throughout the whole radial profile of a galaxy yields its position-velocity diagram that, once it has been corrected from geometrical, atmospheric and instrumental effects, is transformed into the physical rotation curve (RC) of the object. Some of the first attempts to trace the RCs of spiral galaxies were done by observing the 21cm HI emission line on the Andromeda galaxy (van de Hulst, Raimond, and van Woerden 1957). These measurements were later improved by Roberts (1966) and Rubin and Ford (1970), who respectively studied the rotation curve of Andromeda in HI and the optical regime up to two degrees away from the center of the galaxy. In all cases, it was observed that V_{rot} linearly rises at small radius until it turns over and remains relatively constant at large distances from the center of the galaxy. These results were later generalized thanks to the works of Bosma (1978), who studied a sample of 25 nearby spiral galaxies proving that their rotation curves have flat rotation velocities to as far out as they could be measured. However, if the mass distribution of the galaxies followed the light profiles, a Keplerian decline in V_{rot} should be expected in the outskirts of the system. Therefore, flat rotation curves necessarily imply that, at large distances, the mass of the galaxy can not be accounted only by the the visible matter via light to mass ratios, but additional *invisible mass* (dark matter) is required (Freeman 1970, Faber and Gallagher 1979). In Fig. 1.4, we show the different mass components that account for the observed rotation curve of the Andromeda galaxy from Klypin, Zhao, and Somerville (2002) assuming the dark matter halo density profile given by Navarro, Frenk, and White (1997). Only by summing up all components (bulge, disk and dark matter halo) the models can reproduce the observations in the outskirts of the galaxy.

Once the flat rotation curves were discovered, several authors began to investigate how to empirically model the observed rotation curves so that V_{rot}

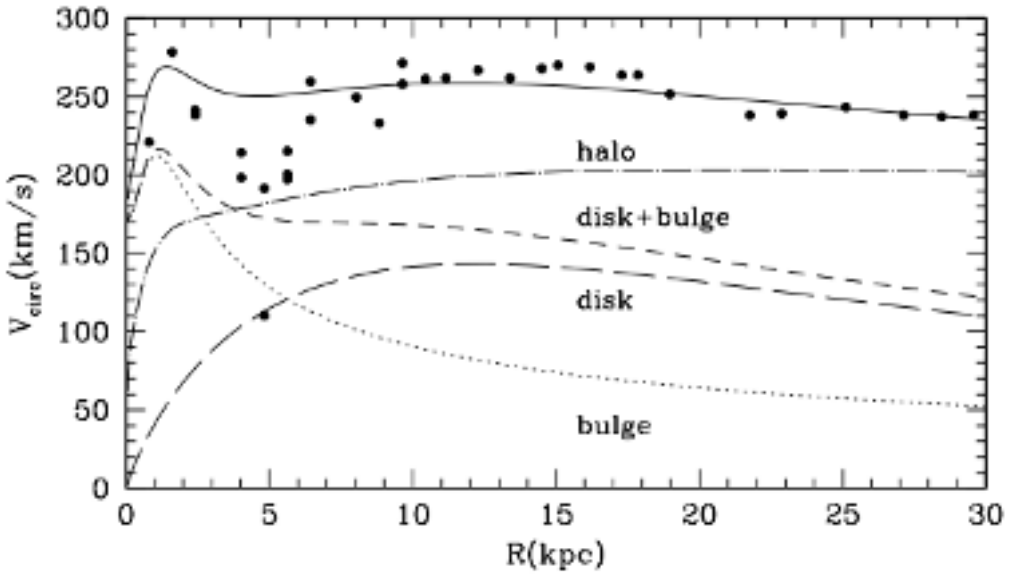

FIGURE 1.4: Rotation curve of the Andromeda galaxy. Each point corresponds with a V_{rot} measurement in CO ($r < 10$kpc) or HI ($r > 10$kpc). Figure taken from Klypin, Zhao, and Somerville (2002).

could be determined in cases were the amount of data was scarce, as well as to understand the underlying mass distribution of the population of spiral galaxies (Universal rotation curve by Persic, Salucci, and Stel 1996, and arctan models by Courteau 1997). These studies allowed to examine the dependencies between the rotation curve shape in the outer parts (mild upturn or downturn gradients) with other galaxy properties such as their stellar mass or luminosity, as well as they contributed to obtain systematic measurements of V_{rot} in a coherent way for large samples of galaxies.

Elliptical galaxies, on the other hand, are dominated by pressure support (quantified by their velocity dispersion σ). However, this simple picture where the kinematics of galaxies is either described by V_{rot} or σ does not reflect the complexity of orbital motions within galaxies. For example, elliptical galaxies may have a stellar component with residual rotation, while spiral galaxies will always have a varying degree of disordered motions measurable through the velocity dispersion of their gas or stellar component. Therefore, σ and V_{rot} can be used as proxies to determine if a given object is pressure or rotation supported. Galaxies with a ratio between these two quantities larger than one ($V_{rot}/\sigma > 1$) are considered to be dominated by rotation while values below that threshold correspond to pressure supported systems. However, this ratio may change during a galaxy's lifetime, since it is subject to internal and external events such as the accretion of mass from

the intergalactic medium, feedback processes causing outflows, mergers and other galaxy-galaxy interactions.

1.5 Galaxy evolution in clusters

The evolution of galaxies across cosmic time requires several different processes acting in a non trivial way to produce the galaxy populations of the local Universe today. The blue star-forming population of galaxies that dominates the universe at z>1 will be progressively transformed into a red quiescent population, giving birth to the bimodality we see in the local Universe (Baldry et al. 2006). To give some examples, mass growth (Cattaneo et al. 2011), morphological transformations (Mortlock et al. 2013), quenching of star formation (Peng et al. 2010b), and redistribution of angular momentum (Harrison et al. 2017) are some of the most important processes playing a role in galaxy evolution. In clusters, these transformations are boosted by the influence of environmental effects acting on both the stellar structure and the gas reservoir. Clusters of galaxies are the most massive systems in the Universe ($M_{cluster} > 10^{14} M_{\odot}$), containing hundreds of galaxies within Mpc scales. The high density conditions enhance the frequency with which interactions happen, either with other galaxies or with the intracluster medium (ICM). This makes clusters perfect laboratories to examine the outcome of such interactions and understand the transformation processes that drive the evolution of star-forming disk galaxies into passive spheroids.

The search for environmental effects and their relevance with respect to the physical parameters of the galaxy populations have been a subject of debate during the last forty years. Dressler (1980) investigated the galaxy populations as a function of the projected number density over a sample of 55 clusters, and found that the relative abundance of the different galaxy morphological types strongly varies between the cluster and field environment. In Fig. 1.5 we can see how the fraction of spiral and irregular galaxies (i.e. star-forming galaxies) drops from 60% in the low density regions ($\log \rho \sim 0$) to roughly 10% in the densest regions of the clusters. On the other hand, the fraction of elliptical galaxies experiences a similar change although in the opposite direction, growing from a $\sim$10% in the low density regions to $\sim$40% in the high density regime, while the lenticular galaxies (S0) experience a modest growth in the same conditions (from 30% to 50%). This evolution of the galaxy populations with density points towards a rapid morphological transformation when galaxies transit from the general field to the innermost regions of clusters. In addition, and as we have discussed in previous sections, the morphological classification reflects the distribution of visible matter within a galaxy, but different morphological types also carry several

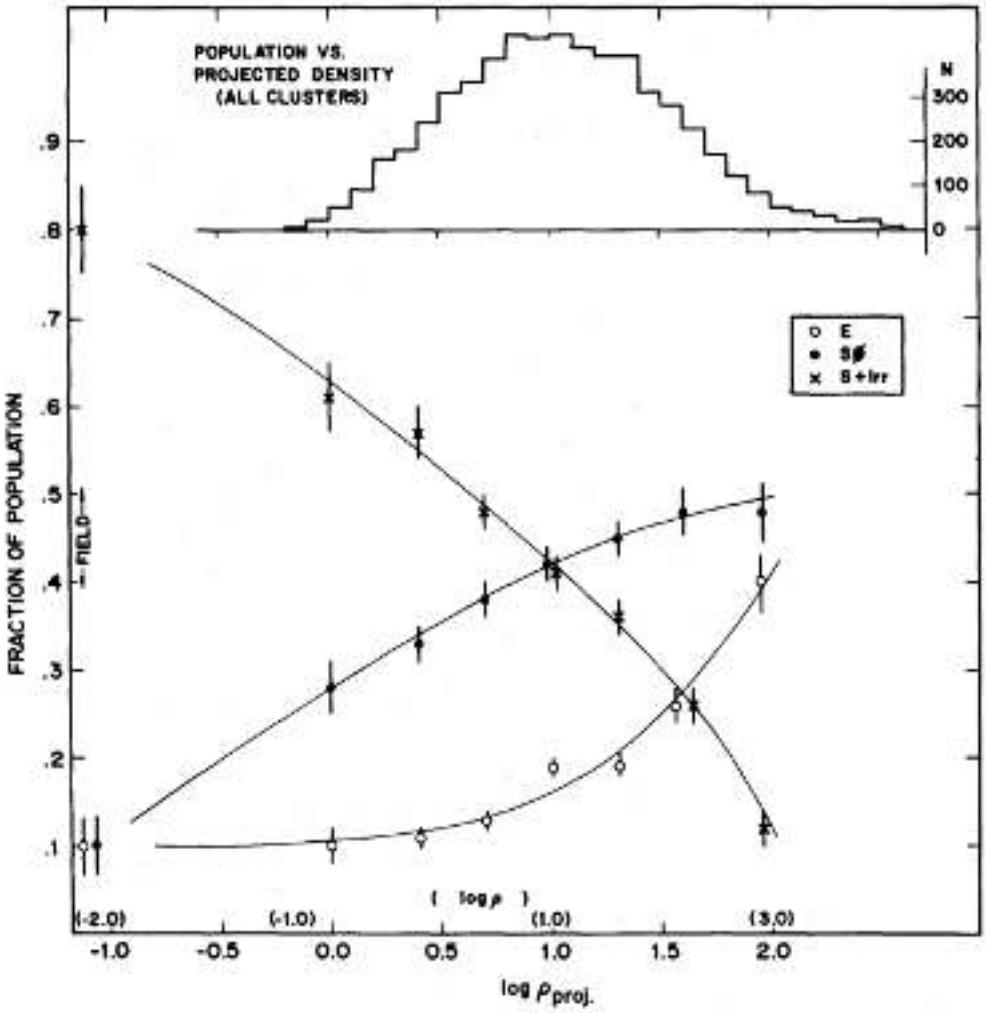

FIGURE 1.5: Morphological variation of populations of galaxies as a function of projected number density in clusters of galaxies. Figure taken from Dressler (1980).

key characteristics properties. The transformation of spiral galaxies into ellipticals implies not only the redistribution of the orbits of their stars (affecting its kinematics and angular momentum), but the depletion of their gas reservoir and the stop of star-formation. In fact, by z$\sim$1 early-type galaxies already dominate the cores of the most massive (and dense) galaxy clusters (Balogh et al. 2016) which may have finished their assembling processes only at z$\sim$1.5-2. This indicates that for a star-forming galaxy entering into the cluster environment at a given time, the maximum time-scale to achieve the bulk of these transformations is in the range of 1-2 Gyrs (Wetzel et al. 2013).

1.5.1 Cluster-specific interactions

In general, cluster-specific interactions can be classified in two groups: hydrodynamical and gravitational. The first includes interactions between the gas component of the galaxy and the hot X-ray emitting gas that fills the ICM, ram-pressure stripping and strangulation are the two main interactions of this kind. The second is mostly related to galaxy-galaxy interactions whose outcome strongly depends on the relative mass of the objects involved and their proximity. Tidal interactions, harassment and mergers enter into this category. A brief description of each of them is presented in the following paragraphs:

Ram pressure stripping: The ICM is the environment where galaxies move during their infalling paths towards the central areas of the cluster and it is filled with large amounts of high temperature gas. When a galaxy travels through this environment, the ICM exerts a dragging force (ram pressure) on the gas reservoir of the galaxy. If the drag overcomes the galaxy's gravitational potential, the gas particle will be no longer attached to the galaxy and will become part of the ICM (Gunn and Gott 1972). The strength of the ram pressure mainly depends on the density of the ICM and the infalling velocity of the galaxy ($P_{ram} = \rho_{ICM} V^2$). Therefore, if the binding force per unit area of the galaxy with respect to the particle is lower than P_{ram}, ram pressure stripping will be at play.

$$P_{ram} = \rho_{ICM} V^2 > 2\pi G \Sigma_{star} \Sigma_{gas} \tag{1.3}$$

where G is the gravitational constant, Σ_{star} is the stellar surface density and Σ_{gas} is the gas surface density. Since ρ_{ICM} increases towards the innermost regions of the cluster, infalling galaxies gradually experience an increasing P_{ram} gradient that will effectively start stripping their gas reservoir at a given clustercentric radius where ρ_{ICM} is high enough. The aftermath of these events are discussed in some of the publications of these thesis. However, in the long term, galaxies end up losing all their gas reservoir which cause the cessation of star-formation as well as the acquisition of redder colors, although the kinematics of their stellar component remains mostly unaffected. Some authors have proposed this mechanism as a possible channel for the increased fraction of lenticular galaxies in clusters (Bösch et al. 2013a). On the other hand, the compression of the inner disk during the early phases

of ram-pressure stripping can be responsible for triggering short-lived star-forming events (Kronberger et al. 2008, Ebeling, Stephenson, and Edge 2014, Steinhauser, Schindler, and Springel 2016, Ruggiero and Lima Neto 2017, Roman-Oliveira et al. 2019). This, however, strongly depends on the stellar-mass of the galaxy as well as on the orientation of the normal vector of the galaxy with respect to its velocity vector (Ruggiero 2019).

Strangulation: Most field galaxies are surrounded by a small halo composed of warm gas that has not yet fallen onto the disk or that has been expelled from it in previous feedback processes and awaits to be cooled down before falling back to the disk. This material can replenish the gas reserves of the interstellar medium (ISM) and prolong star-formation in the galaxy disk, whose star-forming life would last only for a few Gyrs if not counting with this extra gas supply and the additional inflows of pristine gas from the cosmic web. When a field galaxy enters into a dense environment, the heated gas of the ICM cuts external gas supplies in the form of inflows while at the same time, the dragging force we described above as part of the ram-pressure stripping act over the loosely bound galactic gas halo, heating up the gas reservoir and removing part of it in the process even in the outer parts of clusters, where ρ_{ICM} is still not very high. Hence, gas haloes can be depleted in short time-scales in clusters, so that the embedded gas in galaxy disks is the only fuel available to sustain star-formation. As the galaxy slowly runs out of gas, the SFR will gradually decline until it stops completely (Larson, Tinsley, and Caldwell 1980).

Nowadays, strangulation is one of the main mechanism responsible for the quenching of star-formation in galaxies. In fact, it has been shown that the specific star formation rate (SFR per unit mass, sSFR) of cluster galaxies is consistently lower with respect to their field counterparts, and that this effect is already in place beyond the virial radius of the cluster, where ρ_{ICM} is too low to trigger ram pressure stripping (Balogh, Navarro, and Morris 2000, van den Bosch et al. 2008, Wetzel et al. 2013, Peng, Maiolino, and Cochrane 2015, Maier et al. 2016, Maier et al. 2019).

Harassment and tidal interactions: The velocity of galaxies in clusters is similar to the velocity dispersion of the cluster, and typically ranges between $\sim 500 - 1000$ km/s, depending on how massive the cluster is. Therefore, galaxy-galaxy encounters in clusters are, by definition, high velocity interactions. While mergers are not very frequent under these conditions, the continuous exposition to high velocity fly-bys can destabilize the disks of spiral

galaxies in a cumulative process called harassment (Moore et al. 1996). As a consequence, the galaxy's gas component is heated up and in some cases even expelled from the disk, which hinders the star-formation in the galaxy. At the same time, the gravitational pull from the the fly-by galaxy may cause important distortions in the stellar disk such as tidal tails and streams, increasing the overall velocity dispersion of this component and initiating a process of morphological disk transformation towards a more spheroidal appearance. Harassment has proven to be particularly effective in low surface mass galaxies, which in conjunction with previous cluster-specific interactions can explain the large amount of dwarf spheroidals in dense environments (Moore et al. 1999, Mastropietro et al. 2005, Smith, Davies, and Nelson 2010). In extreme cases, a significant fraction of the galaxy can even become independent after a violent encounter in what it is called tidal stripping (Read et al. 2006).

Mergers: These kind of events require the collision of two or more galaxies that will result in a new one after at least one of the progenitors is absorbed by the remnant. In general, the stellar-mass ratio between the galaxies involved play an important role in the determination of the outcome. Following this criterion we can distinguish between major mergers for which the stellar-mass ratio of the merging objects is similar ($0.3 < M_1/M_2 < 1$), and minor mergers for which one of the progenitors is very massive compared to the other ($0 < M_1/M_2 < 0.3$). In the first case, although the collision between stars is highly unlikely, the stellar and gas component distribution of both galaxies is heavily distorted. As a consequence of the gas compression during the interaction, short powerful starburst can be created (Teyssier, Chapon, and Bournaud 2010, Hoyos et al. 2016). In addition, large amounts of gas are expelled to the ICM during the process as well as streams of stars. Elliptical galaxies usually are the end products of a major merger event (Naab and Burkert 2003) which implies a full morphological transformation and the quenching of star-formation of the progenitors. In some cases the channeling of gas towards the inner core of the galaxy during and after the interaction may feed the central black hole of the new system, triggering AGN activity that will heat up the remaining gas in the galactic halo.

Minor mergers, on the other hand, have a more subtle influence on the massive progenitor and the outcome also depends on the amount of gas of the progenitors at the time of the interaction. If the merger happens between gas-rich galaxies,the interaction is defined as a wet merger, while it is called

dry merger if the progenitors have been gas depleted prior to the interaction. The amount of gas of the progenitors has consequences for the survivability of the disk and the angular momentum of the more massive galaxy. Lagos et al. (2018) investigated the influence of minor mergers on the specific angular momentum using hydrodynamical simulations. They found that, while wet minor mergers do not significantly change the angular momentum of the galaxy (specially if the interaction happens in a co-rotating way), dry mergers may have a more prominent effect in decreasing it. The reason behind this difference is that wet mergers provide additional gas to the major body of the interaction and, given enough time, this gas will dynamically cool down, fall into the remnant and even facilitate further star-formation. At the same time this new material will contribute to maintain or even slightly increase the remnant's angular momentum. Dry mergers, on the other hand, add random motions without providing additional gas, so that the interaction with the kinematics and angular momentum of the massive galaxy can not be washed out easily. As we have stated before, the velocity of infalling galaxies in clusters is of the order of the cluster velocity dispersion ($\sim 500 - 1000$ km/s), which favours high-velocity fly-bys (harassment) but hinders merging events unless both galaxies follow radial orbits. Therefore, mergers in clusters are more frequent in intermediate density regions, where the galaxies have not yet sped up too much (Boselli and Gavazzi 2006, Tomczak et al. 2017).

1.6 Kinematic scaling relations

The relationship between baryonic and dark components in galaxies varies with the environment and cosmic time. Integrated properties such as galaxy luminosity, stellar mass and star formation activity are not sufficient to understand galaxy evolution in clusters, where interactions are very frequent. Subtle cluster-specific processes such as strangulation might be responsible for the early quenching of star formation for galaxies within massive clusters. However, in order to achieve a full transformation into passive ellipticals, we still need to comprehend the mechanisms that alter the kinematics of the cluster galaxies and rearrange their three-dimensional structure during their infalling phase. Processes like merging, harassment, ram pressure stripping are probably at act, but also other secondary processes such as the triggering of star formation due to tidal interactions or initial gas disk compression via ram-pressure might intervene in the stronger and accelerated evolution of galaxies living in clusters, although it is still unclear which one predominates. The kinematic scaling relations describe strong trends between physical properties that help us to understand the interplay between the luminous and the dark Universe.

The flat rotation curves of spiral galaxies provide us with a proxy, the rotation velocity (V_{rot}), to trace the total mass of the galaxy (including dark matter) as well as to study its relation with respect to several other baryonic parameters. Some of the key additional parameters that describe the physics of spiral galaxies are the disk size (through the effective radius, R_e, or scale length, R_d), and the stellar population content of the galaxy (via its luminosity or stellar-mass). The rotation velocity, the galaxy size and the luminosity (or stellar mass) conform a three-dimensional space (Koda, Sofue, and Wada 2000) from which several scaling relations can be studied: The Tully-Fisher relation (TFR, Tully and Fisher 1977), the velocity-size relation (VSR, Tully and Fisher 1977) and the Freeman's law between size and luminosity (Freeman 1970). In addition, different combinations between these parameters provide us with other interesting relations such as the angular momentum-stellar mass that are key to understand the processes of morphological transformation and mass redistribution that galaxies suffer during their lifetime. Some of these scaling relations are introduced in the following sections although major discussions in an evolutionary context is carried out throughout the several publications of this thesis in Chap. 2, 3, 4 and 5.

1.6.1 The Tully-Fisher and Velocity-size relation

The TFR is a well defined relation between V_{max} (taken as the rotation velocity in the flat part of the rotation curve) and the luminosity (L) of a spiral galaxy. Therefore, this relation can only be applied to regular rotating disks. It was first introduced by Tully and Fisher (1977) as a distance indicator and can be derived theoretically assuming that spiral galaxies are virialized systems and that the mass-to-light ratio (M/L) between different spirals is nearly constant. Observational studies usually present this relation in the form $L \propto AV_{max}^{\alpha}$, where A is the zero-point and α is the slope of the TFR. This relation has been investigated using several luminous matter indicators. For example, Pierce and Tully (1992) observed that α becomes smaller when taking redder luminosity bands. The luminosity in different bands is highly correlated with the stellar population distribution within the galaxy. Thus, the old stellar populations are given more weight in redder bands (which have more homogeneous M/L) while star-formation features have an important influence on bluer colors, which increases the scatter of the relation. The traditional luminosity TFR is a subset of a more fundamental relation between baryonic mass (stellar and gas content) and rotational velocity. These more general representations include the stellar-mass TFR (Bell and de Jong 2001, Pizagno et al. 2005, Reyes et al. 2011) and the total baryonic mass (i.e. gas + stars, McGaugh et al. 2000, McGaugh 2012, Lelli, McGaugh, and Schombert 2016), which recovers a linear relation over $\sim$5 order of magnitudes in baryonic mass and is useful to investigate galaxies with strong variations in their gas fractions. However, the gas mass fraction can only be observed directly for z$\sim$0 galaxies.

The TFR has been studied up to z$\sim$2 for field galaxies during the last decades (Ziegler et al. 2002, Kassin et al. 2007, Miller et al. 2011, Böhm and Ziegler 2016, Tiley et al. 2016, Harrison et al. 2017, Pelliccia et al. 2017, Übler et al. 2017). Furthermore, Dutton et al. (2011) showed that the observed evolution of the scaling relations involving circular velocity, mass, and size are consistent with a simple CDM-based model of disks growing inside evolving Navarro-Frenk-White dark matter haloes (NFW, Navarro, Frenk, and White 1997). However, comparative studies in the cluster environment are less frequent and usually stop at z$\sim$1. Up to that redshift some authors have reported similar evolution in the cluster and field B-band TFR (Ziegler et al. 2003, Jaffé et al. 2011, Bösch et al. 2013b), or a mild luminosity enhancement (Bamford et al. 2005) and larger TFR scatter in the cluster environment

(Moran et al. 2007, Pelliccia et al. 2019). In this thesis (Chap. 2, 3, 4, and 5) I will examine the different representations of the TFR in clusters at 0.5<z<1.5, shedding light to the kinematic evolution of galaxies and their stellar populations with lookback time.

The velocity-size relation links the growth of discs to the total mass of the galaxy and it is one of the predictions of the CDM cosmological model in relation to the hierarchical growth of structures (Dutton et al. 2011). However, this correlation shows a wider scatter than the TFR (Courteau et al. 2007, Hall et al. 2012). This is partially explained due to the ambiguities in defining the size of a galaxy (R_e, R_d, or other prescriptions) at different wavelengths taking into account the evolution and distribution of the different stellar populations within the galaxy. Furthermore, the presence of a bulge component, and additional selection effects (surface brightness limits) may contribute to hinder its study (Meurer et al. 2018, Lapi, Salucci, and Danese 2018). Nevertheless, in the context of galaxy evolution, this scaling relation remains one of the tools to look for environmental imprints on the disks of galaxies as it is discussed in the following chapters.

1.6.2 The angular momentum

The angular momentum (J) simultaneously connects all the relevant parameters involved in the previous scaling relations, i.e. stellar-mass, size, and rotation velocity. The transference of angular momentum from the dark matter halo to the baryonic component is key to understand the early stages of galaxy formation. The specific angular momentum defined as j_*=J/M_* has proven to be a fundamental quantity to explore galaxy evolution and morphological transformation. Fall (1983) first found a tight relation between j_* and M_* with the form $j_* \propto M^{2/3}$. Its normalization depends on the galaxy morphological type, with parallel sequences towards lower specific angular momentum values for larger bulge-to-disk ratios and early type galaxies, yielding a reduction of angular momentum of up to an order of magnitude in the latter case (Romanowsky and Fall 2012, Fall and Romanowsky 2013; Fall and Romanowsky 2018). The easiest way to compute the specific angular momentum directly from the fundamental observables mentioned above is to use the approximate estimator propose by Romanowsky and Fall (2012):

$$j_* = k_n C_i v_s R_e \tag{1.4}$$

where R_e is the effective radius of the galaxy, v_s is the observed rotation velocity at some arbitrary radius, C_i is an inclination correction factor and k_n is a numerical factor that takes into account the current morphology of the galaxy approximated by its Sérsic index (n) in the following way:

$$k_n = 1.15 + 0.029n + 0.062n^2 \tag{1.5}$$

Spiral galaxies display characteristic exponential surface brightness profiles in most cases ($n \sim 1$). Furthermore, k_n is relatively insensitive to small variations in the surface brightness profile so that n values in the range 0.5<n<1.5 will only introduce small variations in the value of k_n (up to 7%). If, for simplicity, we assume that n=1 for all disks independently of their bulge-to-disk ratio we end up with:

$$j_* \approx 2C_i v_s R_d \tag{1.6}$$

where R_d is the disk scale-length and $R_d \approx 1.678R_e$. Additionally, we may consider that the observed rotation velocity is usually corrected from inclination and seeing effects so that in the end $V_{max} \approx C_i v_s$, and thus $j_* \approx 2V_{max}R_d$. This approach yields the $j_* - \log M_*$ relation as a correlation between two independent variables and makes possible to study the evolution of galaxies using three of their most important properties (i.e. stellar-mass, size, and rotation velocity). It is expected that at higher redshift galaxies display lower angular momentum than in the local Universe (Mo, Mao, and White 1998), although its exact dependency is still unclear. In this thesis we will also investigate possible differences in the specific angular momentum between field and cluster galaxies and their evolutionary paths across cosmic time (see Chap. 4).

Chapter 2

Paper I

Title: Galaxy kinematics in the XMMU J2235-2557 cluster field at z$\sim$1.4

Authors: J. M. Pérez-Martínez, B. Ziegler, M. Verdugo, A. Böhm, M. Tanaka

Year: 2017

Journal: Astronomy and Astrophysics. Published online on September 22nd 2017.
DOI: https://doi.org/10.1051/0004-6361/201630165

Short description: In this work we took spatially resolved slit FORS2 spectra for a sample of cluster galaxies at z$\sim$1.4 using the ESO Very Large Telescope. Our spectroscopy was complemented with deep high resolution HST/ACS and HAWKI imaging that we used to derive accurate structural parameters for our objects. We analyzed the ionized gas kinematics by extracting rotation curves from the [OII]λ3727 emission line in the 2D-spectra. These rotation curves were used to derive the intrinsic maximum rotation velocity (V_{max}) after taking into account all geometrical, observational, and instrumental effects. We studied the B-band and stellar-mass Tully-Fisher relation as well as the velocity-size relation and discuss the implications of our results in the context of galaxy evolution in high redshift clusters.

Personal Contribution: I was responsible of the full data reduction an analysis of the spectroscopic dataset involved in this study (ID 091.B-0778(B)), which include the determination of redshifts, the extraction of position-velocity diagrams, and the determination of the maximum rotation velocity for every object. In addition, I used the high resolution reduced HST and HAWKI photometry to compute the structural parameters of the objects under scrutiny

by applying successive surface brightness profiles. Finally, I had a leading role in the discussion of the manuscript and carried out most of the writing process.

A&A 605, A127 (2017)
DOI: 10.1051/0004-6361/201630165

Astronomy & Astrophysics

Galaxy kinematics in the XMMU J2235-2557 cluster field at z ∼ 1.4⋆

J. M. Pérez-Martínez[1], B. Ziegler[1], M. Verdugo[1], A. Böhm[2], and M. Tanaka[3]

[1] Department of Astrophysics, University of Vienna, Türkenschanzstr. 17, 1180 Vienna, Austria
e-mail: jm.perez@univie.ac.at
[2] Institute for Astro- and Particle Physics, University of Innsbruck, Technikerstr. 25/8, 6020 Innsbruck, Austria
[3] National Astronomical Observatory of Japan 2-21-1 Osawa, Mitaka, 181-8588 Tokyo, Japan

Received 29 November 2016 / Accepted 19 May 2017

ABSTRACT

Aims. The relationship between baryonic and dark components in galaxies varies with the environment and cosmic time. Galaxy scaling relations describe strong trends between important physical properties. A very important quantitative tool in case of spiral galaxies is the Tully-Fisher relation (TFR), which combines the luminosity of the stellar population with the characteristic rotational velocity ($V_{\rm max}$) taken as proxy for the total mass. In order to constrain galaxy evolution in clusters, we need measurements of the kinematic status of cluster galaxies at the starting point of the hierarchical assembly of clusters and the epoch when cosmic star formation peaks.

Methods. We took spatially resolved slit FORS2 spectra of 19 cluster galaxies at $z \sim 1.4$, and 8 additional field galaxies at $1 < z < 1.2$ using the ESO Very Large Telescope. The targets were selected from previous spectroscopic and photometric campaigns as [OII] and H_α emitters. Our spectroscopy was complemented with HST/ACS imaging in the *F775W* and *F850LP* filters, which is mandatory to derive the galaxy structural parameters accurately. We analyzed the ionized gas kinematics by extracting rotation curves from the two-dimensional spectra. Taking into account all geometrical, observational, and instrumental effects, we used these rotation curves to derive the intrinsic maximum rotation velocity.

Results. $V_{\rm max}$ was robustly determined for six cluster galaxies and three field galaxies. Galaxies with sky contamination or insufficient spatial rotation curve extent were not included in our analysis. We compared our sample to the local *B*-band TFR and the local velocity-size relation (VSR), finding that cluster galaxies are on average 1.6 mag brighter and a factor 2–3 smaller. We tentatively divided our cluster galaxies by total mass (i.e., $V_{\rm max}$) to investigate a possible mass dependency in the environmental evolution of galaxies. The averaged deviation from the local TFR is $\langle \Delta M_B \rangle = -0.7$ for the high-mass subsample ($V_{\rm max} > 200$ km s^{-1}). This mild evolution may be driven by younger stellar populations (SP) of distant galaxies with respect to their local counterparts, and thus, an increasing luminosity is expected toward higher redshifts. However, the low-mass subsample ($V_{\rm max} < 200$ km s^{-1}) is made of highly overluminous galaxies that show $\langle \Delta M_B \rangle = -2.4$ mag. When we repeated a similar analysis with the stellar mass TFR, we did not find significant offsets in our subsamples with respect to recent results at similar redshift. While the *B*-band TFR is sensitive to recent episodes of star formation, the stellar mass TFR tracks the overall evolution of the underlying stellar population. In order to understand the discrepancies between these two incarnations of the TFR, the reported *B*-band offsets can no longer be explained only by the gradual evolution of stellar populations with lookback time. We suspect that we instead see compact galaxies whose star formation was enhanced during their infall toward the dense regions of the cluster through interactions with the intracluster medium.

Key words. galaxies: kinematics and dynamics – galaxies: clusters: individual: XMMU J2235.3-2557 – galaxies: high-redshift – galaxies: evolution

1. Introduction

In the past years, we have achieved a good understanding of galaxy evolution from both observations and simulations. To mention a few examples, it is well established now that cosmic star formation (SF) rises strongly out to redshift 1 (Lilly et al. 1996) and then turns into a plateau (Bouwens et al. 2007). At similar epochs, quasar (AGN) activity of L_*-galaxies peaks (Hasinger et al. 2005). Deep fields reveal that $z = 1$ galaxies can already have obtained both regular elliptical and spiral morphologies. Hubble volume simulations are able to reproduce these basic facts (Angulo & White 2010). On the other hand, difficulties persist in some aspects like the mass-dependent shutting-down of SF by feedback processes (Bower et al. 2012) and the gas infall rate sustaining too high SF rates (Tonini et al. 2011). While it is possible to empirically model certain aspects (Peng et al. 2010), we still lack knowledge of the underlying physical mechanisms. For example, the relative contributions to galaxy mass growth by major mergers and gas accretion (Dekel et al. 2009) are still controversial.

A very important quantitative tool in case of spiral galaxies is the Tully-Fisher relation (TFR), which combines the luminosity of the stellar population (SP) with the characteristic rotational velocity taken as proxy for the total mass (including dark matter). It is well established in the local Universe (Pierce & Tully 1992) and was examined for evolution in recent years out to redshift 1, including work by our own group (Ziegler et al. 2003; Böhm et al. 2004; Böhm & Ziegler 2007, 2016).

The traditional TFR is a subset of a more fundamental relation between baryonic mass (stellar and gas content) and rotational velocity. However, the gas mass fraction can only be observed directly for $z \sim 0$ galaxies. For nearby massive L^*-galaxies only a mild brightening was detected that translates into little overall evolution in the baryonic TFR (McGaugh et al. 2000). At higher redshift, Puech et al. (2010) constructed this relation by converting multicolor photometry into stellar masses

⋆ Based on observations with the European Southern Observatory Very Large Telescope (ESO-VLT), observing run ID 091.B-0778(B).

A&A 605, A127 (2017)

assuming some SP model and estimating the gas mass fraction, finding no evolution up to $z \sim 0.6$. This indicates that a significant fraction of spirals have well-established disks at $z = 1$ and do not undergo major mergers until $z = 0$. Dutton et al. (2011) furthermore showed that the observed evolution of the scaling relations involving circular velocity, mass, and size are consistent with a simple CDM-based model of disks growing inside evolving Navarro-Frenk-White (NFW) dark matter haloes. However, challenging measurements of 2D velocity fields at $z \approx 0.5$ reveal disturbances that can be explained by ongoing mass growth through accretion or minor mergers (Puech et al. 2008; Kutdemir et al. 2008; Kutdemir et al. 2010).

In contrast, massive SF galaxies around $z \geqslant 2$ can display various kinematic behaviors from disk rotation through dispersion dominance to major mergers (e.g., Genzel et al. 2006; Förster Schreiber et al. 2009; Lehnert et al. 2009). It was recently found by Wisnioski et al. (2015) using data from the $KMOS^{3D}$ survey that 93% of galaxies at $z \sim 1$ and 74% of galaxies at $z \sim 2$ are rotationally supported, as determined from a continuous velocity gradient and $v_{\rm rot}/\sigma_0 > 1$, while they showed a disk fraction of 58% when applying the additional stricter criteria that the projected velocity dispersion distribution peaks on or near the kinematic center, the velocity gradient is measured along the photometric major axis (for inclined systems), and the kinematic centroid is close to the center of the galaxy continuum. In contrast, applying the morpho-kinematic classification to a $KMOS^{3D}$ subsample, Rodrigues et al. (2017) found that only 25% of $z \sim 1$ galaxies are virialized spirals according to their morpho-kinematic classification. Simons et al. (2016) studied 49 galaxies from CANDELS fields with the Keck/MOSFIRE spectrograph and found that high-mass galaxies ($\log M/M_\odot > 10.2$) at $z \sim 2$ are generally rotationally supported and fall on the TF relation, large portion of less massive galaxies at this epoch are in the early phases of assembling their disks.

A sample of 14 galaxies at $z \sim 2$ was studied by Cresci et al. (2009), who found a significant offset in the M_*-TFR with increased scatter compared to local samples, which is even more prominent in the $z = 3$ study of Gnerucci et al. (2011). This implies a strong evolution within 2–3 Gyr with massive SF galaxies changing their dynamical state dramatically before settling into a more quiescent epoch at $z = 1$. This demands thorough measurements of spatially resolved emission lines of galaxies at $z = 1$–2 in order to understand this transition and its possible causes. A first study by Miller et al. (2012) exploited ultradeep Keck spectroscopy of the most suitable targets in five deep fields (EGS, SSA22, GOODS N&S, and COSMOS) that benefit from multi-wavelength coverage. They found that most galaxies follow an M_*-TFR with a mild offset but strongly increased scatter compared to the local TFR. In a similar way, Vergani et al. (2012) found a lack of any strong evolution of the fundamental relations of star-forming galaxies in at least the past 8 Gyr using a sample of 46 galaxies at $1 < z < 1.6$ from MASSIV (Mass Assembly Survey with SINFONI in VVDS). In contrast, Tiley et al. (2016) found an offset of the TFR for rotationally supported galaxies at $z \sim 1$ to lower stellar mass values (-0.41 dex) for a given dynamical mass but no significant offset in the absolute K-band TFR over the same period, contrary to some previous studies conducted at similar redshift but in agreement with the predictions of hydrodynamical simulations of EAGLE.

Most of these studies were restricted to the field population, while in clusters, additional specific effects should affect the content and structure of galaxies. Galaxy clusters provide special environments to test galaxy evolution across different cosmic epochs. Compared to the field, the number density of galaxies is high, as are the relative velocities. The gravitational potential of a cluster is filled by the intracluster medium (ICM), a hot X-ray emitting gas, and the overall mass-to-light ratio is much higher than for the individual galaxies, indicating the presence of vast amounts of dark matter. This environment exerts a strong influence on the evolution of the cluster galaxies superposed on the (field) evolution that arises from the hierarchical growth of objects and the declining star formation rates over cosmic epochs. In addition to tidal interactions between galaxies, including merging, cluster members are affected by cluster-specific phenomena related to the ICM (such as ram pressure stripping) or the structure of the cluster (such as harassment). Imprints of these interactions can be seen not only in present-day clusters, but they also manifest themselves in a strong evolution of the population of cluster galaxies. One example is the photometric Butcher-Oemler effect of an increasing fraction of blue galaxies with redshift (Butcher & Oemler 1978), implying a rising percentage of star-forming galaxies.

However, comparisons between the TFRs of cluster and field galaxies show no clear results. Milvang-Jensen et al. (2003) and Bamford et al. (2005) found higher B-band luminosities in clusters compared to the field, while Moran et al. (2007) presented a larger scatter for cluster galaxies. On the other hand, cluster and field populations follow the same trends with no significant differences between these two environments according to Ziegler et al. (2003), Nakamura et al. (2006), Jaffé et al. (2011), Mocz et al. (2012), and Bösch et al. (2013). These discrepancies may stem from the necessity to use only regular rotation curves (RC) for a proper TF analysis that is based on the virial theorem.

In order to extend such measurements to higher redshifts and to investigate possible biases, we here present a kinematic study of the massive cluster XMMU J2235-2557 (Mullis et al. 2005) at $z \sim 1.4$. Making use of the multiwavelength data including HST imaging (Rosati et al. 2009; Strazzullo et al. 2010), which allows determining morphologies and accurate deriving of structural parameters (needed for a proper kinematic analysis), we scrutinize the environmental dependence of disk galaxy scaling relations at the highest redshift to date.

The structure of this paper is as follows: in Sect. 2 we describe the target selection, observation conditions, and spectroscopic data reduction. The description of the photometric properties of our sample and details on the derivation of the structural parameters and maximum rotation velocities are shown in Sect. 3. We present and discuss our results in Sects. 4 and 5, followed by a short summary in Sect. 6. Throughout this article we assume a Chabrier (2003) initial mass function (IMF) and adopt a flat cosmology with $\Omega_\lambda = 0.7$, $\Omega_{\rm m} = 0.3$, and $H_0 = 70\ {\rm km\,s^{-1}\,Mpc^{-1}}$. Magnitudes quoted in this paper are in the AB system.

2. Sample selection and observations

We carried out multi-object spectroscopy (MXU) with FORS2 between September 2013 and July 2014 to obtain the spectra of 27 galaxies with one mask. We chose the holographic grism 600z+23, which covers ~3300 Å in the wavelength range 7370−10 700 Å. The slits were tilted and aligned to the apparent major axis of the targets in order to minimize geometrical distortions. Slit tilt angles θ were limited to $|\theta| < 45^{\rm o}$ to ensure a robust sky substraction and wavelength calibration. We used a slit width of $0.7''$, which delivers an instrumental resolution of $\sigma_{\rm ins} = 65\ {\rm km\,s^{-1}}$. This configuration yielded a spectral resolution of $R \sim 1400$ and an average dispersion of 0.81 Å/pix

Table 1. Summary of the imaging data used in this work.

Telescope	Instrument	Filter	Exp. time (s)	PSF *FWHM* (″)	PID
VLT	VIMOS	*U*	21 600	0.80	079.A-0758
...	FORS2	*B*	1590	0.72	087.A-0859
...	...	*R*	2250	0.75	072.A-0706, 073.A-0737
...	...	*z*	1200	0.40	274.A-5024, 091.B-0778
...	HAWKI	*J*	10 560	0.47	060.A-9284(H)
...	...	*Ks*	10 740	0.32	...
CTIO/Blanco	ISPI	*H*	1200	1.07	2009B-0484
HST	ACS/WFC	*F775W*	13 500	0.10	10496, 10531, 10698
...	...	*F850LP*	14 400	0.10	...
Spitzer	IRAC	3.6 μm	6262	1.95	20760
...	...	4.5 μm	6262	2.02	...

with an image scale of 0.25″/pixel. The total integration time for the MXU observations was 9 h per target. In order to diminish the number of cosmic ray hits in our spectra, the observations were divided into 12 observing blocks (OBs) of one hour each, with three subexposures of 15 min per OB plus overheads. We achieved seeing conditions of 0.73 arsec FWHM on average.

The primary targets for the kinematic analysis were 15 cluster galaxies with measured spectroscopic redshifts and [OII]λ3727 Å emission. These galaxies were extracted from two catalogs of previous spectroscopic campaigns in the same cluster field provided by M. Tanaka & V. Strazzullo (priv. comm.). Another set of 5 galaxies with photometric redshift from deep narrow-band imaging corresponding to the rest-frame wavelength of Hα were selected from Grützbauch et al. (2012) at the cluster redshift. The remaining available mask space was filled with galaxies of disk-like appearance and appropriate position angle, but unknown redshift, yielding 27 targets in total.

We performed the spectroscopic data reduction mainly using the ESO-REFLEX pipeline for FORS2 (version 1.19.4). The main reduction steps were bias subtraction, flat normalization, and wavelength calibration. The last was improved by removing some lines from the catalog of arc lines. Additionally, we performed bad pixel and cosmic ray cleaning by coadding the exposures with a sigma-clipping algorithm using IRAF. We show the coordinates, redshifts, rest frame colors, and magnitudes of our final sample in Table A.1.

3. Methods

3.1. Imaging and photometry

To complement the spectroscopy, we made use of imaging data from a variety of sources, including HST/ACS (*F775W* and *F850LP*), VLT/FORS2 (*B*, *R*, *z*-bands), VLT/VIMOS (*U* band), VLT/HAWKI (*J* and *Ks* bands), CTIO/ISPI (*H* band), and *Spitzer* IRAC (3.6 μm and 4.5 μm), encompassing thus from the rest-frame UV to the near-infrared (NIR) at the cluster redshift. The characteristics of these datasets are described in Table 1.

The HAWKI data reduction is described in Lidman et al. (2008) and the processed images were subsequently released as Phase 3 products in the ESO archive, from where we retrieved them. Zero-points were also provided in the Vega system, which we transformed into the AB system.

The FORS2 and VIMOS images were also retrieved from the ESO archive as raw data. Similarly, the CTIO-Blanco/ISPI *H*-band raw frames were downloaded from the NOAO science archive. These datasets were processed with the THELI pipeline (Schirmer 2013), which takes care of all basic reduction steps as well as the astrometric calibration and coaddition. Photometric calibration for the FORS2 *B* and *R* and the VIMOS *U*-band images was performed using a two step approach. First, zero-points were fixed to the official zero-points available at the ESO webpages. However, noticeable differences were detected in the color of stars in comparison to stellar libraries (Pickles 1998). We therefore produced synthetic colors for all available bands and compared them to the observed colors using the stellar locus method (e.g., Kelly et al. 2014), adjusting them until all differences were minimal. The applied corrections ranged from 0.3 to 0.6 mag.

There was no zero-point available for the FORS2 *z* band. Fortunately, the filter transmission curve is nearly identical to the HST/ACS *F850LP* filter available for a significant part of the field. Therefore the FORS2 *z* band was calibrated against that latter dataset. The ISPI H band was calibrated using 2MASS stars available in the field and transformed to the AB system. The remaining space-based images were retrieved fully processed and calibrated, so that no additional steps were necessary before performing the photometry.

The spatial coverage of the different datasets is shown in Fig. 1, where we also mark the targets of the spectroscopic campaign. Clearly, not all galaxies have measurements in all bands. However, they do have enough measurements across a wide wavelength range to reliably determine all parameters necessary for our analysis.

Because of the varying depth, field of view, point-spread function (PSF), pixel scales, and quality of the imaging, special care must be taken in performing the photometry for our target galaxies. We therefore deviated slightly from the standard approaches that use more homogeneous datasets. In particular, we chose to forego degrading the high-quality imaging (HST and HAWKI) to the worst seeing. We did not rebin the images to match the pixel sizes of the rest of the imaging either, as required by dual-band photometry. Instead, we chose to measure magnitudes within an elliptical Kron aperture (Kron 1980) matched to the seeing in each image. To calculate the size of the Kron aperture, we used SExtractor (Bertin & Arnouts 1996) in the high-quality data where we measured the coordinates, the Kron radius, the ellipticity, the position angle, and the Kron magnitudes (`MAG_AUTO`). These parameters where passed to the python `PHOT_UTILS` tools, which replicates many of the functionalities found in SExtractor in a more flexible environment.

To calculate by how much the Kron apertures need to grow to take into account the different seeing values in the other bands,

A&A 605, A127 (2017)

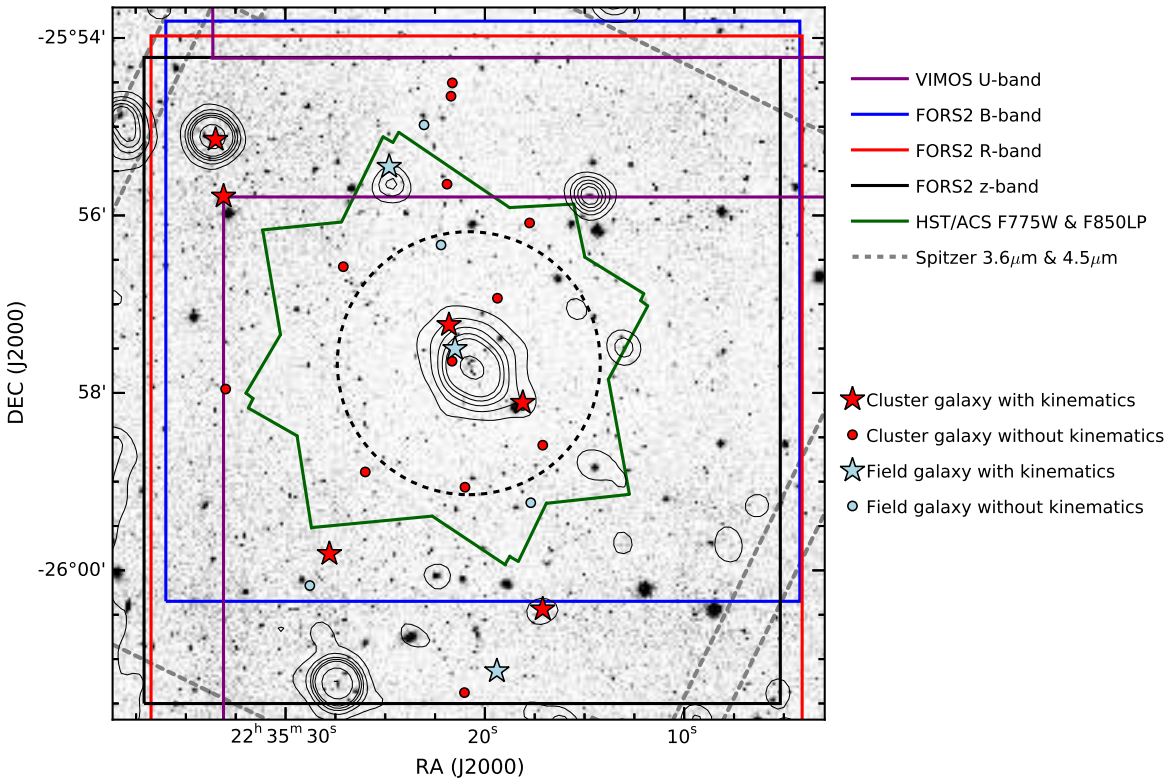

Fig. 1. Portion (8.25×8.25 arcmin^2) of the J-band HAWKI image with *XMM-Newton* X-ray contours overlayed. The field of view of the different instruments used in this work is also shown. The HAWKI J and Ks and ISPI H-band observations cover a field of view much larger than the figure. The FORS2 B-, R- and z-band coverage was obtained from different ESO programs. Most of the X-ray sources are likely distant AGNs, but the extended emission associated with the cluster can be appreciated in the center. The dashed circle marks the $R_{500} = 0.75$ Mpc radius derived by Rosati et al. (2009). We denote the position of the galaxies analyzed in this study by distinguishing between field and cluster and between those that yielded a $V_{\rm max}$ value and those that did not.

we used the software STUFF and SKYMAKER (Bertin 2009) to simulate realistic galaxy fields with different spatial resolutions, where we ran SEXTRACTOR with the same parameters over the same galaxies. In general, the Kron radii growth can be modeled as a simple linear function that depends only on the measurements in the high-quality imaging and the seeing in the lower quality imaging. Magnitudes computed by PHOT_UTILS using the derived apertures are in excellent agreement (at ~0.1 mag level) with those determined directly by SEXTRACTOR.

The above procedures were not applied to the *Spitzer* images, however. With a PSF FWHM of ~2 arcsec, distant galaxies are effectively unresolved in the IRAC images. We therefore used a fixed circular aperture of 6 arcsec and applied the standard correction factors for the missing flux (factors 1.205 and 1.221 in the 3.6 and 4.5 μm bands, respectively). In conclusion, we estimate the total calibration for all bands to have an accuracy of 0.1 mag.

3.2. Stellar masses and rest-frame magnitudes

Rest frame magnitudes and stellar masses were determined using the code LEPHARE of Arnouts & Ilbert (2011; see also Ilbert et al. 2006), which fits stellar population synthesis models (Bruzual & Charlot 2003) to the spectral energy distribution (SED) derived from the photometry. The code is a simple χ^2 minimization algorithm that finds the best match of templates for the given data. To avoid overfitting, we restricted the possible ages to values lower than the age of the Universe at the redshift of the cluster. Thus, we have average errors in absolute magnitude and stellar masses of 0.12 mag. and 0.09 dex, respectively.

To place our sample of cluster galaxies into context, we present in Fig. 2 the color–magnitude diagram in J and K bands for XMMJ2235 galaxy members. The cluster red-sequence fit from Lidman et al. (2008) is shown with a black line, with red-sequence galaxies defined as galaxies redder than 0.2 mag blueward of this fit. The purpose of this comparison is to highlight the nature of our cluster galaxies with [OII]-based kinematics. We would like to mention that two of our galaxies (IDs 8 and 11 in Table A.1) were part of the *Herschel* sample of dust-obscured star-forming galaxies presented in Santos et al. (2013).

Edge-on disks have higher extinction (A_B) than face-on galaxies, and more massive disks are dustier than less massive disks Giovanelli et al. (1995). We corrected the rest frame B-band absolute magnitudes for intrinsic dust absorption following the approach by Tully et al. (1998):

$$A_B = \log(a/b)\left[-4.48 + 2.75\log\left(V_{\rm max}\right)\right]. \quad (1)$$

The extinction is dependent on the inclination angle i, which is related to the ratio between the axes (a/b), and on the $V_{\rm max}$

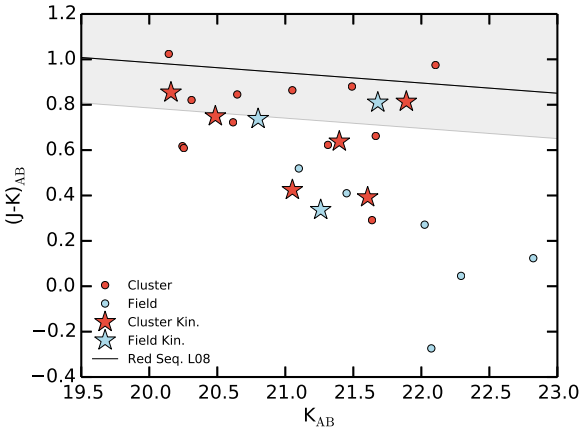

Fig. 2. Color–magnitude diagram. Red stars and circles define spectroscopic cluster members with and without derived kinematics in our sample, respectively. Blue stars and circles show field galaxies with and without derived kinematics in our sample, respectively. The cluster red-sequence fit derived by Lidman et al. (2008) is shown as a black line with a shaded area: red-sequence galaxies are defined as galaxies redder than 0.2 mag blueward of this fit, which is shown with a shaded area. Magnitudes and colors are given in the AB system.

of every galaxy. After applying the extinction correction, the typical errors in B-band luminosity range from 0.2 to 0.3 mag.

3.3. Structural parameters

Owing to the relatively small spatial coverage of the HST images in this cluster, we were able to derive the structural parameters of galaxies from the z-band (*F850LP*) images only in the central regions of the cluster. For galaxies far from the cluster center, we used ground-based HAWKI photometry in K band. We used the GALFIT package by Peng et al. (2002), which allows fitting multiple 2D surface brightness profiles simultaneously to the galaxy under scrutiny. We fit the surface brightness profiles of the galaxies of our sample using two different methods:

1. A single Sérsic profile with free index n_s.
2. A two-component model with an exponential profile ($n_s = 1$) for the disk and a de Vancouleurs profile ($n_s = 4$) for the bulge.

The best parameters from the first method were used as initial guess values for the second. All fit residuals were visually inspected (Fig. A.1), and in a few cases, it was necessary to apply constraints on some parameters in order to avoid a local minimum in the fitting process. We used the bulge/disk decomposition to obtain the disk parameters when possible within the HST coverage. However, an accurate structural decomposition was not feasible with the ground-based K-band data because of the limited spatial resolution. We therefore restricted the GALFIT models to a single Sersic profile for galaxies without available HST imaging. We stress that for the analysis presented here, the most important parameters are the ratio between the axes (a/b), position angle θ, and scale length R_d of the disk.

However, observed scale lengths depend on the wavelength regime. It was shown in de Jong (1996) that the scale length (R_d) is smaller when galaxies are observed in redder filters. The HAWK-I K-band photometry overlaps with the HST z band over a region where a subsample of 14 galaxies can be studied. We carried out the structural parameter determination in both bands, finding that HAWKI K-band-based effective radii (R_e) are on average 25% smaller than z-band-based radii. We corrected HAWKI based R_e onto z band to make them comparable before computing the scale lengths. GALFIT only returns random errors on the best-fit parameters. These are very small (<1%) throughout our sample. We relied on a previous analysis of HST/ACS images using GALFIT in Böhm et al. (2013) to obtain a more realistic estimate of the systematic errors on R_d. In that work, a typical systematic error of 20% on galaxy sizes was found for a negligible central point source. This value hence represents the systematic size error for galaxies with the light profiles of pure disks or disks with only weak bulges; this is the case for the vast majority of galaxies in our sample. We therefore adopt a 20% error on R_d in the following.

The inclination i is the angle between the normal vector of the disk and the line of sight. We computed it from the apparent major axis a and the apparent minor axis b following Heidmann et al. (1972):

$$\cos^2(i) = \frac{(a/b)^2 - q^2}{1 - q^2}. \quad (2)$$

Here the factor q is the ratio between disk scale length and scale height and is fixed to 0.2, which is the observed value for typical spirals in the local Universe (Tully et al. 1998). However, at high redshift, the intrinsic disk thickness (parameter q) may be different. Since GALFIT fitting parameter errors are negligible, the uncertainty in the assumption of parameter q is the main source of error in the determination of i. We allowed different values for the disk thickness in order to simulate a thick disk ($q = 0.3$) and an infinitely thin disk ($q = 0$). The systematic error on the inclination due to the different triaxial configurations is of a few degrees (<5°) for high-i galaxies and almost negligible for low-i galaxies.

The position angle θ denotes the orientation of the apparent major axis in the plane of the sky. Throughout this paper, the convention is that θ gives the angle between the apparent major axis and the horizontal axis, counted counter-clockwise. To minimize the geometric distortions, we constrain the mismatch angle δ, which gives the deviations between the major axis and the slit direction of a certain galaxy to $\delta \leq 30°$.

3.4. Rotation-curve extraction and modeling

Our approach to extract rotation curves from spatially resolved spectra and determine V_{max} is explained in detail in Böhm et al. (2004), Bösch et al. (2013), and Böhm & Ziegler (2016). A summary of the main steps is presented here.

Before the emission line fitting, we use an averaging boxcar of three pixels width, corresponding to 0.75″, for each spatial position in the spectrum to enhance the signal-to-noise ratio (S/N). We then transform red- and blueshifts of the emission lines as a function of galactocentric radius into an observed position-velocity diagram. The kinematic center is determined by minimizing the asymmetry of the observed RC, with a maximum allowed mismatch between kinematic and photometric center of ±1 pixel, corresponding to ∼2 kpc at the redshifts of our targets.

To determine V_{max} for a given galaxy, we simulate its rotation velocity field by taking into account all geometric effects such as disk inclination angle and observational effects like seeing or the influence of the slit width. The simulated velocity field is generated by assuming a linear rise of the rotation velocity $V_{rot}(r)$

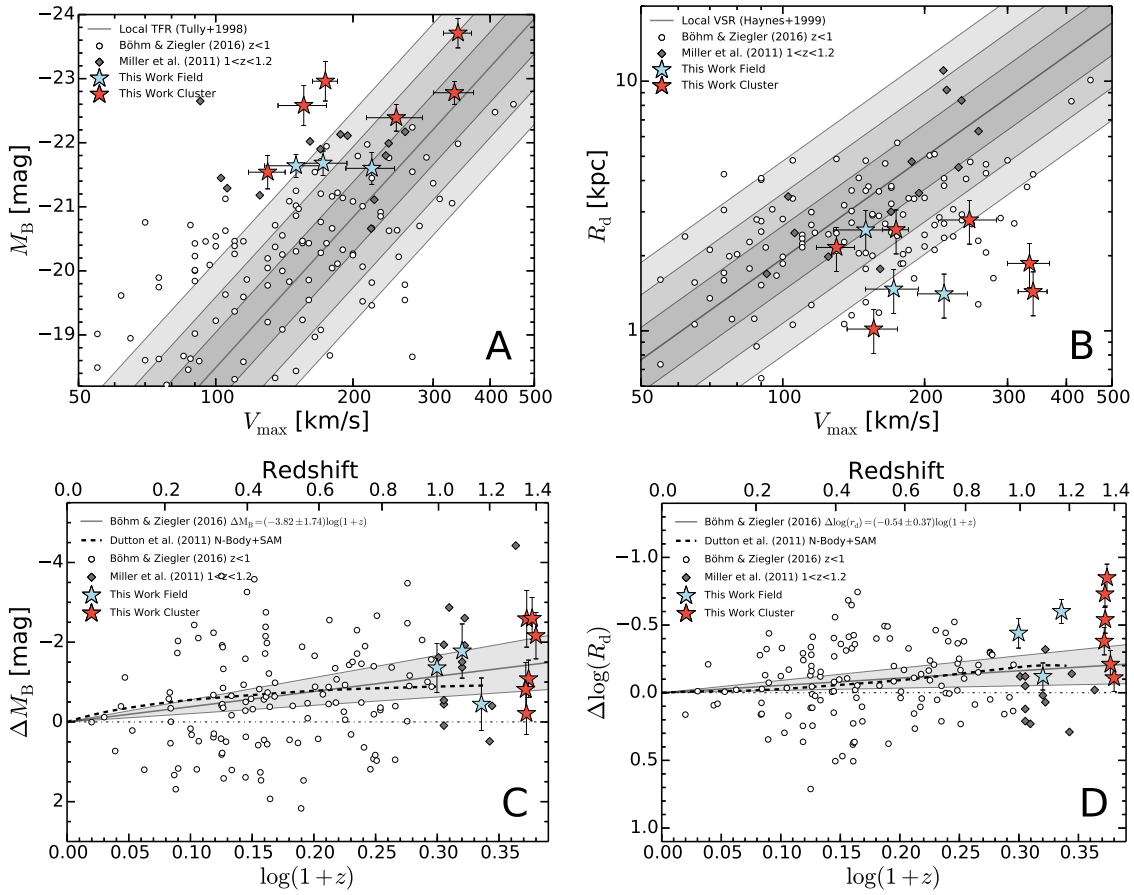

Fig. 3. *A)* Tully-Fisher *B*-band diagram. *B)* Velocity-size relation. *C)* TFR evolution diagram. Offsets ΔM_B of galaxies in our sample from the local TF relation, displayed as a function of redshift. *D)* VSR evolution diagram. Offsets ΔR_d of galaxies in our sample with respect to the local VSR, displayed as a function of redshift. In *A)* and *B)* the gray line represents the local TFR (Tully et al. 1998) and the local VSR (Haynes et al. 1999a), respectively, with 1σ, 2σ, and 3σ shaded regions. Two samples of field galaxies are plotted for comparison: the first comprises 124 disk galaxies out to $z = 1$ from Böhm & Ziegler (2016) and is plotted with black circles. Miller et al. (2011) provided a second field sample composed of 13 disk galaxies at $1 < z < 1.3$ plotted as olive diamonds. The three field galaxies at $1 < z < 1.2$ targeted in our observations are plotted with blue stars. Cluster galaxies are represented by red stars.

at $r < r_t$, where r_t is the turnover radius, and a convergence of $V_{rot}(r)$ into a constant value V_{max} at $r > r_t$ (Courteau 1997).

In most cases, the turnover radius was set as equal to the scale length, R_d, measured from the stellar morphology. However, some galaxies required R_d fitting because the stellar scale length and the turnover radius of our extracted rotation curves were mismatched. In the last step we extract from the synthetic velocity field a simulated rotation curve from which we obtain the intrinsic maximum rotation velocity V_{max} taking into account the structural and observational parameters. The error budget on V_{max} was computed following Eq. (3) in Böhm et al. (2004), taking into account the error from the χ^2-fits of the synthetic to the observed rotation curve, and the propagated errors of the inclination and the misalignment angle. The typical error on V_{max} is 20–30 km s^{-1}. For a complete description of the full process, we refer again to Böhm et al. (2004). The synthetic velocity fields and simulated and observed rotation curves of our sample are shown at the end of this paper.

Although we observed 27 objects, only 25 of them turned out to be emission line galaxies after the analysis of their spectra. Redshift values were computed using IRAF under visual determination of [OII] emission line center, that is, the only emission line available for cluster members. We detected 17 cluster members and 8 field galaxies. However, part of the cluster sample was affected by strong sky line contamination. As a result, 8 cluster galaxies were discarded because of noisy contamination. We extracted 6 RCs of cluster members from the remaining 9 galaxies, discarding 3 galaxies because of their very compact [OII] emission, which prevents us from reaching the flat part in the RC. In addition, 3 RCs were extracted from the field sample, discarding in the process 3 galaxies with sky contamination and 2 galaxies with compact emission.

4. Results

The primary results of this paper are shown in Fig. 3, where we present the TFR and VSR for cluster galaxies (red stars) at $z \sim 1.4$. In Fig. 3A we show the *B*-band TFR, which is related with recent episodes of star formation. The distribution of our

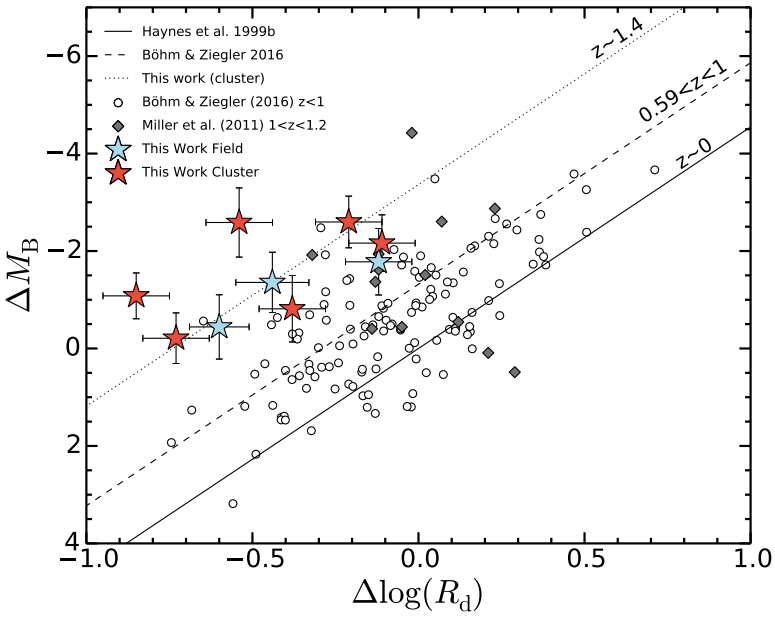

Fig. 4. Correlation diagram between the offsets, ΔM_B, from the TFR and the offsets, $\Delta \log R_\mathrm{d}$, from the VSR for previously presented samples. The solid line shows the linear fit for galaxies studied in the local Universe (Haynes et al. 1999b). By definition, this line goes through the coordinates origin. The dashed black lines plotted in this diagram show the linear fit for galaxies studied in Böhm & Ziegler (2016) at $0.59 < z < 1$, showing that galaxies are shifting away with lookback time toward higher luminosity and smaller sizes. The dotted black line is the linear fit at a fixed slope for our cluster sample, whose zero-point is shifted by –0.69 dex in $\Delta \log R_\mathrm{d}$ with respect to the local sample.

kinematic sample is compared with the local TFR by Tully et al. (1998) and the local VSR derived by Böhm & Ziegler (2016) using data from Haynes et al. (1999b). In addition, two field samples within $0.2 < z < 1.3$ are shown as comparison between different environments.

The first field sample comprises 124 disk galaxies out to $z = 1$ from Böhm & Ziegler (2016, hereafter BZ16) plotted as black circles. This is one of the largest kinematic samples of distant galaxies to date. A second field sample composed of 13 disk galaxies at $1 < z < 1.3$ selected by redshift from a larger sample provided by Miller et al. (2011, hereafter M11) is plotted as gray diamonds. We also display the 3 field galaxies targeted in our observations at $1 < z < 1.2$ (blue stars). On average, cluster galaxies in our sample are brighter by $\langle \Delta M_B \rangle = -1.6$ mag in B band than in the local TFR and smaller by a factor of 3 than in the local VSR (Figs. 3A and B, respectively). In order to determine environmental effects, we compared the results of our cluster sample with Miller's field galaxies at similar redshift and found that our cluster galaxies are brighter on average by $\langle \Delta M_B \rangle = -0.3$ mag in B band and smaller by a factor of 2 than their field counterparts.

In order to explore a possible environmental mass-dependent evolution and considering the position of our cluster galaxies in the Tully-Fisher diagram (Fig. 3A), our cluster sample was divided into two groups: the first is composed of three high total mass ($V_\mathrm{max} > 200$ km s^{-1}) galaxies lying below the 2σ region of the local TFR with $\langle \Delta M_B \rangle = -0.7 \pm 0.6$. The second group is composed of three low-mass galaxies lying between the 4 and 5σ region with respect to the local TFR and showing $\langle \Delta M_B \rangle = -2.4 \pm 0.6$. The cause of this discrepancy between groups might be different physical processes acting on them due to the cluster environment. The errors on ΔM_B are computed through error propagation from the errors on V_max and M_B according to Eq. (3) in Böhm & Ziegler (2016). Because of the limited size of our subsamples, the uncertainty on $\langle \Delta M_B \rangle$ represents the average measurement error.

Figures 3C and D display the offsets ΔM_B and $\Delta \log R_\mathrm{d}$ from the local TFR and VSR as a function of redshift. In panel C field galaxies show increasing overluminosities toward higher redshifts despite the scatter of the samples. This evolution is explained by the rise of SFR and the gradual evolution of SP with lookback time. A simple extrapolation of the luminosity evolution linear fit given by Böhm & Ziegler (2016, gray line) shows that $\Delta M_B = -1.2 \pm 0.4$ mag at $z = 1.4$. As explained in Figure 3A, our cluster sample can be divided into two groups by their total mass. We compare our results with the theoretical predictions of Dutton et al. (2011, dashed line), who found $\Delta M_B = -0.95$ mag at this redshift. Our high total mass group of galaxies is in agreement with the theoretical predictions within the errors, while the low total mass group of galaxies differ by 1.4 mag. In addition, our field sample of galaxies lie within the 1σ scatter area of the predicted luminosity evolution shown in Böhm & Ziegler (2016), and at the same time, they are compatible with predictions from numerical simulations by Dutton et al. (2011).

In panel D previous samples of field galaxies show decreasing sizes toward higher redshifts, although the scatter of the samples is similar to the scatter found in C. According to the extrapolation of the linear fit given in BZ16 (gray line), the size evolution reaches $\Delta \log R_\mathrm{d} = -(0.22 \pm 0.14)$ at $z = 1.4$, where negative values in $\Delta \log R_\mathrm{d}$ mean smaller sizes at a given maximum rotation velocity V_max. In this plot the $z = 1.4$ cluster galaxies do not populate two separate groups, but cover a broad range in size evolution. On average, they are two to three times smaller than their local counterparts, showing $\langle \Delta \log R_\mathrm{d} \rangle = (-0.47 \pm 0.15)$. Our three field galaxies cover a similar range of scale lengths with a slightly higher mean value, $\langle \Delta \log R_\mathrm{d} \rangle = (-0.39 \pm 0.14)$. In contrast, predictions from numerical simulations by Dutton et al. (2011, dashed line) showed that $\Delta \log R_\mathrm{d} = -0.2$ at the same redshift. Errors on $\Delta \log R_\mathrm{d}$ are computed through error propagation from the errors on V_max and R_d following Eq. (6) in Böhm & Ziegler (2016).

To explore the connection between scaling relations for disk galaxies, we compare in Fig. 4 the offsets ΔM_B from the TFR with the offsets $\Delta \log R_\mathrm{d}$ from the VSR. By definition, the median of the two parameters is zero in the local Universe. However,

A&A 605, A127 (2017)

there is a clear correlation between ΔM_B and $\Delta \log R_d$ because luminosity, size, and maximum velocity conform a 3D parameter space in which disk galaxies populate a plane. Thus, these three parameters are correlated, and deviations between local and distant galaxies reflect the evolution of one or several of the parameters. Figure 4 shows the projection of this 3D space on a luminosity-size plane represented by the offsets in disk scale length and absolute magnitude from the local VSR and TFR. This representation was recently used by BZ16 to quantitatively study the galaxy evolution in the field up to $z = 1$. Using fixed-slope fits to determine the offsets from the local relation in terms of $\Delta \log R_d$, these authors found a combined evolution in size and luminosity in their sample with a zero-point $\Delta \log R_d = -0.29$ for field galaxies at $0.59 < z < 1$. slightly larger offset of our field sample (blue stars in Fig. 4) at slightly higher redshift $1 < z < 1.2$. However, Our sample of cluster and field galaxies at $1.2 < z < 1.4$ shows larger offsets and a zero-point of $\Delta \log R_d = -0.74$. Although our cluster sample has large scatter, our data follow the general trend in the BZ16 sample at $0 < z < 1$: distant galaxies are shifting away from the local $\Delta M_B - \Delta \log R_d$ relation toward smaller sizes and higher luminosity with lookback time.

5. Discussion

The brightening detected in the B-band TFR for cluster galaxies can be partially explained by the increasing star formation galaxies experience toward longer lookback times. However, the division of our sample into two groups according to their total mass and B-band luminosity offsets might indicate additional effects that may explain their properties. Several possible explanations have to be considered.

5.1. Observational effects

First, V_{max} might be underestimated. Persic et al. (1996) studied the relation between the mass of a galaxy and the shape of its RC by introducing a complex definition of a universal rotation curve (URC). According to this study, very low-mass spirals show an increasing rotation velocity even at large radii, whereas the rotation curves of very high-mass spirals moderately decline in that regime. These gradients are found as far as 5 optical disk scale lengths. However, our cluster sample mainly covers intermediate masses ($10.03 < \log M_* < 10.91$), where the URC does not introduce a velocity gradient at large galactocentric radii. However, the spatial extent of the rotation curves in our sample (as well as other samples at similar redshifts) is around two to four times R_d, which is insufficient to constrain potential RC gradients in the outer disk. With our RCs, we probe out to radii similar to R_{opt}, and for galaxies with $V_{rot}(R = R_{opt}) > 100$ km s^{-1} (all of our galaxies), the largest possible underestimate in V_{max} due to RC gradients is 10−20% (see Fig. 4 in Persic et al. 1996).

We also checked whether these distributions are caused by a selection effect that is due to a magnitude limit in the spectroscopic and photometric campaigns from which we extracted our targets. Toward higher redshifts, such an apparent magnitude limit corresponds to higher luminosities and in turn higher masses. A fraction of the low-luminosity low-mass (slowly rotating) spiral population is therefore missed in the selection process, while the low-mass galaxies that are selected might preferentially be located at the high-luminosity side of the TF relation. This effect is commonly know as Malmquist bias. Thus, in all redshifts bins, at a given V_{max} any distant galaxy sample with a magnitude limit will show an overluminosity of the low-mass galaxies compared to the local TFR, while the distributions are similar at the high-mass end. Some of the previous studies we used for target selection (Strazzullo et al. 2010; Grützbauch et al. 2012) have magnitude limits of $z_{AB} = 24$ and $H_{AB} = 24.4$. However, our sample is well inside the limits showing average observed magnitudes of $z_{AB} = 22.4$ and $H_{AB} = 21.3$, meaning that the magnitude bias in our target selection should not have a great impact. In addition, we studied the distribution of our targets in B-band luminosity. For the full sample, the mean B-band luminosity value before applying the absorption correction is $\langle M_B \rangle = -21.8$ mag with a scatter of $\sigma_{total} = 0.9$ mag. As stated in Sect. 2.4, 25 out of 27 galaxies showed [OII] emission, but we did not extract RC from all of them for diverse reasons (OH contamination, compactness, faintness). Neglecting galaxies whose emission lines are contaminated leaves us with a clean sample of 17 galaxies with the same $\langle M_B \rangle$ and scatter. This means that the removal of OH-affected galaxies does not introduce a luminosity bias to the clean sample. Now, if we focus on the cluster members, we see that they have similar M_B, but cover a wide range in V_{max}. The high-mass (fast rotating) group shows higher M_B than the clean sample, $\langle M_B \rangle = -23.0$ with scatter $\sigma_{high} = 0.6$, and a high average maximum rotation velocity, $\langle V_{max} \rangle = 308$ km s^{-1}. On the other hand, the overluminous low-mass (slowly rotating) group presents similar M_B, but relatively low V_{max}, $\langle M_B \rangle = -22.4$ with $\sigma_{low} = 0.7$ and $\langle V_{max} \rangle = 154$ km s^{-1}. Thus, both groups have similar B-band luminosities, but only the low-mass group is significantly offset with respect to the local TFR, which might point toward the presence of a magnitude bias. Nevertheless, the small number of galaxies make it hard to draw firm conclusions, and the large B-band offsets in the TFR ($\langle \Delta M_B \rangle = -2.4$ mag for the low-mass cluster galaxies) probably require additional cluster-specific effects to explain the enhanced luminosity.

5.2. Physical effects

The third scenario suggests that we might see rather compact galaxies that became enhanced in SF during their infall toward the dense regions of the cluster. If this is the case, this enhancement should be caused by a process that does not strongly affect galaxy gas kinematics, at least within the galactocentric radial regime probed by our RCs, up to ∼3 scale lengths, and during the infall phase where the ICM density has low to intermediate values.

Kronberger et al. (2008b) and Kapferer et al. (2009) investigated the influence of ram pressure stripping (RPS) on the internal gas kinematics of simulated spiral galaxies by focusing on how the resulting distortions of the gaseous disk translate into the RC and the full 2D velocity field (VF) of galaxies. Distortions and declining RCs were found at distances larger than 12 kpc from the center of the galaxy, indicating the presence of an undisturbed inner part below that radius. The inclination of the galaxy relative to the line of sight changes the degree of disturbance and may shift the luminosity center from the kinematic center. In our sample the RCs cover radii up to ∼10 kpc, and therefore we are not able to investigate possible distortions at larger radii. The absence of irregularities in the inner parts may be a hint toward this type of effect. In addition, the compression of the gas in the central parts that is due to the pressure of the intracluster medium (ICM) can trigger new star formation and a subsequent brightening of the ram-pressure affected galaxy, causing high-luminosity TF offsets. According to Kronberger et al. (2008a), RPS enhances the SFR by up to a factor of 3 over several hundred Myr for a Milky Way-like galaxy. In total, the mass

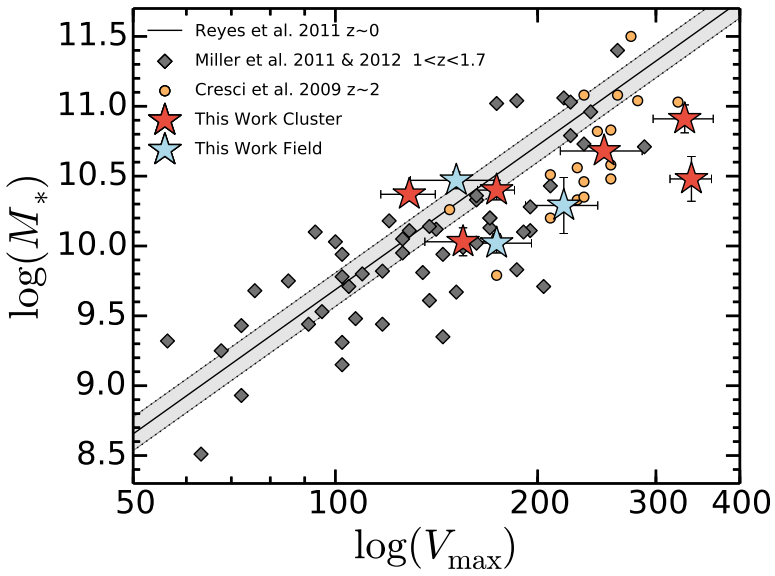

Fig. 5. Stellar mass TFR. Red and blue stars are cluster and field galaxies in our sample, respectively. Gray diamonds show a sample of 42 field galaxies at $1 < z < 1.7$ from Miller et al. (2011) and Miller et al. (2012), who found a well-established M_*-TFR at this redshift. Orange circles are 18 field galaxies from Cresci et al. (2009) at $z \sim 2$. The solid line is the local M_*-TFR from Fig. 23 in Reyes et al. (2011), taking $V_{2.2}$ as $V_{\rm max}$. The shaded area represents 1σ deviation from the previous relation.

of newly formed stars is about twice higher than in an isolated galaxy after 500 Myr of high ram pressure acting. However, these studies do not reach the ICM density conditions usually found in massive clusters. From the observational point of view, Ebeling et al. (2014) showed that cluster galaxies suffering strong RPS can increase their SF and become temporarily brighter than even the BCG of the cluster. Although this is only expected to occur rarely and only in very massive clusters and for small angles between the normal vector of the disk and the vector of movement through the ICM, several such cases have been discovered (e.g., Owen et al. 2006, 2012; Cortese et al. 2007; Ebeling et al. 2014).

However, individual events of this intensity may be rare, requiring a gas-rich galaxy to cross deep within the cluster core at very high velocity. Ruggiero & Lima Neto (2017) closed this gap by simulating Milky Way-like infalling galaxies in clusters around 10^{14}–10^{15} $M_\odot$ and choosing R_{200} at present time as the initial density conditions for the ICM at the beginning of the galaxy infall. This study takes into account three different orientations of the galaxy disk (0°, 45°, and 90°) for a radial infall speed of 0.5 to 2 times the velocity dispersion of the cluster. Their results show that star formation is always initially enhanced by a factor of 1.5 to 3 by the compression of the gaseous disk. Interestingly, the SFR increases by a factor of 2 before the gas loss becomes important (<15% of the total gas mass). On the other hand, Steinhauser et al. (2016) took a similar approach and studied different infalling orbits for three distinct clusters. They found that the SFR rises by up to 60% for galaxies with $V_{\rm max} = 170$ km s^{-1} and $\log M_* \sim 10.6$ in a cluster with similar properties to those we found in XMM2235-2557 after 0.5 Gyr and following an orbit that goes through the very central regions of the cluster. We translated the SFR rise predicted by Ruggiero & Lima Neto (2017) and Steinhauser et al. (2016) into a change in B-band luminosity using the EzGal python code (Mancone & Gonzalez 2012). EzGal is a tool that takes models of how the SED of a stellar population evolves with time and projects it through filters to calculate several physical properties, including magnitude evolution, as a function of redshift. In our case, we used the model libraries from Bruzual & Charlot (2003) to study the evolution of the B-band luminosity evolution after a short starburst caused by the compression of the gas in the inner disk due to RPS. We find a brightening of 0.9 and 0.3 mag for Ruggiero & Lima Neto (2017) and Steinhauser et al. (2016) conditions, respectively.

In summary, results from previous RPS studies and simulations point toward an enhancement of the SFR of the central regions of infalling cluster galaxies after going through the cluster environment for <1 Gyr, but maintaining undisturbed velocity fields in the inner parts, as we find in our study. However, the variety of side effects playing a role in the process, such as inclination of the galaxy with respect to the infalling direction, density of the ICM, infalling velocity, and gas fraction, prevents us from extracting strong conclusions about the nature of the luminosity enhancement of our cluster galaxies without further observations.

5.3. Stellar mass TFR

In virialized galaxies, a higher maximum rotation velocity can only be explained by a higher total mass value, including Baryonic (stellar plus gas) and dark matter content. Since it is not possible to obtain direct information about the gas fraction for distant galaxies, M_* is the only available quantity we have to explore the evolution of the Baryonic mass in galaxies at this redshift. In Fig. 5 we investigate the stellar mass TFR (M_*-TFR) for the field and cluster galaxies in our sample. Again, our cluster sample is composed of two groups divided by their total mass ($V_{\rm max}$): three massive fast-rotating galaxies with $10.5 > \log M_* > 10.9$ embody the first group, while another three slow-rotating galaxies show slightly lower stellar masses, $10.0 > \log M_* > 10.4$. Our results follow the M_*-TFR for spiral galaxies established by Miller et al. (2012) at redshift $1.3 < z < 1.7$ and are in agreement with previous studies at similar redshift, like Miller et al. (2011) $z < 1.3$ and Cresci et al. (2009) at $z \sim 2$. We compare our dataset with the local M_*-TFR established by Reyes et al. (2011) using a subsample of local galaxies from SDSS DR7.

While the B-band TFR is sensitive to recent episodes of star formation, the M_*-TFR tracks the overall evolution of the underlying stellar population. From combining the results from both incarnations of the TFR, we draw the following conclusions: high total mass cluster galaxies show stellar mass $\log M_* \geqslant 10.5$ and lie within the 2σ region of the local B-band TFR, while at the same time they are offset by $\langle \Delta \log M_* \rangle = -0.66$ with respect to the local M_*-TFR. On the other hand, the group of low-mass cluster galaxies show lower stellar mass, $\log M_* \leqslant 10.5$, and are on average offset by 5 sigma toward higher B-band luminosity, with negligible deviations with respect to the local M_*-TFR, $\langle \Delta \log M_* \rangle = -0.05$.

One possible explanation for this behavior would be that high-mass distant galaxies have grown their stellar mass following star formation histories that are compatible with quiescent evolution, excluding starbursting episodes in the last few billion years. In contrast, low-mass galaxies at this epoch are still in the early phases of assembling their disk and are more prone to suffer environmental effects that could enhance their SFR and thus, their B-band luminosity. The tendency for high-mass galaxies to develop their disk first has recently been studied by Simons et al. (2016) for field galaxies at $z \sim 2$ using MOSFIRE. The most massive galaxies in their sample ($\log M_* \geqslant 10.2$) lie below the local M_*-TFR of Reyes et al. (2011) and exhibit similar rotation support as their local counterparts ($V_{\rm rot}/\sigma \geqslant 2-8$), while at lower stellar masses, galaxies start to display small rotation support ($V_{\rm rot}/\sigma \leqslant 1$) and lie on the other side of the relation. In an environmental frame, the combination of the degree of rotational support ($V_{\rm rot}/\sigma$) with tracers of current star formation might be a useful tool to interpret offsets in the different representations of the TFR.

6. Conclusions

Using the FORS2 instrument at the ESO Very Large Telescope, we have studied a sample of 25 galaxies in the XMMU2235-2557 field of view. We carried out a kinematic analysis for 6 cluster members at $z \sim 1.4$ and 3 field galaxies at $1 < z < 1.2$ and determined their maximum rotation velocity $V_{\rm max}$. Structural parameters (such as disk inclination and scale length) were derived on HST/ACS and HAWK-I images. We analyzed the distant Tully-Fisher and velocity-size relations in XMM2235-2557 and compared them with reference samples at similar redshift and the local Universe, taking into account additional results from galaxy evolution simulations. Our main findings can be summarized as follows:

1. At given $V_{\rm max}$, cluster galaxies are more luminous (in rest-frame B band) and smaller (in rest-frame z band) than their local counterparts toward higher redshifts. By $z = 1.4$ we find for cluster members an average brightening of $\langle \Delta M_B \rangle = -1.6$ mag in absolute B-band magnitude and a decrease in size by a factor of ∼2–3.
2. The cluster galaxies in XMM2235 were divided in two subsamples according to their $V_{\rm max}$, occupying two different loci in the TFR. The first is composed of relatively slowly rotating (low total mass) galaxies that appear offset from the local TFR by $\sim 5\sigma$. The second lies within the 2σ deviation region, in agreement with previous observational findings (Böhm & Ziegler 2016) and semi-analytic models for field galaxies at similar redshift (Dutton et al. 2011). The galaxies in our sample show smaller offsets and scatter in the stellar mass TF diagram than in the B-band TF diagram. The subsample of fast-rotating galaxies show $10.5 > \log M_* > 10.9$, while the others have slightly lower stellar masses, $10.0 > \log M_* > 10.4$. Although both subsamples have a similar stellar mass, they might be affected differently by cluster-specific processes, which might enhance the SFRs and, in turn, B-band luminosities in the low-mass subsample.
3. The origin of the TFR offsets for the group of slowly rotating (low total mass) galaxies is not clear. We have discussed several possibilities to explain our results, such as the underestimation of $V_{\rm max}$ as a result of the shape of the RC, a magnitude bias in our sample, and a temporary brightening in the B-band luminosity of these galaxies caused by the interaction with the environment. A combination of the two latter options appears to be the most likely explanation for our findings. The effect of the Malmquist bias is limited and cannot be the sole explanation for the offsets of the slowly rotating subsample: $\langle \Delta M_B \rangle = -2.4$. Results from previous ram pressure stripping studies and simulations show that it is possible to enhance the SFR in the central regions of infalling cluster galaxies (and thus the B-band luminosity) by maintaining undisturbed velocity fields (and RCs) at smaller radii than 3–4 scale lengths, as we find in our sample. However, the small size of our cluster sample together with the variety of effects playing a role in this process, such as the inclination of the galaxy with respect to the infalling direction, density of the ICM, infalling velocity and gas fraction, and the combined possible effect of the magnitude bias prevent us from drawing firm conclusions about the nature of these offsets without further observations.
4. Analysis of the combined offsets in our sample from the Tully-Fisher and velocity-size relations reveal there is a correlation between them. Galaxies with a strong offset toward high B-band luminosity with respect to the local TFR have a similar size than their local counterparts at comparable $V_{\rm max}$, while galaxies offset toward smaller sizes with respect to the local VSR have a B-band luminosity compatible with the local TFR. These results are in agreement with what was shown in a previous paper by Böhm & Ziegler (2016).

In this paper we have explored the kinematics of galaxies in a high-redshift cluster. The distribution of our cluster subsamples in the TFR suggests that a population of galaxies exists that is consistent with the predicted evolutionary state of galaxies at this redshift, while cluster-specific interactions such as RPS might be responsible for the B-band luminosity enhancement suffered by the other half. However, it is not clear how likely this type of events is and whether the luminosity enhancement can be explained by a single process. Distinguishing between the origin of TFR offsets of bright cluster galaxies will require further work, such as examining the difference in star formation rate for distant cluster galaxies and the use of larger data sets covering a wide range of environments within the cluster.

Acknowledgements. We acknowledge the thorough comments by the referee. This publication is supported by the Austrian Science Fund (FWF). A.B. is grateful to the Austrian Science Fund (FWF) for funding (grant number P23946-N16).

References

Angulo, R. E., & White, S. D. M. 2010, MNRAS, 405, 143
Arnouts, S., & Ilbert, O. 2011, Astrophysics Source Code Library [record ascl:1108.009]
Bamford, S. P., Milvang-Jensen, B., Aragón-Salamanca, A., & Simard, L. 2005, MNRAS, 361, 109
Bertin, E. 2009, Mem. Soc. Astron. Ital., 80, 422

Bertin, E., & Arnouts, S. 1996, A&AS, 117, 393
Böhm, A., & Ziegler, B. L. 2007, ApJ, 668, 846
Böhm, A., & Ziegler, B. L. 2016, A&A, 592, A64
Böhm, A., Ziegler, B. L., Saglia, R. P., et al. 2004, A&A, 420, 97
Böhm, A., Wisotzki, L., Bell, E. F., et al. 2013, A&A, 549, A46
Bösch, B., Böhm, A., Wolf, C., et al. 2013, A&A, 554, A97
Bouwens, R. J., Illingworth, G. D., Franx, M., & Ford, H. 2007, ApJ, 670, 928
Bower, R. G., Benson, A. J., & Crain, R. A. 2012, MNRAS, 422, 2816
Bruzual, G., & Charlot, S. 2003, MNRAS, 344, 1000
Butcher, H., & Oemler, Jr., A. 1978, ApJ, 219, 18
Chabrier, G. 2003, PASP, 115, 763
Cortese, L., Marcillac, D., Richard, J., et al. 2007, MNRAS, 376, 157
Courteau, S. 1997, AJ, 114, 2402
Cresci, G., Hicks, E. K. S., Genzel, R., et al. 2009, ApJ, 697, 115
de Jong, R. S. 1996, A&A, 313, 377
Dekel, A., Birnboim, Y., Engel, G., et al. 2009, Nature, 457, 451
Dutton, A. A., van den Bosch, F. C., Faber, S. M., et al. 2011, MNRAS, 410, 1660
Ebeling, H., Stephenson, L. N., & Edge, A. C. 2014, ApJ, 781, L40
Förster Schreiber, N. M., Genzel, R., Bouché, N., et al. 2009, ApJ, 706, 1364
Genzel, R., Tacconi, L. J., Eisenhauer, F., et al. 2006, Nature, 442, 786
Giovanelli, R., Haynes, M. P., Salzer, J. J., et al. 1995, AJ, 110, 1059
Gnerucci, A., Marconi, A., Cresci, G., et al. 2011, A&A, 528, A88
Grützbauch, R., Bauer, A. E., Jørgensen, I., & Varela, J. 2012, MNRAS, 423, 3652
Hasinger, G., Miyaji, T., & Schmidt, M. 2005, A&A, 441, 417
Haynes, M. P., Giovanelli, R., Chamaraux, P., et al. 1999a, AJ, 117, 2039
Haynes, M. P., Giovanelli, R., Salzer, J. J., et al. 1999b, AJ, 117, 1668
Heidmann, J., Heidmann, N., & de Vaucouleurs, G. 1972, MmRAS, 75, 85
Ilbert, O., Arnouts, S., McCracken, H. J., et al. 2006, A&A, 457, 841
Jaffé, Y. L., Aragón-Salamanca, A., Kuntschner, H., et al. 2011, MNRAS, 417, 1996
Kapferer, W., Sluka, C., Schindler, S., Ferrari, C., & Ziegler, B. 2009, A&A, 499, 87
Kelly, P. L., von der Linden, A., Applegate, D. E., et al. 2014, MNRAS, 439, 28
Kron, R. G. 1980, ApJS, 43, 305
Kronberger, T., Kapferer, W., Ferrari, C., Unterguggenberger, S., & Schindler, S. 2008a, A&A, 481, 337
Kronberger, T., Kapferer, W., Unterguggenberger, S., Schindler, S., & Ziegler, B. L. 2008b, A&A, 483, 783
Kutdemir, E., Ziegler, B. L., Peletier, R. F., et al. 2008, A&A, 488, 117
Kutdemir, E., Ziegler, B. L., Peletier, R. F., et al. 2010, A&A, 520, A109
Lehnert, M. D., Nesvadba, N. P. H., Le Tiran, L., et al. 2009, ApJ, 699, 1660
Lidman, C., Rosati, P., Tanaka, M., et al. 2008, A&A, 489, 981
Lilly, S. J., Le Fevre, O., Hammer, F., & Crampton, D. 1996, ApJ, 460, L1
Mancone, C., & Gonzalez, A. 2012, Astrophysics Source Code Library [record ascl:1208.021]
McGaugh, S. S., Schombert, J. M., Bothun, G. D., & de Blok, W. J. G. 2000, ApJ, 533, L99
Miller, S. H., Bundy, K., Sullivan, M., Ellis, R. S., & Treu, T. 2011, ApJ, 741, 115
Miller, S., Ellis, R. S., Sullivan, M., Bundy, K., & Treu, T. 2012, in AAS Meeting Abstracts 219, 202.02
Milvang-Jensen, B., Aragón-Salamanca, A., Hau, G. K. T., Jørgensen, I., & Hjorth, J. 2003, MNRAS, 339, L1
Mocz, P., Green, A., Malacari, M., & Glazebrook, K. 2012, MNRAS, 425, 296
Moran, S. M., Miller, N., Treu, T., Ellis, R. S., & Smith, G. P. 2007, ApJ, 659, 1138
Mullis, C. R., Rosati, P., Lamer, G., et al. 2005, ApJ, 623, L85
Nakamura, O., Aragón-Salamanca, A., Milvang-Jensen, B., et al. 2006, MNRAS, 366, 144
Owen, F. N., Keel, W. C., Wang, Q. D., Ledlow, M. J., & Morrison, G. E. 2006, AJ, 131, 1974
Owers, M. S., Couch, W. J., Nulsen, P. E. J., & Randall, S. W. 2012, ApJ, 750, L23
Peng, C. Y., Ho, L. C., Impey, C. D., & Rix, H.-W. 2002, AJ, 124, 266
Peng, Y.-j., Lilly, S. J., Kovač, K., et al. 2010, ApJ, 721, 193
Persic, M., Salucci, P., & Stel, F. 1996, MNRAS, 281, 27
Pickles, A. J. 1998, PASP, 110, 863
Pierce, M. J., & Tully, R. B. 1992, ApJ, 387, 47
Puech, M., Flores, H., Hammer, F., et al. 2008, A&A, 484, 173
Puech, M., Hammer, F., Flores, H., et al. 2010, A&A, 510, A68
Reyes, R., Mandelbaum, R., Gunn, J. E., Pizagno, J., & Lackner, C. N. 2011, MNRAS, 417, 2347
Rodrigues, M., Hammer, F., Flores, H., Puech, M., & Athanassoula, E. 2017, MNRAS, 465, 1157
Rosati, P., Tozzi, P., Gobat, R., et al. 2009, A&A, 508, 583
Ruggiero, R., & Lima Neto, G. B. 2017, MNRAS, 468, 4107
Santos, J. S., Altieri, B., Popesso, P., et al. 2013, MNRAS, 433, 1287
Schirmer, M. 2013, ApJS, 209, 21
Simons, R. C., Kassin, S. A., Trump, J. R., et al. 2016, ApJ, 830, 14
Steinhauser, D., Schindler, S., & Springel, V. 2016, A&A, 591, A51
Strazzullo, V., Rosati, P., Pannella, M., et al. 2010, A&A, 524, A17
Tiley, A. L., Stott, J. P., Swinbank, A. M., et al. 2016, MNRAS, 460, 103
Tonini, C., Maraston, C., Ziegler, B., et al. 2011, MNRAS, 415, 811
Tully, R. B., Pierce, M. J., Huang, J.-S., et al. 1998, AJ, 115, 2264
Vergani, D., Epinat, B., Contini, T., et al. 2012, A&A, 546, A118
Wisnioski, E., Förster Schreiber, N. M., Wuyts, S., et al. 2015, ApJ, 799, 209
Ziegler, B. L., Böhm, A., Jäger, K., Heidt, J., & Möllenhoff, C. 2003, ApJ, 598, L87

A&A 605, A127 (2017)

Appendix A

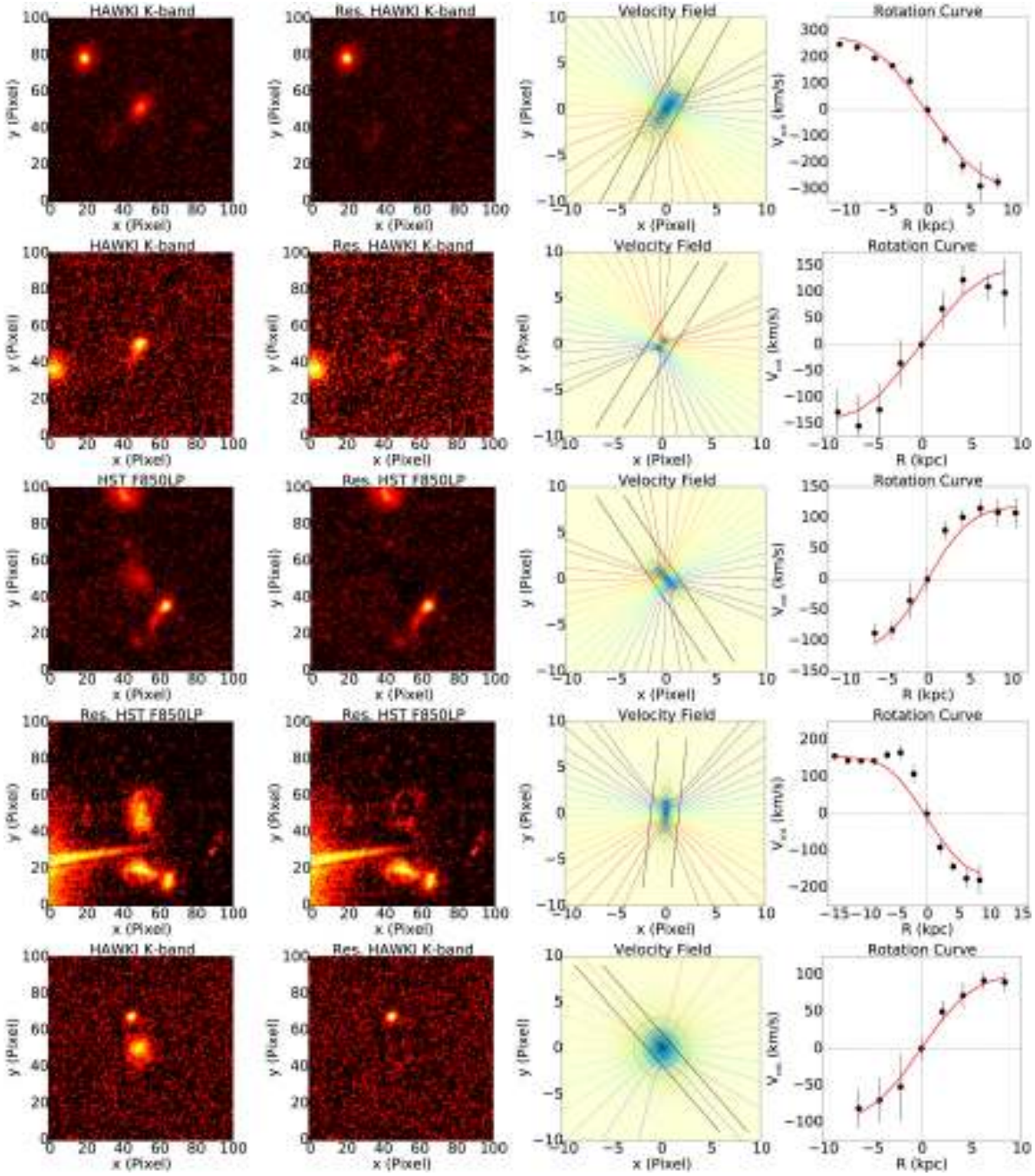

Fig. A.1. Our sample of cluster and field galaxies studied following the methods explained in Sect. 3 and presented in the same order as in Table A.2. The *first column* shows the HAWKI *K*-band or HST-F850LP image centered on the target galaxy. The *second column* displays the residuals after subtracting the 2D model of the galaxy. The *third column* presents the synthetic velocity field based on the observed structural parameters after fitting the simulated rotation curve to the observed curve. The black lines mark the position of the edges of the slit. The *fourth column* displays the rotation curve (black points) in the observed frame, and the fitted simulated RC (red line).

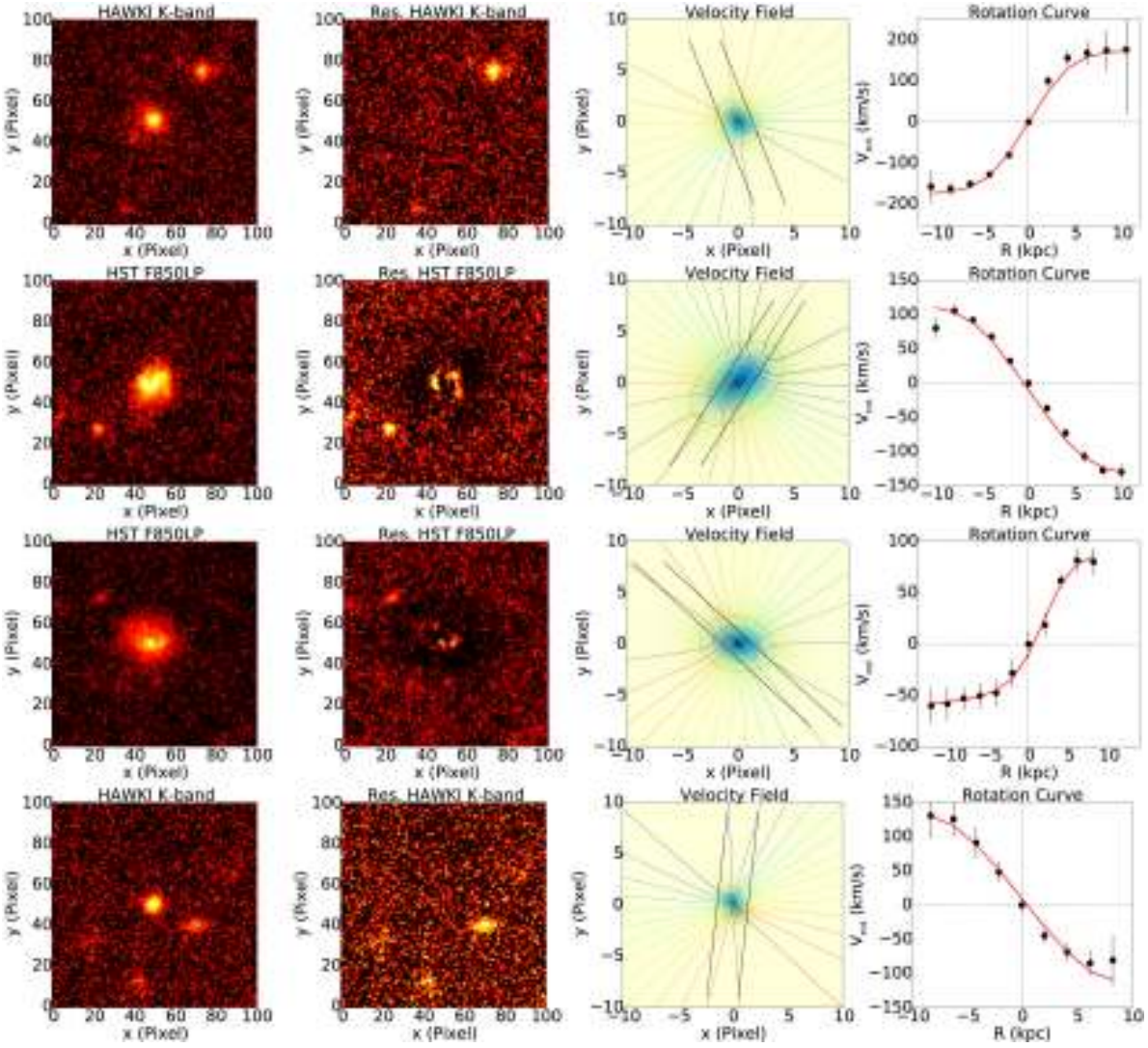

Fig. A.1. continued.

A&A 605, A127 (2017)

Table A.1. General properties of our cluster and field samples.

ID	RA (hh:mm:ss)	Dec (dd:mm:ss)	z	M_B (mag)	m_K (mag)	$J-K$ (mag)	$\log M_*/M_\odot$
1	22:35:21.6	–25:54:30.4	1.364	–22.91 ± 0.16	20.24	0.62	10.96 ± 0.12
2	22:35:21.7	–25:54:39.4	1.391	–22.50 ± 0.13	20.62	0.72	10.90 ± 0.08
3	22:35:33.5	–25:55:08.7	1.366	–22.87 ± 0.11	20.16	0.85	10.48 ± 0.16
4	22:35:21.9	–25:55:38.9	1.391	–22.46 ± 0.12	20.31	0.82	11.16 ± 0.06
5	22:35:33.1	–25:55:47.1	1.358	–21.82 ± 0.11	21.40	0.64	10.03 ± 0.10
6	22:35:27.1	–25:56:34.7	1.386	–21.78 ± 0.13	21.31	0.62	10.59 ± 0.05
7	22:35:19.4	–25:56:56.0	1.380	–21.64 ± 0.12	21.05	0.86	10.78 ± 0.06
8	22:35:21.8	–25:57:14.0	1.399	–20.96 ± 0.11	21.89	0.81	10.37 ± 0.05
9	22:35:21.6	–25:57:38.6	1.389	–20.33 ± 0.12	22.10	0.97	10.43 ± 0.05
10	22:35:33.0	–25:57:57.4	1.390	–22.36 ± 0.15	20.65	0.85	10.98 ± 0.14
11	22:35:18.1	–25:58:06.6	1.382	–22.11 ± 0.14	21.61	0.39	10.40 ± 0.07
12	22:35:17.1	–25:58:35.4	1.395	–22.14 ± 0.11	21.64	0.29	10.18 ± 0.11
13	22:35:26.0	–25:58:53.5	1.388	–22.57 ± 0.12	20.14	1.02	11.18 ± 0.06
14	22:35:21.0	–25:59:03.8	1.395	–21.56 ± 0.11	21.66	0.66	10.30 ± 0.09
15	22:35:27.8	–25:59:48.8	1.353	–22.17 ± 0.14	21.05	0.42	10.68 ± 0.03
16	22:35:17.1	–26:00:26.3	1.357	–22.60 ± 0.11	20.49	0.75	10.91 ± 0.10
17	22:35:21.1	–26:01:22.8	1.397	–21.33 ± 0.10	21.49	0.88	10.69 ± 0.13
18	22:35:23.0	–25:54:58.8	0.560	–19.26 ± 0.15	22.02	0.27	9.27 ± 0.11
19	22:35:24.8	–25:55:27.0	0.994	–21.38 ± 0.10	21.26	0.34	10.02 ± 0.07
20	22:35:17.8	–25:56:05.2	0.765	–23.00 ± 0.14	20.25	0.61	10.66 ± 0.05
21	22:35:22.2	–25:56:20.0	1.511	–21.83 ± 0.13	22.29	0.05	9.92 ± 0.05
22	22:35:21.5	–25:57:30.2	1.091	–21.47 ± 0.11	20.80	0.74	10.47 ± 0.06
23	22:35:17.7	–25:59:14.3	0.884	–20.64 ± 0.07	21.10	0.52	10.34 ± 0.12
24	22:35:28.8	–26:00:10.3	0.986	–21.36 ± 0.11	21.45	0.41	9.66 ± 0.06
25	22:35:19.4	–26:01:08.1	1.167	–21.33 ± 0.17	21.68	0.81	10.29 ± 0.20

Notes. IDs, J2000 coordinates, redshift, AB absolute B-band magnitude before correcting for intrinsic dust absorption, observed K-band magnitude, $J-K$ color, and logarithmic stellar mass.

Table A.2. IDs, redshift, structural parameters instrument (Inst.), intrinsic dust absorption (A_B), B-band-corrected luminosity ($M_{B_{\rm corr}}$), and structural parameters of the cluster and field kinematic samples: scale length ($R_{\rm d}$), inclination (i), position angle (θ), misalignment (δ), and logarithmic stellar mass.

ID	z	Inst.	A_B (mag)	$M_{B_{\rm corr}}$ (mag)	$R_{\rm d}$ (kpc)	i (°)	θ (°)	δ (°)	$V_{\rm max}$ (km s^{-1})	$\log M_*/M_\odot$
3	1.366	HAWKI	–0.84 ± 0.12	–23.71 ± 0.23	1.4 ± 0.3	65 ± 4	–32	5	340 ± 24	10.48 ± 0.16
5	1.358	HAWKI	–0.76 ± 0.20	–22.58 ± 0.31	1.0 ± 0.2	75 ± 8	–34	4	156 ± 19	10.03 ± 0.10
8	1.399	HST/ACS	–0.56 ± 0.15	–21.52 ± 0.26	2.2 ± 0.4	70 ± 5	41	10	130 ± 12	10.37 ± 0.05
11	1.382	HST/ACS	–0.85 ± 0.17	–22.96 ± 0.31	2.5 ± 0.5	76 ± 9	2	4	174 ± 11	10.40 ± 0.07
15	1.353	HAWKI	–0.29 ± 0.07	–22.46 ± 0.21	2.8 ± 0.6	44 ± 1	13	26	249 ± 35	10.68 ± 0.03
16	1.357	HAWKI	–0.19 ± 0.06	–22.78 ± 0.18	1.9 ± 0.4	34 ± 1	34	14	334 ± 34	10.91 ± 0.10
19	0.994	HST/ACS	–0.30 ± 0.09	–21.68 ± 0.19	1.5 ± 0.3	50 ± 2	–46	16	172 ± 22	10.02 ± 0.07
22	1.091	HST/ACS	–0.16 ± 0.06	–21.64 ± 0.18	2.5 ± 0.5	40 ± 1	75	30	150 ± 22	10.47 ± 0.06
25	1.167	HAWKI	–0.27 ± 0.07	–21.60 ± 0.25	1.4 ± 0.3	44 ± 2	–24	18	220 ± 36	10.29 ± 0.20

2.1 Reprint Permission from A&A

Astronomy and Astrophysics
Editor in Chief: T. Forveille

T. Forveille
Astronomy & Astrophysics
Observatoire de Paris
61, avenue de l'Observatoire
75014 Paris, France

Tel.: 33 0(1) 43 29 05 41
Fax: 33 0(1) 43 29 05 57
e-mail: aanda.paris@obspm.fr
Web: http://www.aanda.org

merging
Annales d'Astrophysique
Arkiv for Astronomi
Bulletin of the Astronomical Institutes of the Netherlands
Bulletin Astronomique
Journal des Observateurs
Zeitschrift fur Astrophysik
Bulletin of the Astronomical Institutes of Czechoslovakia

Paris, July 29, 2019

Reprint Permission

Material:
Article by Perez-Martinez et al. 2017, A&A, 605, A127

To be used in:
PhD thesis entitled "Galaxy evolution in the clusters RXJ1347-1145, CL1604+4304 and XMMUJ2235-2557 at 0.5<z<1.5", University of Vienna

Permission granted to:
José Manuel Perez Martinez
jm.perez@univie.ac.at

I hold copyright on the material referred to above, and hereby grant permission for its use as requested herewith.

The article should be reproduced as a whole in a coherent fashion fully consistent with the version published in A&A.

Credit should be given as follows:
Credit: Author, A&A, vol, page, year, reproduced with permission © ESO.

Thierry Forveille
A&A Editor-in-Chief

Sponsored by Argentina, Armenia, Austria, Belgium, Bulgaria, Chile, Croatia, Czech Republic, Denmark, Estonia, Finland, France, Germany, Greece, Hungary, Italy, Lithuania, Netherlands, Norway, Poland, Portugal, Slovak Republic, Spain, Sweden, and Switzerland.
Produced and distributed by EDP Sciences for ESO.

Chapter 3

Paper II

Title: Galaxy kinematics across different environments in the RXJ1347-1145 cluster complex

Authors: J. M. Pérez-Martínez, B. Ziegler, A. Böhm, M. Verdugo

Year: 2019

Journal: Astronomy and Astrophysics. Submitted on July 5th 2019.

Short description: In this work we examine the kinematical behaviour of a sample of galaxies in the RXJ1347 multicluster system at z$\sim$0.45. We use 2-dimensional VIMOS spectra to study the kinematical degree of asymmetry (A) of every object, and its relation with respect to different parameters such as the local number density value of the surroundings, the star-formation rate, the AGN frequency, and the offset with respect to the B-band and stellar-mass Tully-Fisher relation. In addition, we explore the stellar-to-halo mass relation for clusters and field galaxies at intermediate redshift by applying semi-empirical relations and theoretical prescriptions from the literature.

Personal Contribution: I carried out the full spectroscopic analysis of the sample (i.e. redshift determination, flux measurements, and extraction of kinematics) as well as part of the data reduction (run IDs: 087.A-0361(D) and 087.A-0361(D)). I computed absolute magnitude and stellar masses for the whole sample using the publicly available catalogs from the CLASH team

(Cluster Lensing And Supernova survey with Hubble) and applying SED fitting techniques to their results. In addition, I used the SUBARU Suprime-Cam z-band images to compute the structural parameters of our targets by applying successive surface brightness profiles. Finally, I had the leading role in the discussion of the manuscript and the writing process.

Astronomy & Astrophysics manuscript no. 30165_ap
July 5, 2019

Galaxy kinematics across different environments in the RXJ1347-1145 cluster complex ⋆

J. M. Pérez-Martínez[1], B. Ziegler[1], A. Böhm[1], and M. Verdugo[1]

Department of Astrophysics, University of Vienna, Türkenschanzstr. 17, A-1180 Vienna, Austria. e-mail: jm.perez@univie.ac.at

ABSTRACT

Aims. In order to understand the role of the different processes that drive galaxy evolution in clusters, we need comprehensive studies that simultaneously examine several of the most important physical properties of galaxies. In this work we aim to study the interplay between the kinematic state and star formation activity of galaxies in the RXJ1347-1145 cluster complex at z∼0.45.
Methods. We use VLT/VIMOS to obtain slit spectra for 95 galaxies across the 40′x40′ area where the RXJ1347-1145 cluster complex resides. We determine the cluster membership of our targets by identifying one or several of the available emission lines within the wavelength range. Our spectroscopy is complemented with archival SUBARU/Suprime-Cam deep photometric observations in five optical bands (B, V, Rc, Ic, z'). We examine the kinematic properties of our sample attending to the degree of distortion of the extracted rotation curves. Regular rotating galaxies enter our Tully-Fisher analysis while the distorted ones are used to study the role of cluster-specific interactions with respect to star formation and AGN activity.
Results. Our analysis confirmed the cluster membership for approximately half of our targets. We report a higher fraction of galaxies with irregular gas kinematics in the cluster environment than in the field. Cluster galaxies with regular enough rotation display a moderate brightening in the B-band Tully Fisher compatible with the gradual evolution of the stellar populations with lookback time, and no significant evolution in the stellar-mass Tully-Fisher relation, in line with previous studies at similar redshift. Average sSFR values are slightly lower in our cluster sample (-0.15 dex) with respect to the main sequence of star-forming galaxies, confirming the role of the environment in the early quenching of star formation in clusters. In addition, we carried out an exploratory observational study on the stellar-to-halo mass relation finding that cluster galaxies tend to have slightly smaller stellar mass values for a fixed halo mass compared to their field counterparts.

Key words. galaxies: kinematics and dynamics – galaxies: clusters: individual: RXJ1347-1145 - galaxies: evolution

1. Introduction

The general population of galaxies in the local Universe can be divided into two distinct types: Star-forming galaxies have blue colors, disk-like morphologies and a relatively high star formation rate (SFR), whereas quiescent galaxies have redder colors, more spheroidal shape, and a low level of star formation. These properties are the product of a series of processes acting over galaxies throughout their lifetime. To give some examples, mass growth (Cattaneo et al. 2011), morphological transformations (Mortlock et al. 2013), quenching of star formation (Peng et al. 2010), and redistribution of angular momentum (Swinbank et al. 2017) are some of the most important changes that galaxies experience across cosmic time. The scientific community coined the term galaxy evolution to refer to these processes as a whole, and it has been extensively studied up to z∼2 and beyond during the last decade.

In recent times, the mass growth and the environment have been revealed as the two main drivers of galaxy evolution (Baldry et al. 2006). However, both effects act in a similar way over the properties of the general population of galaxies, making it difficult to identify which one is dominant at different cosmic epochs. Dressler (1980) was the first to find that denser environments present higher fractions of quiescent galaxies compared to the field in the local universe. Recently, Socolovsky et al. (2018) linked the under-abundance of star-forming galaxies in clusters to an excess in the population of poststarburst galaxies in clusters at intermediate redshifts (0.5<z<1), pointing once again towards the influence of the environment in galaxy transformation and the quenching of star-formation. However, the exact mechanism causing the stop of star-formation is still a matter of debate, with recent studies proposing a two phase process where a galaxy first slowly consumes most of its gas reservoir in the outskirts of the cluster before being fully quenched due to ram-pressure stripping in the innermost regions (Wetzel et al. 2013, Maier et al. 2019).

This description of galaxy evolution in clusters holds until z∼1, when an increasing fraction of blue galaxies start to populate even the central regions of large scale structures (Butcher & Oemler 1978). At earlier epochs, the star-forming population becomes dominant, and during the cluster assembly, even starbursts are common (Santos et al. 2013, Dannerbauer et al. 2014, Popesso et al. 2015, Casey et al. 2017). On the other hand, Darvish et al. (2016) found that the quiescent fraction increases with stellar mass up to z∼3, becoming almost independent of environment at z>1, with galaxies showing similar SFR and specific SFR (sSFR) values in the field and in (proto-)clusters. Further, Paulino-Afonso et al. (2018) reported lower SFR values in dense environments for galaxies below $\log M_* \leqslant 10.75$ with respect to the field at z∼1, while galaxies above that threshold do not show significant differences, which means that mass quenching is only dominant at very high stellar masses at this epoch.

⋆ Based on observations with the European Southern Observatory Very Large Telescope (ESO-VLT), observing runs ID 386.A-0688(D) and 087.A-0361(D).

A&A proofs: manuscript no. 30165_ap

However, integrated properties such as galaxy luminosity, stellar mass and star formation activity are not sufficient to understand galaxy evolution in clusters, where interactions are frequent. Subtle cluster-specific processes such as starvation might be responsible for the early quenching of star formation for galaxies within massive clusters. However, in order to achieve a full transformation into passive ellipticals, we still need to comprehend the mechanisms that alter the kinematics of the cluster galaxies and rearrange their three-dimensional structure during their infalling phase. Processes like merging, harassment, ram pressure stripping are probably at act, but also other secondary processes such as the triggering of star formation due to tidal interactions or initial gas disk compression via ram-pressure (Ruggiero & Lima Neto 2017) might intervene in the stronger and accelerated evolution of galaxies living in clusters even though it is still unclear which one predominates.

The use of galaxy kinematics to study the evolution of star-forming galaxies in clusters has been traditionally linked to scaling relations such as the Tully-Fisher relation (TFR, Tully & Fisher 1977), that can only be applied to regular rotating disks. While some authors claimed no difference between the cluster and field TFR (Ziegler et al. 2003, Nakamura et al. 2006), others reported that spiral galaxies were slightly overluminous (Bamford et al. 2005) and display a larger TFR scatter (Moran et al. 2007) in the cluster environment at z<1. However, galaxies with irregular kinematics can not be excluded from a comprehensive environmental study since they embody the majority of the population in clusters (Vogt et al. 2004). Following this idea, Bösch et al. (2013a) were able to link ram pressure stripping events with asymmetries in the gas velocity profile of cluster galaxies that do not show significant distortions in their stellar structure.

In this work we choose the multicluster system RXJ1347-1145 to investigate the environmental imprints of galaxy evolution for objects displaying regular and irregular gas kinematic behaviour, focusing on their Tully-Fisher analysis, star-formation and AGN activity. The structure of this paper is as follows: In Sect. 2 we describe the target selection, observation conditions, and spectroscopic data reduction. Sect. 3 contains the description of the methods used during our analysis. We present our results and discussion in Sect. 4 and Sect. 5 respectively, followed by our conclusions in Sect. 6. Throughout this article we assume a Chabrier (2003) initial mass function (IMF), and adopt a flat cosmology with Ω_Λ=0.7, Ω_m=0.3, and H_0=70 km s^{-1}Mpc^{-1}. All magnitudes quoted in this paper are in the AB system.

2. Sample selection and observations

The galaxy cluster RXJ1347.5-1145 (hereafter RXJ1347) at z∼0.45 is one of the most massive and X-ray luminous clusters known (Schindler et al. 1995). RXJ1347 has been the subject of intense research, through spectroscopic (Laganá & Ulmer 2018, Jørgensen et al. 2017, Fogarty et al. 2017), X-ray (Foëx et al. 2017, Ghirardini et al. 2017), lensing (Chiu et al. 2018, Umetsu et al. 2018), and Sunyaev–Zel'dovich effect (Kitayama et al. 2016, Adam et al. 2018) analyses in recent years. However, most previous works were focused on the determination of the cluster internal sub-structures. The presence of two very bright galaxies close to the centre of the cluster and the discovery of shocked gas suggest that RXJ1347 is actually undergoing a major merger. Furthermore, Verdugo et al. (2012) identified a large scale cluster complex that extends diagonally across the field for about 20 Mpc and contains ∼30 additional group-like structures, including two additional prominent galaxy concentrations: one towards the south-east, coincident with the cluster LCDCS 0825 (Gonzalez et al. 2001) and another towards the north-east which was named 'the NE Clump' by Verdugo et al. (2012).

In this work we investigate the physical properties of galaxies that belong to this cluster complex, in particular with regard to their internal kinematics. We carried out multi-object (MOS) spectroscopy with VIMOS/VLT between March 2011 and September 2012 to obtain spectra for 95 galaxies using two pointings around the RXJ1347 main cluster structure at z∼0.45. Our primary targets were cluster galaxies selected from previous medium resolution spectroscopic campaigns carried out by our own group.

We used the high resolution grism HR-orange, which covers the wavelength range 5200 − 7600Å, and tilted slits aligned to the apparent major axis of the targets in order to minimize geometrical distortions. The tilt angles θ were limited to $|\theta| < 45^o$ to ensure a robust sky subtraction and wavelength calibration. We used a slit width of 0.8", which delivers an instrumental resolution of $\sigma_{ins} \approx 47$ km/s. This configuration yielded a spectral resolution of R∼2500 and an average dispersion of 0.6 Å/pix with an image scale of 0.205"/pixel. The total integration time slightly varies between observing runs, being 2.1h for targets observed during period P86 and 1.85h for targets in P87. Our observing program was conducted with average seeing conditions of 0.8" FWHM and airmass ∼1.1 during both observing runs. The spectroscopic data reduction was carried out using the ESO-REFLEX pipeline for VIMOS. The main reduction steps were bias subtraction, flat normalization, and wavelength calibration. Further, we co-add the 2D-spectra exposures using an IRAF sigma-clipping algorithm that performs a bad pixel and cosmic ray rejection.

We use several prominent emission lines ([OII] 3727Å, Hβ 4861Å, [OIII] 4959,5007Å) to measure the redshift of our targets and determine their cluster membership. The distribution of our targets in redshift space is shown in the top panel of Fig. 1. Two peaks are clearly visible at z∼0.45 and z∼0.47, that correspond to the two main structures of the cluster complex, RXJ1347 and LCDCS 0825. However, more than thirty additional smaller group-like structures have been previously reported to be part of the same large-scale structure (Verdugo et al. 2012). In order to encompass most of these structures in redshift space, our cluster membership window is defined as 0.415<z<0.485. Fig. 2 shows the distribution of our targets over the density map of the cluster structure presented in Verdugo et al. (2012). The contours define the galaxy number density of a given area in units of Mpc^{-2}. The first contour starts at 14 Mpc^{-2} which is 1σ above the mean density value in the field and gradually increases up to 200 Mpc^{-2} in the innermost regions of the cluster complex. Most of our cluster sample is located in the low to intermediate density areas. In addition, our spectroscopic campaign benefits from complementary archival Subaru Suprime-Cam wide-field imaging in five bands (B, V, Rc, Ic, z′) and CFHT/MEGACAM g'-band (Umetsu et al. 2014). The depth and seeing of our co-added mosaic images are shown in Table 1. The coordinates, redshifts, rest frame colors, and magnitudes of our final sample are summarized in the Appendix. The combination of the large field of view of Suprime-Cam (34′x 27′), its image quality, depth, and the wealth of our VLT/VIMOS spectroscopic programs allow us to present a comprehensive picture of the physical properties of galaxies in clusters at intermediate redshift.

Table 1: Summary of the imaging data used in this work

Telescope	Filter	Exp. Time (s)	FWHM (")
Subaru/Suprime-Cam	B	1 440	2.20
...	V	2 160	0.75
...	Rc	2 880	0.74
...	Ic	3 240	1.14
...	z′	4 860	0.72
CFHT/MEGACAM	g′	4 200	1.01

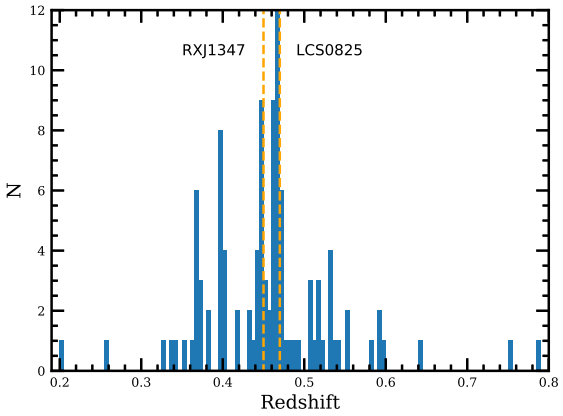

Fig. 1: Distribution of our targets in redshift space. The two dashed orange lines at z∼0.45 and z∼0.47 correspond with the two major structures of the cluster complex identified as RXJ1347.5-1145 and LCDCS 0825 by Verdugo et al. 2012.

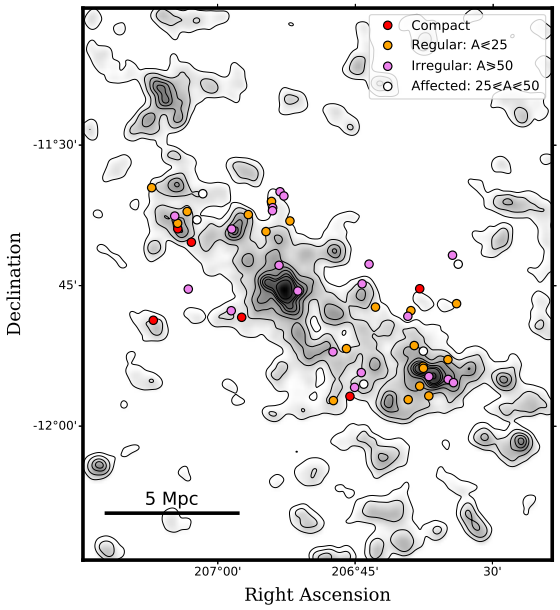

Fig. 2: Spatial distribution of our cluster sample over the galaxy number density map shown in Verdugo et al. (2012) using the nearest-neighbour counting technique. The figure covers an approximate area of 50×50 arcmin^2 around the center of the RXJ1347 cluster complex. Density countours start 1σ above the value of the general field at the redshift of the cluster, and gradually increase up to 200 Mpc^{-1} in the inner regions of the cluster complex. Orange, purple and white points respectively display galaxies classified as regular, irregular and affected according to their gas kinematics as presented in Sec. 3.4.

3. Methods

3.1. Rest frame magnitudes and stellar masses

We used the publicly available photometric catalogs produced by the CLASH team (Umetsu et al. 2014) using SExtractor (Bertin & Arnouts 1996) over PSF matched Subaru images in five bands (B, V, Rc, Ic, z′) to obtain the observed magnitudes of our targets. Stellar masses and rest frame magnitudes have been computed by using Lephare (Ilbert et al. 2006 and Arnouts & Ilbert 2011. This code applies a χ^2 minimization algorithm to match stellar population synthesis models (Bruzual & Charlot 2003) to the spectral energy distribution (SED) derived from the photometry available assuming a Chabrier IMF (Chabrier 2003). We constrained the possible ages to values lower than the age of the Universe at z∼0.45 (i.e. ∼9 Gyrs), and applied Calzetti's attenuation law (Calzetti et al. 2000) with extinction values of $E(B-V) = 0 - 0.5$ mag in steps of 0.1 mag. We estimate the total calibration for all bands to have an accuracy of 0.1 magnitudes and ∼0.15 dex for the logarithmic stellar masses.

To put our sample in context, we plot our galaxies into the BRI color-color diagram (Fig. 3). This kind of diagram splits the galaxies into two different groups, an old-age sequence of quiescent galaxies, and a star forming sequence of galaxies with stronger star formation rates and higher dust contents (Whitaker et al. 2013). These regions are empirically delimited by previous studies so that the passive population is easily distinguished from the star-forming one. Kuchner et al. (2017) recently applied the BRI diagram for this purpose in another cluster at similar redshift and compared their results with those obtained by using the popular UVJ diagram (see Whitaker et al. 2013 and van der Wel et al. 2014) finding a high degree of consistency between both classification schemes. In our study, the vast majority of galaxies lie within the star-forming region with very similar distributions between the cluster and field subsamples.

3.2. Structural parameters

We use the z′-band Subaru Suprime-Cam images to measure the structural parameters of our galaxies. There are two reasons behind this choice, the very good seeing conditions (FWHM∼0.7") achieved during the observations in this band, and the fact that redder filters trace the structure of the disk more accurately and to larger galactocentric radii, avoiding the contamination coming from prominent star formation features that are usually visible in bluer wavelength regimes. This makes the z′-band photometry the best available option for computing the structural parameters of our targets.

We used the GALFIT package (Peng et al. 2002) to model the surface brightness profile of our targets and extract their structural parameters using a two-component fit. For every object we first compute an exponential profile ($n_s = 1$) to model the disk component of our galaxies and subtract it from the original image. We inspect the resultant residuals and keep the modelled structural parameters in case the object under scrutiny does not

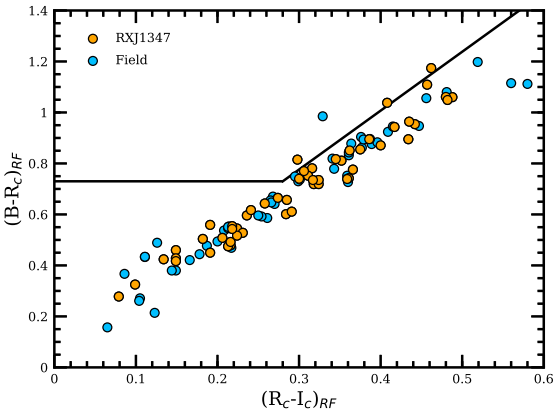

Fig. 3: BRI diagram for our cluster (orange) and field (blue) sample of galaxies. Both samples show very similar distributions in the star-forming region of the diagram with only a few galaxies in the exclusion (passive) area.

show signs of the presence of a bulge. Otherwise, we use these parameters as initial guess values in a two component surface brightness profile with $n_s = 4$ for the bulge. The most important parameters for the analysis presented in this work are the inclination (i), the position angle (θ), and the effective radius (R_e). The inclination, i, is computed from the ratio between the apparent major and minor axis (b/a) following Heidmann et al. (1972) and assuming that the ratio between disk scale length and scale height is consistent with the observed value for typical spirals in the local Universe (i.e. q=0.2, Tully et al. 1998). Finally we define the mismatch angle, δ, as the difference between the position angle of a given galaxy and its slit. We restrict our analysis to galaxies with $|\delta| \leq 45^\circ$ to minimize geometrical distortions.

3.3. Determination of the maximum intrinsic velocity (V_{max})

The rotation-curve extraction and determination of V_{max} from 2D spectra has been explained in full detail in several previous publications within our own group (see Böhm et al. 2004, Bösch et al. 2013b, Böhm & Ziegler 2016). In the following paragraphs we provide a brief summary of our approach to obtain V_{max}.

Typically, [OII] and Hβ are the two brightest spectral features within the wavelength range of our observations, and thus, the sources from which we extract our rotation curves. We generally enhance the signal-to-noise ratio by averaging over up to 3 pixels (i.e. 0.75" in the spatial axis) and examine the red- and blueshifts of the emission line under scrutiny as a function of galactocentric radius. These shifts are later converted into positive and negative velocity values with respect to the kinematic center of the galaxy, that is determined by identifying the photometric center and by allowing a small shift to minimize the mismatch between the photometric and kinematic center for rotating targets. This shift has a maximum value of ∼1.5 kpc in spatial scale at the redshift of our targets.

Finally, we correct the observed velocities from all observational, geometrical and instrumental effects (seeing, disk inclination, misalignment angle and slit width) and compute a simulated velocity field that takes into account the previously obtained structural parameters of our galaxies. We assume an intrinsic rotational law with a linear rise of the rotation velocity up to the turnover radius and a convergence into a constant value, V_{max}, at large galactocentric radii (Courteau 1997). By extracting the simulated rotation curve we obtain the intrinsic maximum rotation velocity V_{max}. The typical error on V_{max} is ∼20 km/s depending on the accuracy of the structural parameters and the quality and extent of the rotation curve. The synthetic velocity fields and simulated and observed rotation curves for our sample can be found in Appendix 6.

3.4. Rotation-curve asymmetry

Through their lifetime, galaxies may suffer interactions of different kind, either with other objects or with the medium where they reside. These interactions alter the motion of the gas and stars orbiting around the center of the galaxy, introducing a certain degree of distortion in their kinematics. To quantify these disturbances Dale et al. (2001) introduced an asymmetry index (A) that measures the difference between the area under the approaching and receding arms of a rotation curve as a function of galactocentric radius. This parameter is particularly sensitive to disturbances affecting the outer parts of the rotation curves and to large offsets between the photometric and the kinematic center of the galaxy. It has been applied successfully to identify distorted galaxies at z∼0.2 by Bösch et al. (2013a) using the following prescription:

$$A = \sum_i \frac{|v(r_i) + v(-r_i)|}{\sqrt{\sigma_v^2(r_i) + \sigma_v^2(-r_i)}} \left[\frac{1}{2} \sum_i \frac{|v(r_i)| + |v(-r_i)|}{\sqrt{\sigma_v^2(r_i) + \sigma_v^2(-r_i)}} \right]^{-1} \quad (1)$$

The pairs $(v(r_i), v(-r_i))$ represent the velocity of the two wings of the rotation curve weighted by their erros $(\sigma_v(r_i), \sigma_v(-r_i))$. For undisturbed galaxies we expect $|v(r_i) + v(-r_i)|$ to be close to zero, and which translates into a very low asymmetry index value, while those galaxies with significant distortions in one side of the galaxy or with completely chaotic kinematics will yield higher A values. Based on the experience of Bösch et al. (2013a) with this index we created three categories according to the degree of asymmetry displayed by our galaxies. Those objects with $A \leqslant 25$ are labeled as regular rotators. Galaxies displaying intermediate A values such as $25 \leqslant A \leqslant 50$ are considered to be affected by recent interactions even if they still show signs of their former regular rotational status. Finally, galaxies with $A \geqslant 50$ are classified as irregulars. We show examples of these three categories in Fig. 4.

4. Results

In this section we study the relation between the kinematic state of our galaxies, the environment, and some of their most important physical properties such as the SFR and the AGN activity. We will investigate the behaviour of our sample with respect to different scaling relations. Our sample is initially comprised of 95 spectroscopically detected galaxies, 50 of them in the cluster and 45 in the field. However, the additional requirements imposed to obtain the physical quantities previously mentioned will progressively diminish the size of our sample.

4.1. Kinematic state and environment

The first step in our analysis consisted on the identification of the kinematic state of our cluster and field samples. To achieve that, we first inspect the spectra of our targets and extract position-velocity diagrams such as those shown in Fig. 4. Those objects

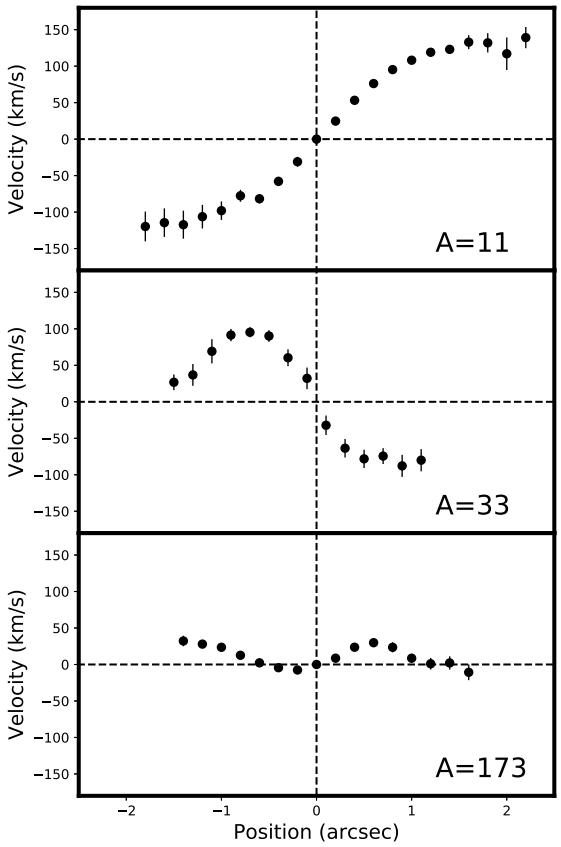

Fig. 4: Three examples of the asymmetry classification scheme used for our sample of galaxies. From top to bottom we can see a case for regular ($A \leqslant 25$), affected ($25 \leqslant A \leqslant 50$), and irregular ($A \geqslant 50$) kinematics.

with kinematic information up to a sufficiently large galactocentric radii will be classified as regulars, affected, and irregulars according to their asymmetry index values. We find that the fraction of irregular galaxies in the cluster environment is higher than in the field (40.0% and 23.3% respectively, see Table 2). However, the total fraction of galaxies that have suffered some kind of disturbance (affected + irregulars) is similar between the cluster and field environment (50% and 41.8%). This suggest that, while the field population of galaxies at 0.3<z<0.6 already contains a significant fraction of galaxies showing some degree of distortion, cluster specific interactions contribute to enhance their asymmetry index, increasing the fraction of irregular galaxies according to our gas kinematics asymmetry criterion. These results are in line with previous studies (Yang et al. 2008, Kutdemir et al. 2010) that reported significant fractions of field galaxies with perturbed kinematics at intermediate redshifts.

4.2. The Tully-Fisher relation

We used galaxies with regular enough kinematics to extract a reliable value for V_{max} for our Tully-Fisher diagrams. Objects classified as regular rotators using the asymmetry index criterion, and those labeled as affected but with sufficiently extended kinematics entered our analysis. In this work we chose the B-band and the stellar mass (M_*) TFR to look for imprints of environmental effects in our cluster galaxies. The B-band is dominated by the light of massive young stars and therefore is very sensitive to recent episodes of star formation. On the other hand, the stellar mass act as proxy to trace the weight of the overall underlying population of old stars within the galaxy. In summary, these two complementary representations of the TFR provide a way to examine the recent and cumulative star formation history of the galaxies through their kinematics.

Table 2: Kinematic state fractions

	Cluster	Field
Regular	38.0% (19/50)	41.8% (18/45)
Affected	10.0% (5/50)	18.6% (8/45)
Irregular	40.0% (20/50)	23.3% (10/45)
Compact	12.0% (6/50)	16.3% (7/45)

Before presenting our results on the B-band TFR, we must emphasize the importance of correcting our absolute magnitudes from extinction. In general, edge-on spiral galaxies show higher values of extinction than their face-on counterparts, the reason is that the light coming from the stars goes through a larger portion of the disk when the galaxy is edge-on with respect to the line of sight. In addition, more massive disks are dustier than lower-mass disks (Giovanelli et al. 1995). We take into account these two effects following the prescription given by Tully et al. (1998) to correct rest frame B-band absolute magnitudes for intrinsic dust absorption. This correction diverges for completely edge-on galaxies (i.e. i=90º), and therefore we exclude from our sample one cluster and four field galaxies for this reason. After applying this correction, the typical errors for the B-band absolute magnitude values in the TFR are ∼0.2-0.3 mag. In addition, two more galaxies (one in the cluster and one in the field) were excluded after finding that their mismatch angles were $\delta \geqslant$45º. Finally, four field galaxies lie beyond the edge of the SUBARU images and were excluded due to the lack of enough photometric bands to extract reliable rest frame magnitudes and stellar masses.

We present our B-band TFR in Fig. 5 (left side). Our final TFR cluster sample is composed of 19 regular and 4 affected objects (orange and white stars respectively). However, we will use only the regular objects to study the evolution of the Tully-Fisher relation. In order to find the best fit for our sample we keep the slope of the local relation by Tully et al. (1998) while we let the intercept vary. We find an average deviation of ΔM_B=-0.7±0.8 mag for our cluster sample. We use three different auxiliary samples to compare with: First, we make use of the 10 remaining field regular galaxies observed by our own program, finding that ΔM_B=-0.6±0.7 mag. In addition we include a sample of 50 cluster star-forming galaxies at z=0.16 studied by Bösch et al. (2013b), who reported ΔM_B=-0.3±0.7 mag with respect to the local TFR. Finally, we compare our results against a sample made of 124 field star-forming galaxies at 0<z<1 that is representative of the typical scatter of this scaling relation in the given redshift range (grey area). We emphasized that, in all these data sets, V_{max} and M_B were computed using the same methods presented in this study, which makes them ideal for a direct comparison. The scatter of our cluster sample at z∼0.45 is consistent with what has been previously found in the field (Böhm & Ziegler 2016), while the reported offset in B-band luminosity is larger than that of the Bösch et al. (2013b) sample

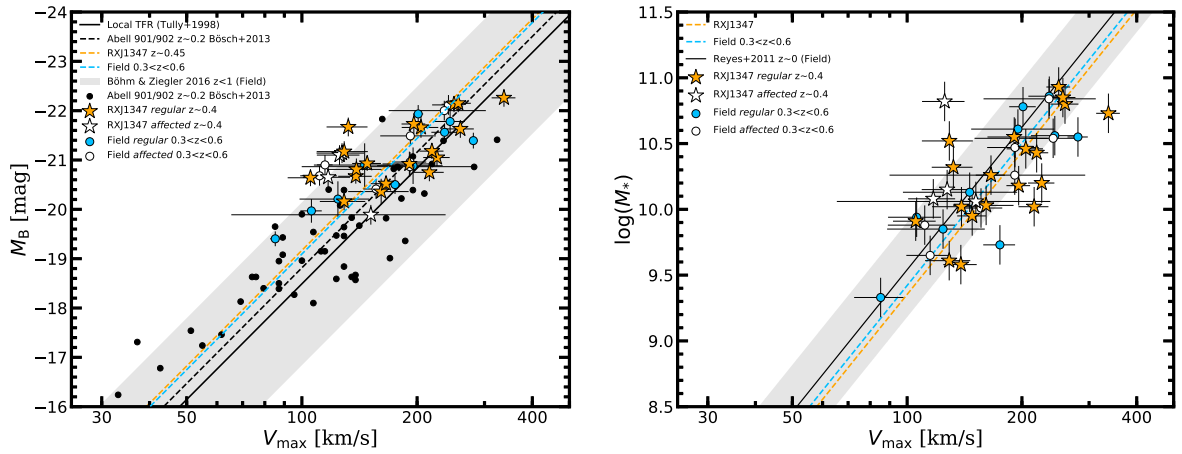

Fig. 5: *Left*: Tully-Fisher B-band diagram. In all diagrams orange and white stars represent regular and affected cluster objects respectively, while blue and white circles represent regular and affected field galaxies respectively. Black circles represent cluster galaxies at z~0.2 from Bösch et al. (2013b). The dark grey solid line shows the local B-band TFR (Tully et al. (1998)) with a 3σ scatter area around reported by Böhm & Ziegler (2016) for galaxies at 0<z<1 (grey area). The orange, blue, and black dashed lines represent the best fit for the cluster anf dield sample of this study, and the cluster sample from Bösch et al. (2013b) respectively. *Right*: Stellar mass Tully-Fisher diagram. The symbols and their colors follow the same description than in the left hand panel. The solid black line shows the local M_*-TFR from Reyes et al. (2011), with a 3σ scatter grey area around it.

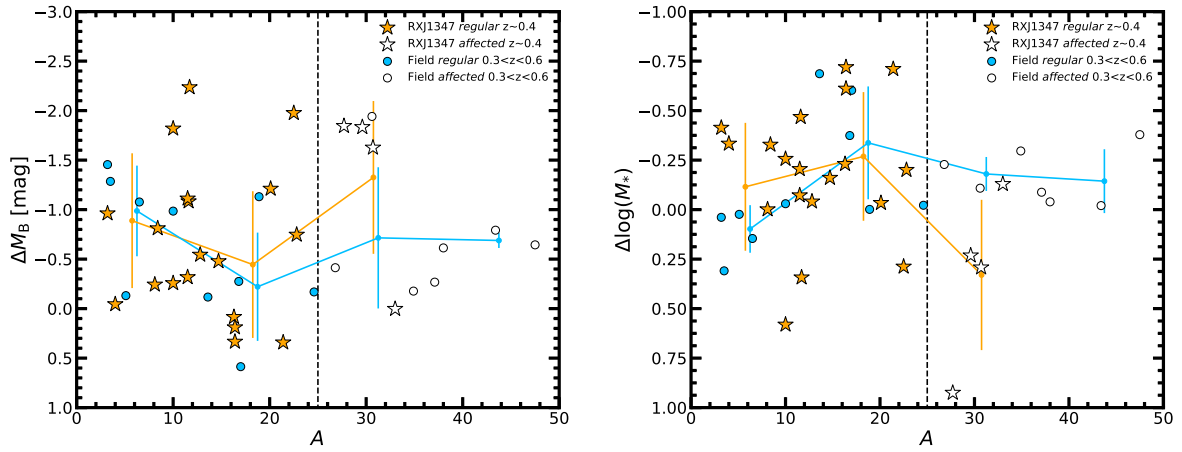

Fig. 6: *Left*: B-band Tully-Fisher offsets with respect to the as asymmetry index. *Right*: M_*-Tully-Fisher offsets with respect to the asymmetry index. In all diagrams orange and white stars represent regular and affected cluster objects respectively, while blue and white circles represent regular and affected field galaxies respectively. The orange and blue dots joint by lines of the same color show the mean values and standard deviation of our cluster and field sample divided in 4 bins according to their asymmetry index ($A \leqslant 12.5$, $12.5 \leqslant A \leqslant 25$, $25 \leqslant A \leqslant 37.5$ and $37.5 \leqslant A \leqslant 50$). The vertical dashed black line at A=25 marks the limit between the kinematically regular and affected categories.

at lower redshift, but in line with what has been found by previous observational studies (Bamford et al. 2005) and predictions from semianalytical models (Dutton et al. 2011). We repeated our analysis for the M_*-TFR (Fig. 5, right side) finding a mild offset (ΔM_*=0.2±0.4) between our targets at z~0.45 and the local relation (Reyes et al. 2011). In the case of our field sample the offset is even smaller (ΔM_*=0.1±0.3). This supports previous results claiming no significant evolution on the M_*-TFR up to z~1 (Pelliccia et al. 2017, Harrison et al. 2017) and points towards a small influence of the environment in the M_*-TFR at this redshift.

In Fig. 6 we analyze the possible relation between the asymmetry index (A) and the residuals from the B-band and M_*-TFR. We bin our objects in 4 bins according to their asymme-

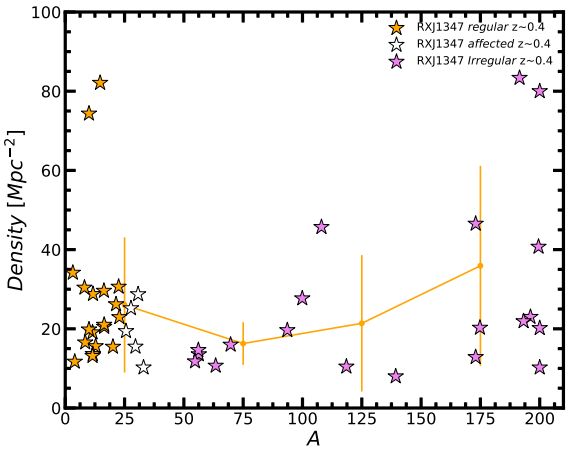

Fig. 7: Galaxy number density of the area where our cluster objects lie (Verdugo et al. 2012) with respect to their asymmetry index. Orange, white and violet stars represent regular, affected and irregular cluster objects respectively. The orange dots joint by lines of the same color show the mean values and standard deviation of our cluster sample divided in 4 bins according to their asymmetry index ($A \leqslant 50$, $50 \leqslant A \leqslant 100$, $100\% \leqslant A \leqslant 150$ and $150 \leqslant A \leqslant 200$).

try index value ($A \leqslant 12.5$, $12.5 \leqslant A \leqslant 25$, $25 \leqslant A \leqslant 37.5$ and $37.5 \leqslant A \leqslant 50$) and compute the average of the residuals in these bins and its standard deviation. We restrict ourselves to study only the first three bins of the cluster sample due to the lack of galaxies in the fourth one. Our results show that the cluster and field samples are similarly distributed with no clear trends. In Fig. 7, we investigate the influence of the local galaxy number density on the asymmetry index of our objects. We find that, within our cluster sample, most objects that entered our Tully-Fisher analysis are located in moderate to low density regions of the structure, while only two regular galaxies are found in the densest areas of the cluster complex. In an environment-based quenching scenario we expect that most star-forming galaxies may either increase their asymmetry index (becoming kinematically irregular, Bösch et al. 2013a) and gradually stop their star-formation during their infalling path towards the central and densest areas of the cluster (Haines et al. 2015). The only two objects lying in these dense regions show $\log M_*$=10.52 and $\log M_*$=10.85, which may indicate that only the most massive star-forming galaxies would still show significant star formation activity across their disks once they reach the central areas of massive clusters. On the other hand, most galaxies with irregular gas kinematics within our sample lie in low to intermediate density regions too, which suggest that a significant fraction of field galaxies infalling into cluster structures already carry gas kinematic distortions before being affected by environmental effects.

4.3. Star-formation activity

The most reliable and most commonly used SFR calibrator is Hα. However, the observation of intermediate to high redshift targets makes difficult to get access to this emission line using optical spectroscopy. This is the case of our VIMOS programs for which we can only detect spectral features for cluster galaxies between 3600 − 5200Å in rest frame. Thus, we rely on the [OII]λ3727 doublet to estimate the SFR of our targets. Due to the slit positioning of our objects with respect to the center of the VIMOS mask, the wavelength range of some objects is slightly offset towards redder or bluer wavelengths. In the former case this may shift the [OII] line out of the visible wavelength range, making it impossible to determine the SFR using this method. This reduces our sample to 31 cluster galaxies split in the same three groups described in Sec. 3.4 according to their asymmetry index. We apply the prescription given by Gilbank et al. (2010) to these objects in order to compute reliable SFR values:

$$SFR_{emp,corr}/(M_{\odot}yr^{-1}) = \frac{L([OII])/3.80 \times 10^{40} ergs^{-1}}{a\tanh[(x-b)/c] + d} \quad (2)$$

where a = -1.424, b = 9.827, c = 0.572, d = 1.700 and x=log $(M_*/M_{\odot})$. This approach includes an empirical mass-dependent correction that takes into account the effects of metallicity and dust extinction over the SFR. However, Gilbank et al. (2010) assume a Kroupa IMF while all the quantities in this paper have been computed following a Chabrier IMF. To maintain consistency, we multiply $SFR_{emp,corr}$ by a factor 0.9 that accounts for the stellar mass transformation between the Kroupa and Chabrier IMFs.

In order to study the star formation activity of our cluster galaxies we present the sSFR-mass relation in Fig. 8 (upper panel). We will use the so-called main sequence (Eq. 1 in Peng et al. 2010) at z∼0.45 as a reference for the expected star formation activity in the field. The goal of this analysis is to study the environmental imprints on the star formation activity of our galaxies, and their relation with their kinematic state. We find that regular cluster galaxies lie on average 0.1±0.3 dex below the main sequence, while irregular galaxies show a slight larger offset of 0.2±0.4 dex. On average, the specific star formation of kinematically irregular galaxies is slightly more suppressed than in their regular counterparts. However, this difference becomes statistically insignificant once we take the errors into account.

4.4. Gas excitation diagnostics

In this section we aim to investigate the ionizing source of the interstellar medium (ISM) in our galaxies, and if it is related to cluster specific interactions that influence their degree of gas kinematic asymmetry at the same time. The two candidate processes are the products of star formation (i.e. hot young stars), and the presence of a supermassive black hole in the center of the galaxy injecting a large amount of energy in the ISM. Given the wavelength constrains of our spectroscopic observations we are unable to apply the often used BPT diagram (Baldwin et al. 1981) for this purpose, and thus we are forced to use other diagnostics that require emission lines in the bluer part of the spectrum. One of these representations is the Mass-Excitation (MEx) diagram introduced by Juneau et al. (2011). This diagram takes the [OIII]λ5007/Hβ ratio from the BPT diagram and substitutes the [NII]/Hα ratio for the stellar mass. It has been tested up to z∼2 with a good degree of consistency with respect to BPT analyses at similar redshift (Juneau et al. 2014).

We present our results in Fig. 8 (bottom panel), where we divide our sample according to their kinematic state in the same way that we described in the previous section. We find that most of our galaxies lie within the star-forming or composite regions, independently of their kinematic classification. There are only two galaxies within the AGN region, being one of them classified as irregular and the other one as regular according to their

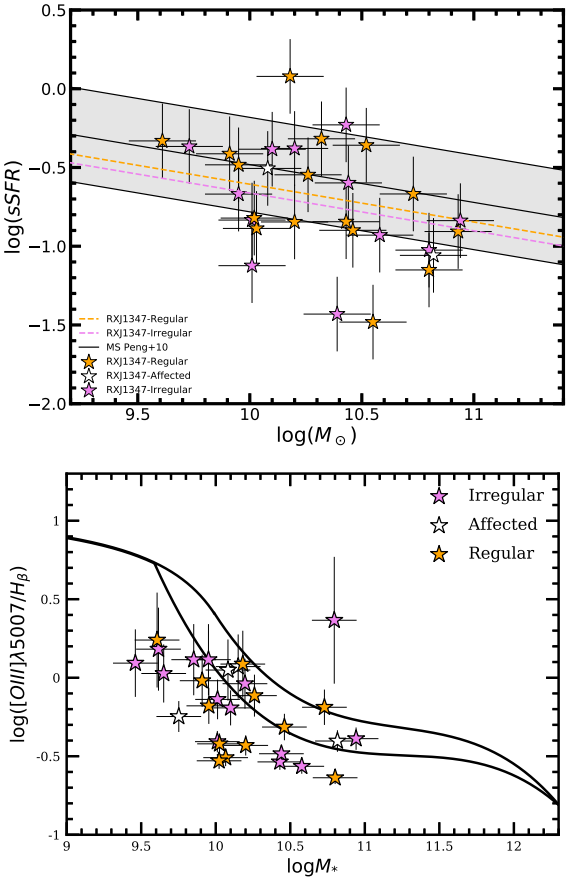

Fig. 8: *Top*: sSFR-log(M_*) diagram. Orange, white, and violet stars respectively represent cluster galaxies classified as regular, affected and irregular according to their kinematic asymmetry index value (A). The black solid line shows the Main sequence of star-forming galaxies at z∼0.45 given by Peng et al. (2010) with a 3σ grey area region. The orange and violet dashed lines represent the best fit linear regressions to our sample of regular and irregular galaxies respectively assuming the slope given by the main sequence and a Chabrier IMF. *Bottom*: Mass-Excitation diagram. Shape and color symbols meanings are identical to the ones shown in the top panel. The diagram is divided in three different regions according to the dominating source of gas excitation: star-forming (bottom left), AGN (top right), and composite (central stripe).

asymmetry index. Our results suggest that AGN activity is not connected with kinematic gas distortions, and thus, interactions between galaxies or with the intracluster medium are not likely to trigger a strong AGN response by channeling gas towards the central regions of the galaxies on our spatial scales.

4.5. Halo masses

Dark matter haloes are key to understand the formation of the first galaxies and the hierarchical growth of structures in the universe. For most individual galaxies, dark matter represents more than eighty percent of their total mass, yet due to the non-interacting nature of dark matter little can be said about its properties. For this reason, galaxy evolution studies are usually focused on the study of the baryonic component of the different populations of galaxies across cosmic time. However, measurements of the halo mass are fundamental to achieve a comprehensive understanding of galaxy formation and evolution since the gravitational potential, dominated by the dark component, drives most of the interactions that a galaxy undergoes during its lifetime.

The presence of dark matter within galaxies is ideally inferred from observations of baryonic matter if possible. The traditional method for measuring the dark matter content of galaxies is through their internal kinematics, and using this to derive their dynamical masses. However, the available baryonic information is usually limited by observational constrains, and the use of models and simulations is needed to translate our observables into the parameters required to compute the dynamical mass. Recently, Conselice et al. 2018 adopted a number of combined observational and theoretical approaches to derive the halo mass of field galaxies up to z∼3. In the next sections, we follow a method introduced by Lampichler et al. (2017) and tested by Conselice et al. (2018) to derive the halo mass values for our sample of galaxies. This method is only valid for objects with $v/\sigma>1$. While we did not carry out a velocity dispersion analysis for our samples, it is reasonable to assume that galaxies labeled as regulars (A<25) according to their asymmetry index comply with this requirement. The halo mass can be defined as:

$$M_h = \frac{v_h^2 R_h}{G} \tag{3}$$

where R_h is the virial radius of the halo, v_h the rotation velocity at R_h, and G is Newton's gravitational constant. However, R_h and v_h can not be directly obtained from our observational data. Thus, we need to find a way to compute these quantities from the effective radius R_e and the maximun rotation velocity V_{max} measured in our study. Kravtsov 2013 established a relationship between the half mass radius (R_m) and the virial radius assuming that the relation between the total mass of halos, M_h, and stellar mass of galaxies they host, M_*, is approximately monotonic, and cumulative abundances of halos and galaxies match ($n_h(>M) = n_g(>M_*)$):

$$R_m \approx 0.015 R_h \tag{4}$$

In the case of disk galaxies, we can convert the half-mass radius into optical half-light radius by using the empirical relation presented in Szomoru et al. (2013) for galaxies at 0.5<z<2.5. In this study the authors use deep HST data in several fields to derive accurate stellar mass surface density profiles, from which R_m will be extracted by assuming a certain M/L ratio dependent on the galaxies' properties. In the low redshift regime, they found that R_m is on average 25% smaller than the restframe optical R_e:

$$R_e \approx 1.33 R_m \tag{5}$$

For a more in depth discussion of the methods used we refer to Szomoru et al. (2013). Equations 4 and 5 provide us with a relationship between the virial radius of the dark matter halo (R_h) and the half-light optical radius (R_e). Finally, to compute the halo mass we need to connect V_{max} with v_h. Several works (Dutton et al. 2010, Papastergis et al. 2011, Cattaneo et al. 2014) have investigated this relation by comparing the rotation velocity measured at several scale lengths from the center of the galaxy

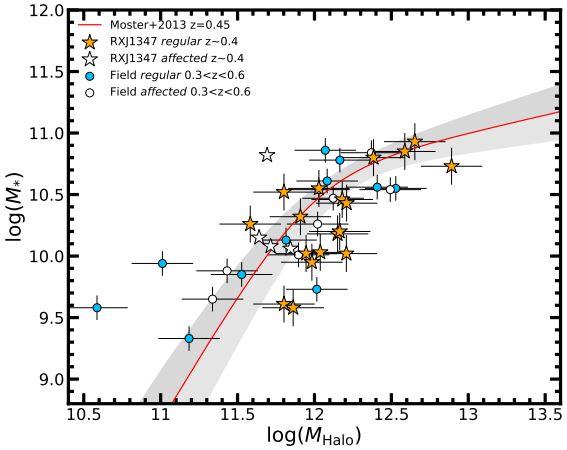

Fig. 9: Stellar-to-halo mass diagram. The red solid line represents the expectations for this relation given by Moster et al. 2013 at z~0.45 with a 1σ grey area. All the other symbols have the same meaning as in Fig. 5.

(v_{opt}) with theoretical models that take into account the contribution of different dark matter halo profiles to obtain the rotation velocity at the virial radius (v_h). Given the description of v_{opt} in those studies we can assume that in our work $V_{max} \approx v_{opt}$ in the following. However, the ratio v_{opt}/v_h is strongly dependant on the model used, ranging from v_{opt}/v_h=1.1 to v_{opt}/v_h=1.5 between different studies. We here adopt the mean value, v_{opt}/v_h=1.3, to compute our halo masses. Taking into account these approximations we can estimate the halo mass of our targets in the following way:

$$M_h \approx \frac{28.3 V_{max}^2 R_e}{G} \quad (6)$$

In Fig. 9 we present the stellar-to-halo mass relation for our sample of cluster and field galaxies at intermediate redshift in comparison with the theoretical relation derived by Moster et al. (2013), that in this case has been parametrized for z~0.45. The distribution of both our cluster and field samples follow the theoretical relation with significant systematic errors inherent to the computation of M_h. Interestingly, most cluster galaxies with log M_*<10.5 lie below the theoretical prediction, while this effect is not seen for field galaxies with similar stellar mass. However, the scatter of the sample and the low number of objects make difficult to draw conclusions about the origin of this difference.

5. Discussion

The study of different galaxy properties provide us with diverse pieces of the galaxy evolution picture. This work is focused on the study of galaxy kinematics, its connection with the environment, and the star formation and AGN activity. The kinematics analysis yielded a higher fraction of irregular galaxies in the cluster environment than in the field according to our asymmetry index criteria. This can be explained by the influence of cluster specific interactions on the population of galaxies that are progressively infalling towards the central regions of the cluster complex. On the other hand, we speculate that the relatively high fraction (41.9%) of field galaxies displaying signs of disturbances (irregular + affected) may be caused by the continuous mass growth of the galaxies in the field via accretion and minor merging events at intermediate redshifts. Our results suggest that field galaxies do not live in complete isolation and are subject to minor interactions with relative frequency, disturbing their gas kinematics to some extent. This scenario was already introduced by Puech et al. (2008) and Kutdemir et al. (2010) in the past.

The Tully-Fisher relation and its evolution for cluster galaxies has been a subject of debate during the last two decades. Nowadays, the dominant view is that there are not significant differences in the slope and the zero point of the relation between field and cluster galaxies at a fixed redshift, but larger scatter has been reported in cluster samples. However, the combination of different representations of the TFR can be useful to obtain information about the evolutionary stage of the stellar populations that are part of the studied galaxies. Some attempts in this direction were made by our own group in Pérez-Martínez et al. (2017) for a small sample of cluster galaxies at z~1.4. However, we do not find remarkable effects for our cluster galaxies at z~0.45. The cluster B-band TFR yielded a moderate brightening of ΔM_B=-0.7±0.8 mag with respect to the local B-band TFR, which can be explained by the gradual evolution of stellar populations with lookback time and the intrinsic scatter of our sample. These results agree within the errors with previous works in the cluster environment (Bamford et al. 2005). In parallel we report no significant evolution in the M_*-TFR (ΔM_*=-0.2±0.4), in line with previous observational studies in the field (Übler et al. 2017, Tiley et al. 2019) and cluster environment (Pelliccia et al. 2019), with semianalytical models (Dutton et al. 2011), and with recent results from the EAGLE hydrodynamical simulations at z~0 (Ferrero et al. 2017). The lack of evolution in the M_*-TFR across environment and cosmic time points towards the presence of a tight link between the stellar mass growth and the changes in dynamical mass (for which V_{max} acts as a proxy) of a given galaxy during its lifetime.

Dense environments accelerate and strengthen the quenching of star formation in galaxies and their morphological transformation (Maier et al. 2016, Rodríguez del Pino et al. 2017, Kuchner et al. 2017). In this work, we have used this information to investigate the star formation activity for cluster galaxies displaying different kinematic behaviours. Our cluster sample agrees with previous results (Maier et al. 2016) showing slightly lower sSFR values with respect to the field main sequence of star forming galaxies at z~0.45. However, some authors have speculated that after a galaxy experiences a gravitational interaction that heavily disturbs its kinematics, a star-formation event might be triggered, enhancing momentarily its SFR (Hoyos et al. 2016). We do not find this effect in our cluster sample. In fact, on average galaxies classified as irregulars display a slightly lower average sSFR value (-0.2 dex) than their regular counterparts (-0.1 dex). This small difference becomes insignificant when taking into account the scatter of our sample. Nevertheless, it shows that the star formation activity is (in general) independent of the galaxy kinematics.

We consider two different explanations for these results. Interactions such as starvation act gradually over the gas reservoir on a relatively long time scale, increasing its strength towards the cluster core regions, and acting as a cumulative effect over the physical properties of a given galaxy. In a similar way, ram-pressure stripping (RPS) may become an important effect when the galaxy approaches the innermost regions of the cluster, acting for several hundred million years. On the other hand, mergers and close encounters can be considered as instantaneous

events, and their effects are strongly dependant on the previous properties of the objects involved. Cluster complexes as big as RXJ1347 grow by accreting infalling groups of galaxies that have been subject to a certain degree of pre-processing, causing a partial depletion of their gas reservoir, and thus, making it more difficult to trigger a strong starburst after a merging event. In addition, starbursts are very short lived events, lasting no more than a few hundred million years at maximum. In a context where the gas reservoir of the host has been already partially depleted due to its interaction with the ICM for some time, the duration of a starburst event may be even shorter. This means that at a given time, very few objects may be experiencing this phase, making their detection difficult. Some recent results by the STAGES collaboration show signs of star formation enhancement for some cases of ram pressure stripping detected thanks to the analysis of deep HST photometry and narrow band H_α images in the Abell 901/902 cluster complex at z$\sim$ 0.16 (Roman-Oliveira et al. 2019). In that work, the authors found that the distribution of RPS-galaxies is enhanced by $\sim$0.2 dex in $\log(sSFR)$ at a fixed M_* with respect to their cluster star-forming mother-sample. If such cases are present within our sample, the kinematic analysis we carried out does not allow us to unambiguously identify them, which may contribute to the scatter of our cluster sample in the sSFR-log(M_*) relation.

In addition, we examine the influence of galaxy kinematics on the AGN activity. Recent results by Poggianti et al. 2017 suggest that some interactions such as ram pressure stripping feed the central black hole of massive disk galaxies, triggering AGN activity. Due to the characteristics of our sample we choose a more simplistic approach by studying the frequency of AGNs in galaxies that display regular and distorted gas kinematics in the cluster environment. Our results, though limited due to the size of our sample, show that the fraction of AGNs is very similar (and very low) for both classes. It seems that in general, interactions in the cluster environment are not likely to channel gas from the outskirts of the galaxy towards its central regions. Thus, the appearance of AGN is probably dominated by the effects of the mass growth as it happens in the field, though attenuated by the partial depletion of the cold gas reservoir due to the influence of the ICM.

Finally, we carried out an exploratory analysis of the stellar-to-halo mass relation using the method outlined by our group (Lampichler et al. 2017) and Conselice et al. (2018). We find that our cluster and field samples follow the theoretical predictions proposed by Moster et al. (2013) at the redshift of our targets. Similarly, Niemiec et al. (2018) studied this relation for satellite cluster galaxies using the Illustris simulations. The authors follow the evolutionary path of every satellite galaxy since it is accretted by the cluster gravitational potential well, finding that satellite cluster galaxies are shifted towards lower halo masses compared to the results for central galaxies. We do not see such trend in our observational study although the scatter in halo masses in our sample, combined with small number statistics do not allow to discard its existence. On the contrary, we report a mild shift of our cluster sample towards smaller stellar mass values for a fixed halo mass with respect to our field comparison sample. However, the method we used to derive the halo mass of our targets is subject to several approximations that introduce uncertainties in our results. For example, the conversion between V_{max} and v_h ranges between 1.1 and 1.5 for different studies (Dutton et al. 2010, Papastergis et al. 2011, Cattaneo et al. 2014). In the same way, the conversion between the half-light and the half-mass radius of late-type galaxies has different values in the literature (e.g. R_e=R_m in Lanyon-Foster et al. 2012 while R_e=1.33R_m in Szomoru et al. 2013). In addition, the bulge growth of late-type galaxies in clusters (Kuchner et al. 2017) adds further uncertainties to the transformation between R_e and R_m in comparison with the field. We estimate these model-dependent uncertainties add 0.1-0.3 dex to the error budget computed in the determination of halo masses. Additional studies in clusters at different epochs are required to shed light onto the halo-mass evolution of cluster galaxies.

6. Conclusions

In this work, we have used the VIMOS/VLT spectrograph to investigate the kinematics of a sample of galaxies in the RXJ1347 cluster complex. In particular, we have studied the possible link between the kinematic asymmetries, the star formation rate, and the gas excitation of the gas disk component. Our kinematic analysis uses the asymmetry index A (Dale et al. 2001 and Bösch et al. 2013a) to measure the degree of disturbance of the gas component of our galaxies. Those objects with regular enough kinematics according to this index enter our Tully-Fisher and stellar-to-halo mass analysis, while those that show significant distortions are the focus of a subsequent star formation and AGN activity analysis. We compare our results with reference samples in the local universe and at intermediate redshift. Our main findings can be summarized as follows:

1. The fraction of galaxies that display strong kinematic asymmetries in the cluster (42.0%) is higher than in the field (23.3%). A possible explanation for this difference is the influence of cluster specific interactions. However, this fraction rises to 41.9% in the field when we combine galaxies with strong irregularities (irregulars) and those with mild but perceptible disturbances (affected). This may be caused by a higher accretion activity and minor merger frequency than expected in the field at intermediate redshifts. This scenario has been proposed by some authors in the past (Puech et al. 2008 and Kutdemir et al. 2010).
2. Cluster galaxies with sufficiently regular rotation curves ($A \leqslant 50$) display a moderate albeit non-significant brightening in the B-band TFR (ΔM_B=-0.7±0.8 mag) and non-significant evolution in the M_*-TFR (ΔM_*=-0.2±0.4 mag). In the field, we find very similar results in both scaling relations at intermediate redshift ΔM_B=-0.6±0.7 mag and ΔM_*=-0.1±0.3 mag. These results suggest that cluster and field galaxies behave similarly in the different representations of the TFR at this redshift. The reported B-band evolution with respect to the local relation can be explained by the successively younger stellar populations towards longer lookback time, while our results in the M_*-TFR agree with recent observational studies in the field and cluster environment that reported no significant evolution up to z=1 (Tiley et al. 2019 and Pelliccia et al. 2019, respectively).
3. We report average lower sSFR values for our cluster sample with respect to the field expectations given by the main sequence of star-forming galaxies (Peng et al. 2010) at z$\sim$0.45. In particular, we find slightly lower sSFR values for those galaxies classified as irregulars according to their asymmetry index ($A \geqslant 50$) with respect to those classified as fully regular ($A \leqslant 25$). We do not see signs of a star formation burst for galaxies that may have suffered an interaction in their recent past in clusters at intermediate redshift.
4. There is no correlation between the kinematic classification of our galaxies and AGN activity measured through the Mass-Excitation diagnostic diagram (Juneau et al. 2011).

5. We explored the stellar-to-halo mass relation for our sample of cluster and field galaxies at intermediate redshift. Our results agree with the theoretical prediction proposed by Moster et al. 2013 parametrized for z=0.45. However a number of cluster galaxies display smaller stellar masses for a given halo mass with respect to the field and in contrast with results from hydrodynamics simulations (Niemiec et al. 2018). However, the scatter and number statistics of our sample does not allow us to investigate the origin of this trend in a systematic way. Additional observations are required to improve our understanding of the stellar-to-halo mass relation in clusters.

After several decades of environmental studies, many aspects of galaxy evolution remain not well understood by the astronomical community even at low to intermediate redshift. We emphasize the importance of carrying out comprehensive studies that investigate galaxy evolution from different perspectives (i.e. with respect to stellar population properties, morphologies, kinematics, etc) and making use of large datasets. In particular, the use of IFU observations in comparison with high resolution simulations will be of key importance to disentangle the influence of different cluster-specific interactions over the physical properties of galaxies in the near future.

Acknowledgements.

References

Adam, R., Hahn, O., Ruppin, F., et al. 2018, A&A, 614, A118
Arnouts, S. & Ilbert, O. 2011, Astrophysics Source Code Library [ascl:1108.009]
Baldry, I. K., Balogh, M. L., Bower, R. G., et al. 2006, MNRAS, 373, 469
Baldwin, J. A., Phillips, M. M., & Terlevich, R. 1981, PASP, 93, 5
Bamford, S. P., Milvang-Jensen, B., Aragón-Salamanca, A., & Simard, L. 2005, MNRAS, 361, 109
Bertin, E. & Arnouts, S. 1996, A&AS, 117, 393
Böhm, A. & Ziegler, B. L. 2016, A&A, 592, A64
Böhm, A., Ziegler, B. L., Saglia, R. P., et al. 2004, A&A, 420, 97
Bösch, B., Böhm, A., Wolf, C., et al. 2013a, A&A, 549, A142
Bösch, B., Böhm, A., Wolf, C., et al. 2013b, A&A, 554, A97
Bruzual, G. & Charlot, S. 2003, MNRAS, 344, 1000
Butcher, H. & Oemler, Jr., A. 1978, ApJ, 219, 18
Calzetti, D., Armus, L., Bohlin, R. C., et al. 2000, ApJ, 533, 682
Casey, C. M., Cooray, A., Killi, M., et al. 2017, ApJ, 840, 101
Cattaneo, A., Mamon, G. A., Warnick, K., & Knebe, A. 2011, A&A, 533, A5
Cattaneo, A., Salucci, P., & Papastergis, E. 2014, ApJ, 783, 66
Chabrier, G. 2003, PASP, 115, 763
Chiu, I. N., Umetsu, K., Sereno, M., et al. 2018, ApJ, 860, 126
Conselice, C. J., Twite, J. W., Palamara, D. P., & Hartley, W. 2018, ApJ, 863, 42
Courteau, S. 1997, AJ, 114, 2402
Dale, D. A., Giovanelli, R., Haynes, M. P., Hardy, E., & Campusano, L. E. 2001, AJ, 121, 1886
Dannerbauer, H., Kurk, J. D., De Breuck, C., et al. 2014, A&A, 570, A55
Darvish, B., Mobasher, B., Sobral, D., et al. 2016, ApJ, 825, 113
Dressler, A. 1980, ApJ, 236, 351
Dutton, A. A., Conroy, C., van den Bosch, F. C., Prada, F., & More, S. 2010, MNRAS, 407, 2
Dutton, A. A., van den Bosch, F. C., Faber, S. M., et al. 2011, MNRAS, 410, 1660
Ferrero, I., Navarro, J. F., Abadi, M. G., et al. 2017, MNRAS, 464, 4736
Foëx, G., Chon, G., & Böhringer, H. 2017, A&A, 601, A145
Fogarty, K., Postman, M., Larson, R., Donahue, M., & Moustakas, J. 2017, ApJ, 846, 103
Ghirardini, V., Ettori, S., Amodeo, S., Capasso, R., & Sereno, M. 2017, A&A, 604, A100
Gilbank, D. G., Baldry, I. K., Balogh, M. L., Glazebrook, K., & Bower, R. G. 2010, MNRAS, 405, 2594
Giovanelli, R., Haynes, M. P., Salzer, J. J., et al. 1995, AJ, 110, 1059
Gonzalez, A. H., Zaritsky, D., Dalcanton, J. J., & Nelson, A. 2001, ApJS, 137, 117
Haines, C. P., Pereira, M. J., Smith, G. P., et al. 2015, ApJ, 806, 101
Harrison, C. M., Johnson, H. L., Swinbank, A. M., et al. 2017, MNRAS, 467, 1965
Heidmann, J., Heidmann, N., & de Vaucouleurs, G. 1972, MmRAS, 75, 85
Hoyos, C., Aragón-Salamanca, A., Gray, M. E., et al. 2016, MNRAS, 455, 295
Ilbert, O., Arnouts, S., McCracken, H. J., et al. 2006, A&A, 457, 841
Jørgensen, I., Chiboucas, K., Berkson, E., et al. 2017, AJ, 154, 251
Juneau, S., Bournaud, F., Charlot, S., et al. 2014, ApJ, 788, 88
Juneau, S., Dickinson, M., Alexander, D. M., & Salim, S. 2011, ApJ, 736, 104
Kitayama, T., Ueda, S., Takakuwa, S., et al. 2016, Publications of the Astronomical Society of Japan, 68, 88
Kravtsov, A. V. 2013, ApJ, 764, L31
Kuchner, U., Ziegler, B., Verdugo, M., Bamford, S., & Häußler, B. 2017, A&A, 604, A54
Kutdemir, E., Ziegler, B. L., Peletier, R. F., et al. 2010, A&A, 520, A109
Laganá, T. F. & Ulmer, M. P. 2018, MNRAS, 475, 523
Lampichler, N., Maier, C., & Ziegler, B. 2017, arXiv e-prints [arXiv:1707.09838]
Lanyon-Foster, M. M., Conselice, C. J., & Merrifield, M. R. 2012, MNRAS, 424, 1852
Maier, C., Kuchner, U., Ziegler, B. L., et al. 2016, A&A, 590, A108
Maier, C., Ziegler, B. L., Haines, C. P., & Smith, G. P. 2019, A&A, 621, A131
Moran, S. M., Miller, N., Treu, T., Ellis, R. S., & Smith, G. P. 2007, ApJ, 659, 1138
Mortlock, A., Conselice, C. J., Hartley, W. G., et al. 2013, MNRAS, 433, 1185
Moster, B. P., Naab, T., & White, S. D. M. 2013, MNRAS, 428, 3121
Nakamura, O., Aragón-Salamanca, A., Milvang-Jensen, B., et al. 2006, MNRAS, 366, 144
Niemiec, A., Jullo, E., Giocoli, C., Limousin, M., & Jauzac, M. 2018, arXiv e-prints [arXiv:1811.04996]
Papastergis, E., Martin, A. M., Giovanelli, R., & Haynes, M. P. 2011, ApJ, 739, 38
Paulino-Afonso, A., Sobral, D., Darvish, B., et al. 2018, A&A, 620, A186
Pelliccia, D., Lemaux, B. C., Tomczak, A. R., et al. 2019, MNRAS, 482, 3514
Pelliccia, D., Tresse, L., Epinat, B., et al. 2017, A&A, 599, A25
Peng, C. Y., Ho, L. C., Impey, C. D., & Rix, H.-W. 2002, AJ, 124, 266
Peng, Y.-j., Lilly, S. J., Kovač, K., et al. 2010, ApJ, 721, 193
Pérez-Martínez, J. M., Ziegler, B., Verdugo, M., Böhm, A., & Tanaka, M. 2017, A&A, 605, A127
Poggianti, B. M., Jaffé, Y. L., Moretti, A., et al. 2017, Nature, 548, 304
Popesso, P., Biviano, A., Finoguenov, A., et al. 2015, A&A, 574, A105
Puech, M., Flores, H., Hammer, F., et al. 2008, A&A, 484, 173
Reyes, R., Mandelbaum, R., Gunn, J. E., Pizagno, J., & Lackner, C. N. 2011, MNRAS, 417, 2347
Rodríguez del Pino, B., Aragón-Salamanca, A., Chies-Santos, A. L., et al. 2017, MNRAS, 467, 4200
Roman-Oliveira, F. V., Chies-Santos, A. L., Rodríguez del Pino, B., et al. 2019, MNRAS, 484, 892
Ruggiero, R. & Lima Neto, G. B. 2017, MNRAS, 468, 4107
Santos, J. S., Altieri, B., Popesso, P., et al. 2013, MNRAS, 433, 1287
Schindler, S., Guzzo, L., Ebeling, H., et al. 1995, A&A, 299, L9
Socolovsky, M., Almaini, O., Hatch, N. A., et al. 2018, MNRAS, 476, 1242
Swinbank, A. M., Harrison, C. M., Trayford, J., et al. 2017, MNRAS, 467, 3140
Szomoru, D., Franx, M., van Dokkum, P. G., et al. 2013, ApJ, 763, 73
Tiley, A. L., Bureau, M., Cortese, L., et al. 2019, MNRAS, 482, 2166
Tully, R. B. & Fisher, J. R. 1977, A&A, 54, 661
Tully, R. B., Pierce, M. J., Huang, J.-S., et al. 1998, AJ, 115, 2264
Übler, H., Förster Schreiber, N. M., Genzel, R., et al. 2017, ApJ, 842, 121
Umetsu, K., Medezinski, E., Nonino, M., et al. 2014, ApJ, 795, 163
Umetsu, K., Sereno, M., Tam, S.-I., et al. 2018, ApJ, 860, 104
van der Wel, A., Franx, M., van Dokkum, P. G., et al. 2014, ApJ, 788, 28
Verdugo, M., Lerchster, M., Böhringer, H., et al. 2012, MNRAS, 421, 1949
Vogt, N. P., Haynes, M. P., Giovanelli, R., & Herter, T. 2004, AJ, 127, 3325
Wetzel, A. R., Tinker, J. L., Conroy, C., & van den Bosch, F. C. 2013, MNRAS, 432, 336
Whitaker, K. E., van Dokkum, P. G., Brammer, G., et al. 2013, ApJ, 770, L39
Yang, Y., Flores, H., Hammer, F., et al. 2008, A&A, 477, 789
Ziegler, B. L., Böhm, A., Jäger, K., Heidt, J., & Möllenhoff, C. 2003, ApJ, 598, L87

A&A proofs: manuscript no. 30165_ap

Appendix A: Additional material

In this section we present the data tables containing all the relevant parameters of the cluster and field galaxies that entered our TFR analysis, i.e those galaxies classified as regular or affected attending to our gas kinematics asymmetry index criterion. In addition, we display the observed and computed rotation curve for the same objects.

Table A.1: General properties of the cluster galaxies that entered our TFR analysis (i.e. regular and affected). IDs, J2000 coordinates, redshift, BRI absolute magnitudes in the AB system, extinction in B-band, effective radius in the z-band, logarithmic stellar mass, star formation rate, maximun rotation velocity, and asymmetry index.

ID	RA (hh:mm:ss)	DEC (dd:mm:ss.s)	z	M_B (mag)	M_{Rc} (mag)	M_{Ic} (mag)	A_B (mag)	R_e (kpc)	$\log M_*$	SFR ($M_\odot/yr$)	V_{max} (km/s)	A
C1	13:48:29.2	-11:34:39.1	0.4195	-21.92	-22.82	-23.25	-0.21	10.93	10.93	10.6	249.7±7.9	12.8
C2	13:48:13.6	-11:37:12.3	0.4457	-20.62	-21.57	-22.01	-0.67	5.49	10.46	3.6	204.7±12.4	22.8
C3	13:48:17.9	-11:38:27.4	0.4609	-20.58	-21.17	-21.41	-1.22	5.58	10.18	18.1	196.1±4.0	3.2
C4	13:47:36.9	-11:36:07.5	0.4551	-20.01	-20.43	-20.58	-0.16	5.79	9.61	1.9	128.9±7.5	8.4
C5	13:47:47.0	-11:37:31.7	0.4488	-21.90	-22.64	-23.00	-0.36	10.40	10.73	11.5	337.2±14.1	21.4
C6	13:47:28.9	-11:38:12.7	0.4700	-20.42	-20.75	-20.85	-0.25	5.77	9.58	-	138.3±3.9	11.6
C7	13:47:39.3	-11:39:20.7	0.4521	-20.45	-21.05	-21.33	-0.59	6.66	9.95	2.9	148.1±2.8	11.5
C8	13:47:04.2	-11:51:50.2	0.4619	-21.33	-22.18	-22.56	-0.32	5.46	10.8	4.5	259.4±11.9	16.3
C9	13:47:09.9	-11:57:22.9	0.4306	-20.77	-21.51	-21.81	-0.28	4.36	10.2	2.3	225.4±7.9	16.4
C10	13:46:34.7	-11:51:30.2	0.4615	-20.96	-21.62	-21.90	-0.70	7.04	10.32	10.1	132.2±6.2	11.7
C11	13:46:19.9	-11:53:00.0	0.4683	-20.32	-21.38	-21.86	-0.60	4.45	10.55	1.2	190.9±18.5	8.1
C12	13:46:30.8	-11:53:43.0	0.4802	-20.91	-21.67	-21.98	-0.28	5.78	10.52	14.5	129.0±9.7	10.0
C13	13:46:30.6	-11:53:55.8	0.4733	-21.26	-22.15	-22.54	-0.56	8.95	10.85	-	256.1±10.2	14.7
C14	13:46:32.3	-11:55:49.9	0.4555	-20.17	-20.73	-20.94	-0.47	3.20	9.91	3.14	105.3±3.5	22.5
C15	13:46:28.3	-11:56:52.7	0.4461	-20.05	-20.83	-21.19	-0.33	6.38	10.03	1.39	161.1±19.0	10.0
C16	13:46:37.3	-11:57:16.6	0.4473	-20.06	-20.80	-21.12	-0.31	5.28	10.02	1.58	215.3±9.4	16.4
C17	13:46:51.6	-11:47:24.1	0.4482	-20.54	-21.15	-21.44	-0.17	6.95	10.02	-	138.8±12.6	20.1
C18	13:46:16.2	-11:47:01.6	0.4604	-20.36	-21.13	-21.44	-0.16	2.11	10.26	5.17	165.9±4.6	11.5
C19	13:46:36.1	-11:47:46.7	0.4695	-20.65	-21.39	-21.70	-0.56	5.14	10.43	3.85	218.6±5.8	4.0
C20	13:48:09.4	-11:38:04.8	0.4690	-20.69	-21.24	-21.46	-0.45	4.09	10.15	-	127.3±8.1	29.6
C21	13:46:56.7	-11:55:37.5	0.4435	-20.92	-21.98	-22.46	-0.18	4.75	10.82	5.78	125.4±6.0	27.7
C22	13:46:30.7	-11:52:06.0	0.4717	-20.24	-20.85	-21.09	-0.41	5.74	10.08	3.75	117.1±6.5	30.7
C23	13:46:15.5	-11:42:48.8	0.4538	-19.72	-20.54	-20.88	-0.17	4.62	10.06	-	151.4±76.0	33.0

Table A.2: General properties of the field galaxies that entered our TFR analysis (i.e. regular and affected). Columns are labeled as in Table .1.

ID	RA (hh:mm:ss)	DEC (dd:mm:ss.s)	z	M_B (mag)	M_{Rc} (mag)	M_{Ic} (mag)	A_B (mag)	R_e (kpc)	$\log M_*$	SFR ($M_\odot$)	V_{max} (km/s)	A
F1	13:48:18.9	-11:44:21.9	0.3834	-19.60	-20.50	-20.88	-0.37	1.39	9.94	1.1	105.9±6.8	3.5
F2	13:48:16.2	-11:35:09.5	0.5326	-21.12	-22.00	-22.36	-0.44	3.21	10.86	14.6	235.9±18.0	24.6
F3	13:48:11.7	-11:35:45.2	0.7878	-20.29	-21.24	-21.65	-0.59	4.82	10.61	-	195.2±38.0	5.1
F4	13:47:42.1	-11:44:46.0	0.5380	-21.37	-21.92	-22.14	-0.41	6.53	10.56	14.4	243.9±22.7	16.8
F5	13:46:51.7	-11:53:48.8	0.4935	-21.08	-21.98	-22.36	-0.85	5.48	10.78	-	201.3±6.1	6.5
F6	13:46:15.3	-11:52:24.2	0.4007	-19.72	-20.31	-20.57	-0.78	5.13	9.73	-	175.1±6.8	13.6
F7	13:46:28.9	-11:53:19.6	0.3701	-20.45	-19.90	-20.93	-0.31	3.31	9.85	0.6	124.2±25.6	10.0
F8	13:47:13.6	-11:45:51.9	0.3998	-20.34	-21.17	-21.53	-0.56	4.01	10.13	2.1	145.9±38.4	18.9
F9	13:46:57.5	-11:47:00.3	0.3284	-19.27	-19.74	-19.96	-0.13	3.20	9.33	-	85.2±2.6	3.2
F10	13:46:32.5	-11:46:19.1	0.3676	-21.15	-22.02	-22.39	-0.24	6.52	10.55	3.3	280.5±7.2	17.0
F11	13:48:21.5	-11:46:54.8	0.5240	-20.73	-21.48	-21.77	-1.39	8.10	10.15	8.5	241.5±22.6	47.5
F12	13:48:32.2	-11:47:51.9	0.5339	-21.32	-21.87	-22.09	-0.17	4.40	10.82	24.4	192.0±31.8	43.4
F13	13:47:46.7	-11:38:03.4	0.3696	-20.10	-20.83	-21.19	-0.31	4.90	10.08	-	156.2±11.4	26.8
F14	13:47:31.5	-11:43:24.7	0.5337	-20.55	-20.82	-20.93	-0.35	2.50	10.06	3.6	114.9±5.4	30.6
F15	13:46:50.1	-11:42:04.2	0.3994	-20.80	-21.57	-21.92	-0.07	4.34	10.15	-	191.5±91.6	34.9
F16	13:47:02.9	-11:46:38.6	0.3679	-20.38	-21.26	-21.64	-0.58	5.47	10.82	1.6	191.7±19.6	37.1
F17	13:46:31.5	-11:46:42.8	0.3515	-20.37	-20.96	-21.22	-0.30	3.32	10.08	1.8	111.2±12.2	25.6
F18	13:46:56.0	-11:53:10.7	0.3990	-21.29	-22.35	-22.80	-0.71	6.42	10.06	-	235.5±66.9	38.0

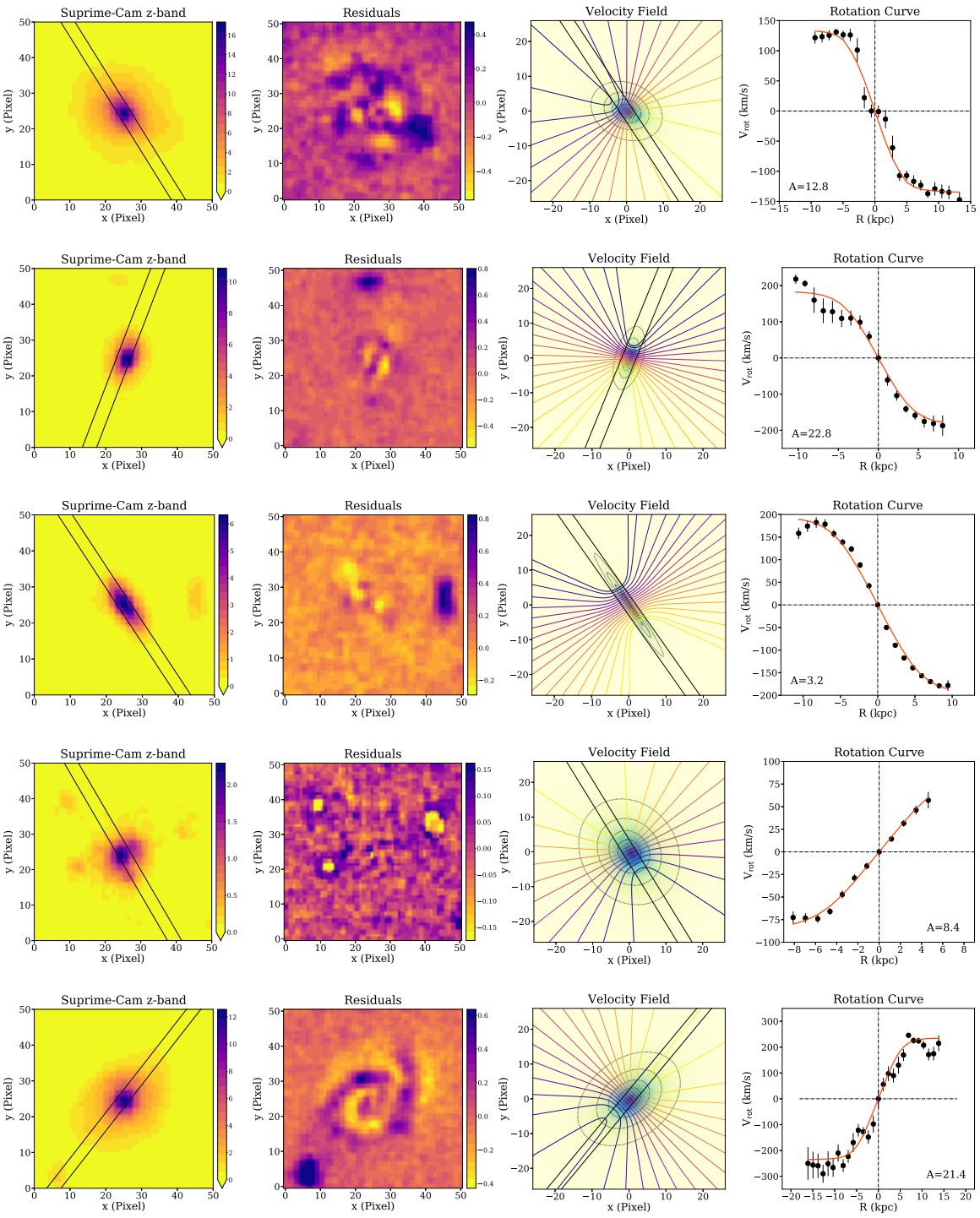

Fig. A.1: Our sample of cluster galaxies studied following the methods explained in Sect. 3 and presented in the same order as in Table .1. The first column shows the z-band Suprime-Cam image centered on the target. The second column displays the residuals after subtracting the 2D model of the galaxy. The third column presents the synthetic velocity field after fitting the simulated rotation curve to the observed curve. The fourth column displays the rotation curve (black dots) in the observed frame, and the simulated RC (red line). The black solid parallel lines in the first and third columns figures depict the position of the edges of the slit.

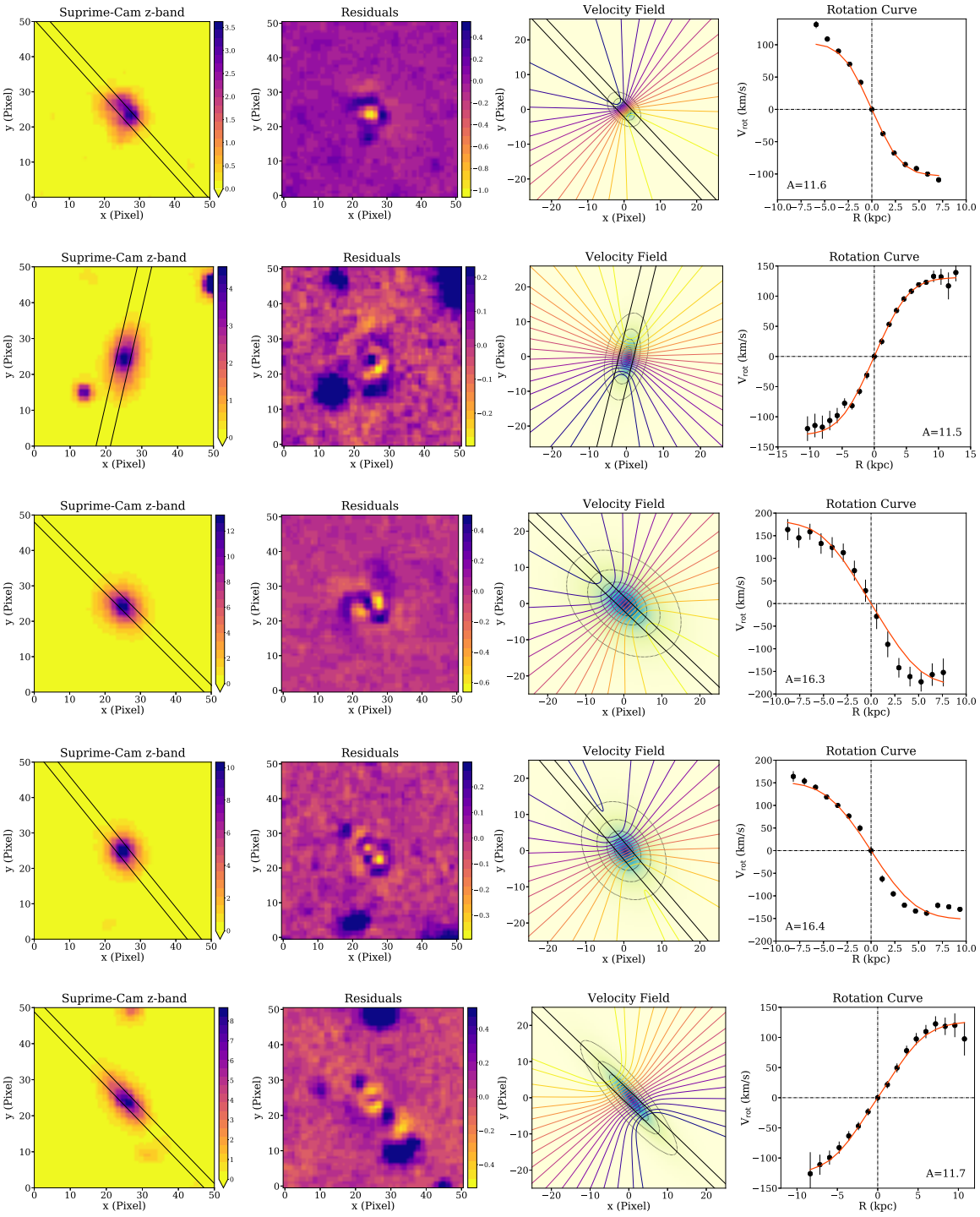

Fig. A.1: (Continued)

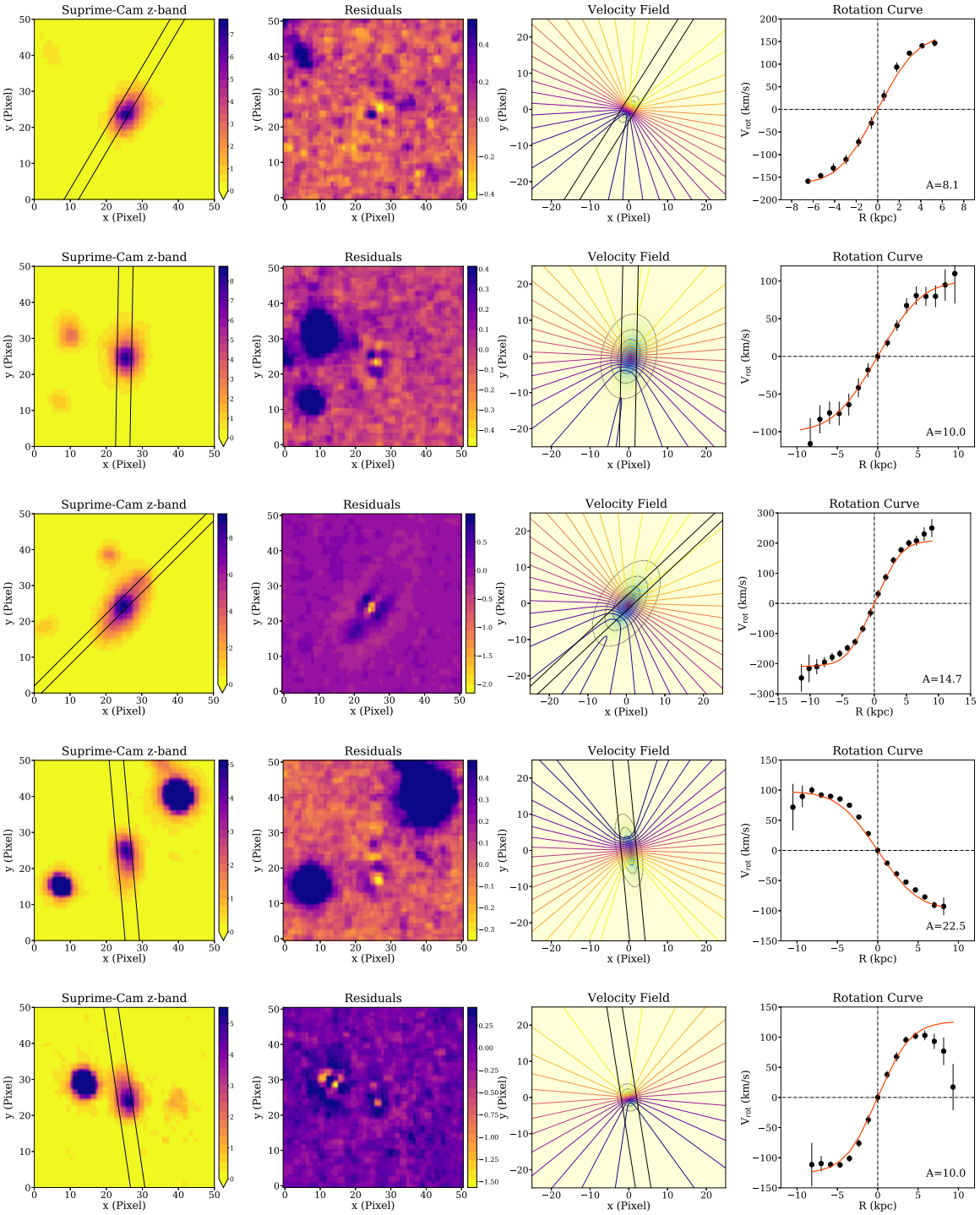

Fig. A.1: (Continued)

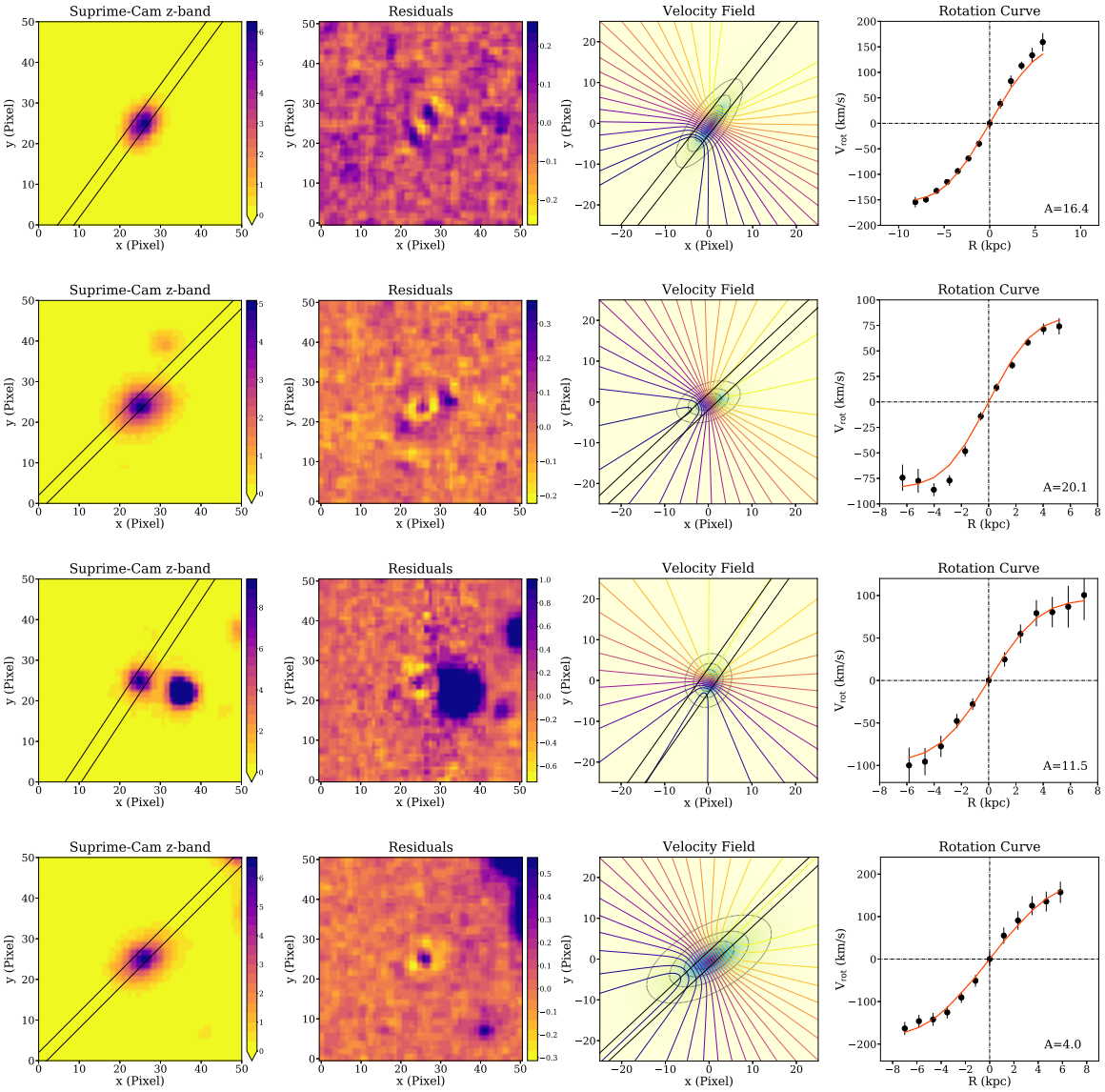

Fig. A.1: (Continued)

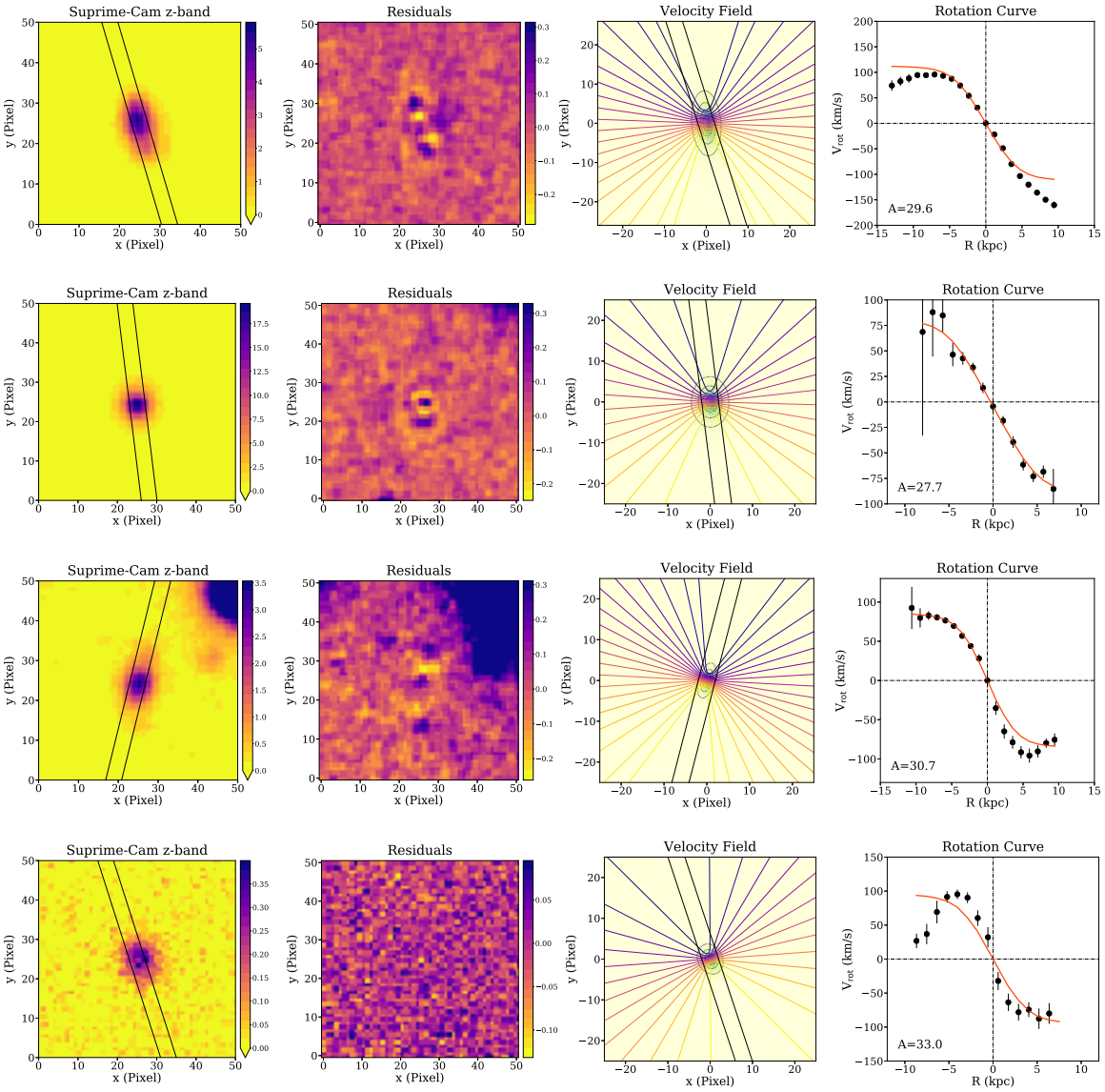

Fig. A.1: (Continued)

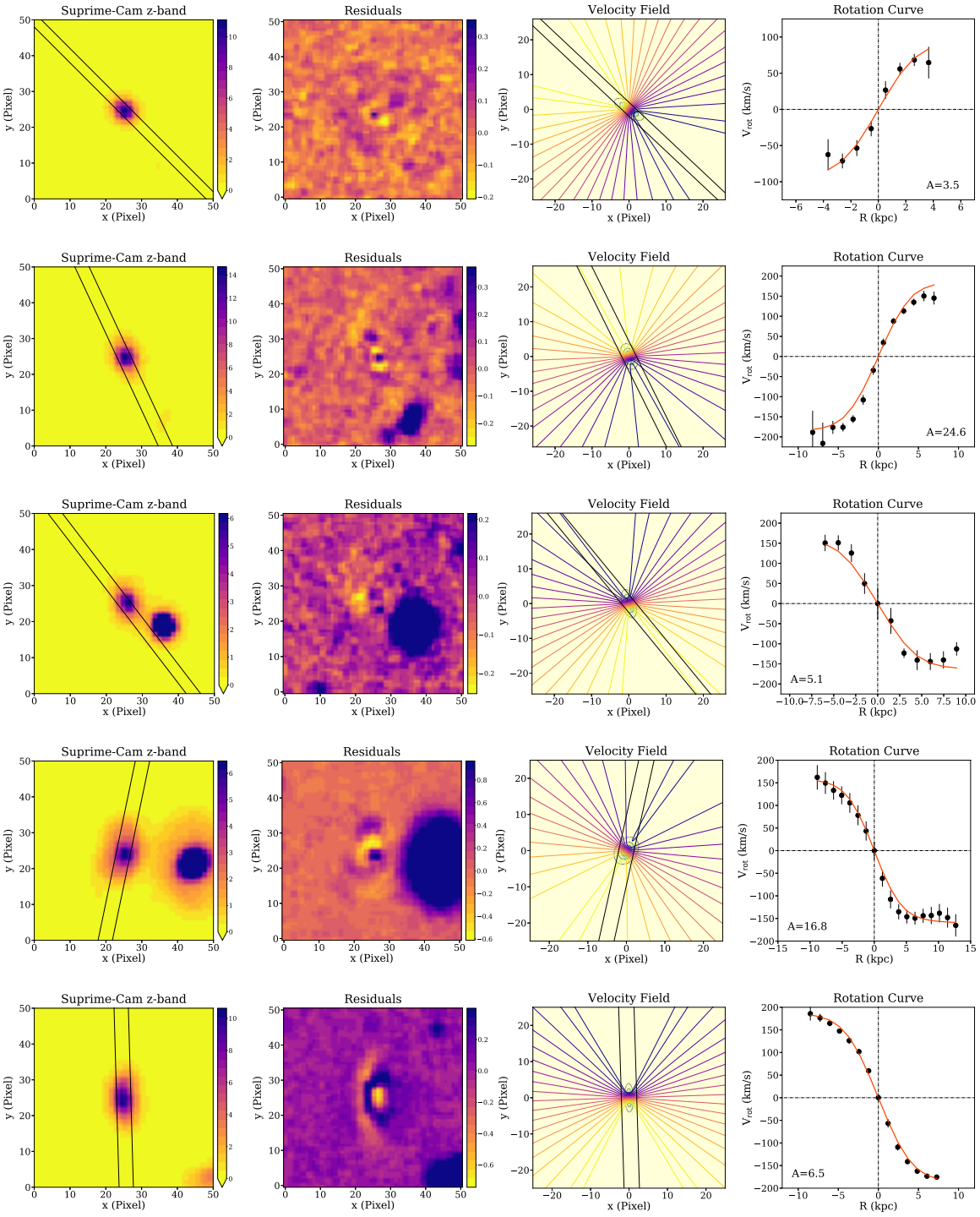

Fig. A.2: Our sample of field galaxies studied following the methods explained in Sect. 3 and presented in the same order as in Table .2. The columns have the same meaning than in Fig. .1.

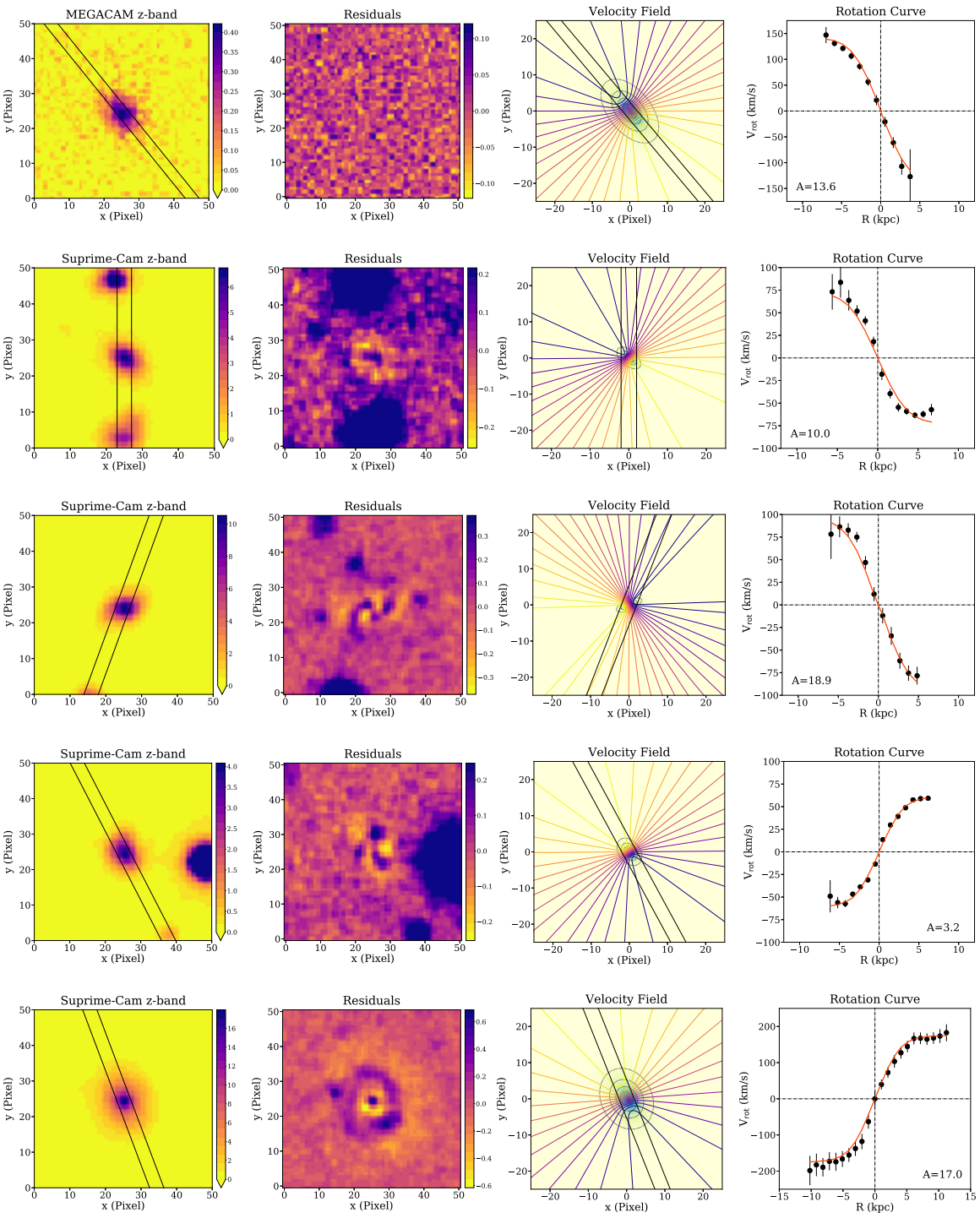

Fig. A.2: (Continued)

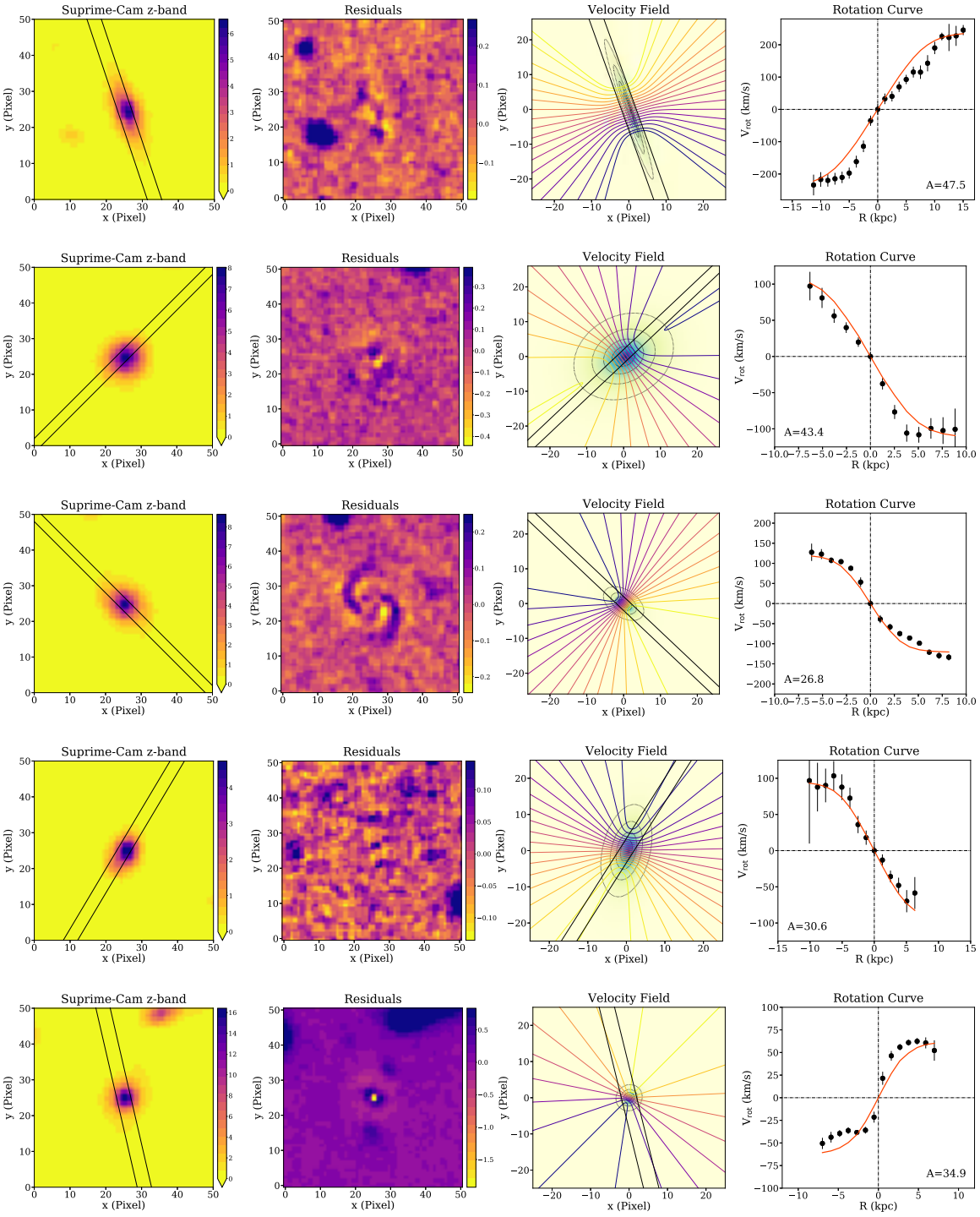

Fig. A.2: (Continued)

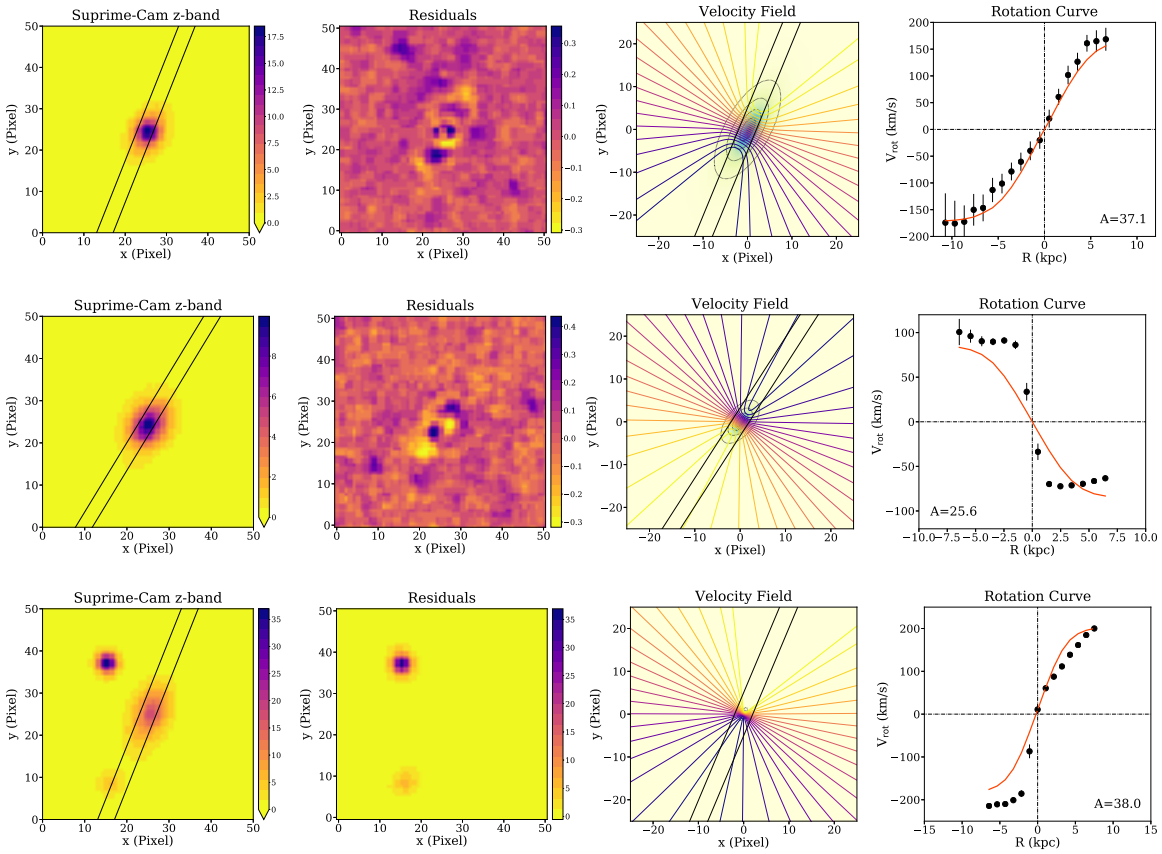

Fig. A.2: (Continued)

Chapter 4

Paper III

Title: The evolution of galaxy scaling relations in clusters at 0.5<z<1.5

Authors: J. M. Pérez-Martínez, B. Ziegler, H. Dannerbauer, A. Böhm, M. Verdugo

Year: 2019

Journal: Astronomy and Astrophysics. Submitted on August 4th 2019.

Short Description: In this work we investigate the redshift evolution of several scaling relations by comparing the results from the cluster samples studied by our group during the last years with several well-known field reference samples analyzed following similar methods. Further, we added new 2D-spectroscopy in the CL1604 cluster system at z$\sim$0.9 to our previous cluster observations. This data was taken with the instrument OSIRIS installed at the 10.4m Gran Telescopio de Canarias (GTC) in La Palma. Our analysis is focused on the study of the Tully-Fisher, velocity-size and angular momentum redshift evolution, comparing our results with theoretical predictions, semi-analitical models and hydrodynamical simulations.

Personal Contribution: I was responsible for the proposal writing and phase 2 preparations of the observations. I carried out the spectroscopic and photometric analysis of the new sample (CL1604). In addition, I collected all the data presented in this work from different cluster and field studies and

presented it in a comprehensive way. As a first author, I led the discussion of our results and carried out the writing process of the manuscript.

Astronomy & Astrophysics manuscript no. output
August 4, 2019

The evolution of galaxy scaling relations in clusters at 0.5<z<1.5 ⋆

J. M. Pérez-Martínez[1,2,3], B. Ziegler[1], H. Dannerbauer[2,3], A. Böhm[1], M. Verdugo[1], A. I. Díaz[4], and C. Hoyos[4]

[1] Department of Astrophysics, University of Vienna, A-1180 Vienna, Austria. e-mail: jm.perez@univie.ac.at
[2] Instituto de Astrofísica de Canarias (IAC), E-38205, La Laguna, Tenerife, Spain.
[3] Universidad de La Laguna, Dpto. Astrofísica, E-38206, La Laguna, Tenerife, Spain
[4] Departamento de Física Teórica and CIAFF, Universidad Autónoma de Madrid, E-28049 Madrid, Spain

ABSTRACT

Aims. In this work we present a collection of cluster samples at different epochs to study the evolution of the most important kinematic scaling relations (Tully-Fisher, velocity-size and angular momentum) in dense environments over cosmic time.
Methods. We use 2D and 3D spectroscopy to analyze the kinematics of our cluster galaxies and extract their maximum rotation velocities (V_{max}), which will be used as the common parameter in all scaling relations under study. We determine the structural parameters of our objects by fitting successive surface brightness profiles using GALFIT, and compute their stellar-mass from aperture photometry by applying SED fitting techniques. Our methods are consistently applied to all our cluster samples which make them ideal for an evolutionary comparison. In addition, we compare our results with field samples spanning the same redshift range and analyzed similarly.
Results. Up to redshift one, our cluster samples show evolutionary trends compatible with previous results in the field and in accordance with semianalytical models and hydrodynamical simulations with regard to the Tully-Fisher and velocity-size relations. At higher redshift, these offsets become more prominent, with a factor ∼3 drop in disk sizes and a B-band luminosity enhancement $\langle \Delta M_B \rangle = 1.9$ mag by z∼1.5. In addition, we find that our intermediate to high redshift cluster galaxies follow a parallel sequence with respect to the local angular momentum-stellar mass relation, although displaying lower mean values than the comparison field samples at similar redshifts. This produces lower mean stellar-to halo angular momentum ratios in the cluster, which can be understood by the stronger interacting nature of dense environments with respect to the field. Finally, we find that field galaxies follow the predicted angular momentum evolution relation ($j_* \propto M_*^{2/3}(1+z)^{-1/2}$) after it is normalized to the general population of spiral galaxies in the local Universe. Our cluster samples, on the other hand, require a steeper trend ($j_* \propto M_*^{2/3}(1+z)^{-1}$) to meet the local angular momentum conditions.

Key words. galaxies: kinematics and dynamics – galaxies: clusters: general - galaxies: evolution

1. Introduction

Scaling relations are strong trends between the main physical parameters of galaxies and are key to understand the different processes at play in galaxy evolution. In spiral galaxies, the flat part of their rotation curves provide us with a proxy, the maximum circular velocity, to trace the total mass of galaxies (including dark matter). This allows us to study the interplay between the dark and the baryonic component of galaxies by making use of some other easily observable parameters such as the stellar-mass (or luminosity) and disk size. These parameters define a three-dimensional space with the potential to describe most of the physical transformations that a galaxy experience during its lifetime. The different projections of this space yield several important scaling relations (Koda et al. 2000) that can be also reproduced by assuming the virial equilibrium of structures and the conservation of angular momentum during the dissipational collapse of cold dark matter haloes (Mo et al. 1998, van den Bosch 2000, Navarro & Steinmetz 2000). Some of the simplest and yet most fundamental scaling relations for spiral galaxies are the Tully-Fisher relation (TFR) and the velocity-size relation (VSR), which were first observed by Tully & Fisher (1977). However, more complex parameter combinations produce other interesting relations such as the angular momentum-stellar mass (Fall 1983, Romanowsky & Fall 2012) that are key to understand the processes of morphological transformation and mass redistribution during galaxy evolution.

The TFR connects the V_{max} (taken as the rotation velocity in the flat part of the rotation curve) and the luminosity (or stellar-mass) of a spiral galaxy. During the last decades, the field TFR has been studied in depth up to z∼2 (Tully et al. 1998, Ziegler et al. 2002, Kassin et al. 2007, Puech et al. 2008, Miller et al. 2011, Böhm & Ziegler 2016, Tiley et al. 2016, Simons et al. 2016, Harrison et al. 2017, Pelliccia et al. 2017, Übler et al. 2017). Different representations of the TFR provide information about the evolution of the galaxies' stellar populations and their stellar mass growth across cosmic time. For example, the study of the B-band TFR yields a luminosity enhancement of up to 1 mag by z∼1 in the field (Böhm & Ziegler 2016), which is in agreement with the predicted gradual evolution towards younger stellar populations in galaxies with lookback time (Dutton et al. 2011). It is expected that the stellar-mass of galaxies grows with time due to the progressive consumption of their gas reservoirs. However, the exact evolution of the stellar-mass TFR is still a matter of debate, specially at high redshift. While some authors claim a strong evolution (0.3-0.5 dex in M_*) towards lower stellar mass values at z∼2 (Price et al. 2016, Tiley et al. 2016, Straatman et al. 2017, Übler et al. 2017), others show results compat-

⋆ Based on observations made with the Gran Telescopio Canarias (GTC), installed at the Spanish Observatorio del Roque de los Muchachos of the Instituto de Astrofísica de Canarias, on the island of La Palma. Program's IDs 122-GTC70/17A and 137-GTC118/18A.

ible with a mild to negligible scenario (Miller et al. 2011, Contini et al. 2016, Di Teodoro et al. 2016, Pelliccia et al. 2017). This conflicting results may arise from the varying morphological and kinematic selection criteria applied in each study and the difficulty to identify rotation dominated systems at high redshift. Interestingly, Molina et al. (2017) report $\Delta M_* - 0.4$ in the stellar-mass TFR for galaxies at z∼2 displaying high rotational support ($V/\sigma > 3$). However, this offset disappears when they consider their full sample of galaxies, regardless of the individual V/σ values. Thus, the use of a common methodological frame is required when investigating the evolution of scaling relations at different redshifts.

The velocity-size relation traces the disks growth inside evolving Navarro-Frenk-White dark matter haloes (NFW, Navarro et al. 1997). However, this correlation is weaker than the TFR and displays a wider scatter (Courteau et al. 2007, Hall et al. 2012). This is partially explained due to the ambiguities in defining the size of a galaxy (R_e, R_d, or other prescriptions) at different wavelengths taking into account the evolution and distribution of the different stellar populations within the galaxy. Furthermore, the presence of a bulge component, and additional selection effects (surface brightness limits) may contribute to hinder its study (Meurer et al. 2018, Lapi et al. 2018). Nevertheless, in the context of galaxy evolution, this scaling relation remains one of the tools to look for environmental imprints over the disks.

During the early phases of galaxy formation, the angular momentum of the collapsing dark matter haloes is transferred to the baryonic matter. This process is key to understand the early formation of disks and the distribution of baryonic matter within them. Thus, the study of the angular momentum allow us to simultaneously connect the rotation velocity, the stellar-mass and the galaxy size into a single scaling relation: the specific angular momentum-stellar mass relation (Fall 1983), which can be influenced over time by several processes such as morphological transformations, galaxy interactions and the presence of inflows. For example, Romanowsky & Fall (2012) observed a decreasing trend in the specific angular momentum of galaxies with increasing bulge-to-disc ratio (see also Fall & Romanowsky 2013 and Fall & Romanowsky 2018), linking the morphological transformation of galaxies with the redistribution of their angular momentum.

In clusters, the baryonic and the dark component of galaxies can be influenced by cluster-specific interactions, either related with the intracluster medium (strangulation and ram-pressure stripping) or due to the high frequency of gravitational interactions caused by the high number density of galaxies in this environment (harassment, tidal interactions and mergers). Up to z∼1, it has been have reported similar evolution in the cluster and field environments with respect to the B-band TFR (Jaffé et al. 2011, Bösch et al. 2013b), while others claim a mild luminosity enhancement (Bamford et al. 2005) and larger TFR scatter in the cluster environment (Moran et al. 2007, Pelliccia et al. 2019). However, the VSR and the angular momentum evolution have been scarcely studied in dense environments up to date. In this work we gather several cluster samples studied by our group in the past together with recent GTC/OSIRIS observation over the multicluster system Cl1604+4304 to investigate in a consistent way the possible influence of the environment over kinematic scaling relations across cosmic time. The Tully-Fisher (TFR), the Velocity-Size (VSR), and the angular momentum stellar-mass relation ($j - M_*$) provide an unique way to search for signs of environmental evolution over the population of cluster galaxies at different cosmological epochs. This work is structured in the following way: Sect. 2 describes the main characteristics of the cluster and field samples that we collected for the different scaling relations. Sect. 3 contains the description of the methods used to analyze our cluster samples. Sect. 4 is devoted to the presentation and discussion of our results while Sect. 5 outline the major conclusions of this study. Throughout this article we assume a Chabrier (2003) initial mass function (IMF), and adopt a flat cosmology with Ω_Λ=0.7, Ω_m=0.3, and H_0=70 km s^{-1}Mpc^{-1}. All magnitudes quoted in this paper are in the AB system.

2. Sample Overview

In this section we describe the main characteristics of the several datasets used in this work. Our primary sample is composed of galaxies from six distant clusters studied by our group: XMMUJ2235-2557 at z∼1.4 (hereafter XMM2235, Pérez-Martínez et al. 2017), HSC-CL2329 and HSC-CL2330 at z∼1.47 (Böhm et al. 2019), RXJ1347-1145 at z∼0.45 (hereafter RXJ1347, Perez-Martinez et al. 2019, submitted to A&A), Abell 901/902 at z∼0.16 (Bösch et al. 2013a,b), and CL1604+4304 at z∼0.9 (hereafter CL1604). We present more details on the latter in the following sections. We emphasize that, in all these samples, the main physical parameters were computed using the same methods applied in this study, which makes them ideal to establish a direct comparison to test the evolution of scaling relations in dense environments at different epochs. For this same reason, we use Böhm & Ziegler (2016) as our main comparison sample in the field whenever it is possible. In addition, we add field samples from other researchers to examine the angular momentum (AM) at 0<z<2.5 (Fall & Romanowsky 2018, Posti et al. 2018, Harrison et al. 2017, Förster Schreiber et al. 2018). That way we explore environmental imprints of galaxy evolution over cosmic time. The application of all these data-sets will be discussed in the following sections.

2.1. Cl1604 at z∼0.9

This cluster complex was first discovered by Gunn et al. (1986) as two separate clusters, Cl 1604+4304 and Cl 1604+4321 at z∼0.90 and 0.92 respectively. Subsequent studies made use of deep multiband imaging and spectroscopy to unveil a much larger structure composed of several massive merging clusters and infalling groups that extends over 12 Mpc along the North-South axis (Postman et al. 2001, Gal & Lubin 2004; Gal et al. 2008, Lemaux et al. 2012, Hayashi et al. 2019). Recently, this cluster complex has been the object of study from different perspectives, including the search for luminous compact galaxies (Crawford et al. 2014, 2016), the study of its BCG (Ascaso et al. 2014), and the integral study of their galaxy populations as part of the ORELSE survey (e.g. Pelliccia et al. 2019, Tomczak et al. 2019). Our observations used this wealth of archival data to preselect a representative sample of star-forming cluster galaxies to study their gas kinematics by using OSIRIS MOS-spectrograph at the 10.4m Gran Telescopio de Canarias (GTC) in la Palma.

Our observing program targeted the two main structures of the cluster complex, Cl1604+4304 and Cl1604+4321, for a total of 10.4h of integration time split between the two fields. The total integration time slightly varies between the two fields, being 4.8h for targets in Cl1604+43216 and 5.6h for targets in Cl1604+4304. We extract the gas kinematics from the [OII] 3727Å emission line, which lies around 7100Å at z∼0.9, with an instrumental resolution of $\sigma_{ins} \approx 50$ km/s and a slit width of 0.9". To achieve this, we used the OSIRIS high resolution grism

R2500R, which covers the wavelength range 5200 – 7600Å. This configuration yielded a spectral resolution of R∼2500 at the central wavelength with an average dispersion of 1 Å/pix and an image scale of 0.25"/pix. The observing program was executed under average seeing conditions of 0.8" FWHM and airmass ∼1.1. We utilized tilted slits aligned to the apparent major axis of the targets in order to minimize geometrical distortions. The tilt angles θ were limited to $|\theta| < 45^{o}$ to ensure a robust sky subtraction and wavelength calibration. The spectroscopic data reduction was carried out using the OSIRIS-GTCMOS pipeline (Gómez-González et al. 2016). The main reduction steps were bias subtraction, flat normalization, wavelength calibration and sky subtraction. Finally, we co-add the 2D-spectra exposures using an IRAF sigma-clipping algorithm that performs a bad pixel and cosmic ray rejection.

In addition to our spectroscopic campaign, we make use of the abundant complementary archival imaging data in this field, including the Hyper Suprime-Cam Subaru Strategic Program (HSC-SSP, Aihara et al. 2018, 2019) in five bands (g, r, i, z, y), the UKIDDS survey (Lawrence et al. 2007) in the near-infrarred (J and Ks), and spaced-based observations with HST/ACS (F606W and F814W) and Spitzer/IRAC (3.6 and 4.5 μm). The depth and seeing of our co-added mosaic images are shown in Table 1. The coordinates, redshifts, rest frame colors, and magnitudes of our final galaxy sample from this cluster are summarized in the Appendix.

Table 1: Summary of the photometric bands available for Cl1604

Source	Filter	Exp. Time (s)	FWHM (")
HSC-SSP	g	600	0.8
...	r	600	0.8
...	i	960	0.6
...	z	1200	0.5
...	y	960	0.5
HST/ACS	F606W	1998	0.1
...	F814W	1998	0.1
Spitzer/IRAC	3.6μm	1152	2.0
...	4.5μm	1152	2.0

2.2. Abell 901/902 at z∼0.16

This is a multicluster system composed of four main substructures that were intensely studied by the STAGES collaboration (Gray et al. 2009). The system as a whole is not yet virialized and thus, it is an interesting laboratory to investigate the interplay between galaxy evolution and environment at low redshift. Our group carried out a kinematic analysis on a subsample of cluster galaxies to study the slope and scatter of the Tully-Fisher relation (Bösch et al. 2013b), a subject that we will further explore in the context of our combined cluster samples at different redshifts.

2.3. RXJ1347 at z∼0.45

RXJ1347 is a large-scale cluster complex composed of 2 merging clusters and up to 30 additional infalling groups at z∼0.45 (Verdugo et al. 2012). This structure is one of the most massive and X-ray luminous clusters known (Schindler et al. 1995) and its properties resemble Cl1604 both in size and total mass, though at a lower redshift. In Perez-Martinez et al. (2019, submitted to A&A) we investigate the physical properties of a sample of star-forming galaxies in RXJ1347 with regard to their internal gas kinematics and star formation activity. We used VLT/VIMOS to obtain high resolution MOS spectroscopy (R∼2500) of ∼50 cluster galaxies, from which 19 displayed regular gas kinematics. In this work, we use this sample of galaxies to study the TFR, VSR and AM in clusters at intermediate redshift. The methodology used to obtain the main physical parameters (rest-frame magnitudes, stellar masses, structural and kinematical parameters) is identical to the one followed to study the CL1604 sample, and described in detail in Section 3. The mean stellar-mass value of this cluster sample is $\log M_{*}$=10.3 with individual values spanning 9.5<$\log M_{*}$<11.0.

2.4. XMM2235 at z∼1.4

In a similar way, XMM2235 is one of the most massive virialized clusters found at z>1 (Mullis et al. 2005, Rosati et al. 2009, Strazzullo et al. 2010). Due to its large mass ($M_{500} > 10^{15} M_{\odot}$) at such an early epoch, XMM2235 can be seen as the progenitor of more complex cluster systems such as CL1604 and RXJ1347 at a later evolutionary stage. Our group carried out slit spectroscopic observations with VLT/FORS2 (R∼1400) to study the gas kinematics of galaxies within the cluster environment. We successfully recovered regular rotation curves for six cluster members and study different scaling relations such as the Tully-Fisher and the Velocity-Size relation. Our sample is composed of relatively massive objects with stellar masses in the range 10.0<$\log M_{*}$<11.0 with an mean value of $\log M_{*}$=10.5. Further details about the analyses of this sample can be found in Pérez-Martínez et al. 2017.

2.5. HSC-Cl2329 and HSC-Cl2330 at z∼1.47

In contrast to the previous samples, these clusters were identified as strong [OII] overdensities exploiting the narrow-band filter NB921 in the HSC-SSP 16deg^2 emission-line survey (Hayashi et al. 2018b) and not by X-ray observations. They are dominated by star-forming galaxies and are more typical progenitors of today's regular population of clusters. Therefore, these HSC clusters offer a window to test the properties of galaxies during the cluster assembling process. Our group carried up 3D-spectroscopy with KMOS (R∼4000) at VLT for both structures, confirming the membership of 34 objects and extracting regular velocity fields for 14 objects, which were used to explore the B-band Tully-Fisher relation at this redshift (Böhm et al. 2019). However, the authors could not compute stellar-masses due to the lack of sufficient photometric bands covering the redder part of the spectral range. In a similar way, the PSF size from the HSC images matches the expected effective radius of galaxies at this redshift, which makes any attempt to determine the galaxy size unreliable. Thus, we restrict the use of this sample to the analysis of the cluster B-band TFR at different epochs. For a more detailed description of the cluster detection and target properties we recommend to visit Hayashi et al. (2018b) and Böhm et al. (2019).

2.6. The field comparison samples

In this section we briefly introduce the main properties of the field comparison samples used in our analysis. Our primary comparison sample is composed of 124 field galaxies at z<1 from Böhm & Ziegler (2016). These galaxies were selected from the

FORS Deep Field (Heidt et al. 2003) and the William Herschel Deep Field (Metcalfe et al. 2001), and count with reliable rotation velocities, B-band absolute magnitudes, and galaxy sizes computed following the same methods applied to our cluster sample, which are described in Sect. 3. We will use this sample in the context of the evolution of the B-band Tully-Fisher and Velocity-Size relation whereas we exclude it from the M_*-TFR and the angular momentum analyses due to the lack of reliable stellar-mass values.

In addition, we selected a number of kinematic studies with reliable values of angular momentum as comparison samples at different redshifts. The first sample is made of 44 galaxies taken from Fall & Romanowsky (2013, 2018). These objects were presented already in Romanowsky & Fall (2012) though with overestimated stellar-mass values. In these papers, the authors study the angular momentum of galaxies of varying morphology at z=0, finding parallel sequences for the different Hubble types. We restrict our comparison sample to objects whose bulge to disk ratio is smaller than 0.3, which according to the authors ensure the selection of late type galaxies (Sa to Sd). After applying this selection criteria, this sub-sample is composed of 43 disc galaxies with an average stellar-mass value of log M_*=10.5 within the following range 9.0<log M_*<11.2 for individual objects. Measurements in the local universe establish a zero point to any scaling relation evolutionary path across cosmic time. To ensure that we are able to reliably fix this zero point, we included a second local universe comparison sample. Posti et al. (2018) revisited previous z=0 studies on angular momentum by using a sub-sample of 92 nearby galaxies from the SPARC survey (Lelli et al. 2016). We follow the same late-type selection criteria we applied to the Fall sample and remove 16 additional galaxies with S0, Irr or compact morphology to end up with a sub-sample of 76 spiral galaxies with stellar-mass values ranging 8.0<log M_*<11.2 and log M_*=10.1 as their mean value.

Our third field comparison sample is composed of galaxies from the KROSS survey (Stott et al. 2016) at z∼0.9. Our selection criteria follow the approach of Harrison et al. (2017) in their angular momentum study whilst adding tighter constraints. We decided to only use galaxies that are rotationally supported (i.e. V_{ROT}/σ>1), and with well determined effective radius and inclination angles from imaging data (quality 1 in Harrison et al. (2017)). In addition, we discard those galaxies whose inclination angles are lower than 25^o due to the high systematic errors that small variations in this parameter may introduce in the determination of the rotation velocity. Our final sample of KROSS galaxies is made of 301 objects with a mean stellar mass value of log M_*=10.1 within a range of 8.7<log M_*<10.0.

We use the SINS/zC-SINF survey (Förster Schreiber et al. 2018) to explore the angular momentum evolution at high redshift (z>2). This sample was originally composed of 35 galaxies from which we remove 7 objects because of their irregular morphological classification and their insufficient rotational support (i.e. V_{rot}/σ<1). We discard 3 additional objects due to their relatively lower redshift (z∼1.5) in comparison with the rest of the sample. Thus, we end up with a sample of 25 disc star-forming galaxies at 2<z<2.5 displaying an average stellar mass value of log M_*=10.1 within a range given by 9.3<log M_*<10.5.

We show the mass distribution of our cluster and field comparison samples in Fig. 1. Cluster samples at intermediate to high redshift tend to display larger stellar masses than the field comparison samples. Galaxies in dense environments tend to suffer an accelerated evolution that leads them to stop their star-formation, while at the same time the number of mergers increases with respect to the field. Typically, less-massive galaxies are more influenced by this kind of processes due to their relatively small gravitational potential. Therefore, the detection low-mass star-forming galaxies in the cluster is more difficult than in the field. This selection bias is responsible of the small range of stellar-masses that our cluster samples encompass in comparison with the field. At the same time, the higher we go in redshift space the fainter these low-mass objects become, which make their detection even more challenging. This effect can be seen in the bottom panel of Fig. 1, where the local samples show a mass distribution with a long tail towards low stellar-mass values, while the KROSS and SINS/zC-SINF samples at z∼0.9 and 2 respectively have a larger fraction of galaxies above log M_*=10. We will discuss the possible impacts of these different mass distributions over angular momentum evolution in Sect. 4.

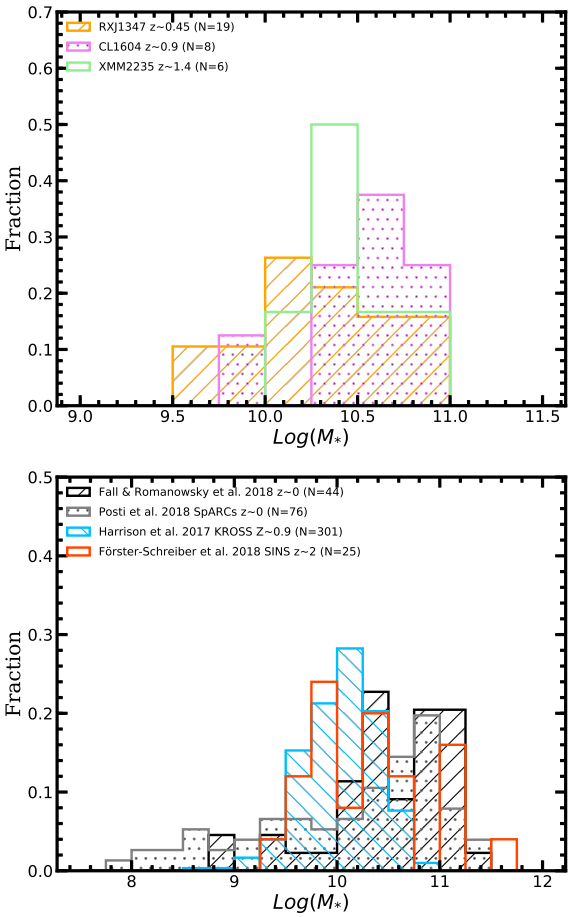

Fig. 1: Mass distribution of our cluster and field comparison samples. Samples without available stellar-mass measurements (HSC-clusters) have been removed. The mass-bin width is equal to 0.25 dex.

3. Parameters of CL1604 galaxies

3.1. Rest frame magnitudes and stellar masses

We use the SED fitting code Lephare (Ilbert et al. 2006, Arnouts & Ilbert 2011) to compute the rest-frame magnitudes and stellar masses in our cluster sample. For every object, Lephare fits the spectral energy distribution given by the available photometric bands to a library of stellar population synthesis models (Bruzual & Charlot 2003) assuming Calzetti's attenuation law (Calzetti et al. 2000). We constrained the models to use extinction values of $E(B-V) = 0 - 0.5$ mag in steps of 0.1 mag, and to produce galaxy ages lower than the age of the Universe at z∼0.9 (i.e. 6.2 Gyrs) assuming a Chabrier IMF (Chabrier 2003). Our rest-frame magnitudes and logarithmic stellar masses are computed this way to an accuracy of 0.1 magnitudes and 0.1 dex respectively. In order to study the resdhift evolution of the Tully-Fisher relation in Sect. 4, we must correct the derived absolute B-band magnitudes for extinction due to their inclination angles with respect to the line of sight. In edge-on spirals, the stellar light has to travel through the galaxy disc, that is filled with dust particles, before reaching our eyes. Therefore, these galaxies possess higher extinction values than their face-on counterparts. In addition, more massive galaxies have higher dust content than low-mass objects (Giovanelli et al. 1995), which introduces a stellar-mass dependence in the inclination extinction correction. We take into account these two effects following the prescription given by Tully et al. (1998). This correction diverges for completely edge-on galaxies (i.e. i=90º), and therefore we exclude them from our sample. After applying this correction, the typical errors for the B-band absolute magnitude values for the CL1604 sample are ∼0.2 mag.

3.2. Structural parameters

Space-based HST observations are ideal to measure the structural parameters of our targets reliably due to their high spatial resolution and depth. The field where CL1604 resides counts with extensive HST imaging in two filters (F606W and F814W) covering most of the structure of the cluster complex, including all but one of our targets. In general, images taken in redder filters capture the light from the old stellar population that dominates the structure of the galaxy which diminishes the contamination coming from prominent star-formation regions. We chose to use the the F814W images as the main source to measure the structural parameters of our cluster members for this reason. In addition, we use the HSC z-band to make the same measurements over the single object without HST imaging due to the depth and seeing conditions (FWHM∼0.5") achieved in this band during the observations.

We model the surface brightness profile of our targets and measure their structural parameters by using the GALFIT code (Peng et al. 2002). The models are produced following a two component approach in which first we applied a single component fit to every galaxy assuming a fix Sèrsic index $n_s = 1$ (exponential disc profile) and subtract it from the original image. After inspecting the residuals we determine if the object under scrutiny shows signs of a bulge presence. If this is not the case, we keep the structural parameters computed with a single exponential disc surface brightness profile. However, if there are strong residuals in the central areas of the galaxy after the model subtraction, we apply a second component fit that takes into account the bulge contribution. In this case, we fix the Sèrsic index to $n_s = 4$ (de Vancouleurs profile) for this component, and use the structural parameters determined after the single component fitting as the initial guess values before restarting the process.

The modelling provide us with the position angle of our objects (θ) with respect to the north direction, the effective radius (R_e) of the disc component, and the ratio between the apparent minor and major axis (b/a). The position angle can be used to identify possible misalignments between the major axis of the galaxy and its slit. This quantity is called mismatch angle (δ) and will be used at a later stage to correct the observed rotation velocities of our targets. In addition, the ratio between the axes, b/a, can be used to compute the inclination (i) of the galaxy with respect to the line of sight, which also plays an important role in the determination of the maximum rotation velocity. In addition, spiral galaxies have a small although significant scale height (q) that enters in the determination of i following the approach given by Heidmann et al. (1972):

$$\cos(i) = \sqrt{\frac{(b/a)^2 - q^2}{1 - q^2}} \quad (1)$$

where $q = 0.2$ represents the typical observed value for local spiral galaxies (Tully et al. 1998). Finally, the three clusters that belong to our primary sample rely on R_e measurements from different filters and at different redshifts. However, the effective radius of disc objects experience significant variation with wavelength. For example, Kelvin et al. (2012) measure a reduction of 25% in R_e for late type galaxies from g to K-band, and established a relation to account for these changes using measurements from the GAMA data base:

$$\log r_{e,disc} = -0.189 \log \lambda_{rest} + 1.176 \quad (2)$$

where λ_{rest} is the observed rest-frame wavelength for the galaxy. We use this relation to normalize the R_e measurements of our three cluster galaxies to the same reference wavelength, λ_{ref} = 8900Å. This value is the rest-frame central wavelength of the HAWKI/Ks-filter for targets at z 1.4, and was used for the R_e measurements of our XMM2235 sample. The correction of the sizes is of the order of 10% for the CL1604 sample (observed with HST/F814W at z∼0.9) and 7% for the RXJ1347 sample (observed with SUBARU Suprime-Cam/z' at z∼0.45).

3.3. Determination of the maximum intrinsic velocity (V_{max})

Our approach to extract the rotation curve from prominent emission lines and the subsequent modelling to determine the maximum rotation velocity (V_{max}) has been extensively described in previous publications within our group (see Böhm et al. 2004, Bösch et al. 2013b, Böhm & Ziegler 2016). However, we provide a brief summary of the most important steps of the process in the following paragraphs for the readers' convenience.

First, we find our prominent spectral feature within the 2D spectra ([OII]3727Å for CL1604)) and measure the central wavelength position of the emission line by fitting a Gaussian profile over it row by row. We average the emission line over three neighbouring rows (i.e. 0.75" in the spatial axis) to enhance the signal-to-noise (S/N) before the fitting. For every row, we inspect the small blue- and redshifts of the central wavelength position in the dispersion axis and transform them into positive and negative velocities with respect to systemic velocity at the center of the galaxy. This way we obtain a position-velocity diagram that displays the rotation velocities as a function of galactocentric radius. We allow for small variations between the photometric and kinematic center of the galaxy of up to ±1pix, i.e. 2kpc in spatial scale at z∼0.9.

The second step of the process involves the correction of the position-velocity diagram from all observational (beam-smearing) and geometrical effects (inclination, misalignment angle, and slit width) that may affect the observed values. To solve this, we generate synthetic velocity fields assuming an intrinsic rotation law, taking into account the seeing conditions at the time of the observations and the structural parameters previously determined through surface brightness modelling. We follow the multiparametric rotation law presented in Courteau (1997) which is characterized by a linear rise at distances smaller than the turnover radius (r_t) and a constant maximum rotation velocity (V_{max}) beyond this point, where the dark matter halo dominates the mass distribution. Finally, we place a slit along the apparent major axis of the object and extract the synthetic rotation velocity values from the model as a function of radius. These values define a synthetic rotation curve that is allowed to change by tuning the V_{max} and r_t in order to fit (via χ^2 minimization) the observational shape directly extracted from the 2D spectra. The precision achieved in the determination of V_{max} is mainly influenced by the accuracy of the structural parameters (specially i) and the quality and extent of the rotation curve, with typical values around ±20 km/s. Only 8 regular rotation curves could be extracted out of 34 observed cluster objects, 12 of which displayed irregular kinematics. The remaining galaxies showed just gradients or too compact emission to asses their kinematic state. The synthetic and observed rotation curves can be found in Appendix A for Cl1604 cluster members. The same information is available for XMM2235 and RXJ1347 in our past publications (Pérez-Martínez et al. 2017 and Perez-Martinez et al. 2019, submitted to A&A).

4. Results and Discussion

The flat rotation curves of spiral galaxies provide us with a proxy, the rotation velocity (V_{rot}), to trace the total mass of the galaxy (including dark matter) as well as to study its relation with respect to several other baryonic parameters. Some of the key additional parameters that describe the physics of spiral galaxies are the disk size (throughout the effective radius, R_e, or scale length, R_d), and the stellar population content of the galaxy (via its luminosity or stellar-mass). The rotation velocity, the galaxy size and the luminosity (or stellar mass) conform a three-dimensional space (Koda et al. 2000) from which its projections provide with different scaling relations such as the The Tully-Fisher relation (TFR) and the velocity-size relation (VSR, Tully & Fisher 1977 in both cases). In addition, different combinations between these parameters provide us with other interesting relations such as the specific angular momentum-stellar mass ($j_* - M_*$) that are key to understand the processes of morphological transformation and mass redistribution that galaxies suffer during their lifetime.

In this work we use the cluster and field samples introduced in Sect. 2 to study the evolution of the TFR, the VSR, and the $j_* - M_*$ relation with respect to environment and time: The B-band TFR, the velocity-size relation, and the angular momentum. In the first two cases we will focus on samples exclusively studied by our own group to achieve full consistency in the methodology to extract the main physical parameters between data-sets. For the angular momentum, on the other hand, we choose additional comparison field samples from the literature that count with all the required parameters for its study (i.e. M_*, R_e and V_max).

4.1. The B-band Tully Fisher and Velocity Size relations

First, we examine the distribution of our targets in the B-band Tully-Fisher diagram (Fig. 2, left panel). Cluster objects are plotted using stars of several colors to express their membership to different clusters, while we use the local TFR (solid black line, Tully et al. 1998) and a sample of 124 filed disc-like galaxies from Böhm & Ziegler (2016) at 0.1<z<1 for comparison. In Fig. 2 we simply represent the field distribution by the grey area whose half-width is equal to three times the scatter of the field sample (3σ), which encompass the majority of the field galaxies. On the other hand, most cluster galaxies lie within the 3σ area of the field distribution, although at a fixed rotational velocity, the objects gradually move towards higher B-band absolute magnitudes with redshift. This is a natural consequence of the gradual evolution of the stellar populations with lookback time, with younger (and hotter) stars contributing more to the luminosity of the galaxy when the universe was at an early stage. This can be seen more clearly in the left-hand panel of Fig. 3 where we display the B-band magnitudes offsets from the local TFR ($\Delta M_B = M_{B,z} - M_{B,z=0}$) as a function of redshift. We take the mean values for our cluster samples and split the field sample in three bins (0<z<0.33, 0.33<z<0.66 and 0.66<z<1.0) for which we do the same. The error bars in the mean values account for the standard distribution of very sample or bin.

Our results show that there is a gradual increase in ΔM_B for cluster galaxies up to z∼1 (colored circles, $\Delta M_B \approx 1$). This trend is replicated by the binned mean values for field galaxies from Böhm & Ziegler (2016) (black circles), which account for the same redshift intervals albeit with larger number statistics. Although the field mean values tend to lie slightly below the clusters' ones, this small difference becomes negligible when taking int account the standard deviation of each sample. On the other hand, the semianalytical models by Dutton et al. (2011) (dashed line) predict a rise in B-band luminosity that is compatible with our results at similar redshift, which points towards little to no influence of the environment over cluster galaxies with regard to the B-band luminosity up to z∼1. However, the two higher redshift cluster samples significantly deviate from the semianalitical predictions ($\Delta M_B = 1.6\pm0.9$ for XMM2235 and $\Delta M_B = 2.2\pm1.1$ for the two HSC clusters). Unfortunately, we do not have a field comparison sample analyzed following the methods described in Sect. 3 at this high redshift. Nevertheless, this behaviour hints towards the presence of unaccounted processes influencing the B-band luminosity of high redshift cluster galaxies. We favor two different scenarios that could explain this enhanced brightening in addition to the regular stellar population evolution. Firstly, it has been shown that during the processes of cluster assembly at high redshift, galaxies posses higher gas fractions than their field counterparts (Noble et al. 2017, Hayashi et al. 2018a). A possible explanation for this behaviour is that the filamentary structure of the cosmic web boost the inflows of pristine gas towards galaxies at its junctions (i.e. at assembling clusters). We speculate that the channeling of fresh cold molecular gas towards the galaxy disk may be responsible of the creation of small starburst that, in turn, enhance the B-band luminosity of the object. Secondly, in the course of ram-pressure stripping, an initial increase of star formation is expected which could temporarily enhance the B-band luminosity of a given object (Ruggiero & Lima Neto 2017; Ruggiero 2019), while the galaxy is still showing disk rotation (Noble et al. 2019). This scenario was discussed in more detail in Pérez-Martínez et al. (2017). While XMM2235 is one of the most massive clusters known at high redshift, with high X-ray luminosity indicating the presence of a dense intracluster medium

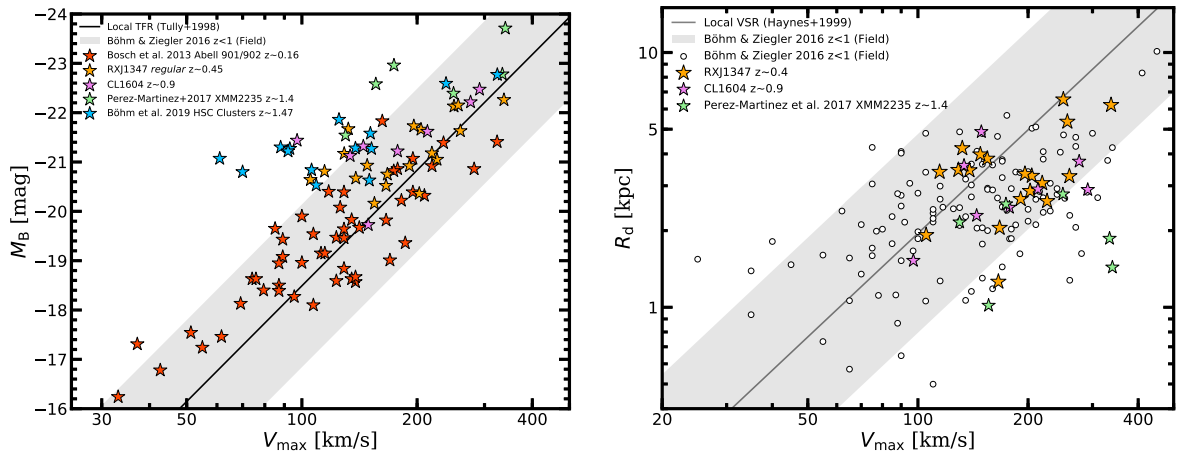

Fig. 2: *Left*: B-band Tully-Fisher relation. Colored stars represent the different cluster samples that entered our study. The black solid line shows the local B-band TFR (Tully et al. (1998)) with a 3σ scatter area around reported by Böhm & Ziegler (2016) for galaxies at 0<z<1 (grey area). *Right*: Velocity-Size diagram. The symbols and their colors follow the same description than in the left hand panel. White circles depict galaxies at 0<z<1 from Böhm & Ziegler (2016). The solid black line shows the local VSR from Haynes et al. (1999), with a 3σ scatter grey area around it.

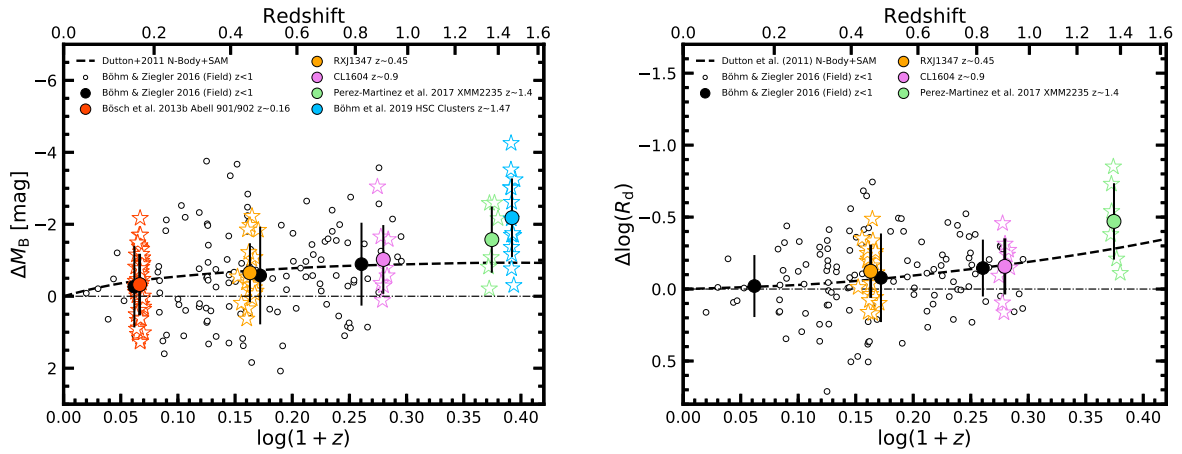

Fig. 3: *Left*: B-band Tully-Fisher offsets evolution. Colored edge stars represent the different cluster samples that entered our study, with their respectively mean values being showed as bigger circles of the same color. Error bars for the mean values account for the standard deviation of every sample. White small circles show the reported offsets for the Böhm & Ziegler (2016) field sample at 0.1<z<1. We binned the field sample in three redshift intervals (0<z<0.33, 0.33<z<0.66, 0.66<z<1). Big black circles depict the mean value and standard deviation of the field sample in every redshift window. The dashed line represents the predicted B-band luminosity evolution by Dutton et al. (2011) in the TFR, while the dashed-dotted line at $\Delta M_B = 0$ means no size evolution. *Right*: Velocity-size offset evolution. Symbol and color schemes are the same than in the right hand panel.

(ICM), the two HSC-clusters, on the other hand, may be at the start of their assembly ($\sigma \sim 400$ km/s, Böhm et al. 2019). Therefore, the two scenarios proposed may respectively fit the evolutionary stage of the clusters of galaxies under scrutiny. However, the small number statistics of our sample and the lack of a proper field comparison sample prevent us from further investigate the origin of the B-band TFR enhancements beyond z~1.

In the right hand diagram of Fig. 2 we show the velocity-size relation for our cluster and field samples. The diagram maintains the same symbols scheme used in the left hand panel with the solid line marking now the local velocity-size relation from Haynes et al. (1999). By construction, our samples are exclusively made of disk galaxies (see Sect. 3). Therefore, we use the disc scale length (R_d) to compare the size of our objects. Galaxies from Abell 901/902 at z~0.16 and from the two HSC

clusters at z∼1.5 are excluded due to the current lack of published size measurements. Originally, R_d was measured using different photometric bands in every sample. However, the extension of a given galaxy disc correlates with the wavelength at which it is observed, with bluer wavelengths providing larger R_d. We use Eq. 2 to re-normalize all measurements to the same rest-frame wavelength in this figure. Cluster objects tend to display lower sizes for a fixed rotation velocity at higher redshifts. This is a consequence of the growth of discs across cosmic time and it is one of the predictions of the ΛCDM cosmological model with respect to the hierarchical growth of structures. We explore the offsets with respect to the local velocity-size relation in the right hand diagram of Fig. 2, where we compare our results once again with the semi-analytical models of Dutton et al. (2011). Interestingly, we find that cluster and field galaxies have a similar average size evolution, with a factor 1.6 drop in size ($\Delta \log R_d = -0.2$) by redshift one for the field and cluster. This is in accordance with the predictions of Dutton et al. (2011), although with a large scatter that is related to the different formation ages of our galaxies and their distinct evolutionary paths. Observational studies in the field such as van der Wel et al. (2014) find that the size growth of disk galaxies with redshift is given by $R_e \propto (1+z)^{-0.75}$, which yields a factor 1.6 growth between z=1 and z=0 at a fixed stellar mass, reinforcing our previous results. However, this empirical relation only predicts a factor 2 growth at z=1.5 (in agreement with Dutton et al. 2011), in contrast with our results in XMM2235 that show smaller sizes by almost a factor 3. Larger cluster samples of rotating discs are required to understand these offsets in the velocity-size relation at high reshift.

4.2. The angular momentum

The angular momentum (J) simultaneously connects all the relevant parameters involved in the previous scaling relations, i.e. stellar-mass, size, and rotation velocity. The transference of angular momentum from the dark matter halo to the baryonic component is key to understand the early stages of galaxy formation. On the other hand, the specific angular momentum defined as j_*=J/M_* has proven to be a fundamental quantity to explore galaxy evolution and morphological transformation. Fall (1983) first found a tight relation between j_* and M_* with the form $j_* \propto M^{2/3}$. Its normalization depends on the galaxy morphological type, with parallel sequences towards lower specif angular momentum values for early type galaxies, pointing towards a loss of angular momentum of up to an order of magnitude (Romanowsky & Fall 2012, Fall & Romanowsky 2013, 2018). In this section we compare the results obtained in the $j_* - \log M_*$ relation for cluster and field galaxies at different epochs. The evolution of this relation has been previously studied for field galaxies at z>0 (e.g. Harrison et al. 2017). In order to maintain consistency between our clusters and comparison samples analyses, we adopt the simple theoretical frame described in Harrison et al. (2017) to study the evolution of angular momentum, for which we present a brief summary in the following paragraphs. First, we use equation 6 in Romanowsky & Fall (2012) as our approximate estimator for specific angular momentum:

$$j_* = k_n C_i v_s R_e \tag{3}$$

where R_e is the effective radius of the galaxy, v_s is the observed rotation velocity at some arbitrary radius, C_i is an inclination correction factor and k_n is a numerical factor that takes into account the current morphology of the galaxy approximated by its Sérsic index (n) in the following way:

$$k_n = 1.15 + 0.029n + 0.062n^2 \tag{4}$$

By construction (see Sect. 3.2), we constrain our samples to only contain disk galaxies, displaying characteristic exponential surface brightness profiles (n=1). Furthermore, small variations of n in the vicinity of the exponential profile (for example 0.5<n<1.5) will only introduce small variations in the value of k_n (up to 7%). Therefore we confidently assume n=1 as our standard value for all further calculations, adding such uncertainty contribution to the specific angular momentum error budget. Additionally, we may consider that our inclination and seeing corrected maximum rotation velocity (V_{max}) is equivalent to $V_{max} \approx C_i v_s$, simplifying Eq. 3 for disc galaxies to just:

$$j_* \approx 2 V_{max} R_d \tag{5}$$

where R_d is the disc scale-length and $R_d \approx 1.678 R_e$. This approach yields the $j_* - \log M_*$ relation as a correlation between two independent variables. In Fig. 4, we present the results obtained for our cluster galaxies in comparison with our selection of field samples, which have analyzed following the same methods described above. The distribution of the local data is fitted by the expectations for disks given by Fall & Romanowsky (2013) (blue line). At higher redshifts, both the field and the cluster samples display lower specific angular momentum values, and in appear to follow sequences with similar slope. However, the scatter and the limited number statistics of our samples makes it difficult to directly quantify this offset. To further explore the possible variations in specific angular momentum as a function of redshift and environment we use a simple predictive model (Romanowsky & Fall 2012 and Obreschkow & Glazebrook 2014 Eq. 18 and 19) assuming that the baryonic fraction can be approximated by $f_b = 0.17$ (Komatsu et al. 2011):

$$\frac{j_{*,pre}}{kpc\ km\ s^{-1}} = 2.95 \cdot 10^4 f_j f_s^{-2/3} \lambda \left(\frac{H[z]}{H_0}\right)^{-1/3} \left[\frac{M_*}{10^{11} M_\odot}\right]^{2/3} \tag{6}$$

where $H[z] = H_0(\Omega_\Lambda + \Omega_m[1+z]^3)^{1/2}$. This model is based on the assumptions that all galaxies reside inside singular isothermal spherical cold dark matter haloes characterized by a spin parameter λ and a specific angular momentum j_h. Therefore, the galaxies embedded in such dark matter haloes possess a fraction of the specific angular momentum of the halo in which they were formed $f_j = j_*/j_{halo}$. This fraction may change between galaxies from different epochs and evolutionary paths since it represents the specific angular momentum retained by the baryons at a given moment, and will be the focus of our analysis. On the other hand, during the processes of galaxy formation the asymmetric collapse of high density regions generates tidal torques that introduce a particular angular momentum value for every mass distribution (Hoyle 1951, Peebles 1969). The spin parameter accounts for this behaviour. N-body simulations and recent observational studies have shown that λ follows a near-lognormal distribution with an expected value $\lambda = 0.035$ and a mean dispersion of 0.2 dex, which remains approximately constant when examining different epochs, galaxy masses, and environment (Macciò et al. 2007, 2008, Romanowsky & Fall 2012, Bryan et al. 2013, Burkert et al. 2016). Finally, f_s represents the stellar mass fraction relative to the initial gas mass. This parameter is a function of the different internal processes that take place within a galaxy as a result of its evolution. Given the difficulty to account for all possible variables involved in the baryonic physics, we need to take an empirical approach. We use

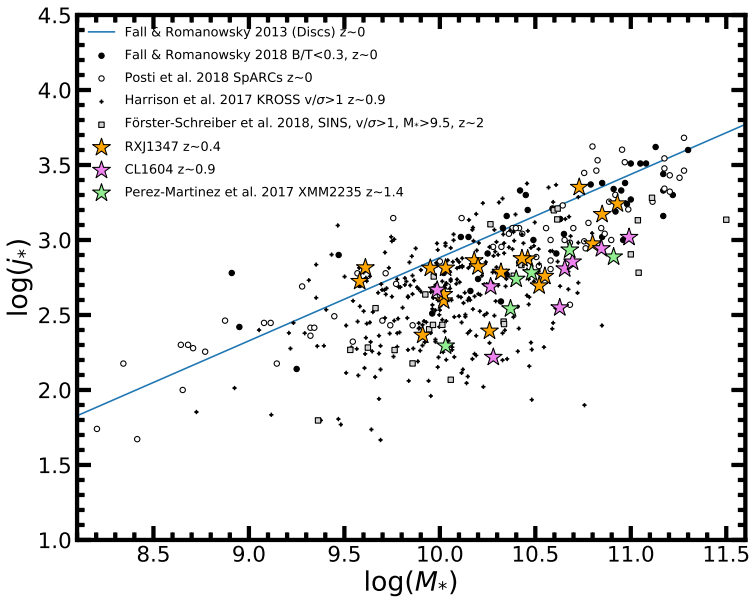

Fig. 4: Specific angular momentum diagram. Orange, violet and light green stars respectively represent the RXJ1347, CL1604 and XMM2235 cluster galaxies studied by our group. Black and white circles account for the local universe disc-like samples from Fall & Romanowsky (2018) and Posti et al. (2018) respectively. The small black crosses show the field objects from KROSS sample at z∼0.9 (Harrison et al. 2017), while SINS/zC-SINF galaxies at z∼2 are displayed by grey squares (Förster Schreiber et al. 2018). The blue solid line depicts the "Fall relation" for discs from Fall & Romanowsky (2013).

the mass-dependent description given by Dutton et al. (2010) for late-type galaxies and revisited in Burkert et al. (2016) for this purpose:

$$f_s = 0.29\left(\frac{M_*}{5\cdot 10^{10} M_\odot}\right)^{1/2}\left(1+\left[\frac{M_*}{5\cdot 10^{10} M_\odot}\right]\right)^{-1/2} \quad (7)$$

Under these assumptions, the only free parameter in $j_{*,pre}$ is the specific angular momentum fraction retained by the galaxy with respect to its dark matter halo ($f_j = j_s/j_{halo}$). We now can consider the idealized case where the baryonic and dark matter component of the galaxy have been well-mixed from the early stages of galaxy formation, meaning that the specific angular momentum in both components is very similar ($j_* \approx j_{halo}$), and thus, $f_j \sim 1$. In Fig. 5 we present the discrepancies between the predicted specific angular momentum (assuming $f_j = 1$) and the values computed following Eq. 3 for all the cluster and field galaxies (i.e $\Delta\log(j_*) = \log(j_*) - \log(j_{pre})$) as a function of stellar mass. This choice of parameters is very useful because the negative values in $\Delta\log(j_*)$ can be re-interpreted as lower fractions of conserved specific angular momentum, $f_j < 1$, for galaxies experiencing different conditions (e.g. redshift or environmental evolution). Thus, it provides a way to directly compare the amount of conserved angular momentum (f_j) as a function of stellar-mass for galaxies with diverse origins.

Due to the large amount of galaxies involved we split Fig. 5 into two panels. In the left hand diagram we show the full distribution of objects (and their scatter) from our field comparison samples with $\Delta\log(j_*) = 0$ marking the limit for $f_j = 1$. Note that objects above this limits are allowed to exist in this model due to the uncertainty in the determination of the spin parameter (λ) and its mean dispersion value (0.2 dex, yellow band). The right hand panel synthesizes the information contained in the previous diagram by binning the field objects within intervals of 0.5 dex in M_*. The solid lines show the resultant mean values and standard deviations as a function of stellar-mass. Due to the limited number statistics of our cluster samples, we avoid the binning and simply compute the mean offset values and standard deviation per cluster (colored circles) but, in addition, we show the whole distribution of our targets in the diagram (colored stars).

We obtain $\Delta\log(j_*) = -0.23 \pm 0.18$ for galaxies in RXJ1347 at z∼0.4, $\Delta\log(j_*) = -0.41 \pm 0.18$ for galaxies in CL1604 at z∼0.9, and $\Delta\log(j_*) = -0.42 \pm 0.11$ for galaxies in XMM2235 at z∼1.4. These three values indicate a significant increase in the angular momentum from z∼1 with little evolution between z∼1 and z∼1.4. As we stated above, we can re-interpret these offsets as lower values in the retained specific angular momentum fraction, f_j. Thus, galaxies from RXJ1347 on average conserve 60% of their halo specific angular momentum (i.e. $\langle f_j\rangle \approx 0.6$) while the cluster members from CL1604 and XMM2235 on average only retain up to ∼ 38% (i.e. $\langle f_j\rangle \approx 0.38$). We now compare these results in dense environments at different epochs with our field comparison samples. In the field at z∼0 there is little dependence between $\Delta\log(j_*)$ and the galaxy's stellar-mass for $\log M_* > 9.5$. These variations are negligible when taking into account the standard deviation of every bin in the local samples (Fall & Romanowsky 2018 in blue and Posti et al. 2018 in red), which display similar average offset values across the mass range under scrutiny. By transforming this offset into the retained angular momentum fraction we obtain $\langle f_j\rangle \approx 0.80$, which is in line with the predictions from numerical models in the local universe (). Examining the selected KROSS disc galaxies at z∼0.9

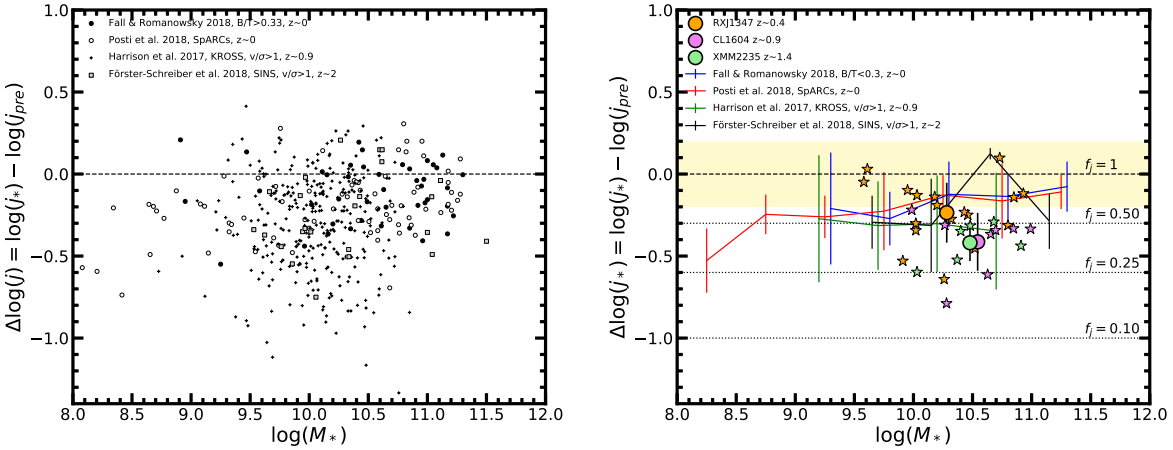

Fig. 5: *Left*: Specific angular momentum offsets ($\Delta\log(j_*)$) as a function of mass for the field samples. Black and white circles represent the local universe disc samples from Fall & Romanowsky (2018) and Posti et al. (2018) respectively. The small black crosses show the objects from KROSS sample at z∼0.9 (Harrison et al. 2017), while SINS/zC-SINF galaxies at z∼2 are displayed by grey squares (Förster Schreiber et al. 2018). The horizontal dashed line marks $f_j = j_*/j_{halo} = 1$. The light yellow band depicts the predicted scatter in the spin parameter λ assuming $f_j = 1$. Dotted lines mark different predicted values of f_j as a function of $\Delta\log(j)$. *Right*: Same diagram as in the left hand panel but including our cluster samples. The orange, violet and light green circles respectively show the mean $\Delta\log(j) - \log(M_*)$ values and their standard deviation for RXJ1347, CL1604 and XMM2235 cluster galaxies. Individual objects from these three clusters are plotted using stars and following the same color scheme. The solid colored lines depict the mean values and standard deviation of the mass-binned field samples using bin widths of 0.5 dex.

(green bins) we find a similar situation with no stellar-mass dependence but an even lower mean offset across the mass range under scrutiny, $\langle f_j \rangle \approx 0.5$. Similar results were previously reported in a larger sub-sample of the KROSS survey by Harrison et al. (2017), who applied less restrictive selection criteria. This behaviour is closely matched by the z>2 galaxies from the SINS/zC-SINF survey (Förster Schreiber et al. 2018) although with lower number statistics per bin due to the observational difficulties at this redshift. Since observed galaxies are not uniformly distributed with mass in the SINS/zC-SINF sample, the bin $10.5 < \log M_* \approx 11$ is populated by only three objects (see left hand panel of Fig. 5), which can explain its outlying nature with respect to the rest of the sample.

Several processes may be responsible for the changes in the specific angular momentum of a galaxy. For example, the outflows of material from the inner parts of a galaxy together with merging events may significantly decrease the specific angular momentum of an object (Lagos et al. 2018), while the accretion of high angular momentum pristine gas in the outskirts of the galaxy and the migration of clumpy star-forming regions towards the central area of the galaxy may increase it (Dekel et al. 2009). In the cluster environment, where interactions are more frequent, the loss of angular momentum may become more prominent. On a first stage, the hot ICM prevents the galaxy for getting inflowing material while at the same time ram pressure stripping removes the outer parts of the disk gas reservoir. At the same time, the higher object number density in the cluster environment enhances the frequency of close encounters between galaxies, which may cause angular momentum exchange and loss through tidal interactions. While the effects of these encounters might be not as destructive for the specific angular momentum as merging events, they contribute to increase the loss of angular momentum with respect to the field population.

Furthermore, the destruction of the galaxy disc via major merger in the cluster environment would immediately exclude that kind of galaxy from our analysis, since the conditions of the cluster will not allow the object to dynamically cool down and rebuild its disc before it is quenched. Only minor mergers should be considered to this regard since, to some extend and depending on the initial conditions of the event (mass ratio, relative velocity and geometry), they may change the angular momentum and the stability of the disc without fully destroying its structure. Lagos et al. (2018) investigated the influence of mergers on the specific angular momentum finding a great variety of behaviours. In general, major mergers will significantly decrease j_* (on average by a factor 2-3) after 1 Gyr, with counter-rotating dry mergers being specially efficient in this task. On the other hand, the effects of minor wet and dry mergers after 1 Gyr seem to be more subtle, with the former slightly contributing to increase j_* by up to a factor 1.25, specially in the cases when the merger involves high relative orbital velocities and co-rotating geometry, and the latter acting in the opposite direction by decreasing j_* by a similar amount. In both cases, however, the results strongly depend on the exact gas fractions and the geometry of the event. If minor mergers do play a major role in decreasing j_* for cluster galaxies, these interactions should be largely dominated by gas-poor mergers. However, we emphasize that the contribution by other cluster-specific interactions (e.g. harassment, fly-by encounters, etc) may be as relevant as in the previous case, although it remains unexplored from the numerical simulation point of view to our best knowledge.

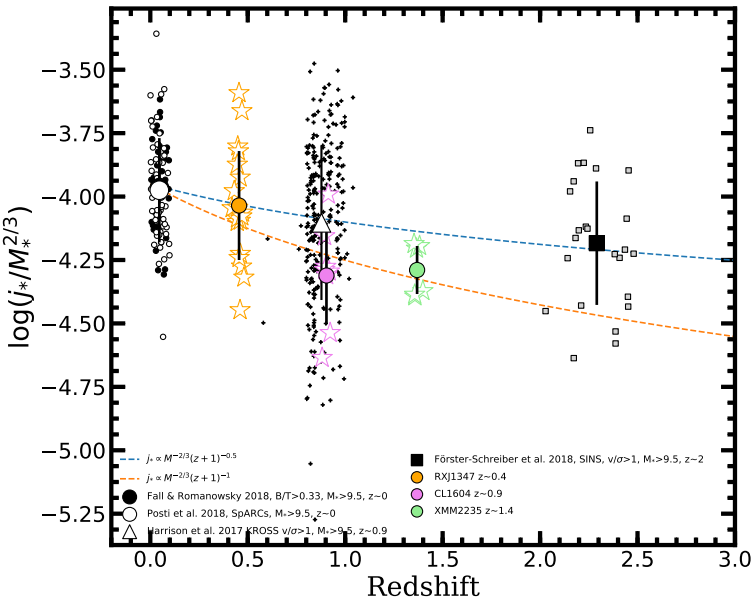

Fig. 6: Redshift evolution of $j_*/M^{2/3}$ from z=0 to z~2.5. The black big circle shows the mean value for local field galaxies from Fall & Romanowsky 2018 (small empty cirles) and Posti et al. 2018 (small black cirles) respectively. The blank triangle depicts the average value for the KROSS sample at z~0.9 (small crosses, Harrison et al. 2017), and the black square represent the field galaxies at 2<z<2.5 from Förster Schreiber et al. 2018 (small grey squares). The average $j_*/M^{2/3}$ value for the RXJ1347, CL1604 and XMM2235 cluster samples are respectively depicted by the orange, violet and light green circles. The standard deviation of every sample is plotted as error bars for each symbol. The dashed lines represent the expected evolution of the angular momentum with redshift according to the ΛCDM cosmology: $j_* = M^{-2/3}(z+1)^{-n}$ with n=0.5 (blue) and n=1 (orange).

4.3. The redshift evolution of angular momentum

In the context of the ΛCDM cosmological model, the specific angular momentum of the dark matter halo has a dependency not only with stellar-mass, but with time (Mo et al. 1998). This dependency scales as $j_h \propto M_h^{2/3}(1+z)^{-n}$, with n=1/2 for spherically symmetric haloes in a matter-dominated Universe (Obreschkow et al. 2015). Assuming that the stellar-to-halo-mass ratio is essentially insensitive to the redshift evolution (Behroozi et al. 2010), the baryonic component should display a similar behaviour $j_* \propto M_*^{2/3}(1+z)^{-1/2}$. These assumptions allow us to investigate the redshift evolution of the specific angular momentum as a function of environment utilizing the cluster and field samples studied above. In this case, we decided to only use galaxies above $\log M_* = 9.5$ for two reasons: First, we showed in Fig. 5 that our field samples at different redshifts had a weak to negligible stellar-mass dependence with respect to their specific angular momentum for moderate to high stellar-mass values. However, the z~0 sample from Posti et al. (2018) hints that in the low stellar-mass regime this dependence may become more important. In addition, our cluster samples are dominated by relatively massive galaxies ($\langle \log M_* \rangle > 10$) and lack objects below $\log M_* = 9.5$.

After applying this new constraint we present the angular momentum redshift evolution in Fig. 6, where the big symbols represent the mean values and standard deviations for each sample included in our angular momentum analysis. We plot the functional form $j_* \propto M_*^{2/3}(1+z)^{-n}$ for n=1/2 and n=1 to allow for different evolutionary paths, and normalize the zero point (z~0) to the mean values measured from our local Universe galaxy samples, which are in remarkable agreement: $\log(j_*/M_*^{2/3}) = -3.96 \pm 0.18$ for Fall & Romanowsky (2018) and $\log(j_*/M_*^{2/3}) = -3.97 \pm 0.21$ for Posti et al. (2018). It is important to emphasize that these two samples are only composed of spiral galaxies, although allowing for small variations in the bulge-to-disc ratios (B/D) to include most late-type galaxies. We find that galaxies at higher redshift (KROSS at z~0.9 and SINS/zC-SINF at 2<z<2.5) follow the scaling of $j_* \propto M_*^{2/3}(1+z)^{-1/2}$ well, with lower specific angular momentum for a given stellar mass at higher redshift. In particular, $\log(j_*/M_*^{2/3}) = -4.10 \pm 0.30$ for the KROSS galaxies and $\log(j_*/M_*^{2/3}) = -4.18 \pm 0.24$ for the higher redshift objects from the SINS/zC-SINF survey. These values are equivalent to a specific angular momentum decrease of a factor 1.3 by z~1 with respect to the local spirals, or a factor 1.6 by z~2, in agreement with the EAGLE numerical simulations that predict the same drop by z~2 (Lagos et al. 2017).

The trend in the cluster samples, on the other hand, is more difficult to interpret. In general we measure lower $\log(j_*/M_*^{2/3})$ values than in the field, specifically for the higher redshift clusters (e.g. -4.31 ± 0.19 for CL1604 at z~0.9, and -4.29 ± 0.10 for XMM2235 at z~1.4, but -4.04 ± 0.21 for RXJ1347 at z~0.45). Our results suggest that, on average, cluster galaxies have a lower specific angular momentum than their field counterparts at a given epoch, which makes them more compatible with $j_* \propto M_*^{2/3}(1+z)^{-1}$. This difference can be explained by the higher probability of interactions that contribute to the angular momentum loss in the cluster environment with respect to the field. In

spite of not knowing what is the exact contribution of each interaction (e.g. tidal and merging events, ram pressure-stripping, supression of inflows), these mechanisms appear to be in place as early as z∼1.4 in virialized systems such as XMM2235. Thus, future studies of galaxies residing in cluster structures during the early stages of their assembly may unveil hints about the nature of such interactions.

5. Conclusions

In this work, we have studied the redshift evolution of the Tully-Fisher relation, the velocity-size relation, and the angular momentum in clusters up to z∼1.5. We use a collection of clusters at different redshifts for this purpose, with many of them being the focus of previous publications: Abell 901/902 at z∼0.16 (Bösch et al. 2013a,b), RXJ1347 at z∼0.45 (Perez-Martinez et al. 2019, submitted to A&A), XMM2235 at z 1.4 Pérez-Martínez et al. 2017 and two HSC clusters at z∼1.5 Böhm et al. 2019). In addition, we present in this work the first results from a sample of galaxies in the CL1604 cluster system at z∼0.9. All cluster samples were studied by our group with similar methods and techniques, which make them ideal for a comparative study between different epochs. We also compare our cluster scaling relations results with field samples between z=0 and z=2.5 (Fall & Romanowsky 2018, Posti et al. 2018, Harrison et al. 2017, Förster Schreiber et al. 2018), cosmological numerical simulations (Dutton et al. 2010, 2011, Lagos et al. 2017, 2018) and other theoretical works such as Obreschkow & Glazebrook (2014) and Obreschkow et al. (2015). Our main findings can be summarized as follows:

1. Cluster and field galaxies at 0<z<1 display similar behaviours and generally follow the B-band TFR although with increasing B-band luminosity values with lookback time. These results are in agreement with the expectations from semianalytical models by Dutton et al. 2011 who predicts $\Delta M_B \approx -1$ mag by z=1. However, cluster galaxies at z∼1.5 strongly from these predictions and show average B-band luminosity enhancements of $\Delta M_B \sim 2$. This behaviour is detected for galaxies residing in massive virialized clusters such as XMM2235 as well as for clusters still in the process of assembling the bulk of their mass such as the two HSC clusters studied here. We speculate that in the latter case, galaxies infalling towards clusters in formation through the filaments of the cosmic web may find their amount of inflowing material increased, which could contribute to create and fuel star-forming regions that in turn are responsible for this B-band luminosity enhancement. On the other hand, in more massive and virialized structures, the early phases of ram-pressure stripping on gas-rich galaxies may induce higher SFRs temporarily, and thus be responsible for this B-band enhancement. We discussed this scenario in Pérez-Martínez et al. 2017, and, indeed, according to simulations it is possible to produce a B-band luminosity enhancement (Ruggiero 2019). However, its strength strongly depends on geometrical factors, and the size of our sample and the limitations of slit spectra do not allow us to explore this hypothesis further.
2. Our results with respect to the velocity-size relation demonstrate that galaxies decrease their disc sizes with redshift at a fixed rotation velocity. Our cluster and field subsamples follow very similar trends with an average size decrement of a factor 1.6 by z=1. This result agrees with previous observational constraints (van der Wel et al. 2014) and with the numerical models of Dutton et al. (2011). However, at higher redshift cluster galaxies in XMM2235 are almost 3 times smaller than their local field counterparts, while the numerical models for field galaxies only predict a factor 2 drop. It remains unknown if this disagreement is caused by systematics affecting the limited number of objects that form part of our high redshift sample or it has a physical origin related with the cluster environment.
3. Cluster galaxies at 0.5<z<1.5 are distributed below the "Fall relation" for local galaxies ($j_* \propto M^{2/3}$ Fall 1983; Fall & Romanowsky 2013) in the j_*-M_* diagram. Assuming a baryonic fraction $f_b = 0.17$, a spin parameter $\lambda = 0.035$, the stellar-to-halo specific angular momentum ratio ($f_j = j_*/j_{halo}$) of cluster galaxies at z∼0.45 is 60%, and drops to less than 40% by redshift unity, a value that seems to remain relatively constant in clusters up to z∼1.4. In contrast, field galaxy samples display higher values than the cluster galaxies at similar redshifts (e.g $f_{j,z\sim1} \approx f_{j,z\sim2} \approx 50\%$). We suggest that these lower ratios are a consequence of the higher abundance of interactions in the cluster environment than in field, and propose several mechanisms (suppression of outflows, tidal interactions, ram-pressure stripping and mergers) to explain this behaviour. Although numerical simulations have shown that mergers are good candidates to decrease the stellar specific angular momentum (Lagos et al. 2018), only major and, to a lesser degree, minor dry mergers are efficient enough to explain this difference. We rule out the former due to the catastrophic consequences that this kind of events would have for the disc structure and the impossibility of reconstructing it in the cluster environment Therefore, minor dry mergers and other unexplored (in terms of angular momentum) cluster-specific interactions may be responsible for these offsets.
4. Our analysis of the evolution of specific angular momentum with time yielded different trends for galaxies in the field and cluster environments. The ΛCDM model predicts a redshift evolution of specific angular momentum in the following form: $j_* \propto M_*^{2/3}(1+z)^{-1/2}$ (Mo et al. 1998, Obreschkow et al. 2015). We normalized the zero point of these tracks by re-analyzing the angular momentum contribution of the disc z∼0 galaxies studied in Fall & Romanowsky (2018) and Posti et al. (2018). The mean values for the field samples analyzed in this study follow the predicted trend up to z∼2.5, although displaying significant scatter (see Fig. 6). However, cluster samples deviate from such a trend, specially at z>1, falling onto a path described by $j_* \propto M_*^{2/3}(1+z)^{-1}$. This difference suggests that the effects of the cluster environment with regard to angular momentum are in place as early as z∼1.4 in virialized structures, although given the small number statistics of our high redshift samples it is still unclear which specific mechanism is responsible for the reported differences between the cluster and field population of disk galaxies. The study of galaxies populating clusters during their assembly may shed light to the nature and importance of these mechanism in the future.

The search for environmental effects and their relative importance on the physical parameters of the galaxy populations have been a subject of debate during the last forty years (Dressler 1980). Scaling relations provide us a way to explore these effects from different perspectives, and the upcome of large surveys in the field at intermediate to high redshift, together with new high precision numerical simulations, give us the perfect tools to establish reliable comparisons. However, it is still necessary to increase the number statistics of the cluster samples in the same redshift range, and to study their most important parameters in a

comprehensive way (i.e. rotation velocity, size, stellar-mass and populations, metallicity, etc) to fully understand the possible environmental effects at play. The use of multiobject IFU observations and cluster-focused new surveys will be of key importance to disentangle the influence of different cluster-specific interactions over the physical properties of galaxies in the next decade.

Acknowledgements. Based on observations made with the Gran Telescopio Canarias (GTC), instaled in the Spanish Observatorio del Roque de los Muchachos of the Instituto de Astrofísica de Canarias, in the island of La Palma. This paper is also based on data collected at the Subaru Telescope and retrieved from the HSC data archive system, which is operated by Subaru Telescope and Astronomy Data Center at National Astronomical Observatory of Japan. The HSC Data analysis was in part carried out with the cooperation of Center for Computational Astrophysics, National Astronomical Observatory of Japan. J.M.P. acknowledges the funding support from the University of Vienna and the Marietta Blau Grant, financed by the Austrian Science Ministry, as well as the support from the Instituto de Astrofísica de Canarias for allowing him to develop his research in their headquarters at the Canary Islands, Spain. H.D. acknowledges financial support from the Spanish Ministry of Science, Innovation and Universities (MICIU) under the 2014 Ramón y Cajal program RYC-2014-15686 and AYA2017-84061-P, the latter one co-financed by FEDER (European Regional Development Funds). This work has been also supported by Dirección General de Investigación Científica y Técnica (DGICYT) grant AYA2016-79724-C4-1-P.

References

Aihara, H., AlSayyad, Y., Ando, M., et al. 2019, arXiv e-prints, arXiv:1905.12221
Aihara, H., Arimoto, N., Armstrong, R., et al. 2018, PASJ, 70, S4
Arnouts, S. & Ilbert, O. 2011, Astrophysics Source Code Library [ascl:1108.009]
Ascaso, B., Lemaux, B. C., Lubin, L. M., et al. 2014, MNRAS, 442, 589
Bamford, S. P., Milvang-Jensen, B., Aragón-Salamanca, A., & Simard, L. 2005, MNRAS, 361, 109
Behroozi, P. S., Conroy, C., & Wechsler, R. H. 2010, ApJ, 717, 379
Böhm, A. & Ziegler, B. L. 2016, A&A, 592, A64
Böhm, A., Ziegler, B. L., Perez-Martinez, J. M., et al. 2019, arXiv e-prints, arXiv:1903.10016
Böhm, A., Ziegler, B. L., Saglia, R. P., et al. 2004, A&A, 420, 97
Bösch, B., Böhm, A., Wolf, C., et al. 2013a, A&A, 549, A142
Bösch, B., Böhm, A., Wolf, C., et al. 2013b, A&A, 554, A97
Bruzual, G. & Charlot, S. 2003, MNRAS, 344, 1000
Bryan, S. E., Kay, S. T., Duffy, A. R., et al. 2013, MNRAS, 429, 3316
Burkert, A., Förster Schreiber, N. M., Genzel, R., et al. 2016, ApJ, 826, 214
Calzetti, D., Armus, L., Bohlin, R. C., et al. 2000, ApJ, 533, 682
Chabrier, G. 2003, PASP, 115, 763
Contini, T., Epinat, B., Bouché, N., et al. 2016, A&A, 591, A49
Courteau, S. 1997, AJ, 114, 2402
Courteau, S., Dutton, A. A., van den Bosch, F. C., et al. 2007, ApJ, 671, 203
Crawford, S. M., Wirth, G. D., & Bershady, M. A. 2014, ApJ, 786, 30
Crawford, S. M., Wirth, G. D., Bershady, M. A., & Rand riamampandry, S. M. 2016, ApJ, 817, 87
Dekel, A., Sari, R., & Ceverino, D. 2009, ApJ, 703, 785
Di Teodoro, E. M., Fraternali, F., & Miller, S. H. 2016, A&A, 594, A77
Dressler, A. 1980, ApJ, 236, 351
Dutton, A. A., Conroy, C., van den Bosch, F. C., Prada, F., & More, S. 2010, MNRAS, 407, 2
Dutton, A. A., van den Bosch, F. C., Faber, S. M., et al. 2011, MNRAS, 410, 1660
Fall, S. M. 1983, in IAU Symposium, Vol. 100, Internal Kinematics and Dynamics of Galaxies, ed. E. Athanassoula, 391–398
Fall, S. M. & Romanowsky, A. J. 2013, ApJ, 769, L26
Fall, S. M. & Romanowsky, A. J. 2018, ApJ, 868, 133
Förster Schreiber, N. M., Renzini, A., Mancini, C., et al. 2018, ApJS, 238, 21
Gal, R. R., Lemaux, B. C., Lubin, L. M., Kocevski, D., & Squires, G. K. 2008, ApJ, 684, 933
Gal, R. R. & Lubin, L. M. 2004, ApJ, 607, L1
Giovanelli, R., Haynes, M. P., Salzer, J. J., et al. 1995, AJ, 110, 1059
Gómez-González, V. M. A., Mayya, Y. D., & Rosa-González, D. 2016, MNRAS, 460, 1555
Gray, M. E., Wolf, C., Barden, M., et al. 2009, MNRAS, 393, 1275
Gunn, J. E., Hoessel, J. G., & Oke, J. B. 1986, ApJ, 306, 30
Hall, M., Courteau, S., Dutton, A. A., McDonald, M., & Zhu, Y. 2012, MNRAS, 425, 2741
Harrison, C. M., Johnson, H. L., Swinbank, A. M., et al. 2017, MNRAS, 467, 1965
Hayashi, M., Koyama, Y., Kodama, T., et al. 2019, arXiv e-prints, arXiv:1905.13437
Hayashi, M., Tadaki, K.-i., Kodama, T., et al. 2018a, ApJ, 856, 118
Hayashi, M., Tanaka, M., Shimakawa, R., et al. 2018b, PASJ, 70, S17
Haynes, M. P., Giovanelli, R., Chamaraux, P., et al. 1999, AJ, 117, 2039
Heidmann, J., Heidmann, N., & de Vaucouleurs, G. 1972, MmRAS, 75, 85
Heidt, J., Appenzeller, I., Gabasch, A., et al. 2003, A&A, 398, 49
Hoyle, F. 1951, in Problems of Cosmical Aerodynamics, 195
Ilbert, O., Arnouts, S., McCracken, H. J., et al. 2006, A&A, 457, 841
Jaffé, Y. L., Aragón-Salamanca, A., Kuntschner, H., et al. 2011, MNRAS, 417, 1996
Kassin, S. A., Weiner, B. J., Faber, S. M., et al. 2007, ApJ, 660, L35
Kelvin, L. S., Driver, S. P., Robotham, A. S. G., et al. 2012, MNRAS, 421, 1007
Koda, J., Sofue, Y., & Wada, K. 2000, ApJ, 531, L17
Komatsu, E., Smith, K. M., Dunkley, J., et al. 2011, ApJS, 192, 18
Lagos, C. d. P., Stevens, A. R. H., Bower, R. G., et al. 2018, MNRAS, 473, 4956
Lagos, C. d. P., Theuns, T., Stevens, A. R. H., et al. 2017, MNRAS, 464, 3850
Lapi, A., Salucci, P., & Danese, L. 2018, ApJ, 859, 2
Lawrence, A., Warren, S. J., Almaini, O., et al. 2007, MNRAS, 379, 1599
Lelli, F., McGaugh, S. S., & Schombert, J. M. 2016, AJ, 152, 157
Lemaux, B. C., Gal, R. R., Lubin, L. M., et al. 2012, ApJ, 745, 106
Macciò, A. V., Dutton, A. A., & van den Bosch, F. C. 2008, MNRAS, 391, 1940
Macciò, A. V., Dutton, A. A., van den Bosch, F. C., et al. 2007, MNRAS, 378, 55
Metcalfe, N., Shanks, T., Campos, A., McCracken, H. J., & Fong, R. 2001, MNRAS, 323, 795
Meurer, G. R., Obreschkow, D., Wong, O. I., et al. 2018, MNRAS, 476, 1624
Miller, S. H., Bundy, K., Sullivan, M., Ellis, R. S., & Treu, T. 2011, ApJ, 741, 115
Mo, H. J., Mao, S., & White, S. D. M. 1998, MNRAS, 295, 319
Molina, J., Ibar, E., Swinbank, A. M., et al. 2017, MNRAS, 466, 892
Moran, S. M., Miller, N., Treu, T., Ellis, R. S., & Smith, G. P. 2007, ApJ, 659, 1138
Mullis, C. R., Rosati, P., Lamer, G., et al. 2005, ApJ, 623, L85
Navarro, J. F., Frenk, C. S., & White, S. D. M. 1997, ApJ, 490, 493
Navarro, J. F. & Steinmetz, M. 2000, ApJ, 538, 477
Noble, A. G., McDonald, M., Muzzin, A., et al. 2017, ApJ, 842, L21
Noble, A. G., Muzzin, A., McDonald, M., et al. 2019, ApJ, 870, 56
Obreschkow, D. & Glazebrook, K. 2014, ApJ, 784, 26
Obreschkow, D., Glazebrook, K., Bassett, R., et al. 2015, ApJ, 815, 97
Peebles, P. J. E. 1969, ApJ, 155, 393
Pelliccia, D., Lemaux, B. C., Tomczak, A. R., et al. 2019, MNRAS, 482, 3514
Pelliccia, D., Tresse, L., Epinat, B., et al. 2017, A&A, 599, A25
Peng, C. Y., Ho, L. C., Impey, C. D., & Rix, H.-W. 2002, AJ, 124, 266
Pérez-Martínez, J. M., Ziegler, B., Verdugo, M., Böhm, A., & Tanaka, M. 2017, A&A, 605, A127
Posti, L., Fraternali, F., Di Teodoro, E. M., & Pezzulli, G. 2018, A&A, 612, L6
Postman, M., Lubin, L. M., & Oke, J. B. 2001, AJ, 122, 1125
Price, S. H., Kriek, M., Shapley, A. E., et al. 2016, ApJ, 819, 80
Puech, M., Flores, H., Hammer, F., et al. 2008, A&A, 484, 173
Romanowsky, A. J. & Fall, S. M. 2012, ApJS, 203, 17
Rosati, P., Tozzi, P., Gobat, R., et al. 2009, A&A, 508, 583
Ruggiero, R. 2019, arXiv e-prints, arXiv:1902.05363
Ruggiero, R. & Lima Neto, G. B. 2017, MNRAS, 468, 4107
Schindler, S., Guzzo, L., Ebeling, H., et al. 1995, A&A, 299, L9
Simons, R. C., Kassin, S. A., Trump, J. R., et al. 2016, ApJ, 830, 14
Stott, J. P., Swinbank, A. M., Johnson, H. L., et al. 2016, MNRAS, 457, 1888
Straatman, C. M. S., Glazebrook, K., Kacprzak, G. G., et al. 2017, ApJ, 839, 57
Strazzullo, V., Rosati, P., Pannella, M., et al. 2010, A&A, 524, A17
Tiley, A. L., Stott, J. P., Swinbank, A. M., et al. 2016, MNRAS, 460, 103
Tomczak, A. R., Lemaux, B. C., Lubin, L. M., et al. 2019, MNRAS, 484, 4695
Tully, R. B. & Fisher, J. R. 1977, A&A, 54, 661
Tully, R. B., Pierce, M. J., Huang, J.-S., et al. 1998, AJ, 115, 2264
Übler, H., Förster Schreiber, N. M., Genzel, R., et al. 2017, ApJ, 842, 121
van den Bosch, F. C. 2000, ApJ, 530, 177
van der Wel, A., Franx, M., van Dokkum, P. G., et al. 2014, ApJ, 788, 28
Verdugo, M., Lerchster, M., Böhringer, H., et al. 2012, MNRAS, 421, 1949
Ziegler, B. L., Böhm, A., Fricke, K. J., et al. 2002, ApJ, 564, L69

Appendix A: Additional material

Table A.1: General properties of the CL1604 galaxy sample. IDs, redshift, B-band absolute magnitudes in the AB system before dust extinction, extinction in B-band, effective radius in the z-band, logarithmic stellar mass, maximun rotation velocity

ID	z	M_B (mag)	A_B (mag)	R_e (kpc)	$\log M_*$	V_{max} (km/s)
G1	0.9228	-20.88	-0.44	3.83	10.63	144.7±16.8
G2	0.9132	-20.70	-0.52	4.12	9.99	177.8±14.3
G3	0.9183	-21.04	-0.58	4.86	10.65	212.8±19.2
G4	0.8815	-21.16	-0.28	2.55	10.28	97.2±16.0
G5	0.8953	-22.30	-0.17	4.84	10.85	291.2±20.5
G6	0.9047	-21.69	-0.53	6.25	10.99	275.9±21.9
G7	0.9005	-19.04	-0.69	8.17	10.70	149.0±14.2
G8	0.8945	-20.93	-0.20	6.02	10.27	133.7±15.8

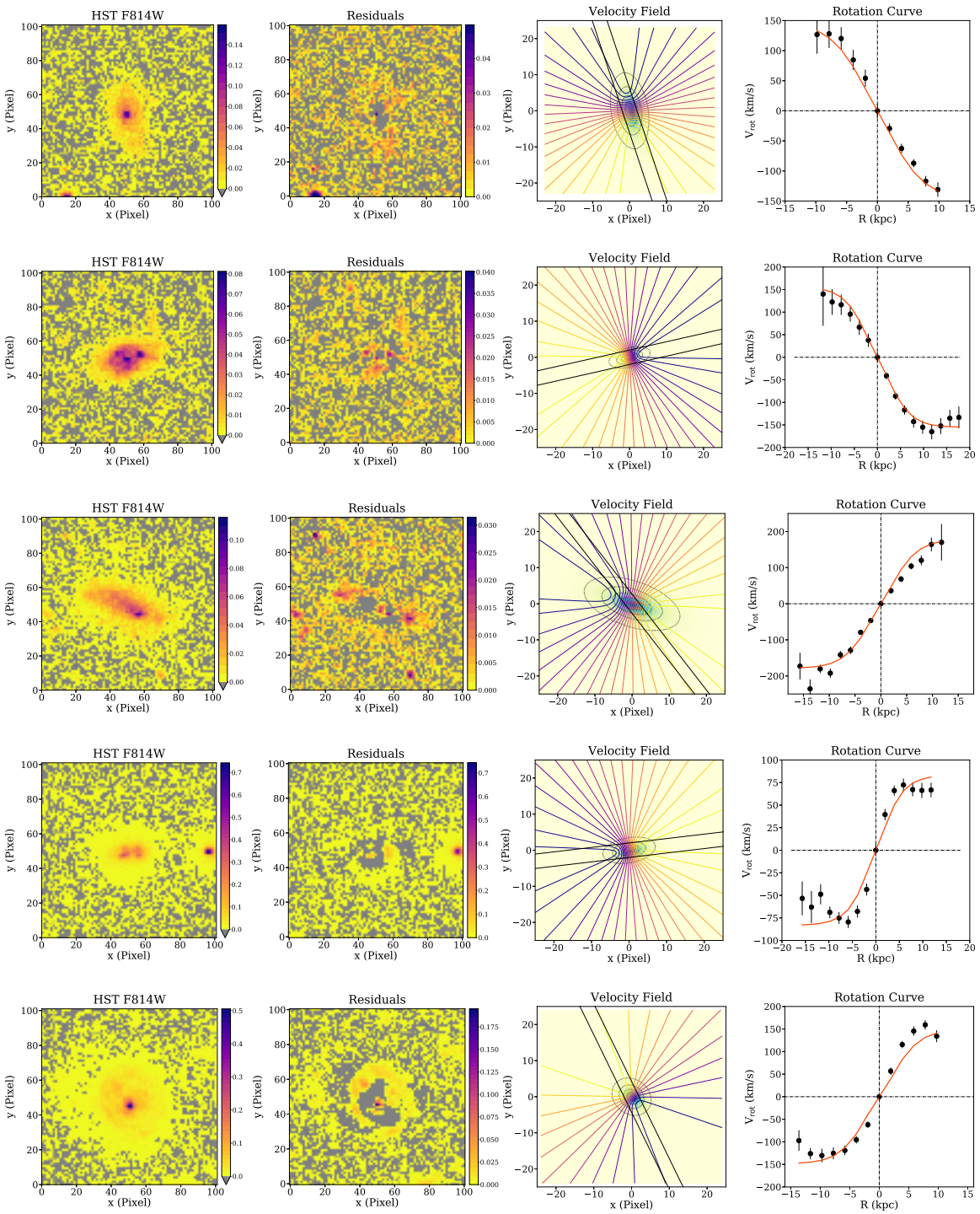

Fig. A.1: The CL1604 sample of galaxies introduced in Sect. 3 and presented in the same order as in Table A.1. The first and second columns respectively show the original HST-F814W or HSC-z-band images centered on the targets and their residuals after subtracting the 2D model of the galaxies. Note that the pixel scale in the first column corresponds to 0.05"/pix for HST images and 0.2"/pix for HSC images. The third column presents the synthetic velocity field after fitting the simulated rotation curve to the observed curve (assuming the pixel scale of OSIRIS, i.e. 0.25"/pix). The black solid parallel lines depict the edges of the slit. The fourth column displays the observed (black dots) and modelled (red line) rotation curve.

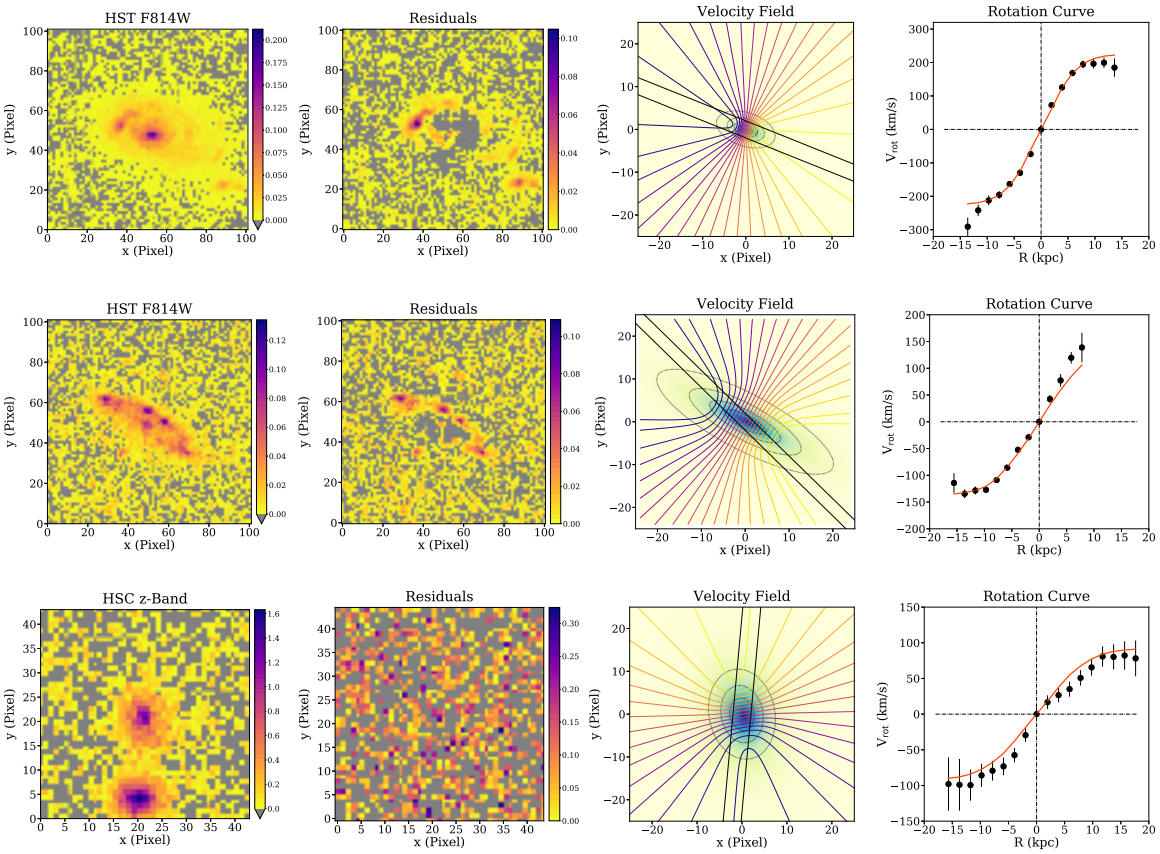

Fig. A.1: (Continued)

Chapter 5

Additional Publications: Paper IV

Title: Kinematics of disk galaxies in clusters at z=1.5

Authors: A. Böhm, B. L. Ziegler, J. M. Pérez-Martínez, T. Kodama, M. Hayashi, C. Maier, M. Verdugo, Y. Koyama

Year: 2019

Journal: Astronomy and Astrophysics. Submitted on March 24th 2019.

Short Description: In this work we examine the kinematics of star-forming galaxies in young clusters at z$\sim$1.5. The HyperSuprimeCam Subaru Strategic Program (HSC-SSP) carried out a [OII] narrow-band survey looking for overdensities dominated by star-forming galaxies at this redshift. We select our objects from two of these overdensities and analyze their kinematical behaviour using H_α integrated field spectroscopy from KMOS/VLT. As a result, we obtained 36 velocity fields, with 14 of them displaying regular rotation. We analyze the position of these regular rotating disks in the Tully-Fisher diagram in connection to their star-formation rate and their gas velocity dispersion. In addition, we used the redshift and spatial distribution of our targets to estimate the total mass of these two young clusters. Finally, we measure the structural asymmetries of the gas and stellar component of our galaxies and analyze these results in the context of galaxy evolution in clusters in formation.

Personal Contribution: I was responsible for the target selection and

phase 2 design of the observations. I determined the cluster membership of our targets by measuring their redshift as well as I had a prominent role in the discussion of the results.

Astronomy & Astrophysics manuscript no. boehmetal2019_subm
March 24, 2019

Kinematics of disk galaxies in clusters at $z = 1.5$ ⋆

A. Böhm[1], B. L. Ziegler[1], J. M. Pérez-Martínez[1], T. Kodama[2], M. Hayashi[3], C. Maier[1], M. Verdugo[1], Y. Koyama[4,5]

[1] Institute for Astronomy (IfA), University of Vienna, Türkenschanzstrasse 17, 1180 Vienna, Austria e-mail: asmus.boehm@univie.ac.at
[2] Astronomical Institute, Tohoku University, Aramaki, Aoba-ku, Sendai 980-8578, Japan
[3] National Astronomical Observatory of Japan, Osawa, Mitaka, Tokyo 181-8588, Japan
[4] Subaru Telescope, National Astronomical Observatory of Japan, 650 North A'ohoku Place, Hilo, HI 96720, USA
[5] Department of Astronomical Science, SOKENDAI (The Graduate University for Advanced Studies), Mitaka, Tokyo 181-8588, Japan

Received 24 Mar 2019

ABSTRACT

Aims. While many aspects of the impact of dense environments on late-type galaxies at redshifts below unity have been scrutinized in the past decades, observational studies of the interplay between environment and disk galaxy evolution at $z > 1$ are still scarce. We observed star-forming galaxies at $z \approx 1.5$ selected from the HyperSuprimeCam Subaru Strategic Program. The galaxies are part of two significant overdensities of [O II] emitters identified via narrow-band imaging and photometric redshifts from *grizy* photometry.
Methods. We used VLT/KMOS to carry out Hα integral field spectroscopy of 46 galaxies in total. Ionized gas maps, star formation rates and velocity fields were derived from the Hα emission line. We quantified morphological and kinematical asymmetries to test for potential gravitational (e.g. galaxy-galaxy) or hydrodynamical (e.g. ram-pressure) interactions.
Results. Hα emission was detected in 36 of our targets. 34 of the galaxies are members of two clusters at $z = 1.47$, confirming our selection strategy to be highly efficient. Two galaxies are field objects at slightly lower redshifts. By fitting model velocity fields to the observed ones, we determined the intrinsic maximum rotation velocity $V_{\rm max}$ of 14 galaxies. Utilizing the luminosity-velocity (Tully-Fisher) relation, we find that these galaxies are more luminous than their local counterparts of similar mass by up to several magnitudes in the rest-frame *B*-band. In contrast to field galaxies at $z < 1$, the offsets of the $z \approx 1.5$ cluster galaxies from the local Tully-Fisher relation are not correlated with their star formation rates but with the ratio between $V_{\rm max}$ and gas velocity dispersion $\sigma_{\rm g}$. This probably reflects that, as is observed in the field at similar redshifts, fewer disks have settled to purely rotational kinematics and high $V_{\rm max}/\sigma_{\rm g}$ ratios. The distributions in morphological and kinematical asymmetries hint that either the two clusters under scrutiny do not have a dense intra-cluster medium yet, or galaxy-galaxy interactions are frequent, making it difficult to identify cases of purely hydrodynamical interactions between the intra-cluster and interstellar medium.

Key words. galaxies: spiral – galaxies: evolution – galaxies: kinematics and dynamics – galaxies: high-redshift

1. Introduction

The evolution of galaxies is affected by their environment in various ways. Observations show that the galaxy population in clusters has changed substantially during the past 5-6 Gyr, with the fraction of spirals decreasing and the fraction of lenticulars (but also dwarf ellipticals) increasing towards $z \approx 0$ (e.g. Desai et al. 2007). Galaxies in dense regions on average have redder colors (e.g. Blanton et al. 2005) and are less frequently star-forming (e.g. Verdugo et al. 2008) than in the field. In the cluster environment, galaxies are subject to a plethora of interaction processes, such as harassment (e.g. Moore et al. 1996), ram-pressure stripping (RPS, e.g. Kronberger et al. 2008), or strangulation (e.g. Balogh et al. 2000). The latter two refer to the impact of the hot intra-cluster medium (ICM) on the interstellar medium of a galaxy moving within a cluster. While strangulation occurs when only the gaseous halo of a galaxy is removed, followed by a phase of gas consumption via star formation on a time scale of Gyrs, RPS affects also the cold gas disk and can quench star formation within ~ 0.5 Gyr in extreme cases (e.g. Steinhauser et al. 2016).

As part of the STAGES survey (Gray et al. 2009) of the multiple cluster system A901/902 at $z = 0.17$, we were able to show in Bösch et al. (2013a) that so-called red spirals are probably produced by the impact of ram-pressure stripping. Red spirals, which show weaker spiral arms and a four times lower specific star formation rate than normal, blue spirals, might be an intermediate stage in the transformation of blue field spirals into cluster S0s. Red spirals are the dominant population in clusters at intermediate cluster-centric radii and galaxy masses, while they are almost absent in the field at $z \approx 0.2$ (e.g. Wolf et al. 2009). In Bösch et al. (2013b), we used the Tully-Fisher relation (TFR; Tully & Fisher 1977) — the scaling relation linking the maximum rotation velocity $V_{\rm max}$ of disk galaxies to their luminosity — to confirm that red spirals are in the process of quenching and that the TFR scatter is increasing towards the inner cluster regions. Other studies investigated the mass-size relation, e.g. finding smaller sizes of star-forming galaxies in clusters at $z \approx 0.5$ than in the field (Kuchner et al. 2017).

In the past decades, a large number of studies have utilized the TFR. Using field spirals at $0.1 < z < 1.0$, Böhm & Ziegler (2016) found that, at given $V_{\rm max}$, disk galaxies ~ 8 Gyr ago were brighter by 1.2 mag in rest-frame *B* and smaller by a factor ~ 1.5 than spirals in the present-day universe. Based on

⋆ Based on observations with the European Southern Observatory Very Large Telescope (ESO-VLT), observing run ID 099.B-0644A.

the stellar-mass TFR, Miller et al. (2012) found only a very small evolution of its zero point corresponding to 0.06 dex smaller stellar masses at $z \approx 1.7$ and fixed $V_{\rm max}$. While these two former studies relied on slit spectroscopy, the usage of Integral Field Units like VLT/KMOS has become more common for kinematic studies of distant galaxies. Übler et al. (2017), e.g., found no evolution in the stellar-mass TFR up to $z \approx 2.3$ using KMOS.

For several years, the results on whether the TFR differs between the field and the cluster environment were somewhat heterogeneous. Ziegler et al. (2003) or Nakamura et al. (2008), e.g., did not find differences between the two regimes, while Milvang-Jensen et al. (2003) or Bamford et al. (2005) found that late-type galaxies in dense environments are more luminous than in the field. Other studies, like Moran et al. (2007) deduced that the TFR scatter in clusters is higher than in low-density environments. It became clearer later that one key factor in such kinematical studies is to compare only galaxies with similar properties. Since various cluster-specific interactions can affect the kinematics of cluster disk galaxies, the fraction of disturbed rotation curves or velocity fields is found to be higher in clusters than in the field (e.g. Vogt et al. 2004). This can introduce an environmental dependence of the TFR unless the same criteria are applied to all kinematic data by using only symmetric rotation velocity fields in the TFR analysis (e.g. Bösch et al. 2013b).

Galaxy clusters at high redshifts $z > 1$ show important differences to those at lower redshifts. While galaxies in the central regions of low-redshift clusters mostly are passive, clusters at high-z frequently show strongly star-forming galaxies in their central regions. E.g., Hayashi et al. (2010) found a high number density of [O II] emitters in the core of XMMXCS J2215.9-1738 at $z = 1.46$. Some clusters already at these early cosmic epochs show a well-established intra-cluster medium (ICM) in hydrostatic equilibrium (e.g. IDCS1426+358 at $z = 1.75$, Brodwin et al. 2016). TFR studies in $z > 1$ clusters still are scarce. Based on a small sample of disk galaxies in a $z = 1.4$ cluster, we found a moderate luminosity evolution of high-mass cluster galaxies, while low-mass cluster galaxies where much brighter than their field counterparts at similar redshifts (Pérez-Martínez et al. 2017).

Multiple observations have shown that, even in the absence of interaction processes typical for the cluster regime, disk galaxies become more kinematically hot towards higher redshifts in the sense that the ratio between their gas maximum rotation velocity $V_{\rm max}$ and velocity dispersion $\sigma_{\rm v}$ decreases. The settling of disks, i.e. $V_{\rm max}/\sigma_{\rm v}$ ratios above a certain threshold, occurs at earlier cosmic epochs for disks of higher mass (e.g. Kassin et al. 2012). As Simons et al. (2016) have found at redshifts $z \approx 2$, this behavior is also reflected in the stellar-mass TFR, where galaxies with low $V_{\rm max}/\sigma_{\rm v}$ ratios tend to show too slow rotation for their stellar mass.

In this paper, we aim to shed light onto the impact of dense environments on the kinematic evolution of disk galaxies nine Gyr ago. The paper is organized as follows: In Sect. 2 we outline the target selection and observations, Sect. 3 briefly describes the data reduction, in Sect. 4 we detail all steps of the analysis, Sect. 5 comprises a discussion and Sect. 6 summarizes our main results.

In the following, we assume a flat concordance cosmology with $\Omega_\Lambda = 0.7$, $\Omega_m = 0.3$ and $H_0 = 70\,{\rm km\,s^{-1}\,Mpc^{-1}}$. All magnitudes are given in the Vega system.

2. Target Selection and Observations

Our target selection relied on the HyperSuprime-Cam Subaru Strategic Program (HSC-SSP, see Aihara et al. 2018). The HSC (Miyazaki et al. 2018, Komiyama et al. 2018, Kawanomoto et al. 2018, Furusawa et al. 2018) is an optical imaging camera operated at the prime focus of Subaru that, with a diameter of 1.5°, features the largest field-of-view of all 10 m-class telescopes. HSC offers five broad-band filters, *g*, *r*, *i*, *z*, *y*, and several narrow-band filters of which the filter NB921 probes the 3727 Å [O II] emission line doublet of galaxies at a redshift $z \approx 1.5$ (Hayashi et al. 2018). The HSC-SSP spans a total of 300 nights at Subaru over 5-6 years. The first data release took place 1.7 years into the survey; it is described in Aihara et al. (2018).

The two target clusters for our spectroscopic follow-up, which we will refer to as HSC-CL2329 and HSC-CL2330 in the following, were identified as strong overdensities (with a significance of $5.7\,\sigma$ and $7.2\,\sigma$, resp.) of [O II] emitters at $z = 1.47$ using the narrow-band filter NB921. Galaxy clusters at these redshifts often show star-forming galaxies in their central regions, while they are preferentially located between intermediate cluster-centric radii and the outskirts of *local* clusters (Dressler 1980). Since HSC-SSP also comprises photometric redshifts (derived via various methods, including SED fitting, machine learning, etc., see Tanaka et al. 2018), we could rule out any contamination by other emission lines, e.g. Hα or [O III], from galaxies at different redshifts. This was later confirmed by the spectroscopic redshift distribution of our sample (see Sect. 4). Since the width of the NB921 filter corresponds to a redshift range of $z = 1.471 \pm 0.018$, or a velocity width of ± 2200 km/s, we were expecting that i) the majority of the [O II] emitters are physically associated cluster members and ii) the cluster sample will be nearly complete within the covered field-of-view, given that the typical velocity dispersion of rich clusters is 1000 km/s.

The K-band Multi Object Spectrograph (KMOS) is a second-generation VLT instrument capable of observing 24 science targets simultaneously in the near-infrared. Each of the individual IFUs offers a field-of-view of $2.8 \times 2.8\,{\rm arcsec}^2$ (with spaxels sizes of 0.2 arcsec) and can be placed within a patrol field of 7.2 arcmin diameter. In the *H*-band, which we chose for our observations, the typical spectral resolution of KMOS is $R \approx 4000$.

We selected our target galaxies to have Hα fluxes $f_{\rm H\alpha} > 6 \times 10^{-17}\,{\rm erg\,s^{-1}\,cm^{-2}}$. Predicted H$\alpha$ fluxes were converted from the observed [O II] fluxes following Kennicutt (1998) assuming the Hα fluxes to be on average a factor of two larger than the [O II] fluxes. The KMOS *H*-band observations were carried out between June and September 2017 with a stare / nod-to-sky strategy. Each Observation Block consisted of an ABA ABA sequence, where "A" denotes that the IFUs were placed on the science targets, and "B" indicates that the IFUs were observing blank sky. The integration time of each exposure was 480 s, the total integration time per cluster was ~ 2.1 h and the total observing time per cluster, including overheads, was four hours. Seeing conditions measured in the optical with the DIMM seeing monitor ranged between 0.7 and 1.0 arcsec for cluster HSC-CL2330, which was executed first, and between 0.5 and 1.2 arcsec for cluster HSC-CL2329. Note that the seeing FWHM in the *H*-band used for the KMOS spectroscopy is considerably smaller, with a median around 0.3 arcsec.

3. Data Reduction

The data reduction was carried out with the official ESO-KMOS pipeline version 1.4.3. We conducted a range of tests as to whether the default settings of the pipeline can be improved. In these tests, we aimed to optimize the S/N in the continuum close to the Hα line and in the Hα line itself, and to minimize night-sky OH residuals mainly ± 200 Å of Hα. We decided to deviate from the default reduction settings in two respects.

Firstly, we detected significant offsets between the IFU object positions from the individual Observation Blocks (OBs) of cluster HSC-CL2329, typically only 1-2 pixels but in three cases as large as four pixels (0.8 arcsec). Although these offsets do not compromise the spatial coverage of our targets, they are much larger than expected based on the IFU-positioning accuracy. They probably are related to a re-calibration of the IFU positioning system during the observation epoch of HSC-CL2329 (M. Hilker, priv. comm.). We accounted for these offsets during the co-addition of the individual exposures.

Secondly, the best data quality in the co-addition of individual exposures is achieved using sigma clipping. The default setting of the pipeline is to first combine exposures from within a single OB before then combining these OBs into final data cubes. The sigma clipping is, however, much more effective when the number of frames used for the final co-addition is maximized, so we modified the default approach and ran the sigma clipping and cube combination on all exposures from all OBs in one go.

After some further tests, we disregarded the two OBs with the worst seeing of around one arcsec FWHM in the final data cube combination in both clusters; i.e. one OB was rejected for each cluster. Due to this, the average DIMM seeing was 0.7 arcsec FWHM for HSC-CL2330 and 0.5 arcsec FWHM for HSC-CL2329, and the total time on target 5760 s for all galaxies.

4. Analysis

We detected Hα in 36 out of 46 targets. Only two galaxies are foreground objects probably not physically associated with the clusters. Our combined narrow-band/photo-z selection strategy thus was confirmed as highly efficient. The redshift distributions and sky positions of our sample are shown in Fig. 1. Given that the projected separation of the two clusters is approx. 19 Mpc, their z-distributions are remarkably similar with peaks at $z \approx 1.46$ and $z \approx 1.475$. This probably hints to Large Scale Structure that both clusters are part of. The gap in the redshift distribution of both clusters (corresponding to $\sim$ 16200 Å) is very unlikely to be due to problems with strong night-sky residuals. Three strong OH lines are located in the vicinity of $z \approx 1.47$ Hα emission: at 16129 Å, 16195 Å, and 16235 Å, with the first and last one being much stronger than the middle one. Among the galaxies with determined redshifts, we have six cases each where the Hα line profile was affected by residuals of the line at 16129 Å or 16235 Å, but no spectra where Hα is affected by the OH line at 16195 Å. The gap in the z-distribution of both clusters hence most probably is physical.

12 of the Hα detections are weak and extend over only a few spaxels in the data cubes. These data only allow to determine the redshift. In the remaining 24 detections, the Hα emission was more spatially extended so that we could use them to extract velocity fields (VFs).

Hα luminosities were transformed into star formation rates (SFRs) following Kennicutt (1998). Since the only prominent emission feature in the data is the Hα line (+ [N II]), the extinction coefficient could not be determined from a traditional source like the Balmer decrement. Instead, we used chemical enrichment models from Ferreras et al. (2014) to determine the mass- and disk inclination-dependent $E(B-V)$ extinction. This was then converted into the A(Hα) extinction coefficient following Ly et al. (2012). In Fig. 2, the SFRs computed from Hα are compared to the [O II]-based ones derived from the NB photometry following Gilbank et al. (2010). We find a good agreement between the two (with a scatter of ~ 0.31 dex), even for cases where the Hα line is affected by night sky residuals.

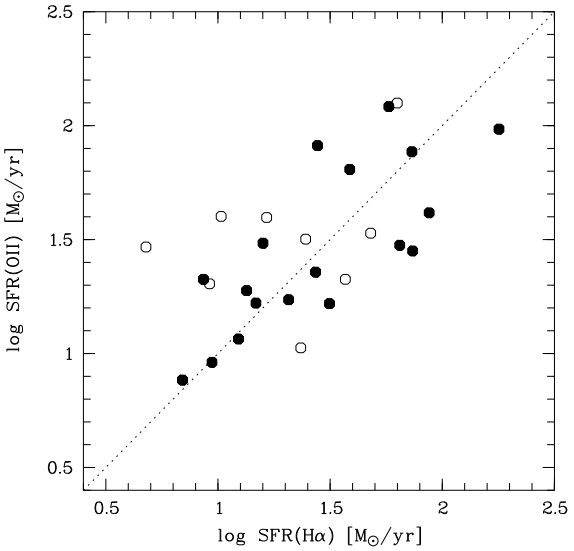

Fig. 2. Comparison between the star formation rates from [O II] fluxes estimated with HSC SSP NB imaging and the new, Hα-based SFRs from the KMOS data. Open symbols depict objects for which the Hα line was affected by night sky residuals, which could lead to underestimated SFRs; however, there is no clear indication for this.

For the determination of the intrinsic maximum rotation velocity $V_{\rm max}$, synthetic VFs were created based on gas disk inclination, kinematic center, kinematic position angle, turnover radius and maximum rotation velocity for a given galaxy. Intrinsically, the rotation velocity is assumed to rise linearly with radius and turn over into a regime of constant rotation velocity $V_{\rm max}$ at a turnover radius $r_{\rm t}$ that is linked to the stellar disk scale length $r_{\rm d}$ via $r_{\rm t} = 2.2\,r_{\rm d}$. The synthetic VFs take into account blurring due to seeing during spectroscopy. The optical DIMM seeing monitor values were transformed into the corresponding H-band values following prescriptions provided by ESO. For our data, the H-band seeing ranged from 0.25 to 0.3 arcsec. The VF models also account for beam smearing stemming from the finite pixel size of 0.2 arcsec.

VFs covering several ten spaxels allow to use all parameters listed above as free fitting parameters. For the VFs with the smallest number of information elements, however, $V_{\rm max}$ is the only free parameter, while all other parameters were determined from the i-band imaging with the GALFIT package (Peng et al. 2002). As a cross-check, we used the output of Source Extractor (Bertin & Arnouts 1996). We used the best-seeing HSC-SSP images available for this, which are i-band frames with a total integration time of 30 min and a FWHM of 0.7 arcsec.

Our $V_{\rm max}$ derivation algorithm does not perform a Levenberg-Marquard minimization nor uses the Monte Carlo

A&A proofs: manuscript no. boehmetal2019_subm

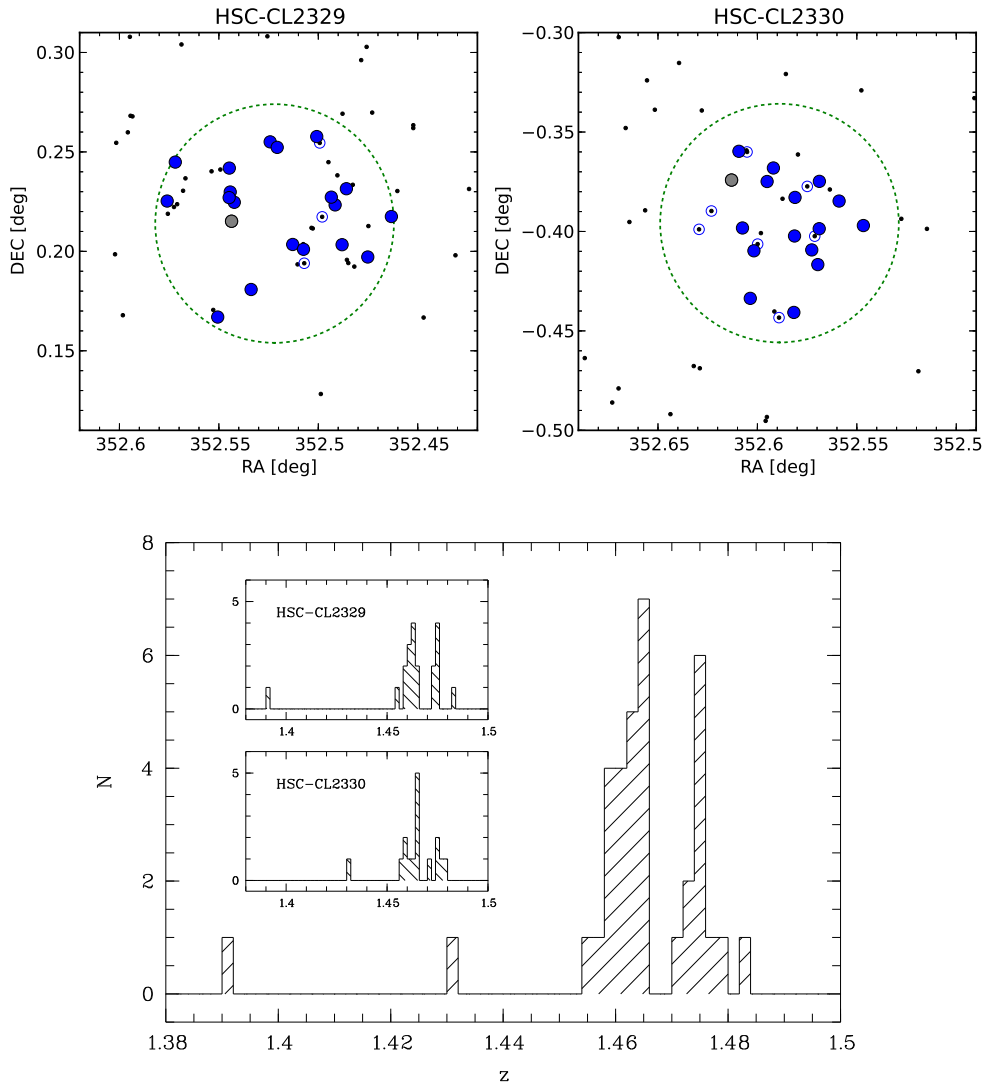

Fig. 1. *Top:* Spatial distribution of our target candidates (small dots), galaxies without Hα detections (open circles), and Hα-detected galaxies (filled circles) for the two observed clusters. The large dotted circle in both plots denotes the available KMOS patrol field with a diameter of 7.2 arcmin or ~ 3.7 Mpc at the clusters' redshifts. *Bottom:* Redshift distribution of all 36 Hα detections for both clusters combined (large plot) and for the two clusters individually (inset graphs). Only two field galaxies are found (shown as grey filled circles in the upper panel), demonstrating the efficiency of the target selection. Both cluster reside at a redshift $z = 1.47$, which we aimed for by selecting overdensities of [O II] emitters at $z \approx 1.5$ with combined broad- and narrow-band data. Interestingly, the two clusters show similar sub-structure in redshift space.

Markov Chain approach but probes the entire parameter space. This is computationally expensive but avoids running into any local χ^2 minima. 14 velocity fields yielded a robust value for $V_{\rm max}$, while the remaining 10 VFs could not be properly fitted due to insufficient extent, strong perturbations or a total lack of a velocity gradient. All these 14 galaxies stem from the two clusters; neither of the two foreground field galaxies yielded a $V_{\rm max}$. Four examples of observed and model VFs, along with *i*-band images and Hα maps, are shown in Fig. 3.

Rest-frame absolute *B*-band magnitudes were computed from the apparent magnitudes in the *y*-filter which, among the available HSC-SSP filters, best probes the rest-frame *B*-band at the redshifts of the KMOS targets. The *k*-corrections for the transformation $y \rightarrow B$ were derived via synthetic photometry. Intrinsic absorption was taken into account using the inclination- and $V_{\rm max}$-dependent prescription from Tully et al. (1998). We also use this work as a local comparison sample to ensure consistency. The *B*-band Tully-Fisher diagram, comprising the $z = 1.47$ cluster galaxies, $z < 1$ field spirals, and the local TFR is shown in Fig. 4.

Note that the stellar-mass TFR is not part of the scope of this paper. The currently available photometry of the HSC-SSP is comprising filters that probe only up to rest-frame wavelengths $\lambda \approx 4300$ Å for galaxies at $z = 1.47$. Stellar mass determinations

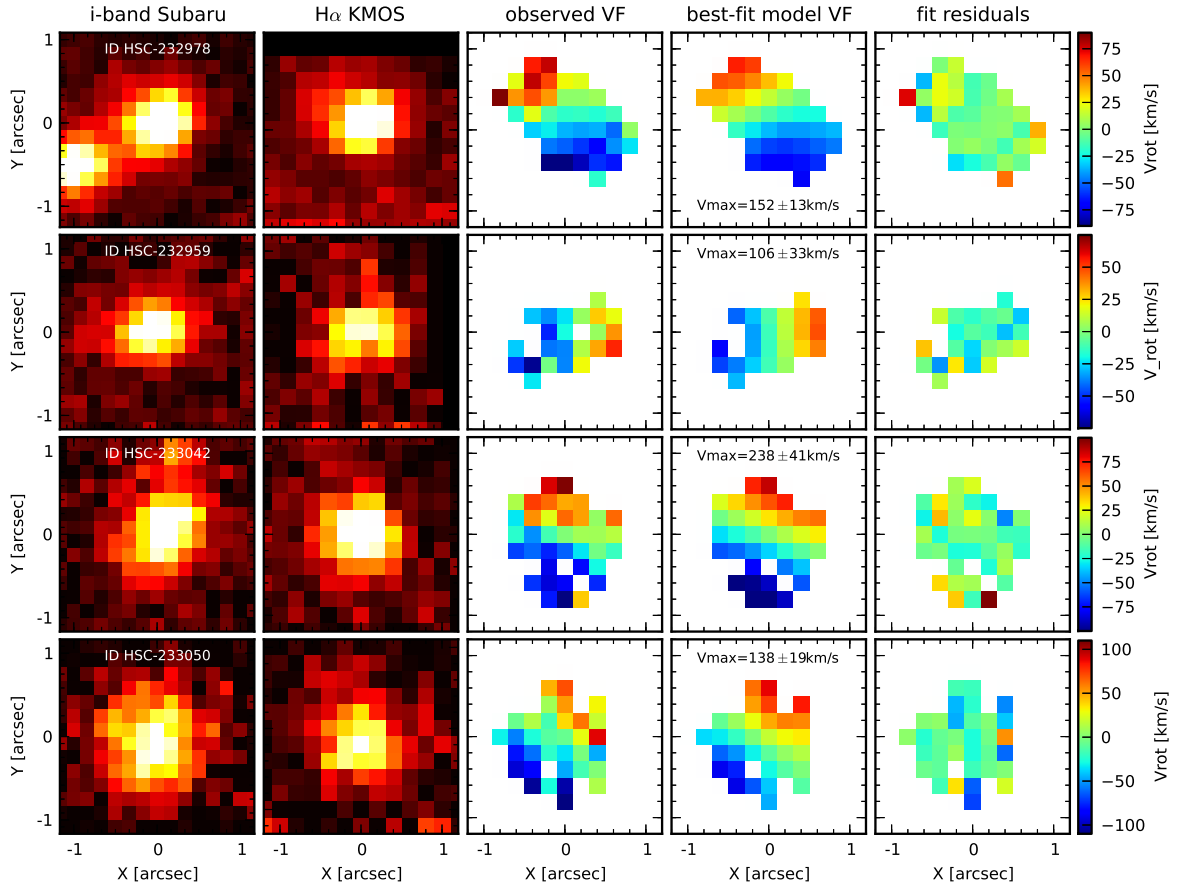

Fig. 3. Four examples of $z \approx 1.47$ cluster galaxies for which the maximum rotation velocity $V_{\rm max}$ could be determined. In the each row, the plots show from left to right: best-seeing *i*-band image from the Subaru HSC survey, ionized gas map as observed in Hα with VLT/KMOS, observed rotation velocity field, best-fit model rotation velocity field used for the determination of the intrinsic $V_{\rm max}$, fit residuals after subtracting the best-fit model from the observed velocity field. Note that the galaxy to the southeast of HSC-232978 (top panel, leftmost figure) is a foreground galaxy with a photometric redshift, depending on the method, in the range $0.7 < z_{\rm phot} < 0.8$, undetected in the KMOS data.

based on the UV / blue part of the spectral energy distribution carry very large systematic errors. Without NIR imaging at our disposal, we prefer to restrict our TFR analysis to the *B*-band.

As an additional tool in our kinematic analysis, we use a measure for the velocity field asymmetry $A_{\rm VF}$. To this end, we have extended the formalism used in Bösch et al. (2013a), which is a variation of the formalism presented by Dale et al. (2001). In these analyzes, slit spectroscopy was used and the kinematics were characterized using rotation curves that describe the rotation velocity as a function of radius.

For a given kinematical center and kinematical position angle, we compute $A_{\rm VF}$ via:

$$A_{\rm VF} = \sum_{i=1}^{N} \frac{|v(\mathbf{r}_i) + v(-\mathbf{r}_i)|}{\sqrt{\sigma_v^2(\mathbf{r}_i) + \sigma_v^2(-\mathbf{r}_i)}} \cdot \left[\frac{1}{2} \sum_{i=1}^{N} \frac{|v(\mathbf{r}_i)| + |v(-\mathbf{r}_i)|}{\sqrt{\sigma_v^2(\mathbf{r}_i) + \sigma_v^2(-\mathbf{r}_i)}} \right]^{-1} \quad (1)$$

Here, $\mathbf{r}_i$ is a vector giving the distance of the *i*-th velocity field pixel from the kinematic minor axis. The sum is taken over all N pixels of the velocity field, comparing the velocity at the positions $\mathbf{r}_i$ and $-\mathbf{r}_i$ (first sum term) and normalizing to the velocities across the whole VF (second sum term). Both terms are weighted by the errors σ_v on the measured line-of-sight velocities. In effect, $A_{\rm VF}$ quantifies asymmetries with respect to the kinematic minor axis. In the computation, the asymmetry $A_{\rm VF}$ is minimized by varying the kinematic center within ± 2 pixels of the photometric center (corresponding to $\sim$ 3.4 kpc at $z = 1.47$) and the kinematic position angle within $\pm 45°$ of the photometric position angle. One galaxy with a smooth VF and a clear velocity gradient, that also could be used to derive a $V_{\rm max}$, yielded a very high kinematic asymmetry $A_{\rm VF} = 1.98$ due to a lopsided gas disk. Although the lopsidedness is some hint to a potential interaction process, this object's VF does not show the strong kinematic perturbations of other galaxies with similar kinematic asymmetries.

We also computed morphological asymmetries $A_{\rm morph}$ on the best-seeing *i*-band images, following the definition of Conselice (2003). The asymmetry compares the original image to a version of itself that is rotated by 180°. To account for contribu-

A&A proofs: manuscript no. boehmetal2019_subm

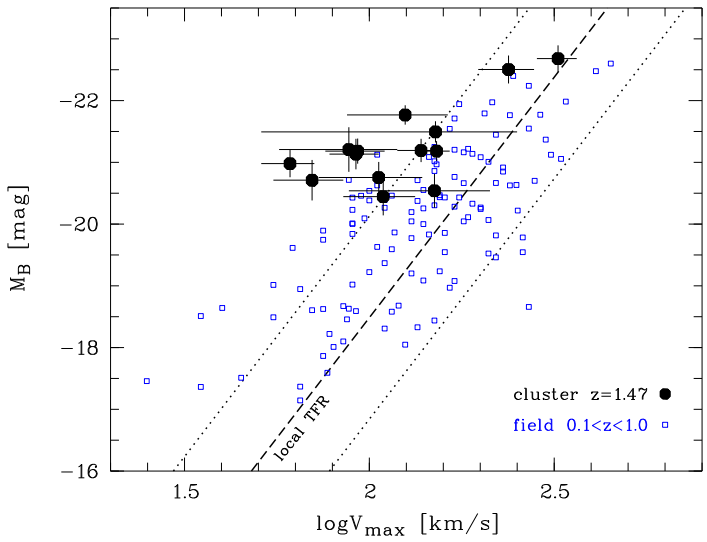

Fig. 4. *B*-band Tully-Fisher diagram showing 14 cluster galaxies at $z = 1.47$ (filled black circles) and field galaxies at $0.1 < z < 1.0$ (open squares) from Böhm & Ziegler (2016) for comparison. The local Tully-Fisher relation from Tully et al. (1998) is depicted by a dashed line; the dotted lines indicate the 3σ scatter.

tions by sky noise, a blank sky region B that has the same size as the object image is included in the computation:

$$A_{\rm morph} = \min\left(\frac{\sum_{i,j}|I - I_{180}|}{\sum_{i,j}|I|} - \frac{\sum_{k,l}|B - B_{180}|}{\sum_{i,j}|I|}\right) \quad (2)$$

Here, I is the original image, I_{180} is the image rotated by 180° about the adopted galaxy center; B and B_{180} are the background and rotated background. The sum is computed over all pixels within the 1σ isophotes of the galaxy, as determined using Source Extractor. B covers the same number of pixels as I. $A_{\rm morph}$ is minimized by allowing small shifts of the assumed position of the rotation axis (i.e. the galaxy center), by a maximum of ± 2 pixels in x- or y-direction.

We furthermore computed the central gas velocity dispersion $\sigma_{\rm g}$. For its derivation, we used the kinematic center as determined in the $V_{\rm max}$ derivation or, for objects with velocity fields not allowing multiple free fitting parameters, the photometric center from the surface brightness profile fits on the i-band images. Using an aperture of a single spaxel (corresponding to ∼ 1.7 kpc), and taking into account the spectral resolution of KMOS in the H-band ($R \approx 4000$), we found gas velocity dispersions in the range $13.4\,{\rm km/s} < \sigma_{\rm g} < 42.8\,{\rm km/s}$. Note that the conclusions drawn in the following discussion would not change if larger apertures were used for the computation of $\sigma_{\rm g}$.

The main parameters derived in our analysis are given in Table 1.

5. Discussion

The partly very large TFR over-luminosities we found for the $z = 1.47$ cluster galaxies could be due to several reasons. The high-z galaxies form stars at much higher rates than local galaxies of similar mass, and the higher fraction of young, high-mass stars arising from a higher SFR translates into a lower rest-frame B-band mass-to-light ratio M/L_B. This effect is the most probable explanation for the redshift-dependent B-band TFR offsets at $0 < z < 1$ discussed in Böhm & Ziegler (2016).

Based on FORS slit spectroscopy, our group previously carried out a Tully-Fisher analysis of cluster disk galaxies at slightly lower redshift $z \approx 1.4$ (Pérez-Martínez et al. 2017). There, we targeted the massive cluster XMMU J2235-2557, which has a well-established intra-cluster medium as confirmed with X-ray observations (Mullis et al. 2005). We compared the luminosity evolution of the cluster spirals to that expected for field galaxies, which amounts to ∼ 1.5 mag in rest-frame B-band at $z \approx 1.4$. Albeit based on a small sample of only six objects with undisturbed kinematics, we found some cluster disk galaxies to be brighter than their field counterparts at the same redshift, while some were fainter than expected in the field. One possible explanation is that the cluster disk galaxies are observed in different phases of ongoing ram-pressure: simulations have shown that ram-pressure can, via compression of the gaseous disk, initially lead to an enhanced SFR for several 100 Myr, followed by the quenching of star formation via massive gas loss (e.g. Ruggiero & Lima Neto 2017).

To investigate the influence of star-formation on the distribution in Tully-Fisher space for our KMOS sample, we show the TFR offsets ΔM_B plotted against SFR in Fig. 5, compared to the field sample from Böhm & Ziegler (2016). For field spirals at $z < 1$, there is a clear correlation between the TFR offsets and SFRs, a Spearman test yields $\rho = -0.46$ and $p = 10^{-4}$. For the high-z cluster galaxies, however, we find no clear correlation: $\rho = 0.27$ and $p = 0.35$. The galaxy with the highest SFR of over $100\,{\rm M_\odot\,yr^{-1}}$ is a slight outlier in the KMOS distribution, but even if one neglects this object in the statistics, the Spearman test result does not change significantly: for the remaining 13 galaxies, we find $\rho = 0.09$ and $p = 0.78$. We note that the SFRs also are not correlated with the kinematic asymmetry $A_{\rm VF}$ ($\rho = 0.11$ and $p = 0.62$), it is hence unlikely that star formation in many of the galaxies is enhanced by tidal interactions.

Table 1. The main parameters of the 14 galaxies from our sample for which a derivation of the maximum rotation velocity V_{max} was feasible.

ID	z	y [mag]	M_B [mag]	σ_{MB} [mag]	V_{max} [km/s]	σ_{vmax} [km/s]	σ_g [km/s]	SFR(Hα) [$M_\odot$/yr]	A_{VF}
HSC-232916	1.4650	23.35	-20.54	0.27	150	62	21.9	6.9	0.56
HSC-232950	1.4822	22.99	-21.21	0.36	88	31	33.2	31.4	0.96
HSC-232953	1.4607	22.72	-21.18	0.20	93	17	25.5	14.8	1.98
HSC-232955	1.4619	23.27	-20.71	0.33	70	15	26.6	23.4	0.72
HSC-232956	1.4625	22.87	-20.98	0.22	61	10	21.3	12.3	0.75
HSC-232959	1.4634	23.16	-20.75	0.25	106	33	13.4	9.4	0.83
HSC-232966	1.4751	22.43	-21.49	0.17	151	100	36.5	16.5	0.73
HSC-232978	1.4641	22.73	-21.18	0.16	152	13	23.3	73.2	0.40
HSC-233036	1.4760	21.98	-22.68	0.21	324	40	25.7	179.0	0.75
HSC-233042	1.4653	22.13	-22.50	0.23	238	41	38.9	38.7	0.55
HSC-233050	1.4650	22.74	-21.19	0.19	138	19	24.3	15.9	0.72
HSC-233051	1.4623	22.88	-21.13	0.25	92	14	14.5	13.4	1.06
HSC-233055	1.4653	22.18	-21.77	0.16	125	38	42.8	57.8	0.94
HSC-233056	1.4707	23.51	-20.44	0.30	109	24	32.4	20.7	0.94

Notes. Magnitudes are given in Vega system. σ_{MB} and σ_{vmax} give the respective errors on the rest-frame B-band absolute magnitude M_B and the maximum rotation velocity V_{max}.

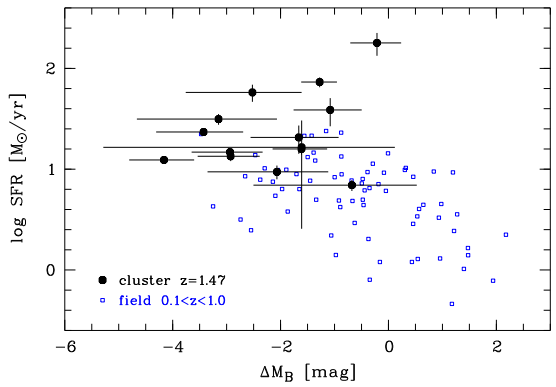

Fig. 5. Hα-based star formation rates versus offsets ΔM_B from the local B-band Tully-Fisher relation. In contrast to field disk galaxies at $z < 1$ (small open squares; taken from Böhm & Ziegler 2016), the TFR offsets of the $z = 1.47$ cluster galaxies (filled circles) are not correlated with star formation rate. See text for details.

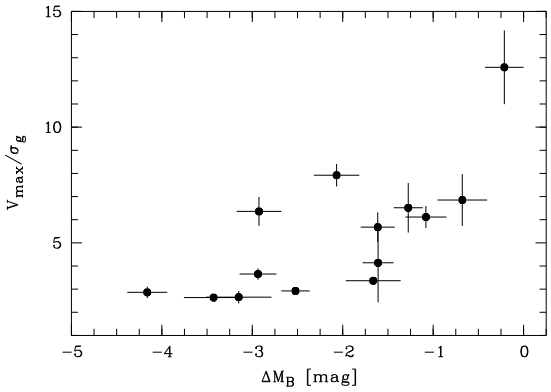

Fig. 6. Offsets from the local Tully-Fisher relation ΔM_B versus ratio between maximum rotation velocity V_{max} and gas velocity dispersion σ_g. Galaxies which are more rotation-dominated show smaller TFR offsets. This indicates that significant non-circular motions in the gas kinematics are contributing to the deviations from the local TFR.

The KMOS sample has some overlap in SFR and ΔM_B with the highest-SFR field galaxies at $z < 1$, but the above tests indicate that there might be an additional parameter that contributes to the TFR offsets at $z \approx 1.5$. Indeed, we find that the TFR offsets depend on the contributions of non-circular motions to the $z = 1.47$ cluster galaxies' gas kinematics. Fig. 6 shows the TFR offsets versus the ratio V_{max}/σ_g between maximum rotation velocity and gas velocity dispersion. This figure demonstrates that galaxies with lower V_{max}/σ_g ratios (less rotation-dominated kinematics) have larger TFR offsets, confirmed by a Spearman test which returns $\rho = 0.77$ and $p = 0.001$. A relatively large velocity dispersion does not necessarily imply gravitational perturbations e.g. by galaxy-galaxy interactions, but could also indicate kinematically "hotter" disks that have also been found in the field regime at similar redshifts (e.g. Simons et al. 2016). We can, however, not compare this result to our own $z < 1$ field sample as we did in Fig. 5, because the spectral resolution of those data, which were taken with VLT/FORS, is too low; the spectral resolution of the FORS grism used in that campaign corresponds to a lower limit $\sigma_g \approx 100$ km/s.

Independent of whether the low V_{max}/σ_g ratios of some objects are due to gravitational interactions or a general trend towards kinematically hotter, thicker disks at higher redshifts (e.g. Wisnioski et al. 2015), we would expect more massive galaxies to be more rotation-dominated than lower-mass ones: higher-mass galaxies are less susceptible to external gravitational forces, and they also settle to high V_{max}/σ_g ratios at earlier cosmic times than low-mass disks (e.g. Kassin et al. 2012). Fig. 7 shows the ratio V_{max}/σ_g between maximum rotation velocity and gas velocity dispersion as a function of V_{max}, which is a proxy for total mass. Indeed, the kinematics of galaxies with higher V_{max}, hence higher mass, are more rotation-dominated than those of low-mass ones (Spearman test: $\rho = 0.67$, $p = 0.0087$). From a theoretical perspective, several scenarios exist to explain the increasing gas velocity dispersion in disks towards higher redshifts. Hung et al. (2019) used cosmological simulations to show that higher gas inflow rates and subsequently enhanced star formation rates lead to larger σ_g at earlier cosmic times.

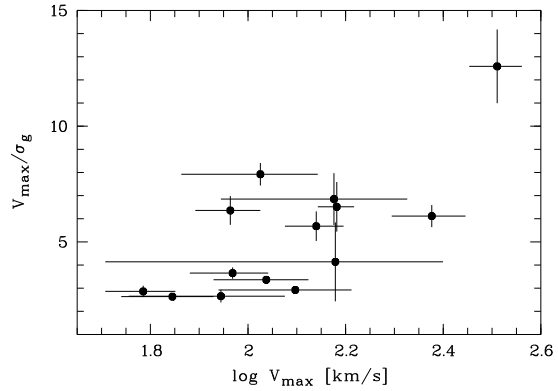

Fig. 7. Ratio between maximum rotation velocity V_{max} and gas velocity dispersion σ_g as a function of maximum rotation velocity. Faster rotators (i.e. disk galaxies of higher mass) have more rotation-dominated kinematics that galaxies of lower mass.

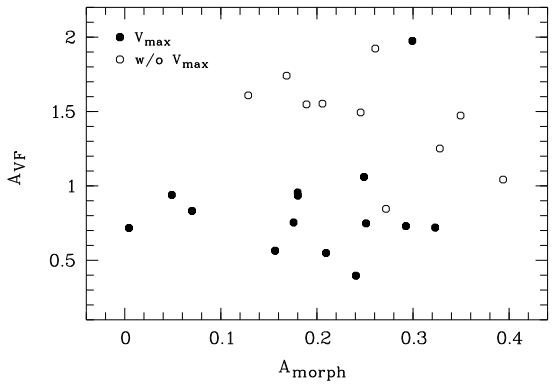

Fig. 8. Morphological asymmetry A_{morph} versus velocity field asymmetry A_{VF}. Filled symbols denote galaxies with determined V_{max}, open symbols represent galaxies with disturbed or non-rotating velocity fields that did not allow to derive V_{max}.

We now want to include morphological information in our analysis, in an attempt to disentangle various possible interaction processes in the high-redshift clusters. In Fig. 8, we show the kinematical asymmetry A_{VF} as a function of morphological asymmetry A_{morph}. The Y-axis of this parameter space is sensitive both to hydrodynamical and gravitational interactions, while the X-axis only probes gravitational interactions; stars are not affected by ram-pressure (e.g., Kronberger et al. 2008). As would be expected, galaxies with velocity fields that could be used for the determination of V_{max} generally have lower kinematic asymmetries A_{VF} than galaxies that did not yield a value for V_{max} (except for the rare case of one galaxy with $A_{VF} = 1.98$, despite of a smooth VF with a clear gradient; the high A_{VF} is due to its lopsided gas disk). Using the median morphological asymmetry $\langle A_{morph} \rangle = 0.23$ to sub-divide our sample, we find that the median kinematical asymmetry is slightly larger towards higher morphological asymmetries ($\langle A_{VF} \rangle = 0.94$ for $A_{morph} < 0.23$, and $\langle A_{VF} \rangle = 1.05$ for $A_{morph} > 0.23$). However, no significant correlation between A_{VF} and A_{morph} is found using a Spearman test: $\rho = 0.16$ and $p = 0.46$.

For the further interpretation of Fig. 8, we can rely on our previous studies at lower redshifts. In the cluster system A901/902 at $z \approx 0.17$, we previously found a population of disk galaxies that, despite having regular morphologies with low A_{morph} values, show high gas kinematical asymmetries (cf. Fig. 17 in Bösch et al. 2013a). This is evidence for hydrodynamical interaction, as this is the sole process in dense environments that only affects the gas distribution and gas kinematics, but not the stellar light morphology. As is clear from Fig. 8, there are very few $z \approx 1.5$ cluster galaxies where a low A_{morph} coincides with a high A_{VF}. This could be due to a too low current density of the intra-cluster medium in the two clusters to invoke detectable ram-pressure events (lacking deep X-ray data, we can not directly test for the presence of a dense ICM component). It is also possible that galaxy-galaxy interactions act *in addition* to ram-pressure in these two clusters, making it impossible to detect hydrodynamical interactions in A_{morph}/A_{VF} space. We note that, in part, high morphological asymmetries in our sample could also stem from the near-UV regime ($\sim$ 3000-3400 Å) that the HSC *i*-band imaging probes in rest-frame. The sensitivity of the NUV to clumpy star-forming regions generally leads to higher A_{morph} than rest-frame optical or NIR images (that are currently not at hand for our sample).

We estimated the galaxy velocity dispersions in the two clusters, assuming that the two peaks in their redshift distributions are physical, since it seems unlikely that strong night-sky residuals are the cause of the observed "gap" at $z = 1.468$ in both clusters. For the two peaks in the *z*-distribution of HSC-CL2329, we find velocity dispersions of $\sigma_v = 304$ km/s and $\sigma_v = 364$ km/s; the distribution in HSC-CL2330 yield values of $\sigma_v = 385$ km/s and $\sigma_v = 361$ km/s, resp. Taken at face value, and using rough estimates for the gravitational radii, these velocity dispersions would be equivalent to a virial mass of $M_{vir} \approx 10^{14}\, M_\odot$ for each cluster. However, given the complex redshift distributions, it is more likely that neither cluster is virialized but in the process of formation. Irrespective of the dynamical status, these σ_v values show that the relative velocities between the cluster galaxies in our sample are low compared to those observed in virialized clusters, and tidal interactions between the galaxies hence are much more efficient than would be expected in a typical cluster environment at later cosmic epochs. This strengthens the interpretation that galaxy-galaxy interactions contribute to the distribution shown in Fig. 8, though we would expect a clear correlation between morphological and kinematical asymmetry if tidal forces would be the *only* interaction process at act.

To summarize, our morpho-kinematical analysis of galaxies in dense environments at $z \approx 1.5$, corresponding to a look-back time of $\sim$ 9 Gyr, has yielded some similarities to the field galaxy population at this epoch, in particular with regard to a high fraction of disks with significant contributions by non-circular motions. However, two points have to be stressed. Firstly, that our sample stems from a cosmic phase that represents the *onset* of environmental influence on galaxy evolution, and not the clear impact observed at lower redshifts. Secondly, the complex redshift distributions of HSC-2329 and HSC-2330 indicate that both structures are in an early, non-virialized stage, and might lack a dense intra-cluster medium at the time of observation, which would weaken the effects from hydrodynamical interactions. More IFU observations of galaxies in clusters, including more evolved structures at high redshifts, will be necessary to shed more light on the impact of environment on galaxy evolution at early cosmic stages.

6. Summary

We used VLT/KMOS to take Integral Field Spectroscopy of the Hα emission in 46 galaxies in two clusters at redshift $z = 1.47$ detected as overdensities of [O II] emitters in HyperSuprimeCam Strategic Survey Program data. In the KMOS data cubes, the Hα line was detected in 36 galaxies, of which 34 are cluster members; only two objects are located in the field, demonstrating the efficiency of our selection strategy. 24 galaxies show spatially extended Hα emission from which velocity fields could be extracted, while in the remaining 12 objects, the Hα emission is spread over only a few pixels and/or is affected by strong residuals of OH night sky lines.

By fitting the observed velocity fields with simulated velocity fields that take into account geometrical effects like disk inclination and position angle as well as seeing and beam smearing, we could derive the maximum rotation velocity $V_{\rm max}$ of 14 galaxies. The velocity fields of the remaining 10 galaxies with extended Hα are disturbed or non-rotating. We computed quantitative morphological and kinematical asymmetries to compare the $z = 1.47$ cluster galaxy data to our own studies of the galaxy population in low-redshift clusters.

Our main findings are:

1. Based on the Tully-Fisher relation (TFR), all $z \approx 1.5$ cluster disk galaxies are more luminous than local spirals at given $V_{\rm max}$, by up to ~ 4 mag in rest-frame B. We did not consider the stellar-mass TFR here as the currently available photometry does not cover rest-frame red optical or NIR colors mandatory for the derivation of robust stellar masses.
2. The deviations from the local TFR are not correlated with star formation rate, but with the ratio between $V_{\rm max}$ and gas velocity dispersion $\sigma_{\rm g}$. In turn, this ratio $V_{\rm max}/\sigma_{\rm g}$ is larger towards higher $V_{\rm max}$, i.e., higher total masses. Besides possible gravitational interactions between cluster members, this might reflect that many low-mass disks have not yet settled to purely rotational kinematics by $z \approx 1.5$. This has also been observed in the field at this epoch.
3. We do not observe galaxies with disturbed gas kinematics and regular stellar morphologies, different from what has been found in low-redshift clusters. Such a combination would hint towards ram-pressure events. The $z \approx 1.5$ clusters hence either have no dense intra-cluster medium yet, or galaxy-galaxy interactions are more frequent in the distant clusters than in dense environments at later cosmic epochs, camouflaging the impact of purely hydrodynamical interactions.

Acknowledgements. BLZ is grateful for an NAOJ visitorship in 09/2018. This publication is supported by the Austrian Science Fund (FWF).

References

Aihara, H., Arimoto, N., Armstrong, R., et al. 2018a, PASJ, 70, S4
Aihara, H., Armstrong, R., Bickerton, S., et al. 2018b, PASJ, 70, S8
Balogh, M. L., Navarro, J. F., & Morris, S. L. 2000, ApJ, 540, 113
Bamford, S. P., Milvang-Jensen, B., Aragón-Salamanca, A., & Simard, L. 1005, MNRAS, 361, 109
Bertin, E., & Arnouts, S. 1996, A&AS, 117, 393
Blanton, M. R.; Eisenstein, D., Hogg, D. W., Schlegel, D. J., & Brinkmann, J. 2005, ApJ, 629, 143
Böhm, A., Ziegler, B. L. 2016, A&A, 592, A64
Brodwin, M., McDonald, M., Gonzalez, A. H., et al. 2016, ApJ, 817, 122
Bösch, B., Böhm, A., Wolf, C., et al. 2013a, A&A, 549, A142
Bösch, B., Böhm, A., Wolf, C., et al. 2013b, A&A, 554, A97
Conselice, C. 2003, ApJS, 147,1
Dale, D. A., Giovanelli, R., Haynes, M. P., Hardy, E., & Campusano, L. E. 2001, AJ, 121, 1886
Desai, V., Dalcanton, J. J.; Aragón-Salamanca, A., et al. 2007, ApJ, 660, 1151
Dressler, A., 1980, ApJ, 236, 351
Ferreras, I., Böhm, A., Ziegler, B. L., & Silk, J., 2014, MNRAS, 437, 1872
Furusawa, H., Koike, M., Takata, T., et al. 2018, PASJ, 70S, 3
Gilbank, G., Baldry, I.K., Balogh, M.L., Glazebrook, K., & Bower, R.G. 2010, MNRAS, 405, 2594
Gray, M. E., Wolf, C., Barden, M., et al. 2009, MNRAS, 393, 1275
Hayashi, M., Tanaka, M., Shimkawa, R., et al. 2018a, PASJ, 70, 17
Hayashi, M., Kodama, T., Koyama, Y., et al. 2010, MNRAS, 402, 1980
Hung, C.-L., Hayward, C.C., Yuan, T., et al. 2019, MNRAS, 482, 5125
Kassin, S. A., Weiner, B. J., Faber, S. M., et al. 2012, ApJ, 758, 106
Kawanomoto, S., Uraguchi, F., Komiyama, Y., et al. 2018, PASJ, 70, 66
Kennicutt, R. 1998, ARA&A, 36, 189
Komiyama, Y., Obuchi, Y., Nakaya, H., et al. 2018, PASJ, 70S, 2
Kronberger, T., Kapferer, W., Unterguggenberger, S., Schindler, S., & Ziegler, B. L. 2008, A&A, 483, 783
Kuchner, U., Ziegler, B.L., Verdugo, M., Bamford, S. & Häußler, B. 2017, A&A, 604, A54
Ly, C., Malkan, M. A., Kashikawa, N., et al. 2012, ApJL, 747, 16
Miller, S. H., Ellis, R. S., Sullivan, M., Bundy, K. , Bunker, A., & Treu, T. 2012, ApJ, 753, 74
Milvang-Jensen, B., Aragón-Salamanca, A., Hau, G. K. T., Jørgensen, I., Hjorth, J.. 2003, MNRAS, 339, 1
Miyazaki, S., Komiyama, Y., Kawanomoto, S., et al. 2018, PASJ, 70, S1
Moran, S. M., Miller, N., Treu, T., Ellis, E. S., & Smith, G. P. 2007, ApJ, 659, 1138
Moore, B., Katz, N., Lake, G., Dressler, A. & Oemler, A. 1996, Nature, 379, 613
Mullis, C.R., Rosati, P., Lamer, G., et al. 2005, ApJ, 623, L85
Nakamura, O., Aragón-Salamanca, A., Milvang-Jensen, B., Arimoto, N., Ikuta, C., & Bamford, S. P 2006, MNRAS, 366, 144
Peng, C. Y., Ho, L. C., Impey, C. D., & Rix, H.-W. 2002, AJ, 124, 266
Pérez-Martínez, J. M., Ziegler, B. L., Verdugo, M., Böhm, A., & Tanaka, M. 2017, A&A, 605, A127
Ruggiero, R., & Lima Neto, G. B. 2017, MNRAS, 468, 4107
Simons, R. C., Kassin, S. A., Trump, J. R., et al. 2016, ApJ, 830, 14
Steinhauser, D., Schindler, S., & Springel, V. 2016, A&A, 591, A51
Tanaka, M., Coupon, J., Hsieh, B.-C., et al. 2018, PASJ, 70, S9
Tully, R. B., Pierce, M. J., Huang, J.-S., et al. 1998, AJ, 115, 2264
Tully R. B., & Fisher, J. R. 1977, A&A, 54, 661
Übler, H., Förster-Schreiber, N., Genzel, R., et al. 2017, ApJ, 842, 121
Verdugo M., Ziegler, B. L., Gerken, B. 2008, A&A, 486, 9
Vogt, N. P., Haynes, M. P., Giovanelli, R., & Herter, T. 2004, AJ, 127, 330
Wisnioski, E., Förster-Schreiber, N., Wuyts, S., et al. 2015, ApJ, 799, 209
Wolf, C., Aragón-Salamanca, A., Balogh, M., et al. 2009, MNRAS, 393, 1302
Ziegler, B. L., Böhm, A., Jäger, K., Heidt, J., & Möllenhoff, C. 2003, ApJL, 598, 87

Chapter 6

Conclusions

Galaxy evolution is a complex process that involves changes in the structure, internal properties and matter content of galaxies. In clusters, galaxy evolution is hastened and strengthened due to the influence of environmental effects acting on both the stellar structure and the gas reservoir. In this thesis, I have investigated the kinematic status and evolution of galaxies in several clusters at 0.5<z<1.5. In the low redshift regime, I focus on the relation between the kinematic status of galaxies with respect to other physical parameters related with the cluster (density) and the galaxies themselves (SFR activity and AGN frequency), while the high redshift samples are mainly used to test the evolution of kinematic scaling relations in clusters beyond z$\sim$1. The following paragraphs present a summary of the main findings carried out in this work:

In RXJ1347, we find that the fraction of galaxies displaying irregular kinematics is higher than in the field. However, this does not clearly correlates with projected cluster-centric distance or density, which implies that cluster-specific interactions must be ubiquitous and supports the scenario where several mechanisms are simultaneously at play. In addition, the majority of the regular and irregular star-forming galaxies within our sample lie in low to intermediate density regions and display similar although slightly lower sSFR than expected with respect to the main sequence of star-forming galaxies. This reinforces the scenario in which cluster-specific interactions start the quenching of star-formation in galaxies at intermediate distances from the cluster core, so that most of them (specially the lower mass galaxies) are in the process of being quenched by the time they reach the densest regions (Wetzel et al. 2013, Maier et al. 2019).

We do not see signs of enhance star-formation in kinematically irregular cluster galaxies at this redshift. Therefore, if the asymmetries in these objects

have been caused by recent interactions (hydrodynamical or gravitational) related with the cluster environment, any possible starburst event associated with the interactions is not visible by the time of our observations. This could be explained by the short-life nature of this kind of events together with the influence of the cluster environment in suppressing star-formation. In addition, the fraction of AGNs within our cluster sample is negligible (only 2 out of 30 objects analyzed) and independent of the reported gas kinematic status of the galaxies. However, our results are limited by the size of our sample. Extensive follow-ups simultaneously examining the kinematics and star-forming properties of galaxies are required to shed light onto the specific mechanisms at play and, in particular, to link them with the different density substructures within these kind of cluster systems.

During this thesis we have studied the evolution of several kinematic scaling relations in clusters at 0.5<z<1.5. The results show that both the TFR and the VSR display very similar values in the cluster and field environments up to z$\sim$1, with an average B-band brightening $\langle \Delta M_B \rangle \approx 1$ mag and a factor 1.6 smaller scale length than in the local Universe. These findings are in agreement with previous observational and computational works (van der Wel et al. 2014, Dutton et al. 2011). However, by z$\sim$1.5 the average offsets have grown to $\langle \Delta M_B \rangle \approx 2$ mag and to almost a factor 3 smaller scale lengths, which implies faster evolution than predicted in both scaling relations (Dutton et al., 2011). The B-band brightening is detected for galaxies residing in massive virialized clusters such as XMM2235 as well as for clusters still in the process of assembling the bulk of their mass (HSC-clusters) at similar redshift (z$\sim$1.5). In the latter case, galaxies infalling towards clusters in formation through the filaments of the cosmic web may be subject to increased inflows, contributing to fuel star-forming regions during a phase in which many disks haven't been fully settled yet. For more massive structures such as XMM2235, we propose that the compression of gas rich disks of star-forming galaxies during their infalling phase the early phases may induce higher SFRs temporarily, and thus be responsible for this B-band enhancement.

Finally, we examine the specific angular momentum stellar-mass relation ($j_* - M_*$). Cluster galaxies at 0.5<z<1.5 lie below the local "Fall relation" ($j_* \propto M_*^{2/3}$ Fall 1983; Fall and Romanowsky 2013). The ΛCDM model predicts the evolution of specific angular momentum towards increasing values of j_* from the cosmic dawn to the local Universe (Mo, Mao, and White 1998,

Obreschkow et al. 2015), which qualitatively agrees with our results. Assuming a spin parameter $\lambda = 0.035$, the average stellar-to-halo specific angular momentum ratio ($\langle f_j \rangle = \langle j_* / j_{halo} \rangle$) of cluster galaxies is lower in cluster galaxies than in the field at similar redshifts. The analysis of the redshift evolution of the specific angular momentum yielded similar results, with cluster and field samples following different evolutionary tracks. Theoretical predictions propose a redshift evolution in the form of $j_* \propto M_*^{2/3}(1+z)^{-0.5}$ (Mo, Mao, and White 1998, Obreschkow et al. 2015), which agrees with the results obtained in our analysis of field galaxy samples at 0<z<2.5 (Fall and Romanowsky 2018, Posti18, Harrison et al. 2017, Förster Schreiber et al. 2018), while our cluster data favours $j_* \propto M_*^{2/3}(1+z)^{-1}$. We interpret this discrepancy as a consequence of the higher abundance of interactions in the cluster environment, where several mechanisms (suppression of outflows, tidal interactions, ram-pressure stripping and mergers) can influence the angular momentum of galaxies. Mergers have been considered a possible explanation for the loss of angular momentum in previous observational studies (Pelliccia et al. 2019). However, only major and, to a lesser degree, minor dry mergers are efficient enough to explain this difference according to hydrodynamical simulations by Lagos et al. (2018). Major merges are ruled because they completely destroy the disk of the galaxies implicated and, in addition, the cluster environment makes highly unlikely to rebuild a star-forming disk by reaccreting the debris expelled during the interaction. Thus, minor dry mergers and other unexplored (in terms of angular momentum) cluster-specific interactions may be responsible for these offsets. However, larger samples of cluster galaxies at different redshift are required to fully track the angular momentum evolution in clusters across cosmic time as well as to examine the possible impact of selection biases (specially in stellar-mass) due to the limited size of our high redshift clusters.

Chapter 7

Zusammenfassung

Die Galaxienentwicklung entlang kosmologischer Epochen erfordert verschiedene physikalische Prozesse, die nichttrivial zusammenspielen, um die heutige Galaxienpopulation im lokalen Universum zu erhalten. In Galaxienhaufen kommen diese Prozesse durch den Einfluss der Umgebung vermehrt vor und wirken sowohl auf die Stern- als auch die Gaskomponente. Kinematische Skalenrelationen beschreiben wichtige Zusammenhänge zwischen physikalischen Eigenschaften, die es ermöglichen, das Zusammenspiel zwischen der leuchtenden und der dunklen Materie im Universum zu verstehen. Die flachen Rotationskurven der Spiralgalaxien ermöglichen über die maximale Rotationsgeschwindigkeit die Gesamtmasse (inklusive Dunkler Materie) einer Galaxie abzuschätzen und damit diese mit den Ausdehnungen und der stellaren Masse der Galaxien zu vergleichen. Mit diesen drei Parametern kann man die Entwicklung der Relationen Tully-Fisher (TFR), Geschwindigkeits-Grösse (VSR) und Drehimpuls-Masse (JMR) studieren. In dieser Doktorarbeit untersuche ich quantitativ den kinematischen Entwicklungsstand von Galaxien in mehreren Galaxienhaufen bei Rotverschiebungen zwischen 0.5 und 1.5 mithilfe von sowohl 2D- als auch 3D-spektroskopischer Daten, die mit den VLT und GTC Observatorien gewonnen wurden. Bei niedriger und mittlerer Rotverschiebung ist der Anteil der Galaxien mit regulärer Rotation geringer als im vergleichbaren Feld. Es gibt keinen Zusammenhang mit dem Abstand zur Haufenmitte oder der lokalen Dichte im Haufen. Dies lässt sich damit erklären, dass in Haufen Wechselwirkungen überall im Gang sind, die sich gegenseitig beeinflussen. Ausserdem unterscheidet sich die Entwicklung der untersuchten Skalenrelationen statistisch nicht signifikant zwischen Haufen- und Feldgalaxien bis Rotverschiebungen z=1. Nur bei den höchsten studierten Rotverschiebungen gibt es eine bestimmte Galaxienpopulation, die in der blauen TFR eine sehr viel hellere Leuchtkraft aufweisen, geringere Ausdehnungen in der VSR

zeigen und einen anderen Trend in der zeitlichen Entwicklung der JMR als Feldgalaxien haben. In meiner Doktorarbeit untersuchte ich die möglichen Ursachen und Auswirkungen der gefundenen Ergebnisse im grösseren Rahmen der allgemeinen Galaxienentwicklung bei verschiedenen kosmologischen Epochen.

Bibliography

Abazajian, K. et al. (2003). "The First Data Release of the Sloan Digital Sky Survey". In: 126, pp. 2081–2086. DOI: 10.1086/378165. eprint: astro-ph/0305492.

Baldry, I. K. et al. (2006). "Galaxy bimodality versus stellar mass and environment". In: 373, pp. 469–483. DOI: 10.1111/j.1365-2966.2006.11081.x. eprint: astro-ph/0607648.

Balogh, Michael L., Julio F. Navarro, and Simon L. Morris (2000). "The Origin of Star Formation Gradients in Rich Galaxy Clusters". In: 540.1, pp. 113–121. DOI: 10.1086/309323. arXiv: astro-ph/0004078 [astro-ph].

Balogh, Michael L. et al. (2016). "Evidence for a change in the dominant satellite galaxy quenching mechanism at z = 1". In: 456.4, pp. 4364–4376. DOI: 10.1093/mnras/stv2949. arXiv: 1511.07344 [astro-ph.GA].

Bamford, S. P. et al. (2005). "The Tully-Fisher relation of distant cluster galaxies". In: 361, pp. 109–127. DOI: 10.1111/j.1365-2966.2005.09135.x. eprint: astro-ph/0503648.

Bell, Eric F. and Roelof S. de Jong (2001). "Stellar Mass-to-Light Ratios and the Tully-Fisher Relation". In: 550.1, pp. 212–229. DOI: 10.1086/319728. arXiv: astro-ph/0011493 [astro-ph].

Böhm, A. and B. L. Ziegler (2016). "Disk galaxy scaling relations at intermediate redshifts. I. The Tully-Fisher and velocity-size relations". In: 592, A64, A64. DOI: 10.1051/0004-6361/201527063. arXiv: 1507.07353.

Bond, J. Richard, Lev Kofman, and Dmitry Pogosyan (1996). "How filaments of galaxies are woven into the cosmic web". In: 380.6575, pp. 603–606. DOI: 10.1038/380603a0. arXiv: astro-ph/9512141 [astro-ph].

Bösch, B. et al. (2013a). "Ram pressure and dusty red galaxies - key factors in the evolution of the multiple cluster system Abell 901/902". In: 549, A142, A142. DOI: 10.1051/0004-6361/201219244. arXiv: 1211.4750 [astro-ph.CO].

Bösch, B. et al. (2013b). "Tully-Fisher analysis of the multiple cluster system Abell 901/902". In: 554, A97, A97. DOI: 10.1051/0004-6361/201321561. arXiv: 1304.6186 [astro-ph.CO].

Boselli, Alessandro and Giuseppe Gavazzi (2006). "Environmental Effects on Late-Type Galaxies in Nearby Clusters". In: 118.842, pp. 517–559. DOI: 10.1086/500691. arXiv: astro-ph/0601108 [astro-ph].

Bosma, A. (1978). "The distribution and kinematics of neutral hydrogen in spiral galaxies of various morphological types". PhD thesis. -.

Bournaud, Frédéric et al. (2014). "The Long Lives of Giant Clumps and the Birth of Outflows in Gas-rich Galaxies at High Redshift". In: 780.1, 57, p. 57. DOI: 10.1088/0004-637X/780/1/57. arXiv: 1307.7136 [astro-ph.CO].

Brinchmann, J. et al. (2004). "The physical properties of star-forming galaxies in the low-redshift Universe". In: 351.4, pp. 1151–1179. DOI: 10.1111/j.1365-2966.2004.07881.x. arXiv: astro-ph/0311060 [astro-ph].

Cattaneo, A. et al. (2011). "How do galaxies acquire their mass?" In: 533, A5, A5. DOI: 10.1051/0004-6361/201015780. arXiv: 1002.3257 [astro-ph.CO].

Courteau, S. (1997). "Optical Rotation Curves and Linewidths for Tully-Fisher Applications". In: 114, p. 2402. DOI: 10.1086/118656. eprint: astro-ph/9709201.

Courteau, Stéphane et al. (2007). "Scaling Relations of Spiral Galaxies". In: 671.1, pp. 203–225. DOI: 10.1086/522193. arXiv: 0708.0422 [astro-ph].

Daddi, E. et al. (2007). "Multiwavelength Study of Massive Galaxies at z$\sim$2. I. Star Formation and Galaxy Growth". In: 670.1, pp. 156–172. DOI: 10.1086/521818. arXiv: 0705.2831 [astro-ph].

Daddi, E. et al. (2010). "Very High Gas Fractions and Extended Gas Reservoirs in z = 1.5 Disk Galaxies". In: 713.1, pp. 686–707. DOI: 10.1088/0004-637X/713/1/686. arXiv: 0911.2776 [astro-ph.CO].

Dannerbauer, H. et al. (2014). "An excess of dusty starbursts related to the Spiderweb galaxy". In: 570, A55, A55. DOI: 10.1051/0004-6361/201423771. arXiv: 1410.3730 [astro-ph.GA].

Davis, M. et al. (1985). "The evolution of large-scale structure in a universe dominated by cold dark matter". In: 292, pp. 371–394. DOI: 10.1086/163168.

de Lapparent, V., M. J. Geller, and J. P. Huchra (1986). "A Slice of the Universe". In: 302, p. L1. DOI: 10.1086/184625.

de Vaucouleurs, G. (1953). "On the distribution of mass and luminosity in elliptical galaxies". In: 113, p. 134. DOI: 10.1093/mnras/113.2.134.

de Vaucouleurs, Gerard (1948). "Recherches sur les Nebuleuses Extragalactiques". In: *Annales d'Astrophysique* 11, p. 247.

Dressler, A. (1980). "Galaxy morphology in rich clusters - Implications for the formation and evolution of galaxies". In: 236, pp. 351–365. DOI: 10.1086/157753.

Dutton, A. A. et al. (2011). "On the evolution of the velocity-mass-size relations of disc-dominated galaxies over the past 10 billion years". In: 410, pp. 1660–1676. DOI: 10.1111/j.1365-2966.2010.17555.x. arXiv: 1006.3558.

Ebeling, H., L. N. Stephenson, and A. C. Edge (2014). "Jellyfish: Evidence of Extreme Ram-pressure Stripping in Massive Galaxy Clusters". In: 781, L40, p. L40. DOI: 10.1088/2041-8205/781/2/L40. arXiv: 1312.6135.

Elbaz, D. et al. (2007). "The reversal of the star formation-density relation in the distant universe". In: 468.1, pp. 33–48. DOI: 10.1051/0004-6361:20077525. arXiv: astro-ph/0703653 [astro-ph].

Faber, S. M. and J. S. Gallagher (1979). "Masses and mass-to-light ratios of galaxies." In: 17, pp. 135–187. DOI: 10.1146/annurev.aa.17.090179.001031.

Fall, S. M. (1983). "Galaxy formation - Some comparisons between theory and observation". In: *Internal Kinematics and Dynamics of Galaxies*. Ed. by E. Athanassoula. Vol. 100. IAU Symposium, pp. 391–398.

Fall, S. Michael and Aaron J. Romanowsky (2013). "Angular Momentum and Galaxy Formation Revisited: Effects of Variable Mass-to-light Ratios". In: 769.2, L26, p. L26. DOI: 10.1088/2041-8205/769/2/L26. arXiv: 1305.1626 [astro-ph.CO].

– (2018). "Angular Momentum and Galaxy Formation Revisited: Scaling Relations for Disks and Bulges". In: 868.2, 133, p. 133. DOI: 10.3847/1538-4357/aaeb27. arXiv: 1808.02525 [astro-ph.GA].

Förster Schreiber, N. M. et al. (2018). "The SINS/zC-SINF Survey of z 2 Galaxy Kinematics: SINFONI Adaptive Optics-assisted Data and Kiloparsec-scale Emission-line Properties". In: 238.2, 21, p. 21. DOI: 10.3847/1538-4365/aadd49. arXiv: 1802.07276 [astro-ph.GA].

Freeman, K. C. (1970). "On the Disks of Spiral and S0 Galaxies". In: 160, p. 811. DOI: 10.1086/150474.

Gunn, James E. and III Gott J. Richard (1972). "On the Infall of Matter Into Clusters of Galaxies and Some Effects on Their Evolution". In: 176, p. 1. DOI: 10.1086/151605.

Hall, Melanie et al. (2012). "An investigation of Sloan Digital Sky Survey imaging data and multiband scaling relations of spiral galaxies". In: 425.4,

pp. 2741–2765. DOI: 10.1111/j.1365-2966.2012.21290.x. arXiv: 1111.5009 [astro-ph.CO].

Harrison, C. M. et al. (2017). "The KMOS Redshift One Spectroscopic Survey (KROSS): rotational velocities and angular momentum of z 0.9 galaxies". In: 467, pp. 1965–1983. DOI: 10.1093/mnras/stx217. arXiv: 1701.05561.

Hopkins, Philip F. et al. (2006). "The Relation between Quasar and Merging Galaxy Luminosity Functions and the Merger-driven Star Formation History of the Universe". In: 652.2, pp. 864–888. DOI: 10.1086/508503. arXiv: astro-ph/0602290 [astro-ph].

Hoyos, C. et al. (2016). "Linking the structural properties of galaxies and their star formation histories with STAGES". In: 455, pp. 295–307. DOI: 10.1093/mnras/stv2321. arXiv: 1510.01115.

Hubble, E. P. (1926). "Extragalactic nebulae." In: 64, pp. 321–369. DOI: 10.1086/143018.

– (1936). *Realm of the Nebulae*.

Hubble, Edwin (1929). "A Relation between Distance and Radial Velocity among Extra-Galactic Nebulae". In: *Proceedings of the National Academy of Science* 15.3, pp. 168–173. DOI: 10.1073/pnas.15.3.168.

Jaffé, Y. L. et al. (2011). "The effect of the environment on the gas kinematics and the structure of distant galaxies". In: 417, pp. 1996–2019. DOI: 10.1111/j.1365-2966.2011.19384.x. arXiv: 1107.0963.

Kartaltepe, Jeyhan S. et al. (2010). "A Multiwavelength Study of a Sample of 70 μm Selected Galaxies in the COSMOS Field. II. The Role of Mergers in Galaxy Evolution". In: 721.1, pp. 98–123. DOI: 10.1088/0004-637X/721/1/98. arXiv: 1006.4956 [astro-ph.CO].

Kassin, Susan A. et al. (2007). "The Stellar Mass Tully-Fisher Relation to z = 1.2 from AEGIS". In: 660.1, pp. L35–L38. DOI: 10.1086/517932. arXiv: astro-ph/0702643 [astro-ph].

Klypin, Anatoly, HongSheng Zhao, and Rachel S. Somerville (2002). "ΛCDM-based Models for the Milky Way and M31. I. Dynamical Models". In: 573.2, pp. 597–613. DOI: 10.1086/340656. arXiv: astro-ph/0110390 [astro-ph].

Koda, Jin, Yoshiaki Sofue, and Keiichi Wada (2000). "A Unified Scaling Law in Spiral Galaxies". In: 531.1, pp. L17–L20. DOI: 10.1086/312509. arXiv: astro-ph/0001249 [astro-ph].

Koyama, Yusei et al. (2013). "On the evolution and environmental dependence of the star formation rate versus stellar mass relation since z 2". In: 434.1, pp. 423–436. DOI: 10.1093/mnras/stt1035. arXiv: 1302.5315 [astro-ph.CO].

Kronberger, T. et al. (2008). "On the influence of ram-pressure stripping on the star formation of simulated spiral galaxies". In: 481, pp. 337–343. DOI: 10.1051/0004-6361:20078904. arXiv: 0801.3759.

Lacey, Cedric and Shaun Cole (1993). "Merger rates in hierarchical models of galaxy formation". In: 262.3, pp. 627–649. DOI: 10.1093/mnras/262.3.627.

Lagos, Claudia del P. et al. (2018). "Quantifying the impact of mergers on the angular momentum of simulated galaxies". In: 473.4, pp. 4956–4974. DOI: 10.1093/mnras/stx2667. arXiv: 1701.04407 [astro-ph.GA].

Lapi, A., P. Salucci, and L. Danese (2018). "Precision Scaling Relations for Disk Galaxies in the Local Universe". In: 859.1, 2, p. 2. DOI: 10.3847/1538-4357/aabf35. arXiv: 1804.06086 [astro-ph.GA].

Larson, R. B., B. M. Tinsley, and C. N. Caldwell (1980). "The evolution of disk galaxies and the origin of S0 galaxies". In: 237, pp. 692–707. DOI: 10.1086/157917.

Lelli, Federico, Stacy S. McGaugh, and James M. Schombert (2016). "The Small Scatter of the Baryonic Tully-Fisher Relation". In: 816.1, L14, p. L14. DOI: 10.3847/2041-8205/816/1/L14. arXiv: 1512.04543 [astro-ph.GA].

Leroy, Adam K. et al. (2008). "The Star Formation Efficiency in Nearby Galaxies: Measuring Where Gas Forms Stars Effectively". In: 136.6, pp. 2782–2845. DOI: 10.1088/0004-6256/136/6/2782. arXiv: 0810.2556 [astro-ph].

Madau, P. and M. Dickinson (2014). "Cosmic Star-Formation History". In: 52, pp. 415–486. DOI: 10.1146/annurev-astro-081811-125615. arXiv: 1403.0007.

Maier, C. et al. (2016). "CLASH-VLT: Strangulation of cluster galaxies in MACS J0416.1-2403 as seen from their chemical enrichment". In: 590, A108, A108. DOI: 10.1051/0004-6361/201628223. arXiv: 1602.00686.

Maier, C. et al. (2019). "Slow-then-rapid quenching as traced by tentative evidence for enhanced metallicities of cluster galaxies at z ϑ 0.2*intheslowquenchingphase*". In: 621, A131, A131. DOI: 10.1051/0004-6361/201834290. arXiv: 1809.07675.

Mastropietro, Chiara et al. (2005). "Morphological evolution of discs in clusters". In: 364.2, pp. 607–619. DOI: 10.1111/j.1365-2966.2005.09579.x. arXiv: astro-ph/0411648 [astro-ph].

McGaugh, S. S. et al. (2000). "The Baryonic Tully-Fisher Relation". In: 533.2, pp. L99–L102. DOI: 10.1086/312628. arXiv: astro-ph/0003001 [astro-ph].

McGaugh, Stacy S. (2012). "The Baryonic Tully-Fisher Relation of Gas-rich Galaxies as a Test of ΛCDM and MOND". In: 143.2, 40, p. 40. DOI: 10.1088/0004-6256/143/2/40. arXiv: 1107.2934 [astro-ph.CO].

Meurer, Gerhardt R. et al. (2018). "Cosmic clocks: a tight radius-velocity relationship for H I-selected galaxies". In: 476.2, pp. 1624–1636. DOI: 10.1093/mnras/sty275. arXiv: 1803.04716 [astro-ph.GA].

Miller, S. H. et al. (2011). "The Assembly History of Disk Galaxies. I. The Tully-Fisher Relation to z ˜= 1.3 from Deep Exposures with DEIMOS". In: 741, 115, p. 115. DOI: 10.1088/0004-637X/741/2/115. arXiv: 1102.3911 [astro-ph.CO].

Mo, H. J., Shude Mao, and Simon D. M. White (1998). "The formation of galactic discs". In: 295.2, pp. 319–336. DOI: 10.1046/j.1365-8711.1998.01227.x. arXiv: astro-ph/9707093 [astro-ph].

Moore, Ben et al. (1996). "Galaxy harassment and the evolution of clusters of galaxies". In: 379.6566, pp. 613–616. DOI: 10.1038/379613a0. arXiv: astro-ph/9510034 [astro-ph].

Moore, Ben et al. (1999). "On the survival and destruction of spiral galaxies in clusters". In: 304.3, pp. 465–474. DOI: 10.1046/j.1365-8711.1999.02345.x. arXiv: astro-ph/9811127 [astro-ph].

Moran, S. M. et al. (2007). "Dynamical Evidence for Environmental Evolution of Intermediate-Redshift Spiral Galaxies". In: 659, pp. 1138–1152. DOI: 10.1086/513005. eprint: astro-ph/0701156.

Mortlock, A. et al. (2013). "The redshift and mass dependence on the formation of the Hubble sequence at z 1 from CANDELS/UDS". In: 433, pp. 1185–1201. DOI: 10.1093/mnras/stt793. arXiv: 1305.2204.

Naab, Thorsten and Andreas Burkert (2003). "Statistical Properties of Collisionless Equal- and Unequal-Mass Merger Remnants of Disk Galaxies". In: 597.2, pp. 893–906. DOI: 10.1086/378581. arXiv: astro-ph/0110179 [astro-ph].

Navarro, Julio F., Carlos S. Frenk, and Simon D. M. White (1997). "A Universal Density Profile from Hierarchical Clustering". In: 490.2, pp. 493–508. DOI: 10.1086/304888. arXiv: astro-ph/9611107 [astro-ph].

Noeske, K. G. et al. (2007). "Star Formation in AEGIS Field Galaxies since z=1.1: The Dominance of Gradually Declining Star Formation, and the Main Sequence of Star-forming Galaxies". In: 660.1, pp. L43–L46. DOI: 10.1086/517926. arXiv: astro-ph/0701924 [astro-ph].

Obreschkow, Danail et al. (2015). "Low Angular Momentum in Clumpy, Turbulent Disk Galaxies". In: 815.2, 97, p. 97. DOI: 10.1088/0004-637X/815/2/97. arXiv: 1508.04768 [astro-ph.GA].

Pelliccia, D. et al. (2017). "HR-COSMOS: Kinematics of star-forming galaxies at z 0.9". In: 599, A25, A25. DOI: 10.1051/0004-6361/201629064. arXiv: 1606.01934.

Pelliccia, Debora et al. (2019). "Searching for environmental effects on galaxy kinematics in groups and clusters at z 1 from the ORELSE survey". In: 482.3, pp. 3514–3549. DOI: 10.1093/mnras/sty2876. arXiv: 1807.04763 [astro-ph.GA].

Peng, C. Y. et al. (2010a). "Detailed Decomposition of Galaxy Images. II. Beyond Axisymmetric Models". In: 139, pp. 2097–2129. DOI: 10.1088/0004-6256/139/6/2097. arXiv: 0912.0731.

Peng, Y., R. Maiolino, and R. Cochrane (2015). "Strangulation as the primary mechanism for shutting down star formation in galaxies". In: 521.7551, pp. 192–195. DOI: 10.1038/nature14439. arXiv: 1505.03143 [astro-ph.GA].

Peng, Y.-j. et al. (2010b). "Mass and Environment as Drivers of Galaxy Evolution in SDSS and zCOSMOS and the Origin of the Schechter Function". In: 721, pp. 193–221. DOI: 10.1088/0004-637X/721/1/193. arXiv: 1003.4747 [astro-ph.CO].

Persic, M., P. Salucci, and F. Stel (1996). "The universal rotation curve of spiral galaxies - I. The dark matter connection". In: 281, pp. 27–47. DOI: 10.1093/mnras/281.1.27. eprint: astro-ph/9506004.

Pierce, M. J. and R. B. Tully (1992). "Luminosity-line width relations and the extragalactic distance scale. I - Absolute calibration". In: 387, pp. 47–55. DOI: 10.1086/171059.

Pizagno, J. et al. (2005). "Dark Matter and Stellar Mass in the Luminous Regions of Disk Galaxies". In: 633, pp. 844–856. DOI: 10.1086/491614. eprint: astro-ph/0504581.

Read, J. I. et al. (2006). "The tidal stripping of satellites". In: 366.2, pp. 429–437. DOI: 10.1111/j.1365-2966.2005.09861.x. arXiv: astro-ph/0506687 [astro-ph].

Reyes, R. et al. (2011). "Calibrated Tully-Fisher relations for improved estimates of disc rotation velocities". In: 417, pp. 2347–2386. DOI: 10.1111/j.1365-2966.2011.19415.x. arXiv: 1106.1650.

Roberts, Morton S. (1966). "A High-Resolution 21-CM Hydrogen-Line Survey of the Andromeda Nebula". In: 144, p. 639. DOI: 10.1086/148645.

Roman-Oliveira, F. V. et al. (2019). "OMEGA-OSIRIS mapping of emission-line galaxies in A901/2-V. The rich population of jellyfish galaxies in the multicluster system Abell 901/2". In: 484, pp. 892–905. DOI: 10.1093/mnras/stz007. arXiv: 1812.05629.

Romanowsky, Aaron J. and S. Michael Fall (2012). "Angular Momentum and Galaxy Formation Revisited". In: 203.2, 17, p. 17. DOI: 10.1088/0067-0049/203/2/17. arXiv: 1207.4189 [astro-ph.CO].

Rubin, Vera C. and Jr. Ford W. Kent (1970). "Rotation of the Andromeda Nebula from a Spectroscopic Survey of Emission Regions". In: 159, p. 379. DOI: 10.1086/150317.

Ruggiero, Rafael (2019). "Galaxy Evolution in Clusters". In: *arXiv e-prints*, arXiv:1902.05363, arXiv:1902.05363. arXiv: 1902.05363 [astro-ph.GA].

Ruggiero, Rafael and Gastao B. Lima Neto (2017). "The fate of the gaseous discs of galaxies that fall into clusters". In: 468.4, pp. 4107–4115. DOI: 10.1093/mnras/stx744. arXiv: 1703.08550 [astro-ph.GA].

Sersic, Jose Luis (1968). *Atlas de Galaxias Australes*.

Smith, R., J. I. Davies, and A. H. Nelson (2010). "How effective is harassment on infalling late-type dwarfs?" In: 405.3, pp. 1723–1735. DOI: 10.1111/j.1365-2966.2010.16545.x. arXiv: 1004.4602 [astro-ph.CO].

Speagle, J. S. et al. (2014). "A Highly Consistent Framework for the Evolution of the Star-Forming "Main Sequence" from z ~0-6". In: 214.2, 15, p. 15. DOI: 10.1088/0067-0049/214/2/15. arXiv: 1405.2041 [astro-ph.GA].

Springel, Volker and Lars Hernquist (2003). "Cosmological smoothed particle hydrodynamics simulations: a hybrid multiphase model for star formation". In: 339.2, pp. 289–311. DOI: 10.1046/j.1365-8711.2003.06206.x. arXiv: astro-ph/0206393 [astro-ph].

Steinhauser, D., S. Schindler, and V. Springel (2016). "Simulations of ram-pressure stripping in galaxy-cluster interactions". In: 591, A51, A51. DOI: 10.1051/0004-6361/201527705. arXiv: 1604.05193.

Tacconi, L. J. et al. (2010). "High molecular gas fractions in normal massive star-forming galaxies in the young Universe". In: 463.7282, pp. 781–784. DOI: 10.1038/nature08773. arXiv: 1002.2149 [astro-ph.CO].

Tacconi, L. J. et al. (2013). "Phibss: Molecular Gas Content and Scaling Relations in z ~1-3 Massive, Main-sequence Star-forming Galaxies". In: 768.1, 74, p. 74. DOI: 10.1088/0004-637X/768/1/74. arXiv: 1211.5743 [astro-ph.CO].

Teyssier, Romain, Damien Chapon, and Frédéric Bournaud (2010). "The Driving Mechanism of Starbursts in Galaxy Mergers". In: 720.2, pp. L149–

L154. DOI: 10.1088/2041-8205/720/2/L149. arXiv: 1006.4757 [astro-ph.CO].

Tiley, A. L. et al. (2016). "The KMOS Redshift One Spectroscopic Survey (KROSS): the Tully-Fisher relation at z ˜1". In: 460, pp. 103–129. DOI: 10.1093/mnras/stw936. arXiv: 1604.06103.

Tomczak, Adam R. et al. (2016). "The SFR-M* Relation and Empirical Star-Formation Histories from ZFOURGE* at 0.5 < z < 4". In: 817.2, 118, p. 118. DOI: 10.3847/0004-637X/817/2/118. arXiv: 1510.06072 [astro-ph.GA].

Tomczak, Adam R. et al. (2017). "Glimpsing the imprint of local environment on the galaxy stellar mass function". In: 472.3, pp. 3512–3531. DOI: 10.1093/mnras/stx2245. arXiv: 1709.00011 [astro-ph.GA].

Tully, R. B. and J. R. Fisher (1977). "A new method of determining distances to galaxies". In: 54, pp. 661–673.

Übler, H. et al. (2017). "The Evolution of the Tully-Fisher Relation between z ˜2.3*andz*0.9*withKMOS*^{3D}". In: 842, 121, p. 121. DOI: 10.3847/1538-4357/aa7558. arXiv: 1703.04321.

van de Hulst, H. C., E. Raimond, and H. van Woerden (1957). "Rotation and density distribution of the Andromeda nebula derived from observations of the 21-cm line". In: 14, p. 1.

van den Bosch, Frank C. et al. (2008). "The importance of satellite quenching for the build-up of the red sequence of present-day galaxies". In: 387.1, pp. 79–91. DOI: 10.1111/j.1365-2966.2008.13230.x. arXiv: 0710.3164 [astro-ph].

van der Wel, A. et al. (2014). "3D-HST+CANDELS: The Evolution of the Galaxy Size-Mass Distribution since z = 3". In: 788, 28, p. 28. DOI: 10.1088/0004-637X/788/1/28. arXiv: 1404.2844.

Wetzel, A. R. et al. (2013). "Galaxy evolution in groups and clusters: satellite star formation histories and quenching time-scales in a hierarchical Universe". In: 432, pp. 336–358. DOI: 10.1093/mnras/stt469. arXiv: 1206.3571.

Whitaker, Katherine E. et al. (2014). "Constraining the Low-mass Slope of the Star Formation Sequence at 0.5 < z < 2.5". In: 795.2, 104, p. 104. DOI: 10.1088/0004-637X/795/2/104. arXiv: 1407.1843 [astro-ph.GA].

Wolf, C. et al. (2003). "The evolution of faint AGN between z =∼1 and z =∼5 from the COMBO-17 survey". In: 408, pp. 499–514. DOI: 10.1051/0004-6361:20030990. arXiv: astro-ph/0304072 [astro-ph].

Ziegler, B. L. et al. (2002). "The Evolution of the Tully-Fisher Relation of Spiral Galaxies". In: 564.2, pp. L69–L72. DOI: 10.1086/338962. arXiv: astro-ph/0111146 [astro-ph].

Ziegler, B. L. et al. (2003). "Internal Kinematics of Spiral Galaxies in Distant Clusters". In: 598, pp. L87–L90. DOI: 10.1086/379623. eprint: astro-ph/0309267.